The UNIVERSITY of LIVERPOOL

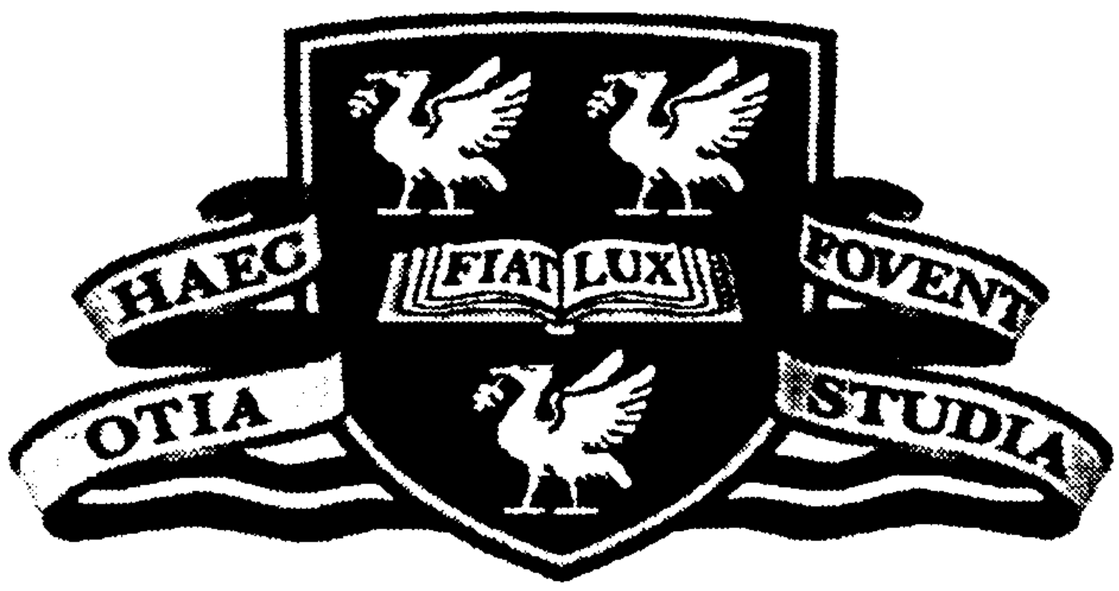

The Application of Ground Penetrating Radar to the Characterisation of Multi-layered Media

Thesis submitted in accordance with the
requirements of the University of Liverpool
for the degree of Doctor of Philosophy

in

Electrical Engineering and Electronics

by

Mansor Nakhkash

June 1999

In The Name Of The Most High

The Application of Ground Penetrating Radar to the Characterisation of Multi-layered Media

by

Mansor Nakhkash

Copyright **1999**

To my dear parents Mr. Nakhkash and Mrs. Mojahed
and my loving family Minou, Fatemah and Mohammad.

Abstract

An inverse scattering method for reconstructing the permittivity, conductivity and permeability profiles of a multi-layered medium is developed. The inversion is based on the minimization of an objective function that is defined as the mean square error between the measured and simulated scattering data. The method is employed to find the dielectric parameters of layered media using the data collected by Ground Penetrating Radar (GPR). A GPR facing a multi-layered medium is modelled by a new formulation, which relates the received signal to the reflection coefficient of the medium. The antenna-medium coupling has been taken into account in the model. Thus, the GPR antenna can be placed in the close proximity to the medium under investigation. This results in a higher signal-to-noise ratio, lower diffraction from the edge of the medium and lower extraneous reflections.

Instead of using a nonlinear integral equation, an exact closed-form expression is used for the reflection coefficient. The gradient of the objective function is also derived analytically. A substantial improvement in the efficiency of the inverse method can therefore be achieved. The necessary condition for the unique reconstruction of the profile of layered media from the reflection coefficient data is also derived.

Reconstructions have been carried out using simulated annealing and Multi-Level Single-Linkage (MLSL) method to minimize the objective function. It has been demonstrated that the MLSL method provides a superior performance in terms of both reliability and efficiency. Further improvement in the performance has been achieved by combining the MLSL with a novel optimisation technique especially developed for this project.

Using both experimental and simulated data, various reconstruction examples of layered media have been presented.

Acknowledgements

I would like to express my sincere thanks to my supervisors Dr. Y. Huang and Professor M.T.C. Fang for their invaluable help, encouragement and guidance throughout this work. The support and wise advice from Professor Fang are especially appreciated. I am also indebted to Professor J.D. Parsons for his support and introducing me the beauty of mobile radio communication.

I wish to acknowledge the financial support provided by Ministry of Culture and Higher Education of Iran during the course of this project.

I am deeply grateful to Civil Engineering Department, particularly Mr. A. Al-Shaari who sacrificed many hours of his time to assist in collecting data. I would like to express my appreciation to my friends and colleagues, Mr. C. Dixon, Mr. D.C. Kemp, Mr. S. Naruniranat, Mr. W. Al-Nuaimy and Mr. P.S.H. Leather for their invaluable discussions. I also wish to acknowledge my appreciation to Mrs. J. Cowan and Mrs. B. Lussey for their constant help.

I would like to thank Dr. T. Nguyen and Dr. M.J. Quick of shell Research Ltd. (UK) and Dr. A. Eriksen of GSI Ltd. (UK) for providing SIR2 system and GPR data. Also, appreciation and thanks go to Cray Research Inc. (Minnesota 55121 USA), especially Mr. K. Thomas for providing LC and technical support, Professor L. Ingber and other contributors (Lester Ingber Research, Mclean, USA) for providing ASA code.

Finally, my warmest appreciation goes to my dear parents and my loving family for their understanding, support and encouragement.

Contents

List of Figures

List of Tables

Abbreviations, acronyms and symbols

The symbols listed below are those which have been used consistently and frequently throughout the thesis. Due to the large number of quantities to be represented, it has been necessary to use some symbols to represent different quantities at different times. In every instance, the symbol has been defined where it is introduced so as to avoid misinterpretation of its meaning.

Abrev.	Description
GPR	Ground Penetrating Radar
IS	Inverse Scattering
EIS	Electromagnetic Inverse Scattering
1D	1-Dimensional
ADC	Analog-to-Digital Converter
SNR	Signal-to-Noise Ratio
MLSL	Multi-Level Single-Linkage
GA	Genetic Algorithms
SA	Simulated Annealing
ASA	Adaptive Simulated Annealing
ARS	Adaptive Random Search
MLSLARS	combination of MLSL and ARS methods
RMBI	Reflectivity Model-Based Inversion
MSE	Mean Square Error
FDTD	Finite-Difference Time-Domain
FR model	the model considering the First Reflection
AM model	the model considering the Antenna-Medium coupling
AM-MW	AM model with Metal-Water approach

continued on next page

continued from previous page

Abrev.	Description
AM-MM	AM model with Metal-Metal approach
GSSI	Geophysical Survey Systems Incorporation
NAG	Numerical Algorithm Group
t	time
ω	angular frequency
σ	conductivity
ϵ	permittivity
ϵ_r	relative permittivity
ϵ_0	permittivity of free space
μ	permeability
μ_r	relative permeability
μ_0	permeability of free space
h	thickness of a medium or length of a transmission line
γ	propagation constant
γ_0	propagation constant of free space
θ	incident angle
c	velocity of light in free space
Y	characteristic admittance
W	surface admittance
Γ	reflection coefficient of a multi-layered medium
Υ	reflection coefficient of a half-space medium
Re[a]	Real part of a
$\mathbb{R}$	set of real number
$\mathbf{x}$	a point in a multi-dimensional real space
f	objective function
δ	δ-function

continued on next page

continued from previous page

Abrev.	Description
sgn	sign function
GF	gamma function

Chapter 1

Introduction

The need for remote sensing of subsurface anomalies has increased significantly over the past few years. Knowledge of an industrial site is now required prior to plant construction and for site remediation when industrial plants are dismantled. The presence of contaminants in the subsurface is nowadays one of the greatest concerns because they may be hazardous to public health. Non-destructive inspection of high-value structures, like highway pavements, bridges and buildings, is also growing in importance. Such structures need to be properly monitored and maintained; otherwise, they can pose a threat to safety. Another example is the need for the detection of buried land mines, which is a problem of military and humanitarian concern.

Ground Penetrating Radar (GPR) has been found to be an attractive solution to the above remote sensing problems. GPR is an electromagnetic system employed for non-intrusive detection and identification of subsurface objects and structures. It provides inexpensive quick surveys by allowing non-destructive investigation of media without resorting to digging, drilling, or taking core sample. GPR was Originally developed for military applications [53], such as the detection of tunnels and buried mines. Since then, its application has been extended to diverse areas ranging from geophysics to civil engineering

and archaeology. These applications include the prediction of concrete deterioration [10], pavement profiling [61], monitoring subsurface contaminations [16], [27], and ice thickness profiling [28]. A general description of the ground penetrating radar system together with its applications is given in [15].

The principle of operation of GPR is similar to that of conventional radar. A series of short pulses are propagated into the medium under examination. The reflected wave from target (generally any discontinuity in the electromagnetic parameters) is received and processed to extract useful information. Compared with conventional radar, the interpretation of GPR data however requires sophisticated signal processing because of differences in the type of targets and the host medium. The signal received by a conventional radar is the reflection of electromagnetic wave from large metallic objects or land masses through air, a known non-dispersive medium. Nevertheless, for GPR applications the targets can be non-metallic objects located in an unknown host medium with significant attenuation, such as the ground. The interpretation of GPR data has therefore been the main concern in its application and still remains as an active research area after 25 years of usage of the system.

1.1 Review of Previous Works and Relevant Problems

The interpretation of GPR data is primarily based on the identification of typical response signatures resulting from the contribution of particular subsurface anomalies and inhomogeneities to the scattered field. The interpretation is therefore largely comparative and requires considerable skill and experience, which are basically obtained from experiments conducted. The experience can also be acquired from a systematic study of the influences of various factors based on a laboratory model of the problem, such as the work of Bungey *et al.*

---

[10] and that of Smith and Scott [60]. A cheap and quick alternative to gain a better understanding of the scattering responses for the GPR data interpretation is to use numerical simulation, for example, finite-difference time-domain (FDTD) method [7], [8]. The identification and analysis of the response signatures may be facilitated and automated by employing image processing and pattern recognition methods [3], [20], [41].

The aforementioned techniques aim at recognition and discrimination of the targets without providing the information on their location, shape and profile. Inverse scattering (IS) methods should be employed for the extraction of such information. Johansson and Mast [35] have used synthetic aperture focusing to locate the steel reinforcing bars in a concrete slab. The application of this technique is limited to the cases where the host media are non-dispersive with a known wave propagation velocity. Diffraction tomography [43] has the capability to generate the target profile using GPR data. However, this method can only be applied under certain restrictions [59], which are imposed on the properties of the host medium and target. In general, these restrictions are not met for many GPR applications. Such limitations have stimulated the development of spatial-iterative methods for the reconstruction of arbitrary profiles [12], [29], [34], [52]. Weedon *et al.* [66] have employed a spatial-iterative techniques known as the distorted-Born iterative to reconstruct plastic PVC pipes located in air. Promising results have been reported. The main disadvantage of the spatial-iterative methods are their computational inefficiency, especially when dealing with 3-dimensional problems. High computation cost has restricted the application of these methods in the area where 3-dimensional effects are important. However, the rapid advancement in computer technology may alleviate this problem in future [52].

1-Dimensional (1D) IS methods are computationally efficient and realisable in real time. They can be used to reconstruct the profile of layered media. The ground and other host media are of multi-layered structures for many GPR

applications. The targets for some GPR usages, such as pavement profiling, stratigraphic and permafrost mapping, are layered media. When the dimensions of a finite-size target are large comparing with the radiated wavelength, such a target may be considered as a planar layer as well. Consequently, 1D IS techniques are useful for the interpretation of GPR data in various applications. Such an approach has successfully been used by Spagnolini [61] for finding the profile of road pavements and by Golden *et al.* [26] for reconstructing the profile of a layered medium consisting of drywall and polystyrene foam on top of sand.

The 1D IS techniques can be divided into two categories: the direct and the model-based inversions. Layer-stripping method that belongs to the direct category has been used for finding the parameters of a multi-layered medium [9], [21], [22], [26]. The method involves solving for the parameters of each layer consecutively. In this way, the medium is mathematically stripped away layer by layer, and the properties of the medium are derived in the process. The layer-stripping technique is fast but it is often unstable. The model-based inversions rely on an optimisation procedure in which the profile of a medium is reconstructed by minimizing a suitable objective function. Various algorithms using different optimisation techniques in this category have been applied to the inverse problem of layered media [26], [30], [49], [64]. The model-based methods have the advantage of being robust and broadly applicable; their disadvantage is that they tend to be computationally intensive. In addition, the optimisation procedure employed in the model-based inversions should converge to the lowest (global) minimum; otherwise, the true profile is not found. Local optimisation techniques, such as the conjugate gradient method, have often been used [26], [30], [49], [64]. These methods are likely to get stuck in a local minimum, thus giving a wrong solution. In order to overcome this problem, Sen and Stoffa [57] have suggested employing genetic algorithm (GA) and simulated annealing (SA). Although GA and SA improve the reliability of

finding the global minimum, they tend to increase the computational cost.

1.2 Overview of the Thesis

As explained in the previous section, 1D inversion is at present a practicable approach for the interpretation of GPR data in many applications. The primary objective of this research is therefore to develop a 1D inverse technique that employs GPR data to characterise layered media. This study addresses and discusses in more details the issues outlined in Section 1.1 for GPR data interpretation, inverse scattering and optimisation. We aim to develop a 1D inverse method that provides better stability, efficiency and reliability in comparison with the previous 1D inverse methods.

The thesis focuses on inverse scattering problem, global optimisation and the modelling of GPR. The organisation of the thesis is as follows:

★ *Chapter 2* describes a GPR system and some standard preprocessing techniques. The methods used to interpret GPR data are formulated and the difficulties associated with them are discussed. Finally, the chapter provides some conclusions that justify the use of 1D inversion for GPR.

★ *Chapter 3* elaborates on the formulation of 1D electromagnetic forward and inverse problems. Two mathematical forward models, the 1D nonlinear integral equation [6] and the reflectivity formulation [65], are introduced. Layer-stripping method is described in detail and an example of its application to reconstruct the profile of a 3-layer medium is presented. The example demonstrates the instability of the layer-stripping technique. This chapter covers our contribution to the development of a novel 1D model-based inverse method, reflectivity model-based inversion (RMBI), in which the computational efficiency is greatly improved by using the reflectivity formulation. We also derive the necessary condition for the unique reconstruction of the parameters of a layered medium in this chapter. It is finally demonstrated that a global optimisation

technique should be used in the RMBI.

★ *Chapter 4* provides a comparative study of four global optimisation methods, genetic algorithm, simulated annealing, adaptive simulated annealing (ASA) and multi-level single-linkage (MLSL). GA and the MLSL have already been compared by Renders and Flasse [56]. Their results indicate that the MLSL method has a higher accuracy and efficiency than GA. Thus, several reconstruction examples of layered media are presented to compare three other techniques. It is shown that a significant improvement in accuracy, efficiency and reliability can be achieved by using the MLSL method. Despite good performance of the MLSL, it fails or needs a substantial amount of computation time to solve those 1D inverse problems in which the medium comprises a relatively large number of layers. This is especially true when the deepest layer is unknown, the observed data is rather incomplete and/or the optimisation has to be carried out within a large space of the medium parameters. In order to remedy such a deficiency, a hybrid optimisation method is proposed by combining the MLSL method with another optimisation algorithm, the adaptive random search. The application of the hybrid method to various reconstruction examples confirms the improvement in the efficiency and reliability.

★ *Chapter 5* deals with the mathematical modelling of a GPR antenna above the surface of a layered medium. Inspired by free-space measurement techniques [2], [36], [37], we derive a model that relates the signal received by the antenna to the reflection coefficient of the medium. The model takes into account the antenna-medium coupling. This makes it possible to considerably reduce the separation between the GPR antenna and medium in comparison with conventional free-space methods. Experimental investigations and numerical examples verify that the separation might be of the order of a wavelength or less. The application of the proposed model to the measurement of the electromagnetic properties results in a higher accuracy as well. This chapter also details a FDTD model of a commercial GPR and the considerations required

for the simulation of the GPR antenna.

★ *Chapter 6* presents a summary of the work and discusses the future continuation of the research.

1.3 Major Contributions

1. Development of a novel 1D model-based inverse method, the reflectivity model-based inversion (RMBI).

2. Derivation of the necessary condition for the unique solution to 1D electromagnetic inverse problems.

3. Characterisation of layered dielectric medium using the reflection coefficient ([31]).

4. Application of the MLSL method to the inverse problem of layered media ([45], [47]).

5. A hybrid global optimisation technique.

6. Modelling of a GPR above a multi-layered medium and its application to the measurement of the complex permittivity ([46]).

Chapter 2

GPR System and Signal Processing

2.1 Introduction

Ground penetrating radar is based on the same principle as conventional radar. Electromagnetic energy propagates through a medium and is partially scattered from discontinuities in the electromagnetic parameters of the medium, i.e. the conductivity, permittivity and permeability. The scattered wave, which returns to the receiving antenna, is detected and processed to extract the information.

Two modes of operation can be classified for GPR systems: The first is the frequency-domain mode and the second is the time-domain mode. The radiated signal in the frequency-domain mode comprises a number of narrow-band signals that cover a broad band of frequency as a whole. These signals are transmitted by sweeping through a range of frequencies and the magnitude and phase of the received signal are recorded at each frequency as radar data. The systems operated in this mode are referred to as step-frequency radar. In the time-domain mode, a short-duration pulse (ideally an impulse) is transmitted

and the received signal is sampled in the time-domain as radar data. This kind of radar is called pulse radar. Through the use of Fourier transform, the data in the time domain may be converted to the frequency domain and vice versa. Thus, most of the processing techniques described in this thesis are equally applicable to both systems.

Due to the popularity of pulse radar, and for completeness, it is described in Section 2.2 in some detail. Section 2.3 introduces several preprocessing techniques. The processing and interpretation of the GPR data are discussed in Section 2.4. Finally, Section 2.5 is devoted to concluding remarks that justify the direction of this research.

2.2 Principles of Operation

Figure 2.1 illustrates a typical pulse GPR. After the synchroniser triggers the pulse generator and the sampler, the transmitting antenna is excited by a pulse and radiates a signal which penetrates into the ground. The signal is partially scattered from the object or in general from any discontinuities in the electromagnetic parameters in the subsurface. A portion of the scattered signal returns to the surface, where it excites the receiving antenna. The received signal is then filtered, sampled and recorded. Figure 2.2 shows SIR-2 system, a pulse GPR manufactured by Geophysical Survey Systems Incorporation (GSSI). This system can be used with a range of antennas for various frequencies. A 400 MHz antenna is shown in Fig. 2.2.

2.2.1 Pulse generator

The pulse generator produces a train of short-duration step pulses ($p(t)$). Pulse width of such a pulse is usually of the order of a few nanoseconds and its amplitude is typically within the range 20-200 V. A reasonable approximation

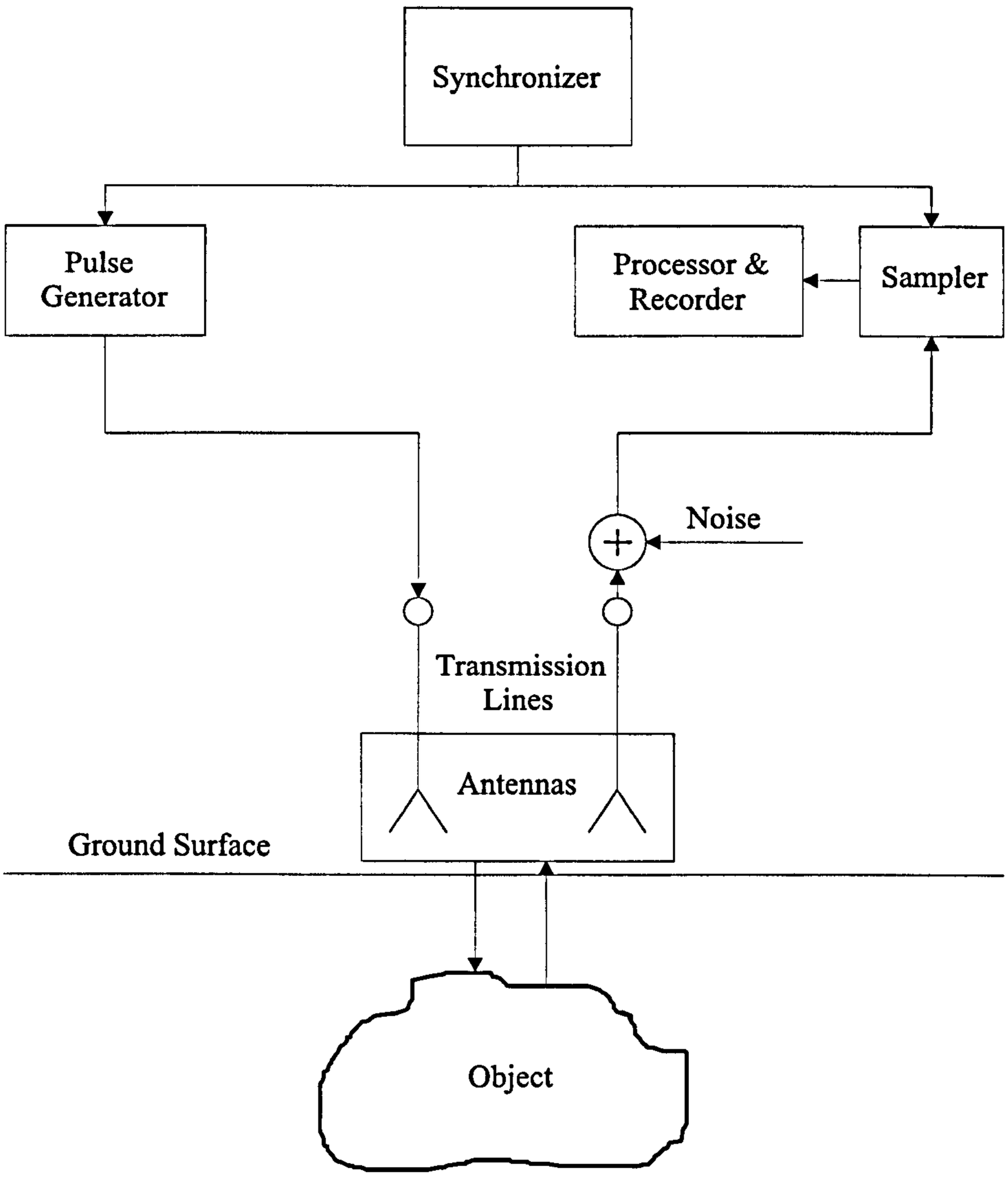

Figure 2.1: Schematic diagram of a typical pulse GPR.

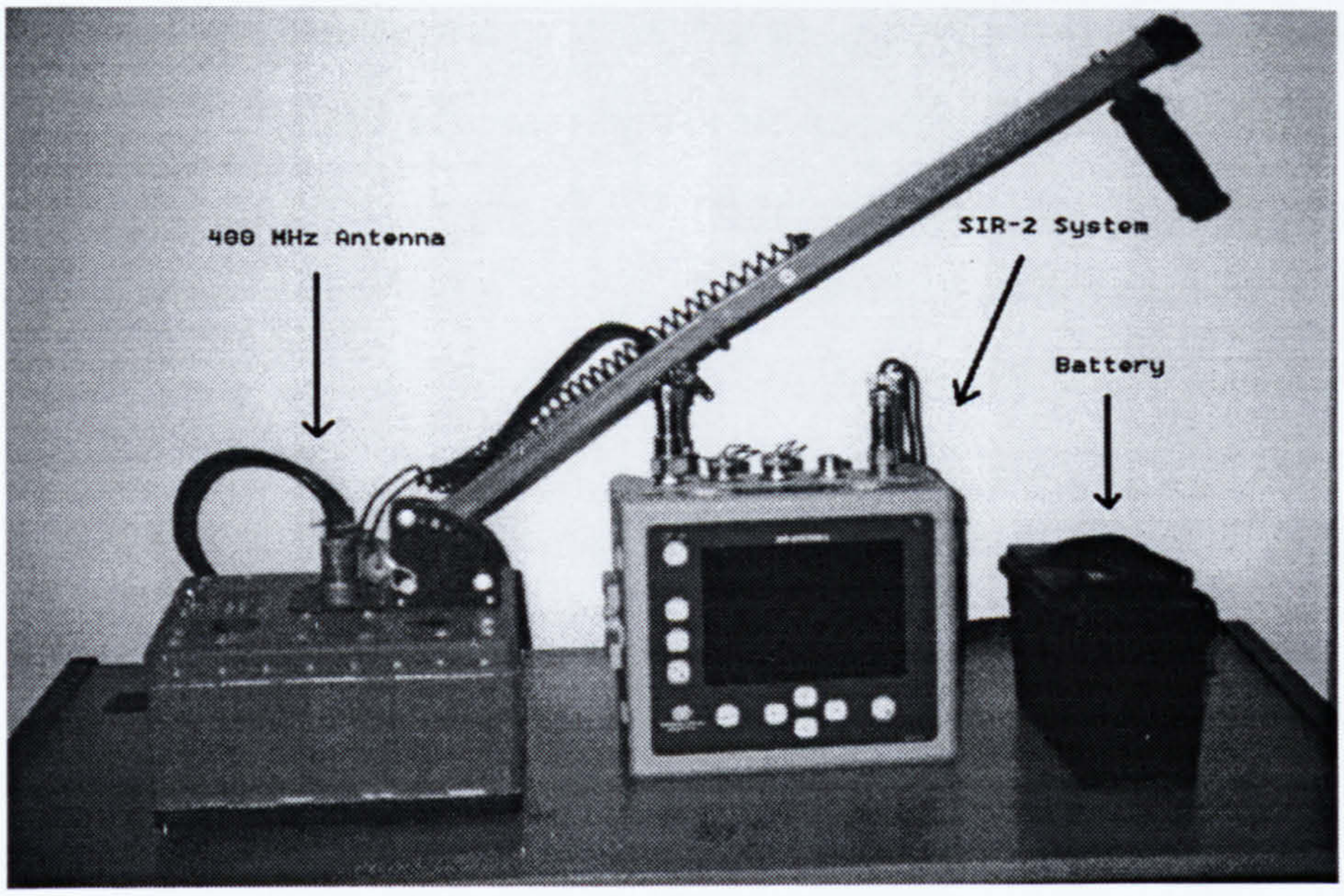

Figure 2.2: SIR-2 system and 400 MHz antenna.

for $p(t)$ is a Gaussian pulse [7], [53]

$$p(t) = V_0 \exp\left[-\frac{1}{2}\left(\frac{t}{\tau_0}\right)^2\right] \tag{2.2.1}$$

where V_0 is the peak amplitude of the pulse and τ_0 determines the pulse width. The spectrum of this pulse is broad and equal to [62, Page 178]

$$P(\omega) = V_0\sqrt{2\pi}\,\tau_0 \exp\left[-\left(\frac{\omega}{\omega_0}\right)^2\right] \quad , \quad \omega_0 = \frac{\sqrt{2}}{\tau_0} \tag{2.2.2}$$

Normalised $p(t)$ and $P(\omega)$ are shown in Fig. 2.3. The sign pulse in this figure will be referred to in Subsection 2.2.3 for comparison.

2.2.2 Sampler

The received analog signal may be converted to digital data using a fast Analog-to-Digital Converter (ADC). This sampling system captures the complete waveform in one pulse transmission period. However, ADCs are not fast

enough to be able to sample wideband GPR signals. The digital data are therefore mostly acquired using what is known as equivalent time sampling system [15, Chapter 5]. In this system, only a single discrete data point is acquired during each pulse transmission period. The first data point is acquired during the first pulse period, the second one during the second pulse period and so forth. In other words, the complete waveform is constructed from displaced samples of successive periods of the analog signal. Thus, if a received digital

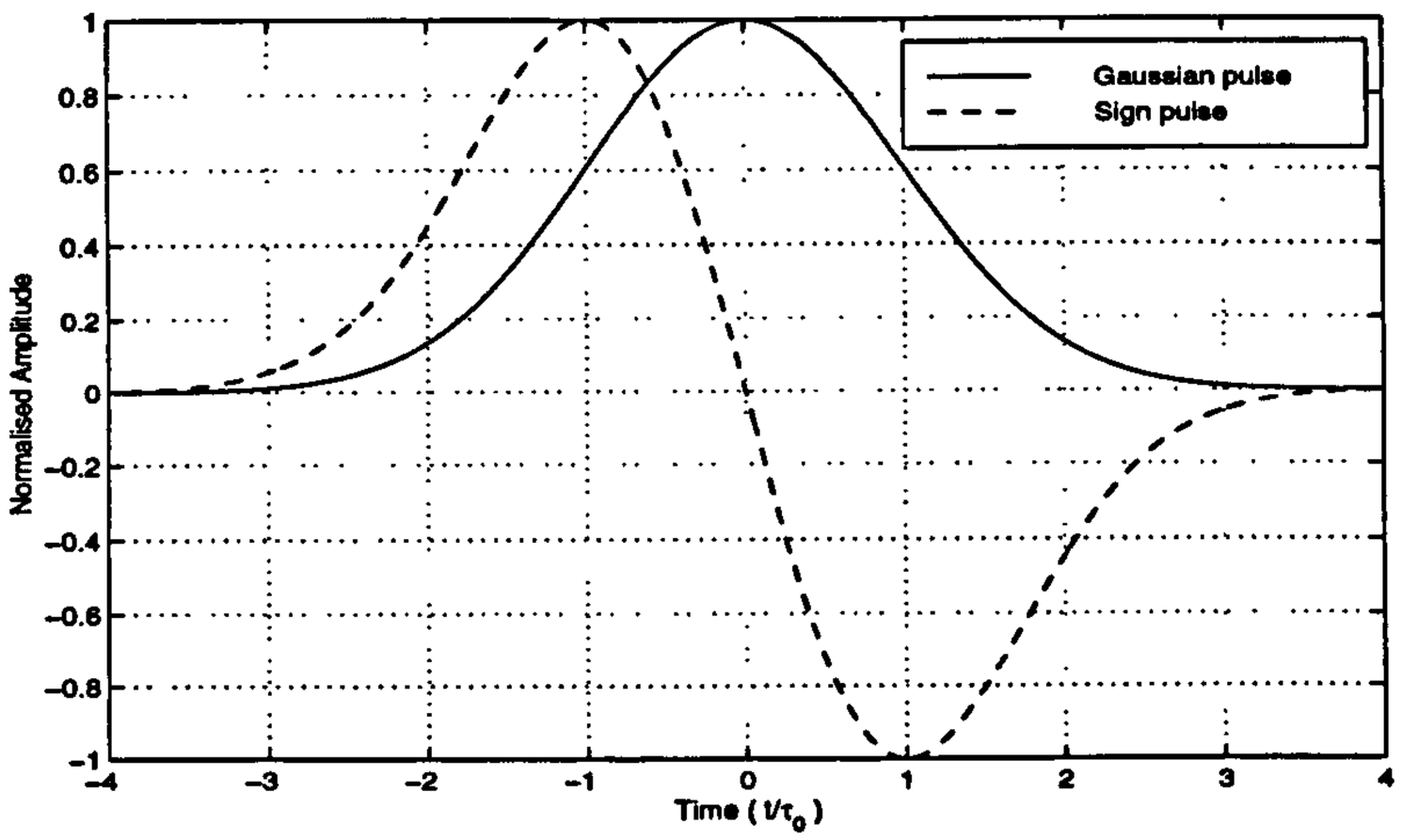

(a)

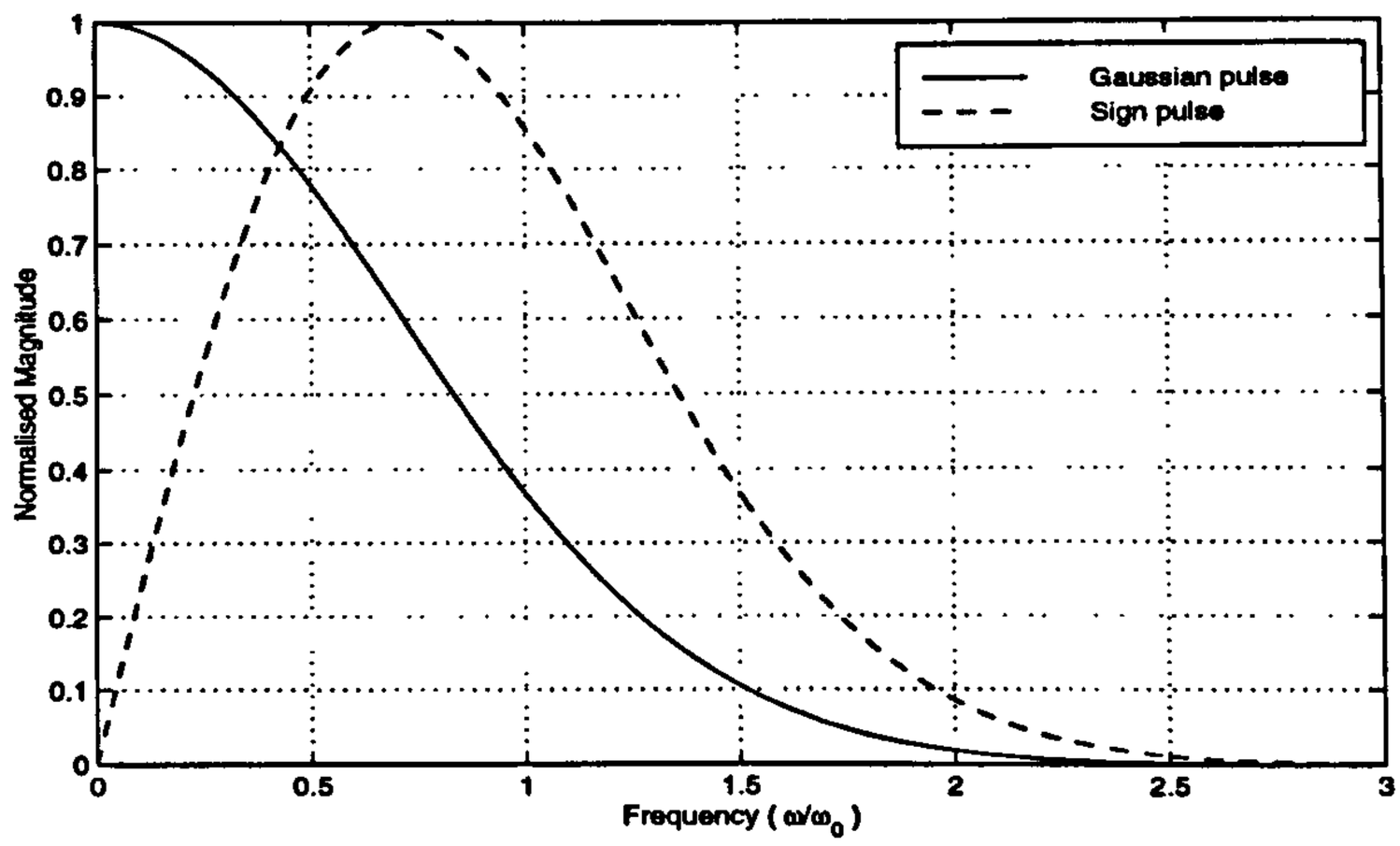

(b)

Figure 2.3: Gaussian and Sign pulses normalised to their amplitudes. (a) Time domain (b) Frequency domain.

signal consists of N samples, N pulses need to be transmitted.

The pulse generator and the sampler must be synchronised (the function of synchroniser) not only to preserve both the phase and amplitude information but also due to an essential need for the equivalent time sampling system. Any drift in synchronisation between the sampler and the pulse generator within the acquisition of a signal results in non-uniform sampling which distorts the received signal.

2.2.3 Antenna

There are two popular antenna configurations for GPR: monostatic and bistatic. The same antenna is used for transmitting and receiving in a monostatic configuration, whereas separate antennas are employed in a bistatic configuration. The antennas for a bistatic GPR can be mounted inside a box a finite distant apart, as shown in Fig. 2.1. The most common antennas used for GPR are dipole, bow-tie and horn antennas. Crossed dipoles or the time-domain monopulse antenna can also be used for bistatic configuration so as to minimize the energy directly coupled from the transmit to the receive antenna [53].

GPR antennas are loaded in order to make them broad band and to reduce the antenna ringing that could extend into the range window of the desired signal [53]. The radiated field (transmit wavelet) from a loaded antenna is nearly the time derivative of the driving pulse [15, Chapter 4], i.e. the antenna acts as first order high-pass filter in the bandwidth of the driving pulse. Assuming the driving pulse is Gaussian, the transmit wavelet will then be a Sign pulse $p^s(t)$

$$p^s(t) = -V_0^s \left(\frac{t}{\tau_0}\right) \exp\left[-\frac{1}{2}\left(\frac{t}{\tau_0}\right)^2\right] \tag{2.2.3}$$

The spectrum of $p^s(t)$ can be found by introducing $j\omega$ and a correction factor

(according to (2.2.3)) in (2.2.2). Thus

$$P^s(\omega) = jV_0^s\sqrt{4\pi}\,\tau_0\left(\frac{\omega}{\omega_0}\right)\exp\left[-\left(\frac{\omega}{\omega_0}\right)^2\right] \quad , \quad j=\sqrt{-1} \tag{2.2.4}$$

Fig. 2.3 shows a normalised Sign pulse and its spectrum. When an antenna is in the vicinity of the ground, the radiated field is determined by not only the antenna geometry but also its interaction with the ground (the antenna-ground coupling). This may also occur where two antennas are in close proximity, e.g. bistatic configuration. In such a situation, the transmitting frequency response of the antenna becomes more selective; thus the pulsewidth of the radiated field is increased. Furthermore, the wavelet might no longer be a sign pulse but a pulse that has many lobes such as Ricker pulse [54].

2.2.4 Data acquisition and representation

In order to conduct GPR surveys, the antenna is towed continuously over the ground. This can be carried out by pulling the GPR antenna by hand, or with a vehicle. Sampled waveforms are acquired at equally spaced points across the ground surface. The recorded data from each point is called a trace, or a scan. An ensemble of scans forms a 2-dimensional image referred as a 'B-scan' or 'radargram'. Each vertical line of a radargram corresponds to a sampled waveform (scan), whose amplitude is represented by the intensity of gray scale. A typical radargram is shown in Fig. 2.4(a) where the horizontal axis is the distance along the surface, and the vertical axis is two-way travel time from the antenna to a reflector in the subsurface. The reflector in this survey is a steel pipe buried in desert at a depth of 37 cm (to the top of the pipe). The antenna is operated at 900 MHz. The pipe can be detected from the hyperbola, whose top is at scan number 125 (the hyperbola can hardly be seen). The phenomenon of hyperbolae appearing in GPR images due to the presence of buried objects will be discussed in Section 2.4. The waveform of

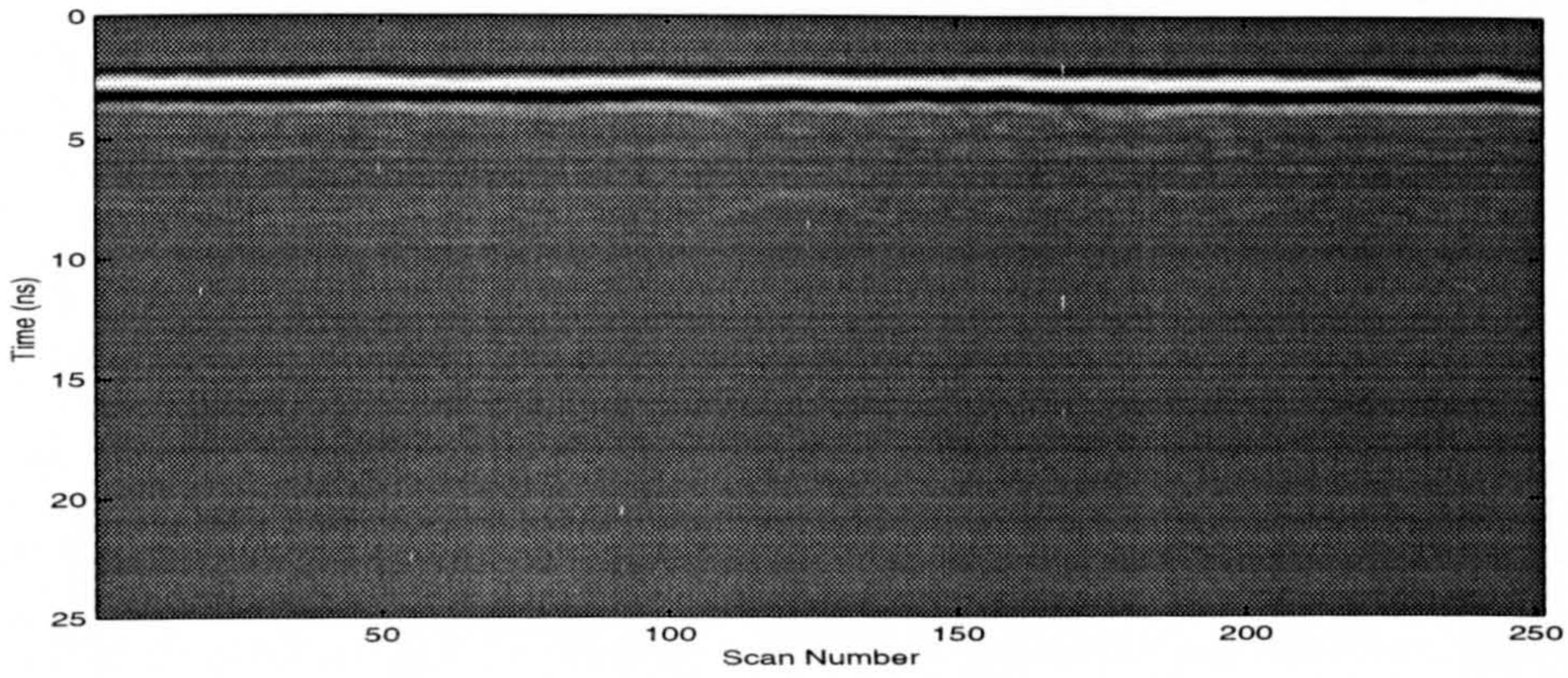

(a)

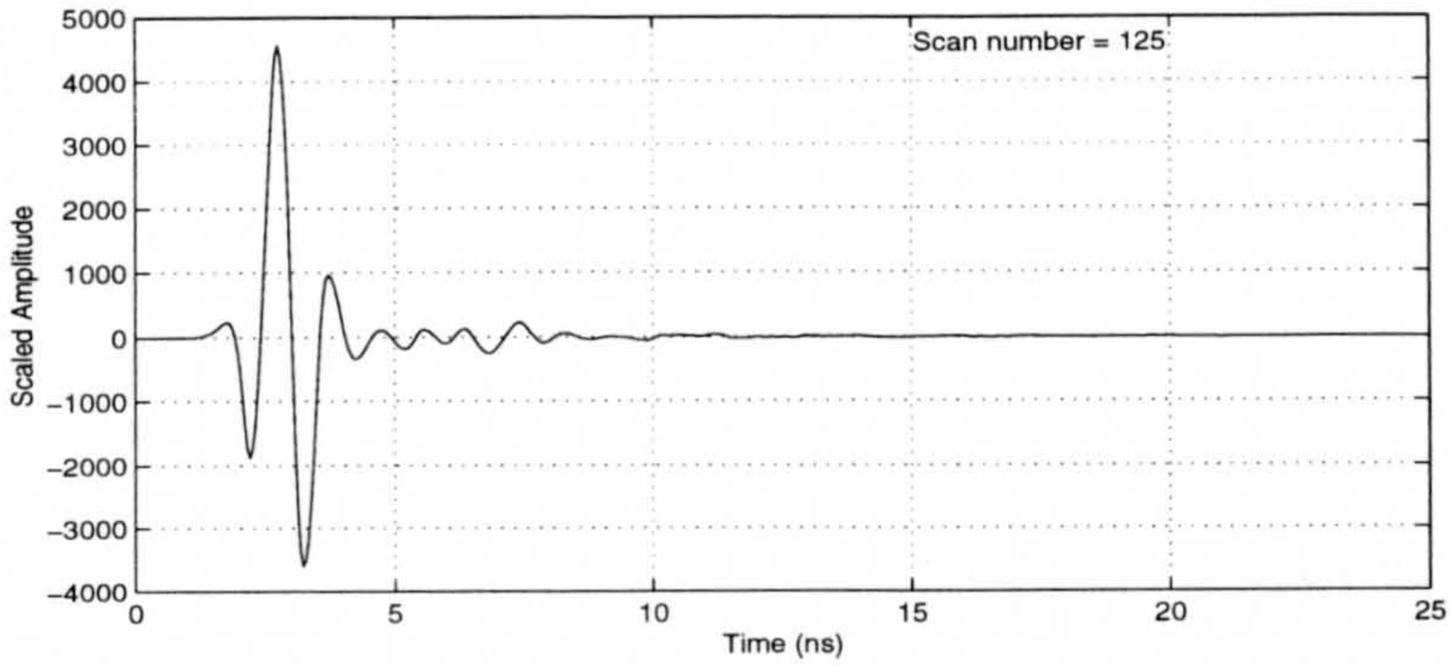

(b)

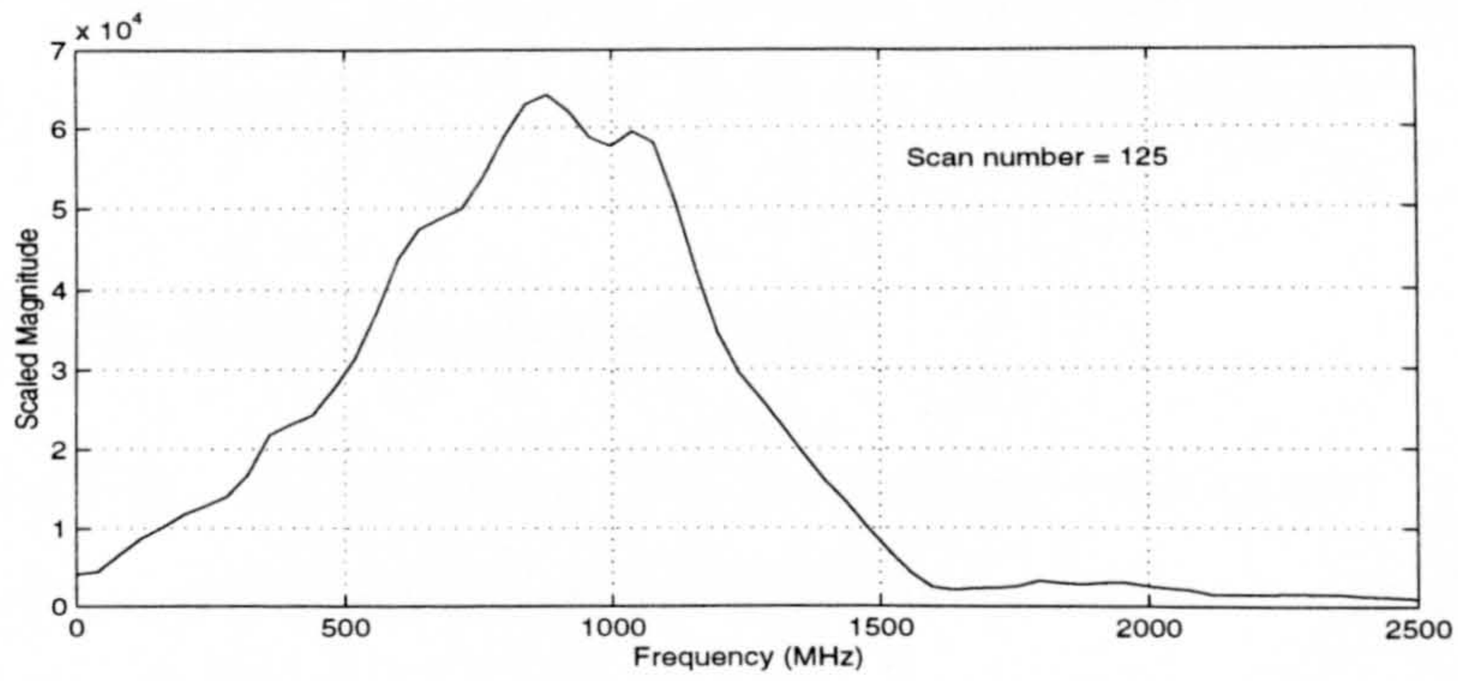

(c)

Figure 2.4: (a) A GPR image acquired in desert using 900 MHz antenna. Scan number 125 in (b) time-domain (c) frequency-domain.

scan number 125 in the time domain and frequency domain are shown in Fig. 2.4(b) and 2.4(c) respectively. The strong reflection at the beginning is the combination of the ground surface reflection, the internal antenna reflection and/or the antenna transmit-receive coupling signal. This reflection serves to establish a time-reference point for return-depth determination. The time delay to the first reflection is determined either automatically or manually to prevent sampling the portion that results from the delay in the transmission lines. The reflection from the pipe, which is hard to see in Fig. 2.4(b), lies nearly in the interval [5 ns, 7.5 ns].

2.3 Preprocessing

The raw GPR data needs to be preprocessed to enhance the part of the data related to the reflection from the target. This requirement can be understood from Fig. 2.4 in which the information from the pipe can hardly be observed. Three undesired effects, noise, common clutter and path loss are removed in the preprocessing stage. In this section, the widely used preprocessing techniques, i.e. path loss compensation, background removal, averaging and filtering are described. The description of other methods like pulse deconvolution can be found in [15, Chapter 6].

2.3.1 Path loss compensation

As a result of path loss both by the ground conductivity and by the spreading effect, the received signal is attenuated when compared with the transmitted one. This attenuation depends on the range of the reflector (r). If the reflector is flat enough in comparison with the wavelength, the spreading loss is in proportion to $\frac{1}{r}$. Otherwise, it is proportional to $\frac{1}{r^2}$ [15, Chapter 2]. The

medium (ground) loss (*Loss*) is given by

$$Loss = \mathrm{e}^{2\alpha r} \quad , \quad \alpha = \omega \sqrt{\frac{\mu\epsilon}{2}\left[\sqrt{1+\left(\frac{\sigma}{\omega\epsilon}\right)^2}-1\right]} \tag{2.3.1}$$

where σ, ϵ and μ are respectively the conductivity, permittivity and permeability of the medium and α is the *attenuation constant* .

Path loss is compensated by applying a time-variable gain (range gain) as shown in Fig. 2.5(a). The gain in decibel is selected as a piecewise linear function of time [24]. Assuming that the two-way travel time relates to r through a constant value, this selection can be justified by deriving *Loss* in decibel

$$Loss(dB) = 20 \log_{10} Loss = 17.372\,\alpha r \tag{2.3.2}$$

The above equation does not take account of the spreading loss. This might be because the medium loss is usually the dominant factor in path loss.

2.3.2 Background removal

In radar literature, those reflections that are unrelated to the target scattering characteristics but have similar spectral features to the target echo, are regarded as clutter. The common clutter is defined as the clutter that occurs in the same time window of several scans, e.g. the surface reflection, antenna ringing and the echoes from the subsurface planar interfaces.

Background removal eliminates the common clutter in GPR data. It is useful where there are a limited number of targets and they are well separated. Background removal is attained by dividing the radargram into vertical strips, taking an average of the scans across each strip and subtracting the average from each scan of the strip. The width of each strip is specified in terms of the relative location of the targets to each other. As a rule of the thumb, the

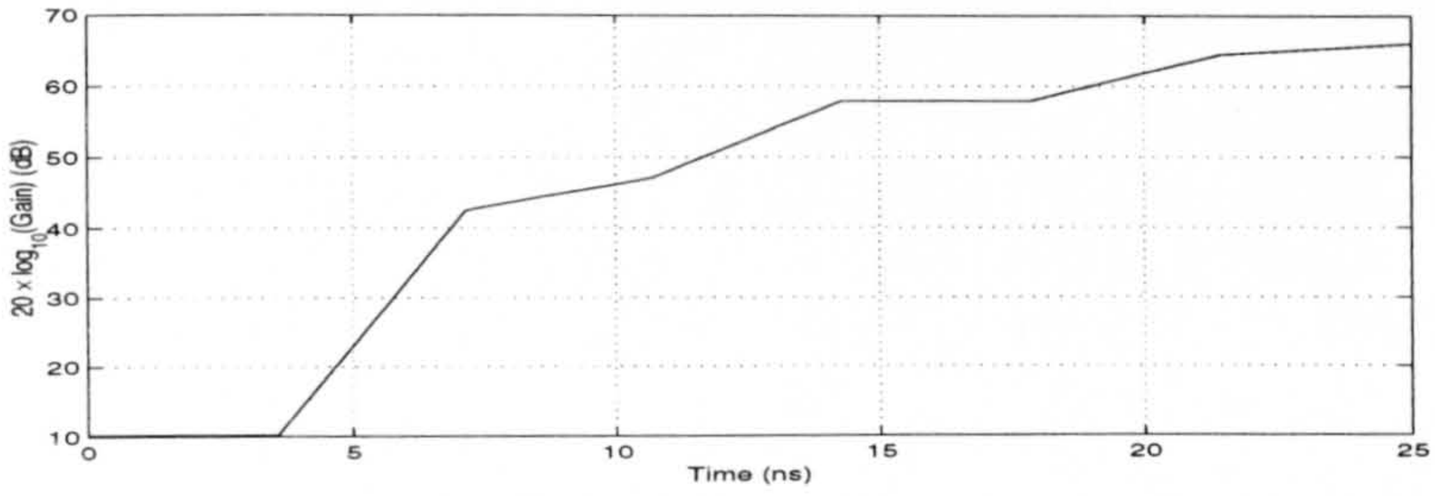

(a)

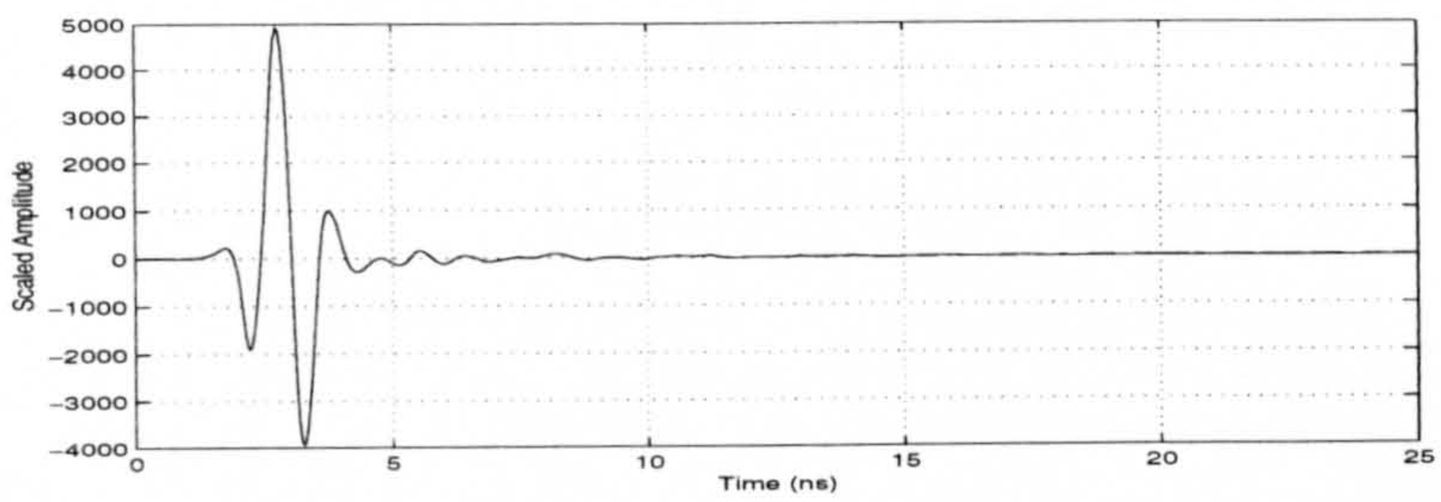

(b)

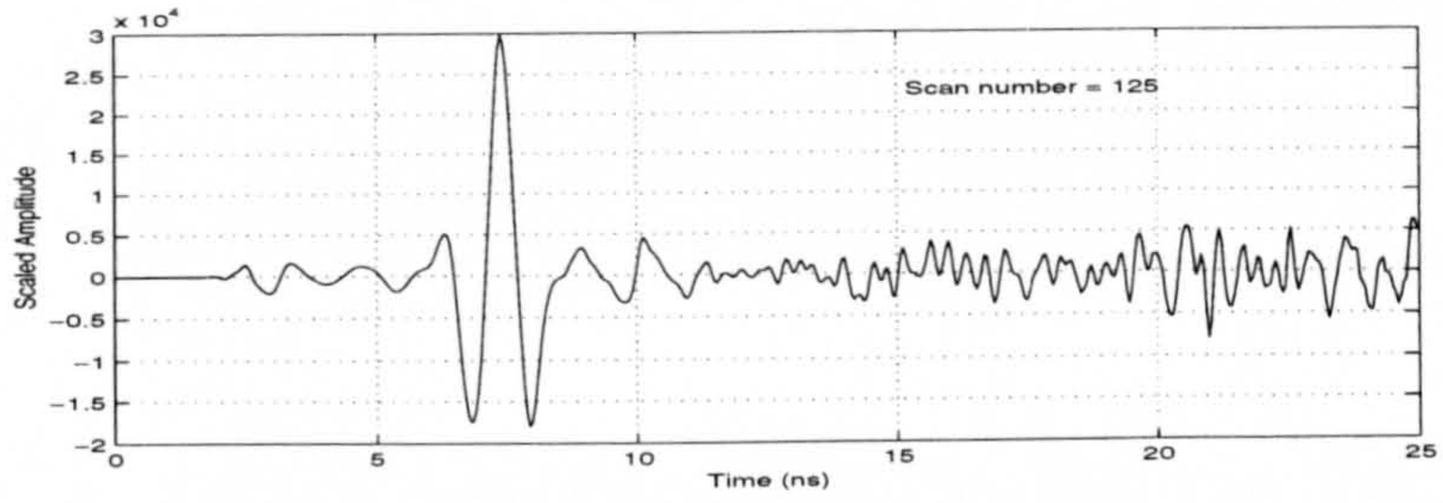

(c)

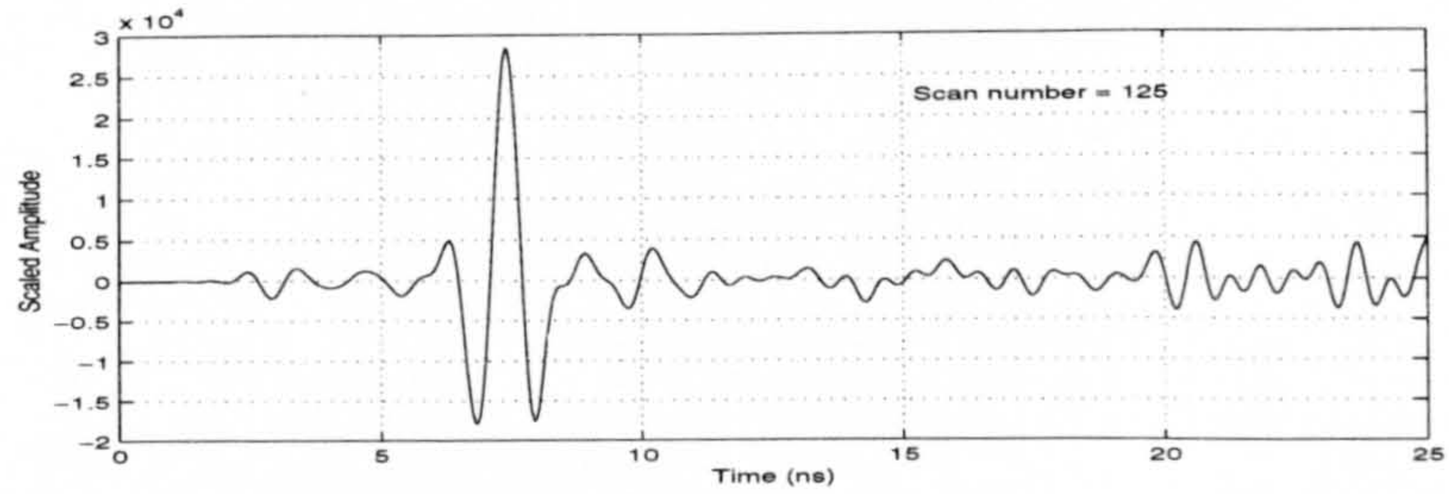

(d)

Figure 2.5: (a) Applied range gain to the image 2.4(a). (b) Background signal, the ensemble mean of the scans across the image. (c) Signal of scan number 125 after background removal and applying the range gain. (d) Filtered version of the above signal using a FIR low-pass filter with 1800 MHz cutoff frequency.

width for all strips is equally set to the number of scans of the largest target [24].

Figure 2.5(b) shows the background signal that is the average of 251 scans of the radargram 2.4(a). The echo from the steel pipe ([5 ns, 7.5 ns]) is clearly visible in Fig. 2.5(c) and 2.6(b) after background removal and applying the range gain.

2.3.3 Averaging and filtering

Averaging is one of the techniques used to eliminate the effect of noise. The average of a number of radar signals, taken at a single point on the ground, is considered as the received waveform for that point. Viewing the noise as additive white Gaussian noise, it can be shown that averaging N radar signals improves Signal-to-Noise Ratio (SNR) N times [51].

Another method to improve SNR is low-pass filtering, in which high frequency noise, especially visible in the lower portion of the radargram is removed. It is suggested in [24] that cutoff frequency of the low-pass filter should be twice the antenna frequency.

The effect of low-pass filtering can be observed in Fig. 2.5(d) where the reduction of the noise level is visible at late times. The effects of the preprocessing on the radargram 2.4(a) are illustrated in Fig. 2.6.

2.4 Interpretation of GPR data

The major problem with the application of GPR is the interpretation of its data. The standard methods used for conventional radar are not generally applicable to GPR because of two major differences. Firstly, in conventional radar the main objects reflecting radar signals are large metallic objects (e.g. an aircraft) or land masses, whereas in GPR, reflections can be caused by

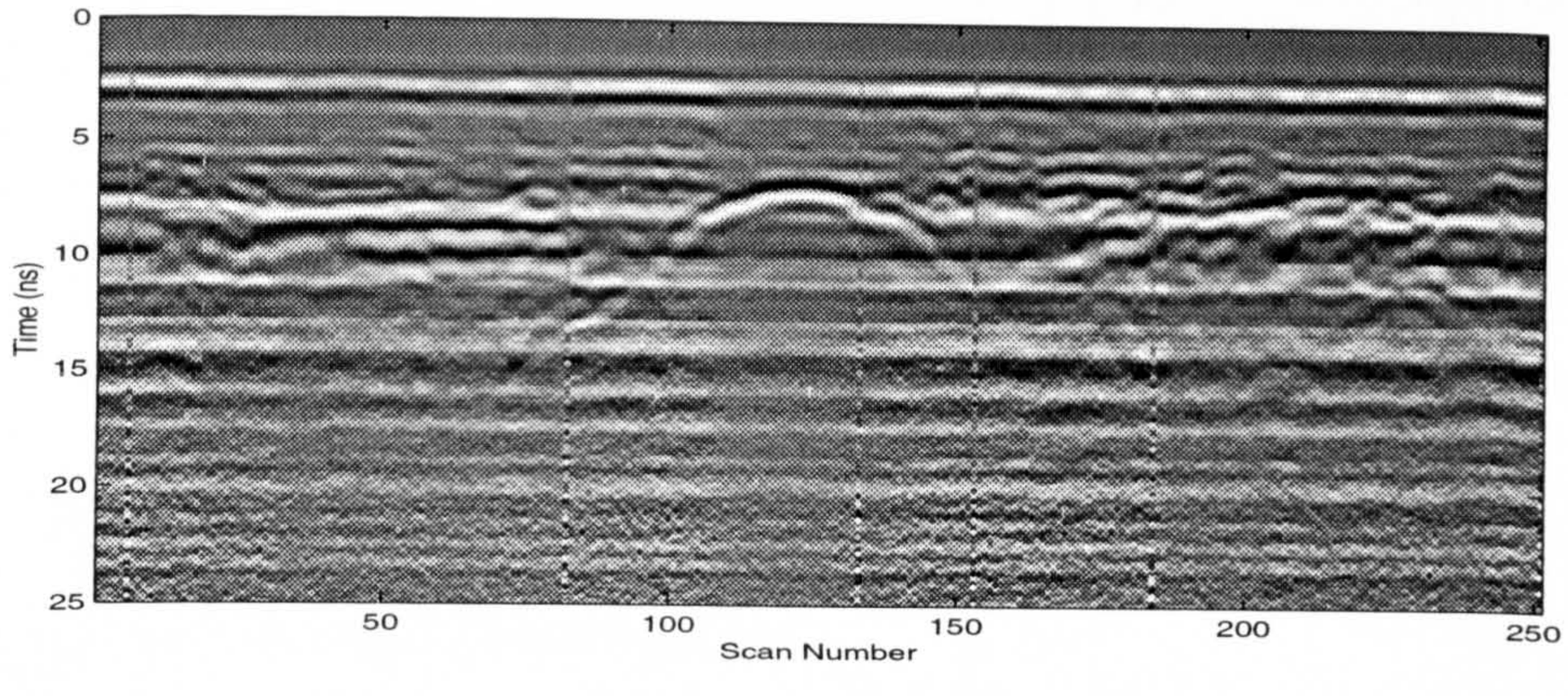

(a)

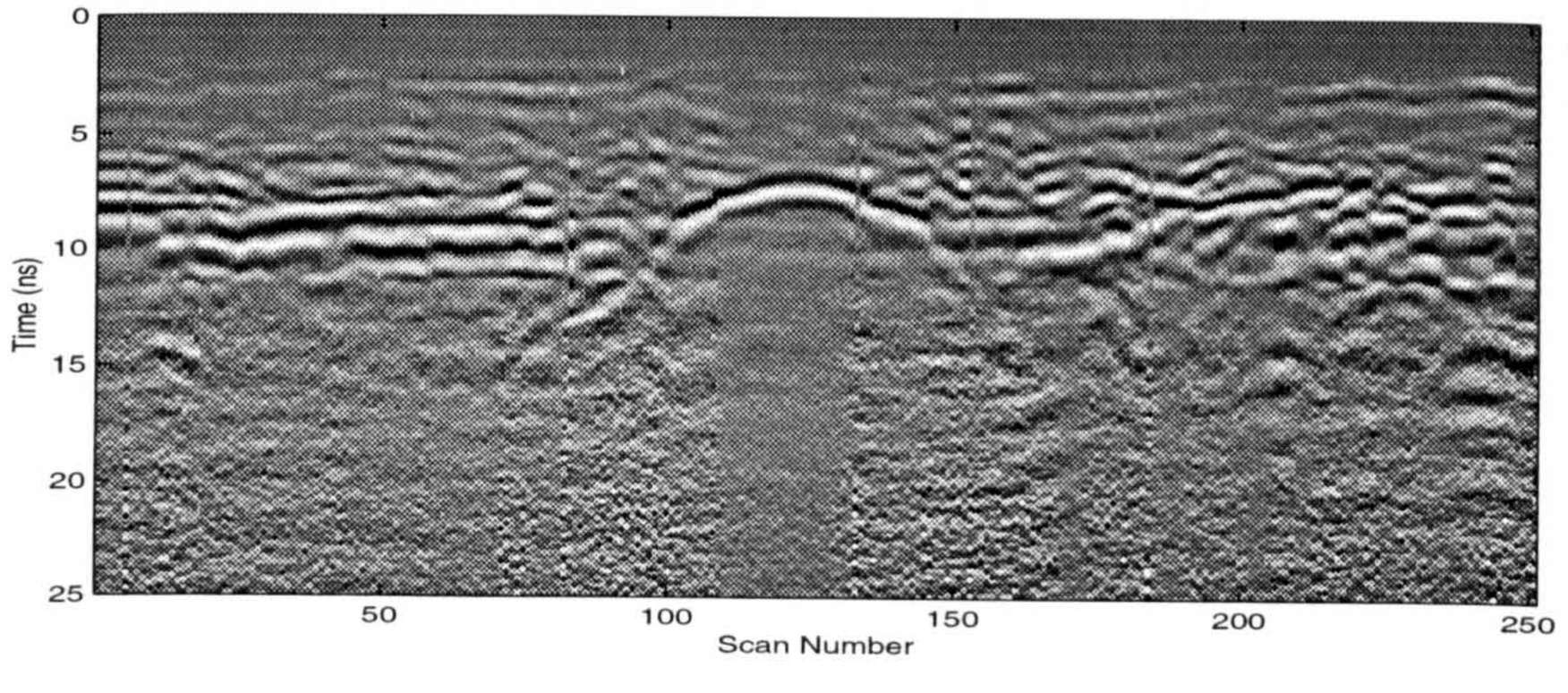

(b)

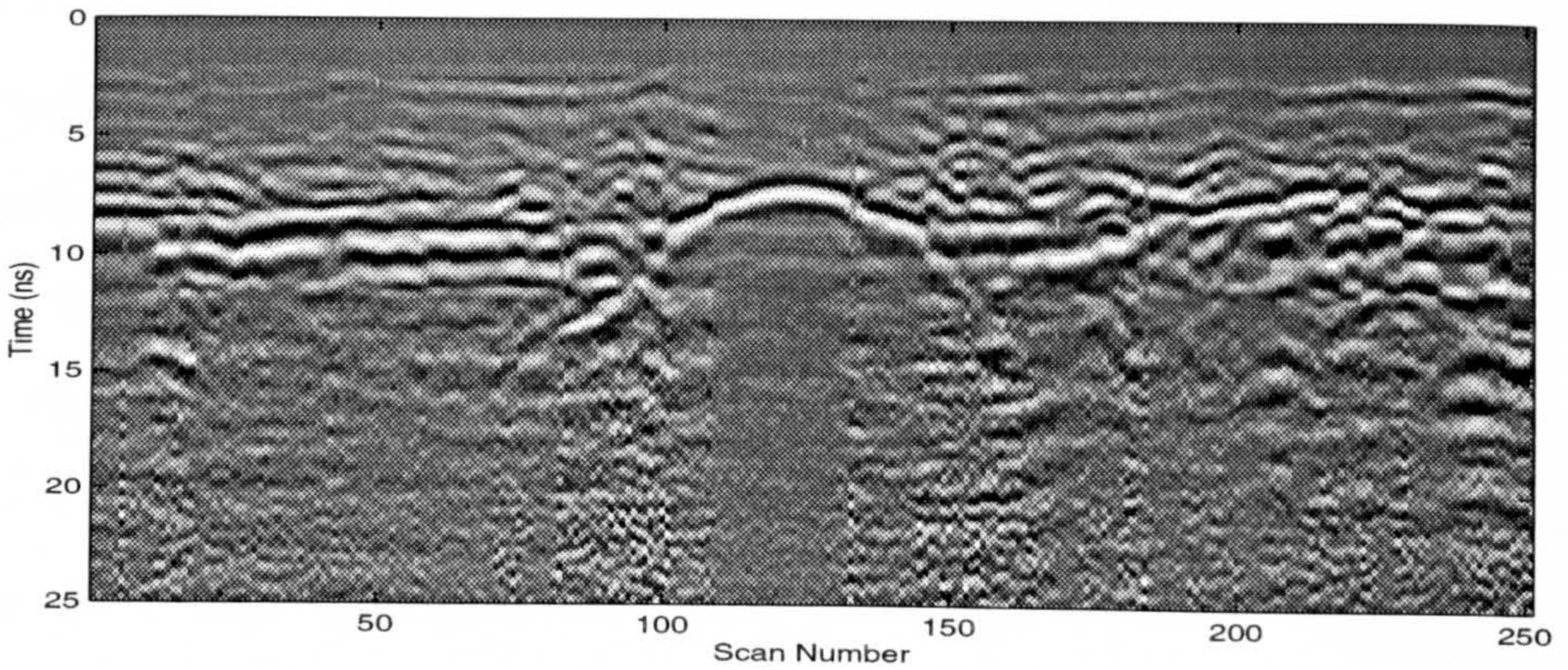

(c)

Figure 2.6: Illustration of enhancement of the image 2.4(a) by (a) applying the range gain, (b) background removal and (c) low-pass filtering.

nonmetallic buried objects, voids, change in density, etc. Secondly, the host medium for conventional radar is air, a known medium with low attenuation, but for GPR the medium is often an unknown dispersive medium consisting of several layers.

Depending on the information to be derived, GPR is commonly used for

1. recognising and discriminating the targets.
2. imaging the subsurface structure.

The methods adopted for the first purpose simplify and speed up the interpretation of radar records. The techniques used are pattern recognition, Prony's method and image processing. Pattern recognition is used to discriminate echoes from buried targets and unwanted signals. Neural networks are frequently used for pattern classification [3]. On the basis that every object possesses a unique natural resonance, Prony's methods can be employed for discriminating and recognising targets from clutter [15, Chapter 6], [53]. This target resonance may be fed into the pattern recognition procedure in conjunction with other target features. The goal of image processing is to enhance some aspects of GPR image, such as edges, and to extract lines and curves like hyperbolic anomalies caused by finite scatterers.

Imaging the subsurface structure can be viewed as either locating the target, or constructing the target profile. Among the techniques used to locate the objects is synthetic aperture focusing [35]. Of the techniques that are useful in generating target profile are diffraction tomography [43] and the spatial-iterative methods [12], [52], [66]. The aforementioned imaging methods belong to a larger group known as the inverse scattering methods whose objective is to solve an inverse problem so as to estimate the target's properties from the scattered field.

The methods employed for imaging the subsurface structure are directly concerned with the interpretation of GPR data. The methods used for the

recognition and discrimination of the targets have the same objectives as those of preprocessing. They may therefore be put into preprocessing stage. A brief description of synthetic aperture time-domain focusing, diffraction tomography and a spatial-iterative method, iterative Born technique, is given below.

2.4.1 Synthetic aperture time-domain focusing

Inherent in the application of synthetic aperture focusing is that the host medium is non-dispersive. In other words, the loss tangent of the host medium $\left(\frac{\sigma}{\omega\epsilon}\right)$ satisfies

$$\left(\frac{\sigma}{\omega\epsilon}\right)^2 \ll 1 \tag{2.4.1}$$

in the frequency bandwidth of the transmission wavelet. Suppose the radargram consists of N scans and the position of antenna for the nth scan is $(x_n, z_n = 0)$ where x-axis is on the surface and z-axis is perpendicular to the ground (Fig. 2.7). Having known the propagation velocity of the medium v, an estimate of the object distribution at a point (x, z) is given by [35]

$$\hat{o}(x,z) = \frac{1}{N}\sum_{n=1}^{N} s_n\left(\frac{2r_n}{v}\right) \tag{2.4.2}$$

where $s_n(t)$ is the nth received waveform and

$$r_n = \sqrt{(x-x_n)^2 + z^2} \tag{2.4.3}$$

The quantity $\frac{2r_n}{v}$ represents the two-way travel time needed for an electromagnetic pulse to travel between the antenna located at $(x_n, 0)$ and the point (x, z) in the object distribution. Thus, the image formation process is simply an average over the received waveforms evaluated at the travel time for each particular antenna position.

The presence of a finite-size scatterer forms hyperbolic anomalies in the GPR radargram, as illustrated by Fig. 2.7. Considering the vertical axis

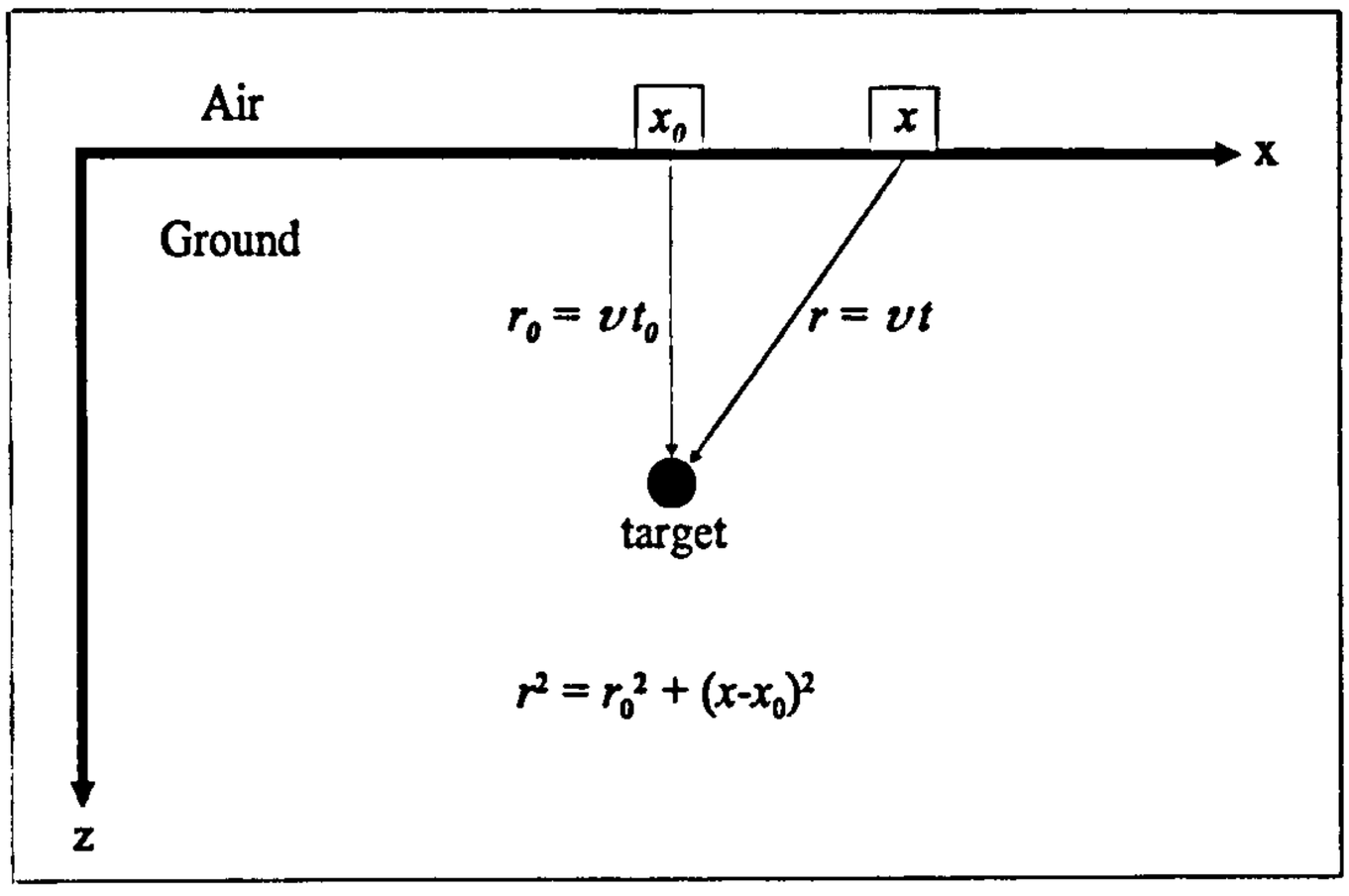

Figure 2.7: Formation of a hyperbola anomaly.

represents the two-way travel time (i.e. $t = \frac{2r}{v}$) in a radargram, the equation of the hyperbola can be written as

$$t^2 = t_0^2 + \frac{4}{v^2}(x - x_0)^2 \tag{2.4.4}$$

The velocity v can be evaluated from hyperbolic anomalies. The four quantities t_0, x_0, t and x are known from the radargram. The propagation velocity is computed from [3]

$$v = 2\sqrt{\frac{\sum(x - x_0)^2}{\sum(t^2 - t_0^2)}} \tag{2.4.5}$$

The sums are taken over several points on the hyperbola so as to reduce the effect of noise.

2.4.2 Diffraction tomography and iterative Born method

These two methods theoretically present the entire information available from GPR data, i.e. the location, geometry and material of targets. Both methods are based on the source-type integral equation that relates constitutive parameters (conductivity, permittivity and permeability) of the objects to the scattering field. Consider the geometry of a 3-dimensional electromagnetic

problem shown in Fig. 2.8. The geometry consists of two half-spaces, region

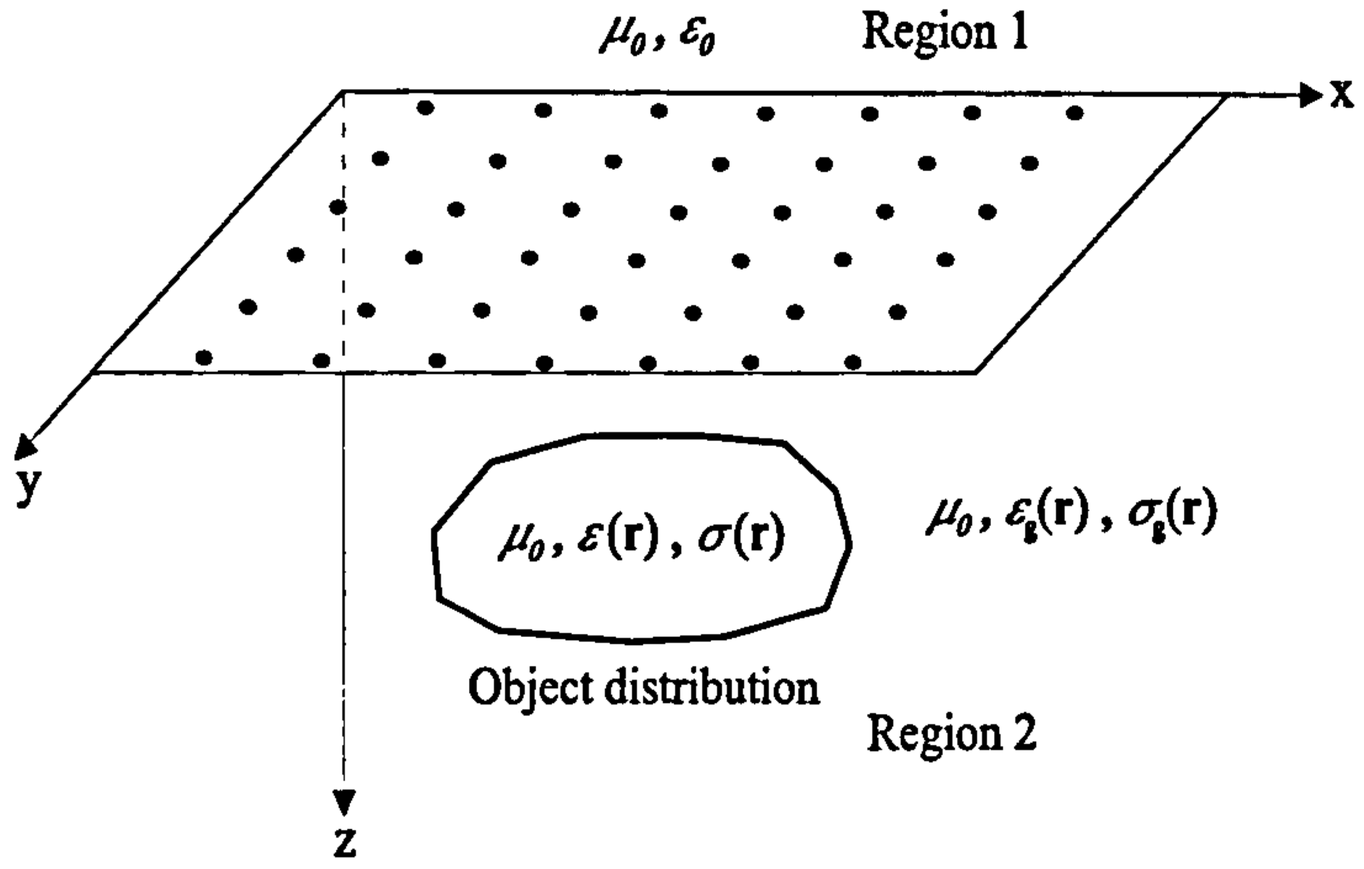

Figure 2.8: The geometry for 3-dimensional electromagnetic problem.

1 is free space and region 2 is an inhomogeneous half-space representing the ground. An inhomogeneous object of finite-size is located in the ground. At any point specified by the position vector $\mathbf{r} = (x, y, z)$, the total field $\phi(\mathbf{r})$ is given by [34]

$$\phi(\mathbf{r}) = \phi^{inc}(\mathbf{r}) + \int O(\mathbf{r}') \left[\phi(\mathbf{r}') \cdot \mathbf{G}_b(\mathbf{r}, \mathbf{r}')\right] d\mathbf{r}' \tag{2.4.6}$$

where $\phi^{inc}(\mathbf{r})$ is the incident field produced by sources in the absence of the object (the scatterer). The object profile $O(\mathbf{r})$ is defined as

$$O(\mathbf{r}) = \gamma^2(\mathbf{r}) - \gamma_b^2(\mathbf{r}) \tag{2.4.7}$$

where $\gamma(\mathbf{r})$, the *propagation constant* , is given by

$$\gamma^2(\mathbf{r}) = \begin{cases} -\omega^2\mu_0\epsilon_0 & , \ \mathbf{r} \in \text{Region 1} \\ j\mu_0\sigma_g(\mathbf{r})\omega - \omega^2\mu_0\epsilon_g(\mathbf{r}) & , \ \mathbf{r} \in \text{Region 2} \\ j\mu_0\sigma(\mathbf{r})\omega - \omega^2\mu_0\epsilon(\mathbf{r}) & , \ \mathbf{r} \in \text{object} \end{cases} \tag{2.4.8}$$

and $\gamma_b(\mathbf{r})$ defines a background propagation constant as

$$\gamma_b^2(\mathbf{r}) = \begin{cases} -\omega^2\mu_0\epsilon_0 & , \ \mathbf{r} \in \text{Region 1} \\ j\mu_0\sigma_g(\mathbf{r})\omega - \omega^2\mu_0\epsilon_g(\mathbf{r}) & , \ \mathbf{r} \in \text{Region 2} \end{cases} \tag{2.4.9}$$

$\mathbf{G}_b(\mathbf{r},\mathbf{r}')$ is the dyadic Green's function that is a solution of the differential equation [13, Chapter 9]

$$[\nabla\nabla - \nabla^2\mathbf{I} + \gamma_b^2(\mathbf{r})\mathbf{I}] \cdot \mathbf{G}_b(\mathbf{r},\mathbf{r}') = -\mathbf{I}\,\delta(\mathbf{r}-\mathbf{r}') \tag{2.4.10}$$

where $\mathbf{I}$ is the unit matrix. It can be concluded from (2.4.6) that the scattered field containing the information about the object is equal to

$$\phi^{sca}(\mathbf{r}) = \int O(\mathbf{r}')\,[\phi(\mathbf{r}') \cdot \mathbf{G}_b(\mathbf{r},\mathbf{r}')]\,d\mathbf{r}' \tag{2.4.11}$$

The scattered field inside the object is a function of itself, making a nonlinear relation between the profile $O(\mathbf{r})$ and the scattered field.

Diffraction tomography employs an approximate linear version of (2.4.11). When the scattered field inside the object is small compared to the incident field, (2.4.11) can be approximated by [59]

$$\phi^{sca}(\mathbf{r}) = \int O(\mathbf{r}')\,[\phi^{inc}(\mathbf{r}') \cdot \mathbf{G}_b(\mathbf{r},\mathbf{r}')]\,d\mathbf{r}' \tag{2.4.12}$$

which is linear in $O(\mathbf{r})$. This approximation is referred as the Born or weak scattering approximation. The tomographic nature of the data in conventional diffraction tomography is obtained from rotation of the object. However, for GPR the tomographic information is obtained from a wideband pulse transmitted into the host medium at several points equally spaced in a grid on the interface between air and the host medium (Fig. 2.8). Each wavelength in the received waveform (scan) represents a different portion of the spectrum of the object distribution. Superimposing the spectral components from each wavelength, the object distribution on a plane parallel to the interface is derived by a 2-dimensional inverse Fourier transform. The details of the method are presented in [43].

For many geophysical applications where the contrast between the propagation constant of the host medium and object is considerable, the linear approximation is too restrictive. Iterative Born method directly deals with

the nonlinear integral equation [12]. In this technique, the use of the moment method transforms integral (2.4.11) into a matrix relation. This is done by discretising the region of space and then expanding the object profile into a set of J expansion functions. If a total of K receiver-transmitter pairs are used and each received waveform consists of N samples in the frequency domain, there will be a set of $K \times N$ linear equations with J unknown values. At each iteration by the use of the object profile provided in the previous iteration, a forward scattering problem is solved to compute the total field inside the object. Using the resulting field, the inverse solution of the matrix relation yields a new profile for the object. Various scattering algorithms can be used for the forward problem, such as the finite-difference time-domain method or the discretised version of equation (2.4.6).

The iterative Born technique (or generally the spatial-iterative methods) are computationally inefficient and especially, their application to the 3-dimensional problems requires a huge amount of memory and intensive computation [52]. On the other hand, profiting from fast numerical algorithms (fast fourier transform), the diffraction tomography is efficient and works well when nonlinear effects are negligible.

2.5 Discussion and Conclusion

Preprocessing algorithms, image processing methods, pattern recognition etc. highlight the features of GPR data that are related to targets. These methods automate some tasks in the analysis of radar data. Application of these techniques often enables a geophysicist to detect the targets and to recognise roughly their spatial extent (e.g. being finite-size objects or planar interfaces).

The methods particularly pertaining to the interpretation of GPR data are inverse scattering techniques. There exist limitations associated with each inverse technique discussed in Section 2.4. These techniques share one limitation

that the electromagnetic parameters and structure of the host medium have to be known in advance. When the host medium is homogenous and non-dispersive, it is possible to measure the permittivity (the propagation velocity) of the host medium using hyperbolic anomalies. However, some constitutive materials of such media are lossy especially when they are mixed with water. The conductivity of material is highly dependent on water content, e.g. $0.001 \leq \sigma_{\text{dry clay}} \leq 0.1$ (S/m) and $0.1 \leq \sigma_{\text{wet clay}} \leq 1$ (S/m). Furthermore, the host medium is inhomogeneous (consists of planar layers) for many GPR applications, such as detection of objects buried under a road that comprises two/three layers of asphalt and a layer of concrete.

3-dimensional spatial-iterative methods can be used to obtain the profile of a dispersive, inhomogeneous medium, but they are inefficient and not feasible as realtime problems. The iterative Born method is capable of finding the whole subsurface profile including that of the host medium. However, including the host medium in the discretisation domain significantly increases the computation time and computer memory. It is also not practical to construct the profile of the host medium by diffraction tomography due to the considerable contrast between parameters of air and the host medium (e.g. the ground).

The ground and other host media are multi-layered media for many GPR applications. Development of an efficient method for characterising multi-layered media would therefore be useful in this respect. The targets for some GPR usages, such as pavement profiling, permafrost mapping and ice thickness profiling, are also layered media. In addition, finite objects sometimes can be regarded as a layer if their dimensions are large compared with the effective transmitted wavelengths. Being efficient and feasible in real-time, 1-dimensional (1D) IS methods may be employed to characterise layered media using GPR data. In this research, we therefore investigate and assess the use of 1-dimensional IS techniques for GPR applications.

Chapter 3

One-Dimensional Inverse Scattering Methods

3.1 Introduction

The inverse scattering problem is to reconstruct the properties of a medium from the scattering data. On the contrary, the goal in a forward problem is to generate the data scattered from a known medium. In a way, IS problems can be viewed as system identification problems in which the parameters of a predefined model of the system are derived. These problems arise in various areas including physics, geophysics, medicine and electrical engineering [14]. The determination of the dielectric properties of a medium, identification of the impedance profile of transmission lines and the design of digital filters in cascade form are examples of inverse scattering problems posed in electrical engineering.

Inverse scattering methods may be classified into two categories [57]. The first category includes all direct inversions, which extract the model parameters directly by applying a mathematical operator to the measured scattering data. The operator is recognised or designed on the basis of the physics of

the forward problem. A well-known direct inversion is the layer-stripping algorithm principally used for 1D problems [9], [21], [22], [26] where the parameters of the media vary in one spatial dimension. This technique can be used for 2-dimensional problems [67] as well.

The second group comprises the so-called model-based inversions. These techniques rely on an optimisation procedure in which the parameters of a model of a medium are reconstructed by optimising a suitable objective function. The value of this function indicates the closeness between the observed (measured) scattering data and the synthetic data. The synthetic data is generated by solving the forward scattering problem. In contrast to direct inverse methods, no attempt is made to reverse the forward process in a model-based inverse technique. Several algorithms in this category have been developed [12], [23], [26], [29], [30], [49], [57], [64].

Inverse scattering problems might be ill-posed due to the nonlinearity of the forward problem and inadequacy of the measured data. A problem having the properties of existence, uniqueness and stability of the solution is called well-posed [14, Chapter 4]. The third property, stability, indicates how small errors in the measured data propagate into the estimation of the model parameters. Low stability of an inverse problem means that small perturbations of the data lead to large errors in the reconstruction of the model. A problem is said to be ill-posed if one of these properties fails to hold.

If an IS problem is ill-posed, the performance of the model-based inversions is superior to the direct ones. Particularly, when the measured data is incomplete and/or contaminated by noise, the direct inversions suffer more from instability. The model-based methods are more robust and broadly applicable [57, Chapter 2]. The advantage of the direct methods over the model-based ones is their efficiency in terms of computation time and sometimes the amount of memory required.

This chapter is devoted to the investigation of 1D Electromagnetic Inverse

Scattering (EIS) methods applied to characterisation of inhomogeneous layered media. Formulation of the inverse methods in both the categories mentioned are mainly based on either a nonlinear integral equation or a wave differential equation. Section 3.2 deals with the detailed extraction of nonlinear integral equations for use in 1D EIS methods. Wave differential equations for 1D problems can be solved analytically to give an explicit closed-form expression, which is known as the reflectivity formulation and is introduced in Section 3.3. Making use of this expression, the layer-stripping method is described and a numerical example is also provided. This example demonstrates the instability of the direct techniques, suggesting the use of the model-based approach for GPR applications. Employing the reflectivity formulation, a new 1D model-based inverse method is proposed in the final section. The new method provides an improvement in efficiency. The necessary condition for the unique solution to 1D EIS problems is also discussed.

3.2 1D Nonlinear Integral Equation

The model used in numerous 1D EIS methods is based on a nonlinear integral equation, which was presented in the previous chapter for 3-dimensional problems. The 1D version of this equation is derived for normal wave incidence in [6] and can be extended to the TE wave incidence as follows. Figure 3.1 illustrates the geometry of the problem where a TE wave is incident on an inhomogeneous slab with angle θ. The permittivity $\epsilon(z)$ and conductivity $\sigma(z)$ of the slab are functions of the depth z. The incident electric field $E_y^{\mathbf{i}}$ polarised along y coordinate is given by

$$E_y^i = E_0 \mathrm{e}^{-\gamma_0 \cos\theta\, z} \times \mathrm{e}^{-\gamma_0 \sin\theta\, x} \tag{3.2.1}$$

where $\gamma_0 = j\omega\sqrt{\mu_0\epsilon_0}$. The total field E_y satisfies the wave equation

$$\left[\nabla^2 - \gamma^2(z)\right] E_y = 0 \tag{3.2.2}$$

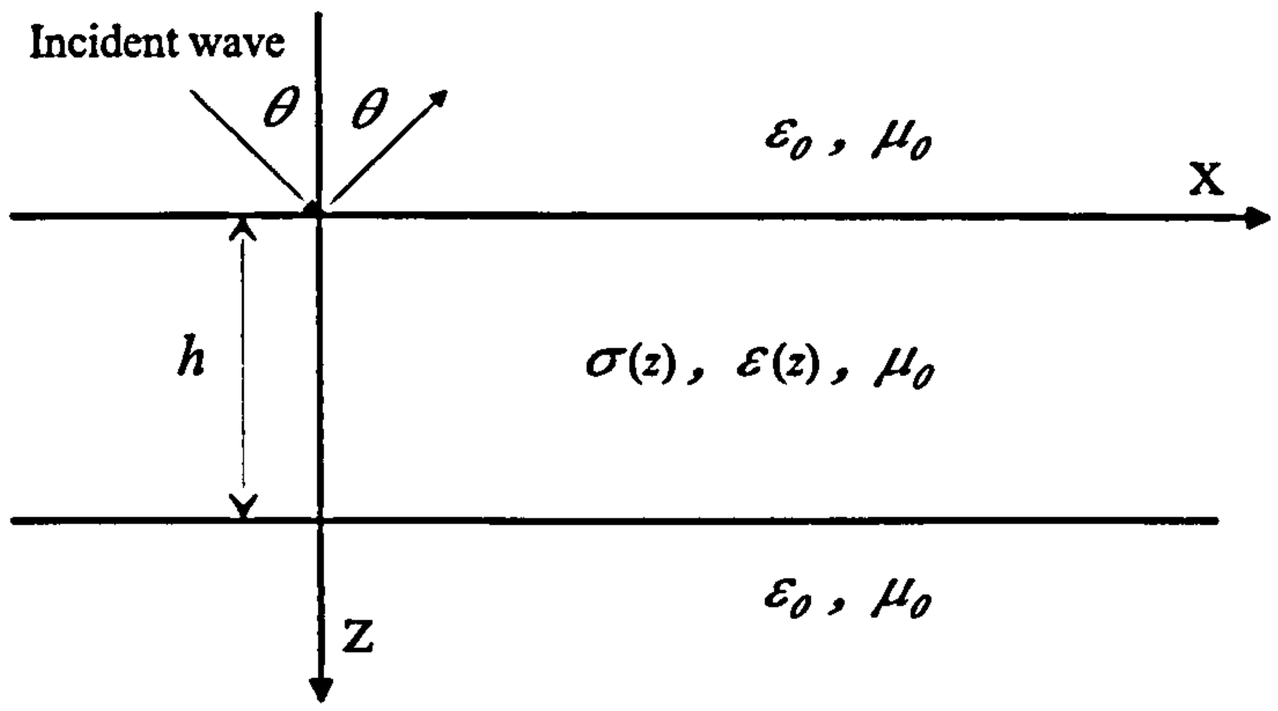

Figure 3.1: A one-dimensional inhomogeneous slab placed in free space.

where

$$\gamma^2(z) = \begin{cases} -\mu_0\epsilon_0\omega^2 & , \quad z < 0\,,\, z > h \\ j\mu_0\sigma(z)\omega - \mu_0\epsilon(z)\omega^2 & , \quad 0 < z < h \end{cases} \tag{3.2.3}$$

The general solution of (3.2.2) is of the form

$$E_y = \phi(z)\, \mathrm{e}^{-\gamma_0 \sin\theta\, x} \tag{3.2.4}$$

where ϕ is merely a function of z. Substituting (3.2.4) into (3.2.2), one can derive

$$\frac{d^2\phi}{dz^2} - \left[\gamma^2(z) - \gamma_0^2 \sin^2\theta\right]\phi = 0 \tag{3.2.5}$$

Now subtracting $\gamma_0^2\,\phi$ gives

$$\frac{d^2\phi}{dz^2} - \gamma_0^2 \cos^2\theta\,\phi = \left[\gamma^2(z) - \gamma_0^2\right]\phi \tag{3.2.6}$$

Let $G(z, z')$ be the Green's function which satisfies the equation

$$\frac{d^2\phi}{dz^2} - \gamma_0^2 \cos^2\theta\,\phi = -\delta(z - z') \tag{3.2.7}$$

According to (3.2.1), we know that $\phi(z) = \phi^{inc} = E_0 \mathrm{e}^{-\gamma_0 \cos\theta\, z}$ in the absence of the slab (ϕ^{inc} is the incident field ϕ). Thus, the solution for $\phi(z)$ can be written as

$$\phi(z) = \phi^{inc} - \int_0^h \left[\gamma^2(z') - \gamma_0^2\right]\phi(z')G(z, z')\, dz' \tag{3.2.8}$$

Taking the Laplace transform of (3.2.7), the Green's function is given by

$$G(z,z') = \frac{c}{2j\omega\cos\theta}\,\mathrm{e}^{-j\frac{\omega}{c}\cos\theta|z-z'|} \tag{3.2.9}$$

where we made use of $\gamma_0 = j\omega/c$, and c denotes the speed of light in free space. Substituting (3.2.9) into (3.2.8), the field $\phi(z)$ can be expressed as

$$\begin{aligned}\phi(z) = \quad & \phi^{inc} - \tfrac{\eta_0}{2\cos\theta}\int_0^h \sigma(z')\,\phi(z')\,\mathrm{e}^{-j\frac{\omega}{c}\cos\theta|z-z'|}\,dz' \\ & -\tfrac{\eta_0}{2\cos\theta}\int_0^h j\omega\epsilon_0[\epsilon_r(z')-1]\,\phi(z')\,\mathrm{e}^{-j\frac{\omega}{c}\cos\theta|z-z'|}\,dz'\end{aligned} \tag{3.2.10}$$

where $\eta_0 = \sqrt{\mu_0/\epsilon_0}$ is the impedance of free space and $\epsilon_r(z)$ is the relative permittivity of the slab.

In 1D EIS problems, the slab is approximated by M homogeneous layers. Thus, Equation (3.2.10) is rewritten as

$$\phi(z) = \phi^{inc} - \frac{\eta_0}{2\cos\theta}\sum_{m=1}^{M}\sigma_m\,\psi_m(z) - \frac{j\omega\,\eta_0\,\epsilon_0}{2\cos\theta}\sum_{m=1}^{M}[\epsilon_{rm}-1]\,\psi_m(z) \tag{3.2.11}$$

where ϵ_{rm} and σ_m are respectively the relative permittivity and conductivity of the mth layer. $\psi_m(z)$ is equal to

$$\psi_m(z) = \int_{z_{m-1}}^{z_m}\phi(z')\,\mathrm{e}^{-j\frac{\omega}{c}\cos\theta|z-z'|}\,dz' \tag{3.2.12}$$

where $z_0 = 0$ and $z_M = h$. The scattering data is the reflected field $\phi^{ref}(z)$ measured at several frequencies and/or incident angles at a point in the region $z \leqslant 0$, say $z = 0$. Hence,

$$\begin{aligned}\phi^{ref}(0) = \phi(0) - \phi^{inc}(0) = \quad & -\tfrac{\eta_0}{2\cos\theta}\textstyle\sum_{m=1}^{M}\sigma_m\,\psi_m(0) \\ & -\tfrac{j\omega\,\eta_0\,\epsilon_0}{2\cos\theta}\textstyle\sum_{m=1}^{M}[\epsilon_{rm}-1]\,\psi_m(0)\end{aligned} \tag{3.2.13}$$

This equation can be used within the iterative Born algorithm to find the dielectric profile of inhomogeneous slabs. Such an algorithm is described in [63] where a time domain version of (3.2.13) has been employed. It is straightforward to transform it to the time domain

$$\begin{aligned}\phi^{ref}(z=0,t) = \quad & -\tfrac{\eta_0}{2\cos\theta}\textstyle\sum_{m=1}^{M}\sigma_m\int_{z_{m-1}}^{z_m}\phi(z',t')\,dz' \\ & -\tfrac{\eta_0\,\epsilon_0}{2\cos\theta}\textstyle\sum_{m=1}^{M}[\epsilon_{rm}-1]\int_{z_{m-1}}^{z_m}\frac{\partial\phi(z',t')}{\partial t}\,dz'\end{aligned} \tag{3.2.14}$$

where $t' = t - \frac{z' \cos\theta}{c}$. Other versions of (3.2.13) have also been used in 1D EIS methods [64]. All inverse methods that have employed the nonlinear integral equation so far belong to the model-based category. Perhaps the iterative Born method cannot strictly be included in this category since the dielectric parameters are obtained by the inversion of a matrix equation derived from (3.2.13). However, this matrix inversion is not performed directly but through analytic minimization of an objective function.

In order to employ the nonlinear integral equation in a 1D EIS technique, the total field $\phi(z)$ has to be evaluated for the present medium profile at each iteration. One way is to use other kinds of forward modelling, such as the finite-difference time-domain method. Another way is to solve (3.2.11) numerically by assuming $\phi(z) = \phi(z_k^{mid})$ within kth layer where $z_k^{mid} = (z_{k-1} + z_k)/2$. Thus, one can derive

$$\begin{aligned}\phi(z_k^{mid}) &= \phi^{inc}(z_k^{mid}) - \frac{\eta_0}{2\cos\theta} \sum_{m=1}^{M} \sigma_m \, \phi(z_m^{mid}) \int_{z_{m-1}}^{z_m} \mathrm{e}^{-j\frac{\omega}{c}\cos\theta |z_k^{mid} - z'|} \, dz' \\ &\quad - \frac{j\omega\eta_0\epsilon_0}{2\cos\theta} \sum_{m=1}^{M} [\epsilon_{rm} - 1] \, \phi(z_m^{mid}) \int_{z_{m-1}}^{z_m} \mathrm{e}^{-j\frac{\omega}{c}\cos\theta |z_k^{mid} - z'|} \, dz' \qquad (3.2.15) \\ &\quad k = 1, 2, \ldots, M\end{aligned}$$

which consists of M linear equations and can be solved for unknown total fields $\phi(z_k^{mid})$.

As it can be inferred from the above explanation, the application of the nonlinear integral equation in a 1D EIS is involved matrix inversion and/or optimisation of function of $2M$ variables $(\sigma_m, \epsilon_{rm}, m = 1, \ldots, M)$. These inverse techniques are not therefore efficient even if the medium is discretised to small number of layers. For example, a function in 30-dimensional space must be optimised when $M = 15$.

3.3 1D Wave Differential Equation

It is demonstrated in this section that the solution of the 1D wave differential equation results in an exact closed-form expression for the reflection coef-

ficient of a multi-layered medium. This expression has been used in the layer-stripping algorithm to reconstruct the profile of layered media. The derivation of the reflection coefficient of a non-uniform transmission line is also given in this section. Due to common mathematical foundation for two cases, we can use the experimental data acquired by a network analyser from a non-uniform transmission line to evaluate the performance of a 1D inverse method for the real data. For the case of multi-layer media, only TE wave incidence is considered. Nevertheless, the derived expressions can easily be extended to TM wave incidence.

3.3.1 Forward modelling of multi-layered media

The geometry of the problem is illustrated in Fig. 3.2(a). The specifications of this figure are the same as Fig. 3.1 except that the medium consists of M homogeneous layers. Suppose the incident electric field E_y^i is given by Equation (3.2.1). Thus, the electric field in the entire space has only a y component that for the mth layer is a solution of the equation

$$\left[\nabla^2 - \gamma_m^2\right] E_{my} = 0 \quad , \quad \gamma_m^2 = j\mu_m\sigma_m\omega - \mu_m\epsilon_m\omega^2 \tag{3.3.1}$$

The goal is to derive the reflection coefficient of the medium, which is the ratio of the reflected field to the incident field at the interface $z = 0$. We follow a procedure similar to that in [65] while going through more details. The solution for E_{my} can be expressed as

$$E_{my} = \left[a_m \mathrm{e}^{-u_m z} + b_m \mathrm{e}^{u_m z}\right] \mathrm{e}^{-\gamma_0 \sin\theta\, x} \tag{3.3.2}$$

where

$$u_m = \sqrt{\gamma_m^2 - \gamma_0^2 \sin^2\theta} \tag{3.3.3}$$

Maxwell's equations give the x component of the magnetic field H_{mx} as

$$H_{mx} = \frac{1}{j\mu_m\omega}\frac{\partial E_{my}}{\partial z} = Y_m \left[-a_m \mathrm{e}^{-u_m z} + b_m \mathrm{e}^{u_m z}\right] \mathrm{e}^{-\gamma_0 \sin\theta\, x} \tag{3.3.4}$$

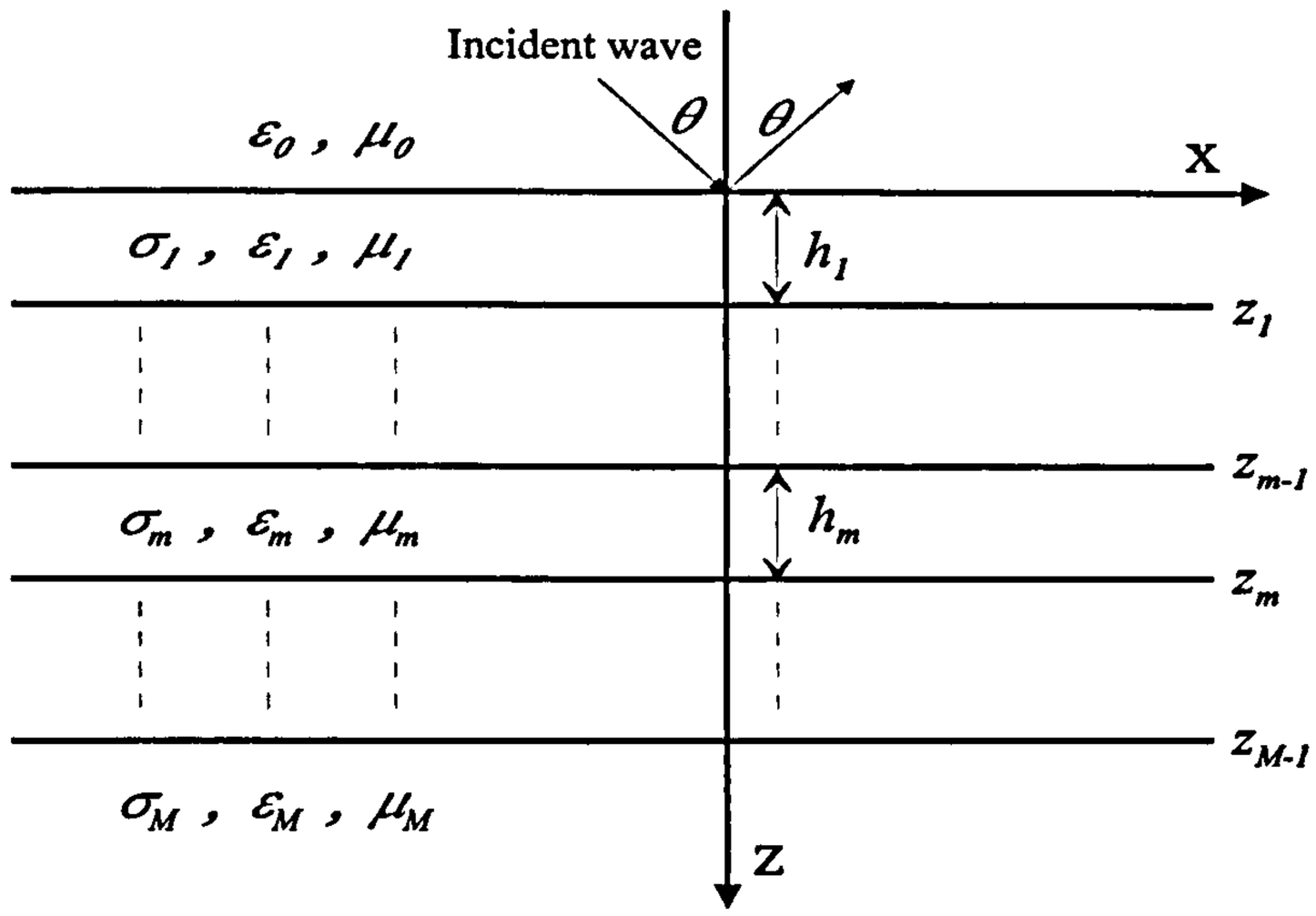

(a)

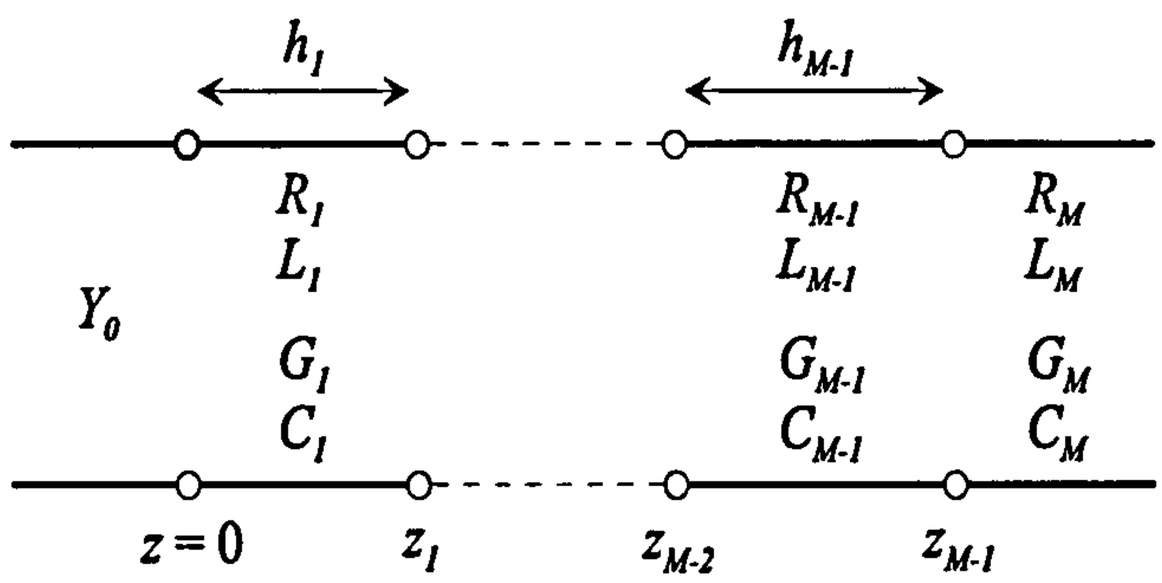

(b)

Figure 3.2: (a) A stratified medium. (b) A non-uniform transmission line.

where Y_m, termed by analogy to transmission line as the characteristic admittance of the mth layer, is given by

$$Y_m = \frac{u_m}{j\mu_m\omega} \tag{3.3.5}$$

Let the surface admittance W_m be defined as

$$W_m = -\frac{H_{(m-1)x}}{E_{(m-1)y}}\bigg|_{z_{m-1}} \tag{3.3.6}$$

Owing to the boundary conditions

$$\begin{bmatrix} E_{(m-1)y} = & E_{my} \\ H_{(m-1)x} = & H_{mx} \end{bmatrix}_{z_{m-1}} \tag{3.3.7}$$

W_m can be rewritten as

$$W_m = -\frac{H_{mx}}{E_{my}}\bigg|_{z_{m-1}} = -Y_m \frac{-\mathrm{e}^{-u_m z_{m-1}} + \frac{b_m}{a_m}\mathrm{e}^{u_m z_{m-1}}}{\mathrm{e}^{-u_m z_{m-1}} + \frac{b_m}{a_m}\mathrm{e}^{u_m z_{m-1}}} \tag{3.3.8}$$

Similarly, the surface admittance at $z = z_m$ is

$$W_{m+1} = -\frac{H_{mx}}{E_{my}}\bigg|_{z_m} = -Y_m \frac{-\mathrm{e}^{-u_m z_m} + \frac{b_m}{a_m}\mathrm{e}^{u_m z_m}}{\mathrm{e}^{-u_m z_m} + \frac{b_m}{a_m}\mathrm{e}^{u_m z_m}} \tag{3.3.9}$$

Deriving $\frac{b_m}{a_m}$ from the above equation yields

$$\frac{b_m}{a_m} = \mathrm{e}^{-2u_m z_m}\left(\frac{Y_m - W_{m+1}}{Y_m + W_{m+1}}\right) \tag{3.3.10}$$

By the substitution of (3.3.10) into (3.3.8), it follows that

$$W_m = Y_m \frac{W_{m+1} + Y_m \tanh u_m h_m}{Y_m + W_{m+1}\tanh u_m h_m} \tag{3.3.11}$$

where $m = 1, 2, \ldots, M-1$. There is no upgoing wave in the lowest layer, i.e. $b_M = 0$. Hence, for $m = M$ Equation (3.3.8) gives

$$W_M = Y_M \tag{3.3.12}$$

From (3.3.2) and (3.3.10), one can conclude that the reflection coefficient of the medium made up of layers $m+1$, $m+2$, ... and M is given by

$$\Gamma_m(\omega) = \mathrm{e}^{2u_m z_m}\frac{b_m}{a_m} = \frac{Y_m - W_{m+1}}{Y_m + W_{m+1}} \tag{3.3.13}$$

Substituting $m = 0$, the reflection coefficient of whole multi-layered medium $\Gamma(\omega)$ will be

$$\Gamma(\omega) = \frac{Y_0 - W_1}{Y_0 + W_1} \tag{3.3.14}$$

where $Y_0 = \sqrt{\epsilon_0[1 - \sin^2\theta]/\mu_0}$.

Using Equations (3.3.11), (3.3.12) and (3.3.14), the reflection coefficient of a multi-layered medium can be computed through a recursive scheme that is started from the bottom layer. These equations are known as the reflectivity formulation of 1D problems. They can also be used for calculating the reflection coefficient of a continuous 1D medium (where ϵ, σ and μ are continuous function of z) by dividing the medium into thin homogeneous layers.

3.3.2 Forward modelling of a non-uniform transmission line

Figure 3.2(b) shows a non-uniform transmission line with M uniform sections. R_m, L_m, G_m and C_m are respectively the series resistance, series inductance, shunt conductance and shunt capacitance per unit length. h_m denotes the length of the mth section. The non-uniform line is excited at $z = 0$ from a uniform transmission line with a characteristic admittance Y_0. There is a direct analogy between a multi-layered medium and a non-uniform transmission line. Replacing the electric field E_y by voltage V and the magnetic field H_x by current I [55, Chapter 6], the expressions derived in the previous subsection are equally applicable here. In addition, $\theta = 0°$ (i.e. $u_m = \gamma_m$) and the expression for γ_m is changed to

$$\gamma_m = [(R_m + j\omega L_m)(G_m + j\omega C_m)]^{1/2} \tag{3.3.15}$$

the characteristic admittance of the mth section Y_m is given by

$$Y_m = \frac{u_m}{R_m + j\omega L_m} \tag{3.3.16}$$

3.3.3 Layer-stripping method

The layer-stripping method has been used for identification of layered media, such as non-uniform transmission lines. It was originally developed by

geophysicists in order to obtain a layered model of earth from acoustic wave propagation. Starting from the first layer, the algorithm computes the parameters of each layer consecutively. After identification of a layer, all reflections including the multiple reflections associated with this layer are removed from the received signal then the process is repeated for the remaining layers. In other words, the layers are successively peeled off by downward continuation (layer stripping) while deriving the properties of each layer. The model employed in the method is generally based on the reflectivity formulation of the 1D forward problems. The description of the method given herein is based on the idea taken from [57, Chapter 2].

The measured scattering data is the field $S(\omega)$ reflected from the medium when an impulsive plane wave is incident on its surface. $S(\omega)$ is related to the incident pulse $P(\omega)$ by

$$S(\omega) = P(\omega)\Gamma(\omega) \tag{3.3.17}$$

In the time domain, this field can be written as a superposition of echoes of $p(t)$ (the incident pulse).

$$s(t) = p_0(t) + p_1(t) + \sum_{i=2}^{\infty} p_i(t) \tag{3.3.18}$$

$p_0(t)$ and $p_1(t)$ are respectively the first echoes from layers 1 and 2. The third term in (3.3.18) consists of all multiple reflections together with the first reflections from the other layers. The assumption made in the layer-stripping method is that $p(t)$ is short enough (i.e. broadband in the frequency domain) so that $p_0(t)$ and $p_1(t)$ can be separated individually from the rest of $s(t)$. Let Υ_{01} denote the reflection coefficient of layer 1 when the first layer is a half space ($h_1 \to \infty$). $P_0(\omega)$, the frequency component of $p_0(t)$, is given by

$$P_0(\omega) = \Upsilon_{01}\, P(\omega) = \frac{Y_0 - Y_1}{Y_0 + Y_1}\, P(\omega) \tag{3.3.19}$$

Thus, the characteristic admittance of the first layer is obtained from P_0 using

$$Y_1 = Y_0 \frac{P(\omega) - P_0(\omega)}{P(\omega) + P_0(\omega)} \tag{3.3.20}$$

We can also use Equations (3.3.5) and (3.3.3) to derive

$$Y_m^2 = \frac{1}{\mu_0 \mu_{rm}} \left[\frac{\epsilon_0 \left(\epsilon_{rm} \mu_{rm} - \sin^2 \theta \right)}{\mu_{rm}} - j \frac{\sigma_m}{\omega} \right] \tag{3.3.21}$$

Providing one parameter among $\{\sigma_m, \epsilon_m, \mu_m\}$ is known, the other two parameters may be calculated from the real and imaginary parts of Y_m^2 . For most applications, the medium consists of non-magnetic materials and thus $\mu_{rm} = 1$.

In order to find the thickness h_1, the echo $p_1(t)$ has to be manipulated. Under the condition that layers 1 and 2 are non-dispersive within the frequency band of the incident pulse, h_1 can be obtained from the time delay between $p_0(t)$ and $p_1(t)$. However, it is possible to ease this constraint by considering $p_1(t)$ in the frequency domain (P_1). Let Υ_{12} be the reflection coefficient of the second layer. P_1 is given by

$$P_1 = P \left(1 - \Upsilon_{01}^2\right) \Upsilon_{12} \, \mathrm{e}^{-2u_1 h_1} \tag{3.3.22}$$

Let us introduce a new quantity P_1' as

$$P_1' = \frac{P_1}{P\left(1 - \Upsilon_{01}^2\right)} = \Upsilon_{12} \, \mathrm{e}^{-2u_1 h_1} \tag{3.3.23}$$

If ω_H is the highest frequency at which the magnitude of the quantity P_1' is considerable compared to noise and other disturbances, the phase drift of $P_1'(\omega_H)$ from its actual value is negligible. Assuming layers 1 and 2 are non-dispersive at this frequency (i.e. $\frac{\sigma_1}{\omega_H \epsilon_1} << 1$, $\frac{\sigma_2}{\omega_H \epsilon_2} << 1$), the thickness h_1 can be computed from the equation

$$\Delta \left(\angle P_1' \right) = -2 \frac{\Delta \omega}{c} \sqrt{\epsilon_{r1} \mu_{r1} - \sin^2 \theta} \; h_1 \tag{3.3.24}$$

where $\angle P_1'$ denotes the phase of P_1' and $\Delta\omega$ is the incremental difference in the frequency around ω_H.

The echoes associated with the first layer are now removed from $S(\omega)$ or equivalently from $s(t)$. This is performed by solving (3.3.11) for W_{m+1}

$$W_{m+1} = Y_m \frac{W_m - Y_m \tanh u_m h_m}{Y_m - W_m \tanh u_m h_m} \tag{3.3.25}$$

Finding W_1 by employing

$$W_1 = Y_0 \frac{P(\omega) - S(\omega)}{P(\omega) + S(\omega)} \tag{3.3.26}$$

one can obtain W_2 from (3.3.25) and then obtain the total reflection coefficient of a new medium comprising $M-1$ layers from

$$\Gamma_1 = \frac{Y_1 - W_2}{Y_1 + W_2} \tag{3.3.27}$$

The reflected field from this new medium is given by

$$S^1(\omega) = P^1(\omega)\Gamma_1(\omega) \tag{3.3.28}$$

where P^1, the incident pulse on the new medium, is

$$P^1(\omega) = P(\omega)\left(1 - \Upsilon_{01}^2\right) \mathrm{e}^{-2u_1 h_1} \tag{3.3.29}$$

The algorithm is now at the stage where it started but the first layer is peeled off. Consequently, the parameters of other layers can be found successively by repeating the same procedure.

When the data is not sufficiently broadband and contaminated by noise, the layer-stripping method has the reputation of being unstable as it proceeds through the reconstruction procedure. Although lack of enough bandwidth for the data and noise may introduce small error in the parameters of the top layers, this error grows rapidly and accumulates for the parameters of deeper layers. The reasons for such behaviour are :

1. As the incident field propagating into the layers, its power and its frequency bandwidth are reduced. This can be seen from Equation (3.3.29) in which $\left(1 - \Upsilon_{01}^2\right) \mathrm{e}^{-2u_1 h_1}$ behaves like a low-pass filter and

$$\left|\left(1 - \Upsilon_{01}^2\right) \mathrm{e}^{-2u_1 h_1}\right| \leq 1 \tag{3.3.30}$$

2. Any error in the parameters of a layer, e.g. Y_m, u_m etc, influences the estimated incident and reflected field of the subsequent layered media as can be understood by (3.3.25).

Despite its disadvantages, the layer-stripping method is computationally efficient. Unlike the 1D inversions based on the nonlinear integral equation, there is no need to discretise the medium into thin layers and a layer is fully characterised including its thickness during one iteration. There exist other versions of the algorithm [9], [22] in which the medium under consideration is viewed as consisting of N thin layers, where N is the number of samples in the reflected signal $s(t)$. Nonetheless, these versions of the layer-stripping method are also efficient since they do not involve computationally costly operations, such as matrix inversion or optimization of a function of a large number of variables.

A numerical example is presented here to demonstrate the performance of the layer-stripping method.

Example 3.1. The multi-layered medium is made up of 3 non-magnetic layers as shown in Fig. 3.3. Utilizing the reflectivity formulation, the reflected data

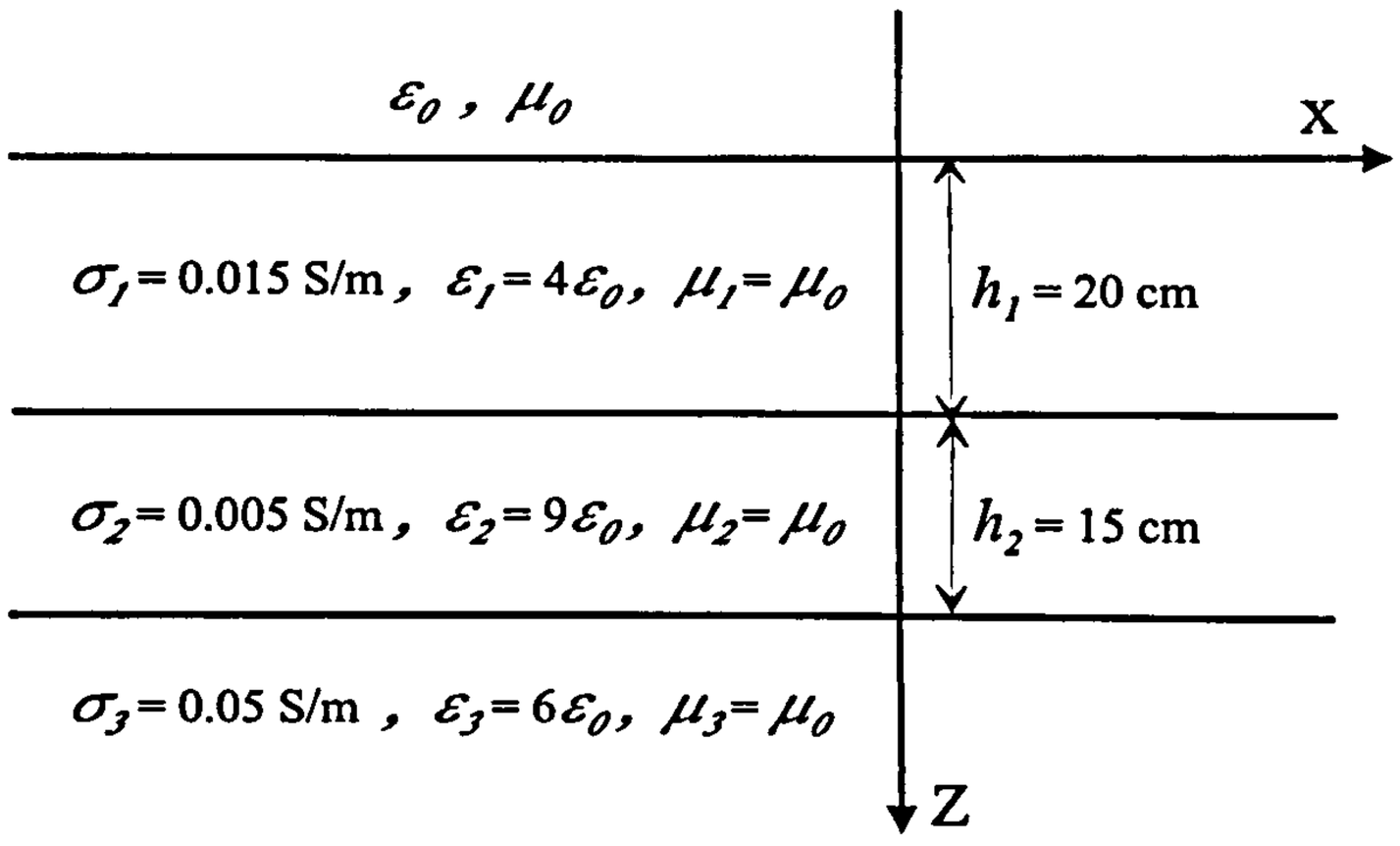

Figure 3.3: A 3-layer medium.

is generated for a normally incident wave ($\theta = 0°$). The layer-stripping method is applied to this data to reconstruct the medium. For ease of explanation, let us refer to the 3-layer medium as medium 1, to the medium containing layer 2 and 3 as medium 2 and finally to layer 3 as medium 3.

The main incident pulse (solid line) and those produced by the algorithm as the incident pulses on medium 2 and 3 are shown in Fig. 3.4. It can be observed that the width of the main incident pulse in the time domain is increased or equivalently its frequency bandwidth is decreased while propagating into the deeper layers. The power of the incident pulses are also descending function of the depth. The same things can be seen for the reflected fields as indicated in Fig. 3.5. The echoes of medium 1 are separable, whereas those of medium 2 are overlapped. This is the consequence of decreasing the frequency bandwidth.

Fig. 3.6 shows the reconstructed profiles. The negative value for the conductivity of the third layer indicates that the method becomes unstable. This can be explained by Fig. 3.7. With respect to Equation (3.3.21), the imaginary part of Y_m^2 should be negative for all layers. However, that of Y_3^2 is positive for wide range of frequency. Note that there is no noise in the data and the error is introduced on account of overlap between the echoes of medium 2. This overlap causes a rather small error in obtaining the parameters of layer 2 but this error propagates and is enlarged for the next layer. Another interesting thing that can be observed from Fig. 3.7 is the effect of reduction in the bandwidth. The real part of Y_m^2 is frequency independent (constant) (Equation (3.3.21)). This figure shows that the frequency band over which Y_m^2 is nearly constant reduces from the top to the bottom layer.

As this example demonstrates and is also stated by other authors (Sen [57, Chapter 2]), the direct methods are generally unstable for incomplete data, especially in the presence of noise. Golden *et al* [26] have proposed a stable version of the layer-stripping algorithm by imposing the causality at every

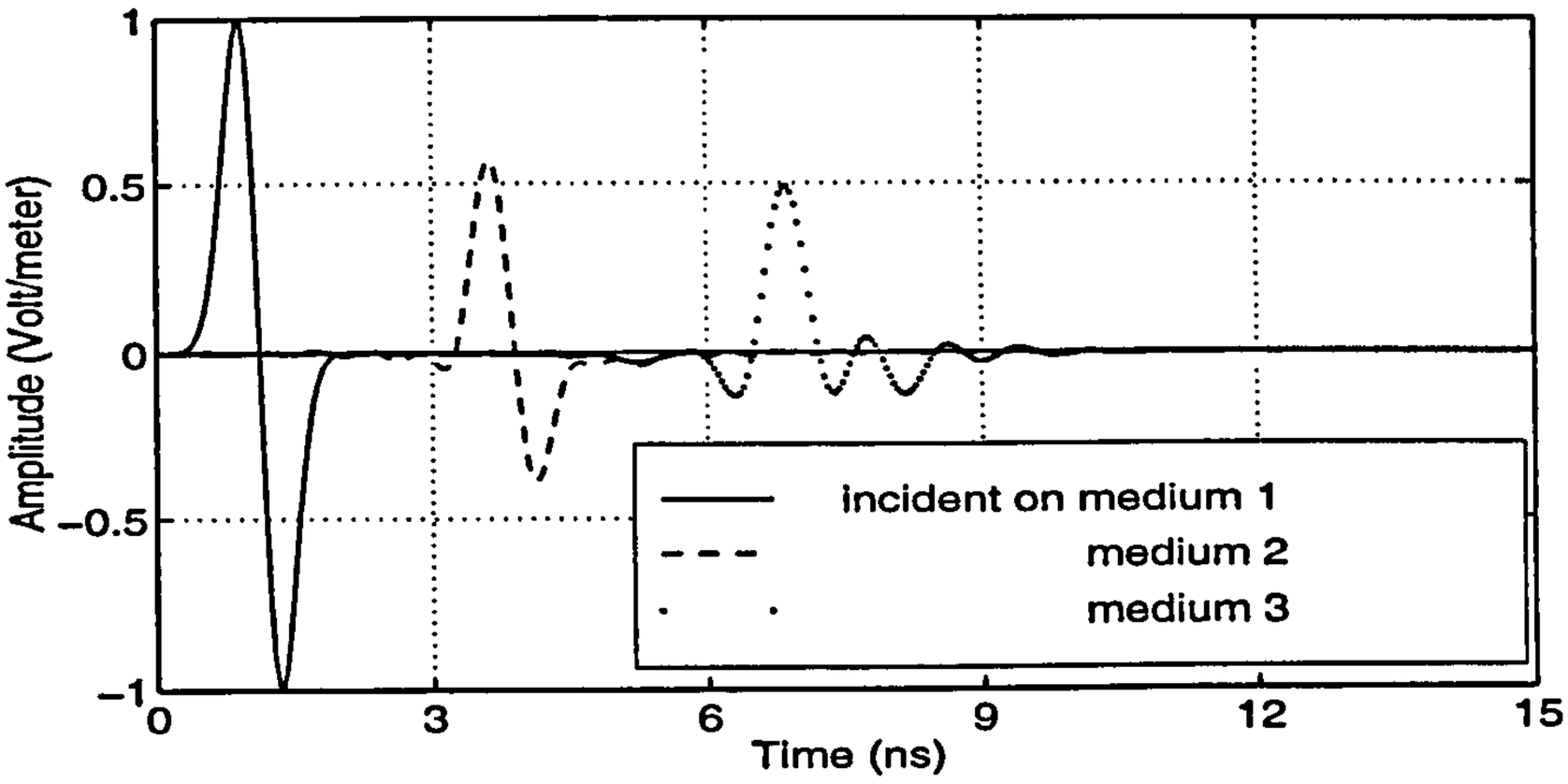

(a)

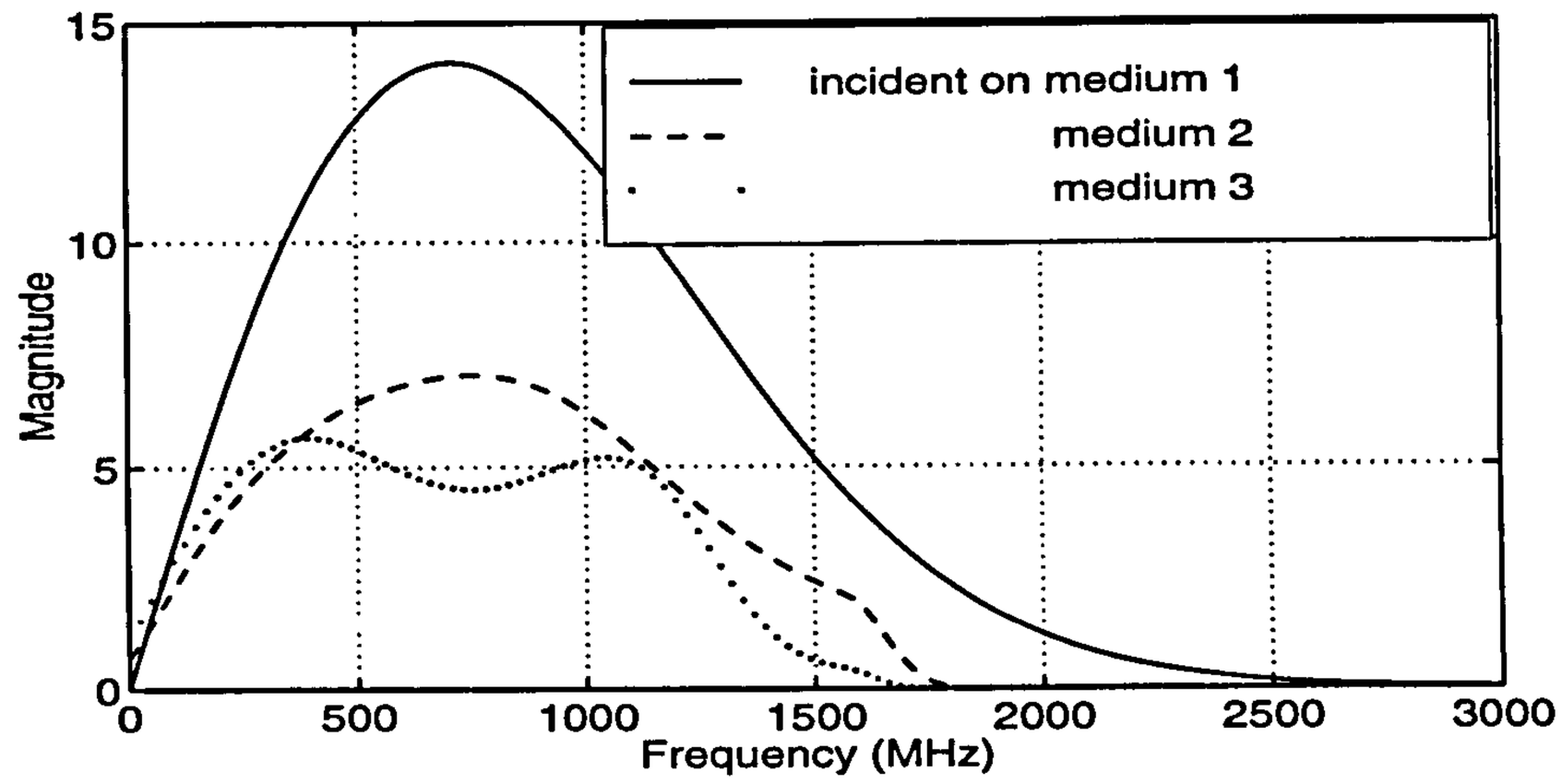

(b)

Figure 3.4: The incident pulses (a) in the time domain (b) in the frequency domain.

depth on the estimate of the depth-varying reflection coefficient. However, their algorithm does not seem to be appropriate for GPR applications. This is because firstly the algorithm is formulated for lossless media (i.e. $\sigma = 0$). Secondly, the reconstruction of the permittivity profile of a 3-layer medium by a model-based method and also by this algorithm shows that the model-based method provides a more accurate profile [26]. Overall, the direct methods

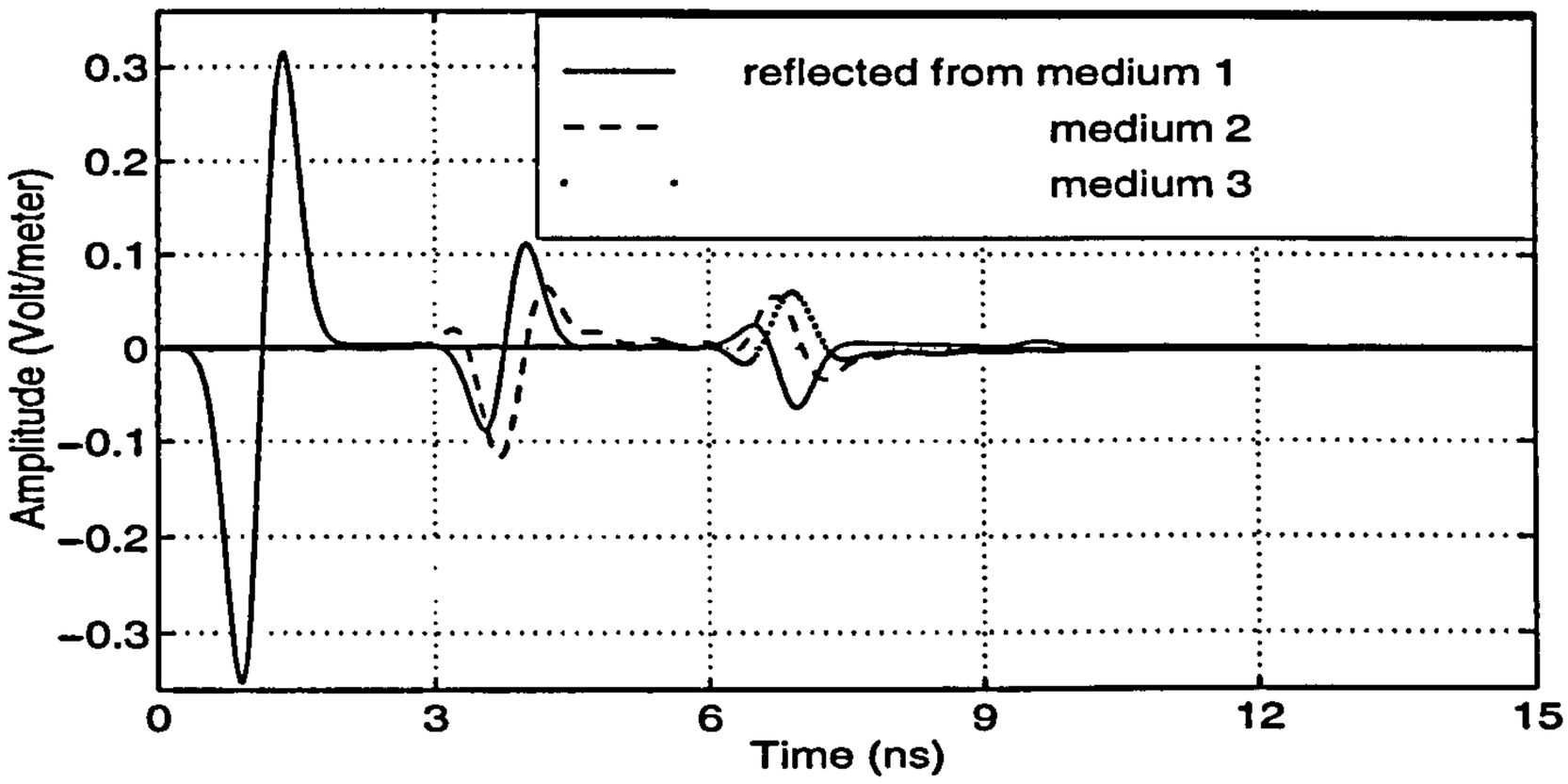

(a)

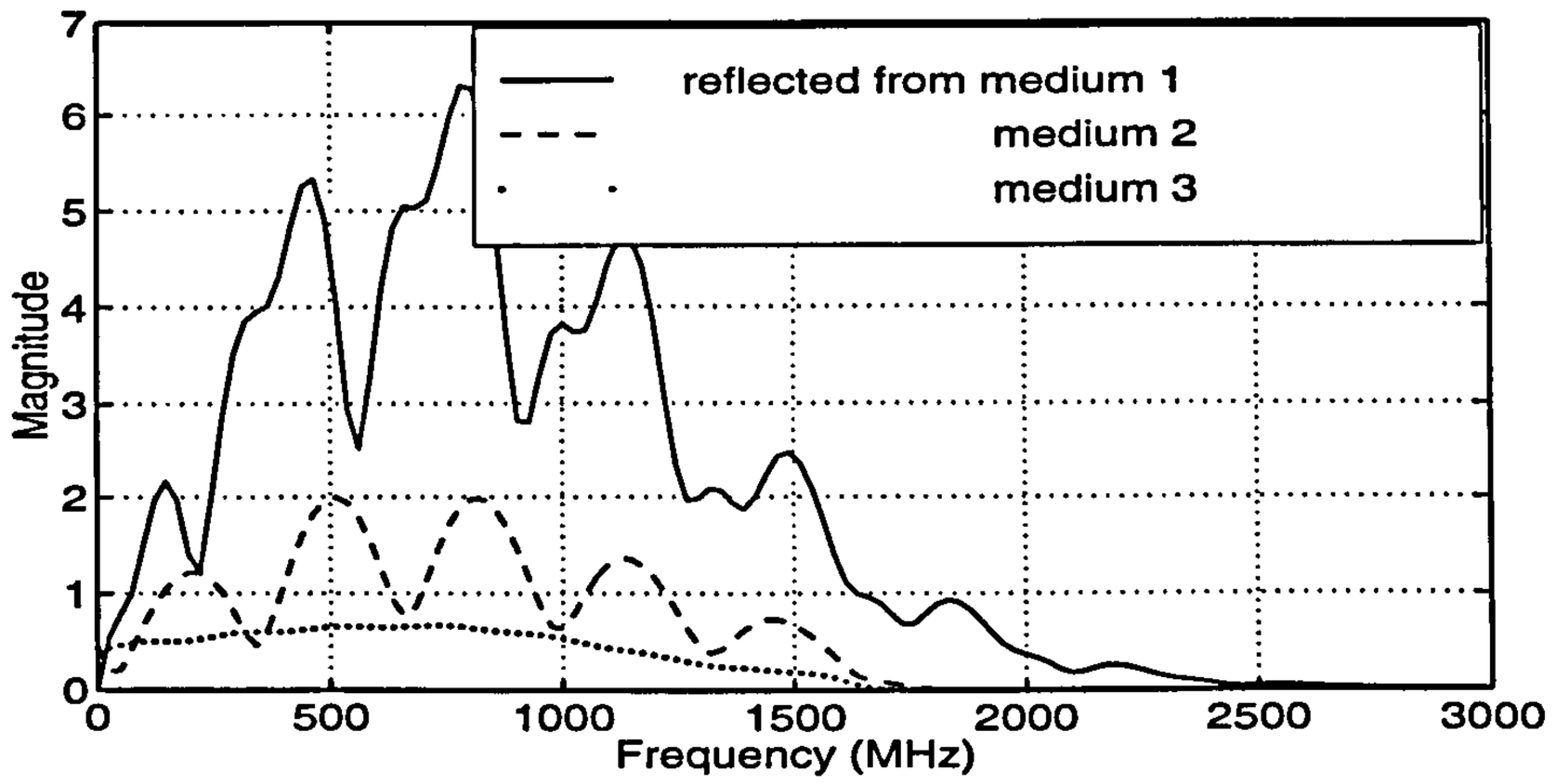

(b)

Figure 3.5: The reflected fields (a) in the time domain (b) in the frequency domain.

are not suitable for GPR applications since GPR data is not usually enough broadband (incomplete) and is inevitably contaminated by noise and clutter.

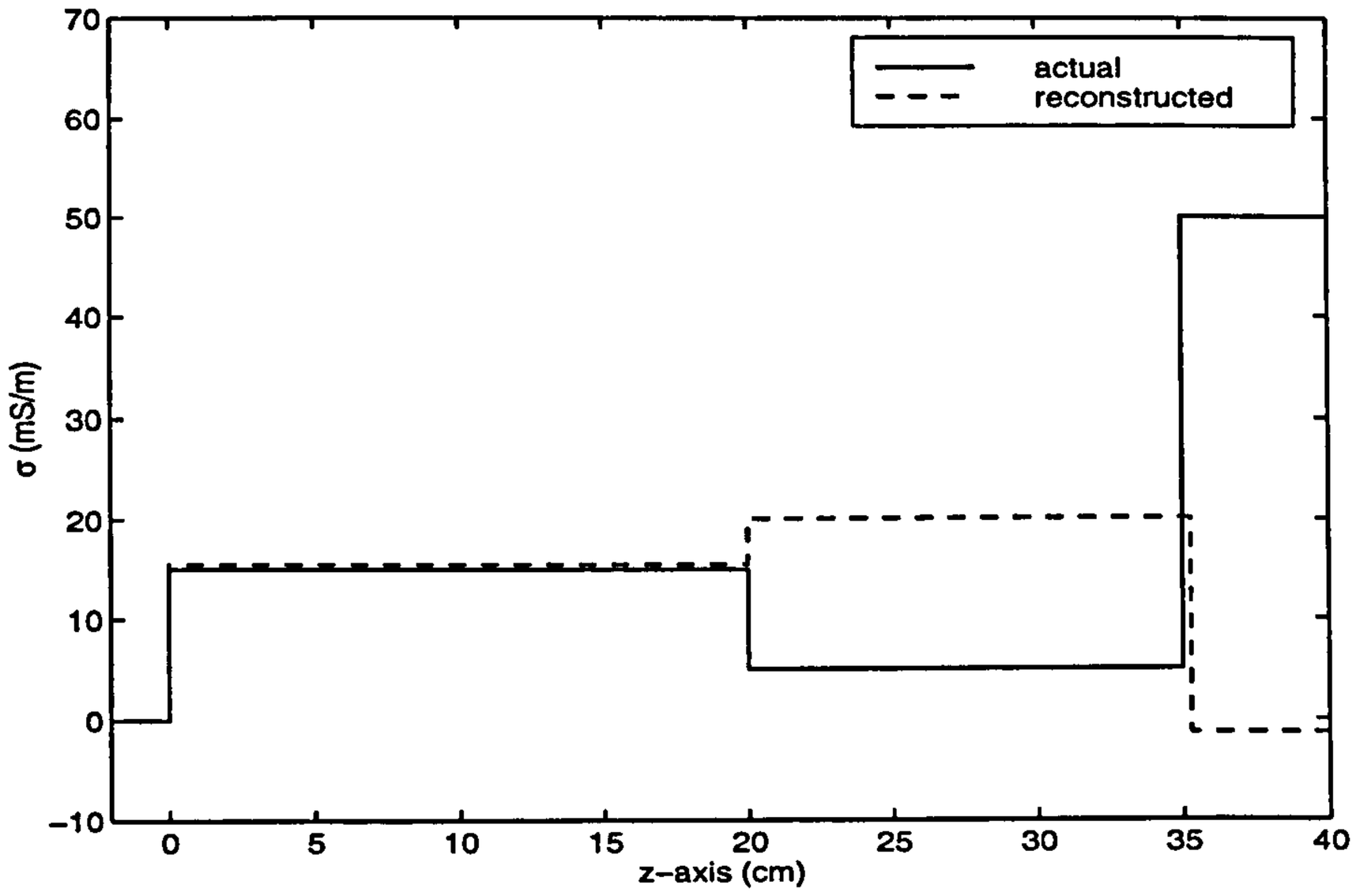

(a)

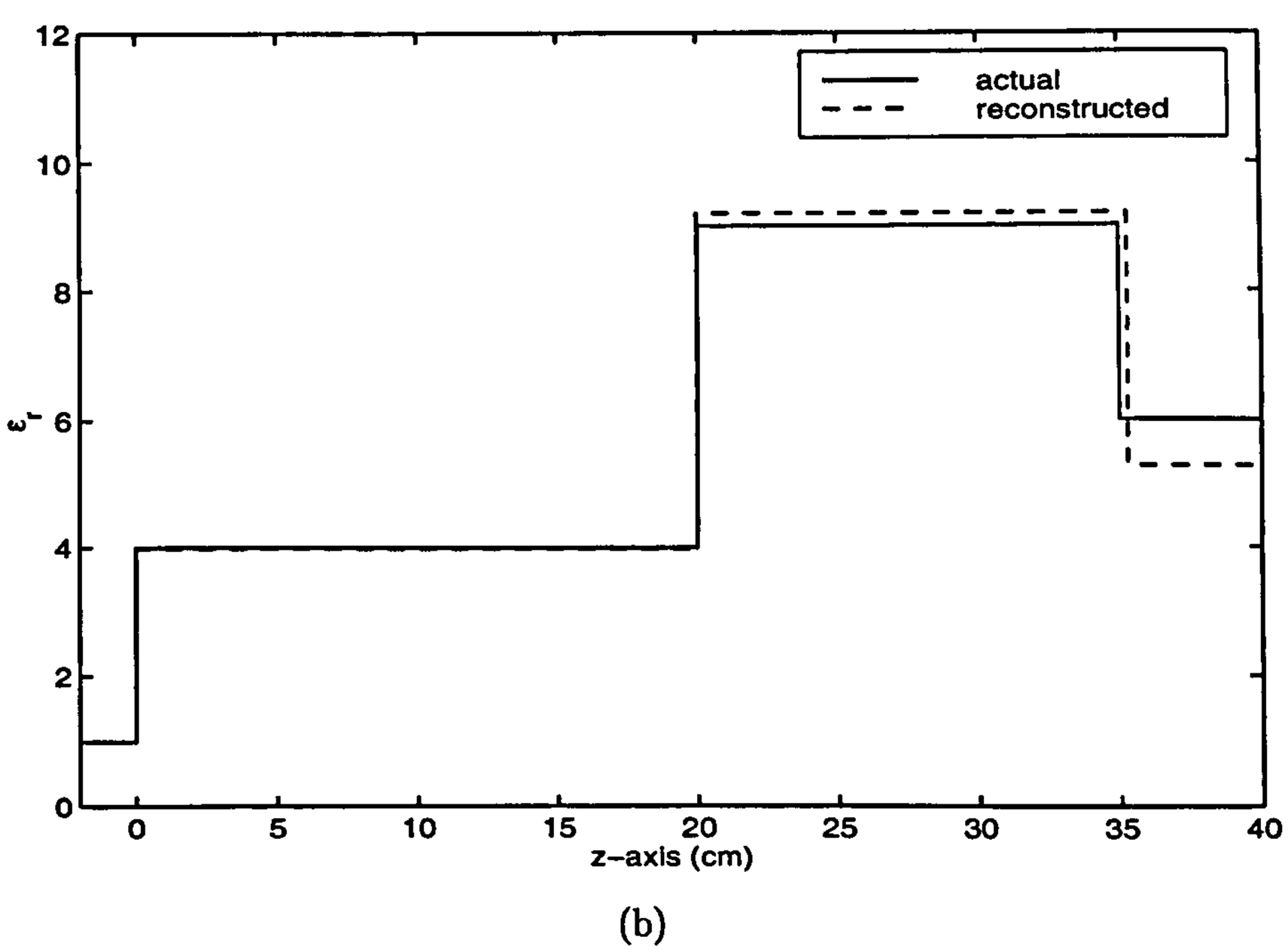

(b)

Figure 3.6: The reconstructed profiles of the 3-layer medium using the layer-stripping method.

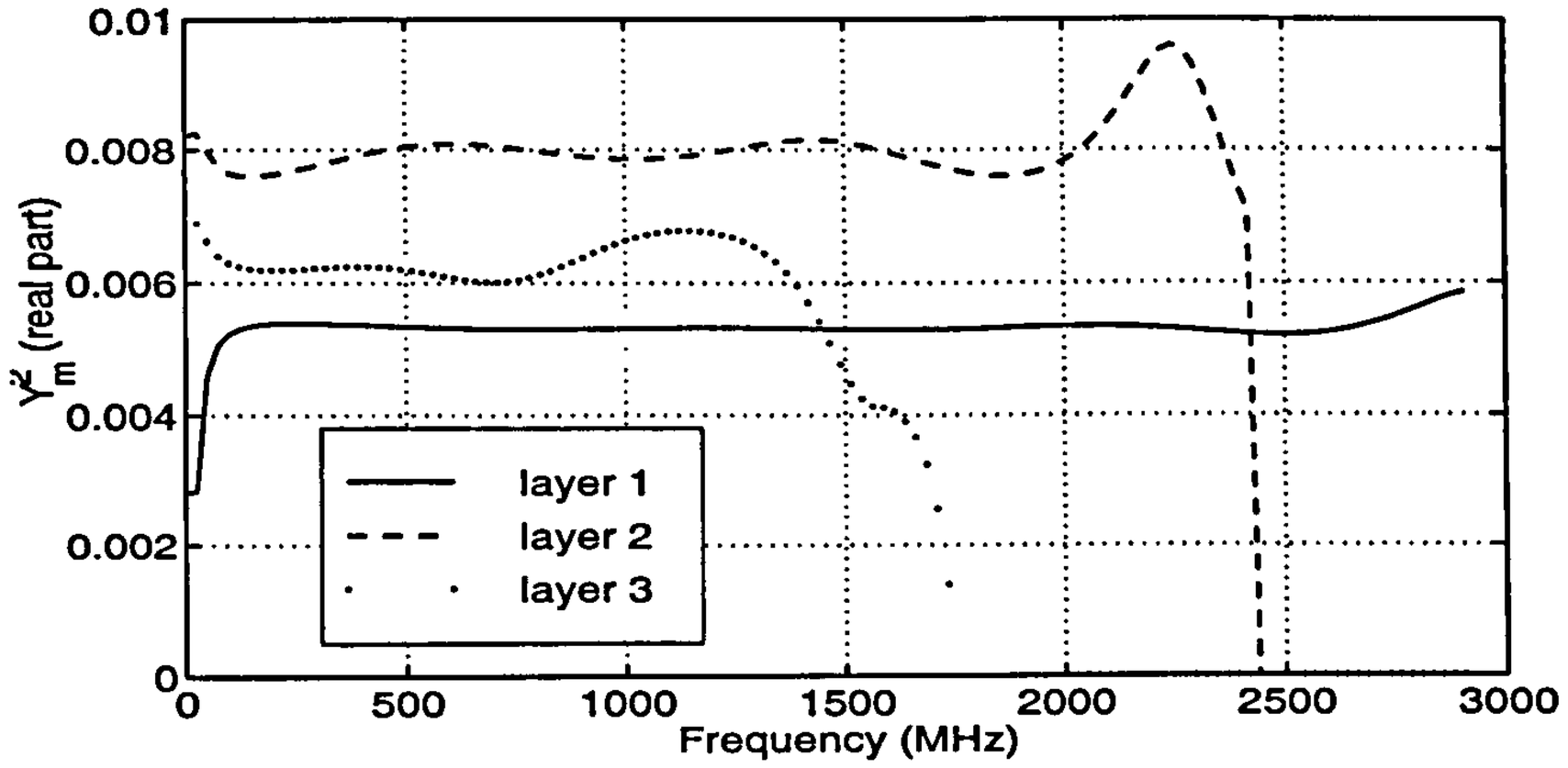

(a)

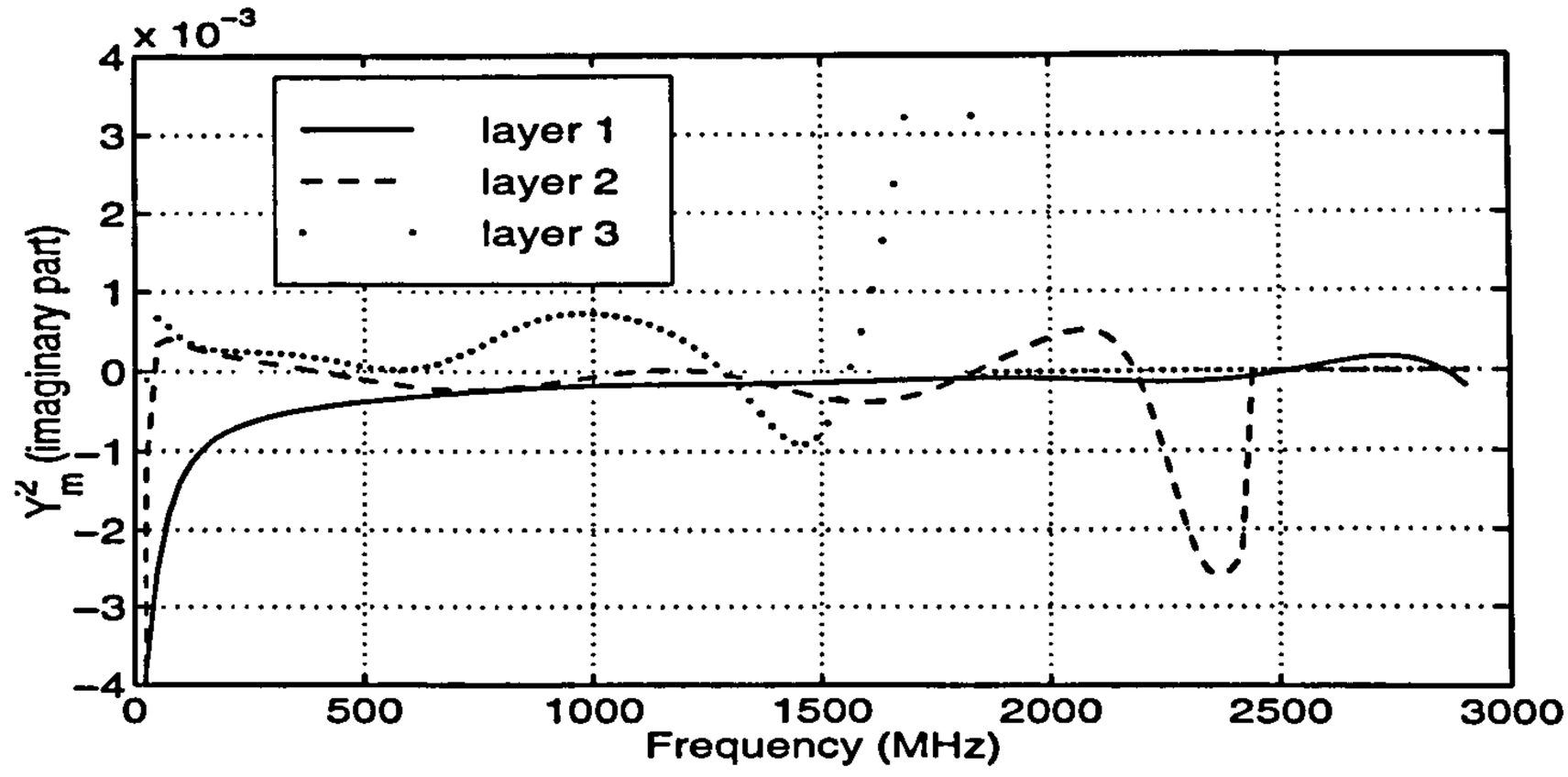

(b)

Figure 3.7: The square of the admittance of each layer.

3.4 Reflectivity Model-Based Inversion

The model-based approach could provide a robust, stable and reliable inversion [57]. The use of the nonlinear integral equation however makes the model-based methods computationally inefficient. In order to overcome this problem, a 1D model-based inverse method that employs the reflectivity formulation instead of the nonlinear integral equation is proposed in this section. The new method is referred to as the Reflectivity Model-Based Inversion (RMBI).

In the RMBI, the profile of a multi-layered medium (or non-uniform transmission line) is reconstructed by successive minimization of the Mean Square Error (MSE) obtained from the difference between the scattering data and those calculated from the reflectivity formulation (the forward model). In this way, the 1D EIS problem turns into parameter optimisation of an objective function that here is the MSE function. Either the reflection coefficient or the reflected field measured at different frequencies and/or incident angles can be regarded as the scattering data.

The application of the reflectivity formulation as the forward model in the RMBI method offers computational efficiency because:

1. the forward model is exact and in a closed-form. Thus, the calculation of the MSE function does not involve numerical solution. Considering a M-layer medium, the reflectivity formulation requires $O(M)$ arithmetic operations to calculate the reflected field from this medium for one incident angle and at one frequency. If the nonlinear integral equation is numerically solved for this problem by using Equation (3.2.15) with M_I divisions where $M_I > M$, the number of computations needed is $O(M_I^3)$. A substantial improvement in efficiency is therefore obtained by using the reflectivity formulation.

2. the gradient of the MSE function required in the optimisation procedure

---

THE APPLICATION OF GPR

can also be derived analytically in a closed-form. This greatly increases the efficiency of the inversion. As it will be seen in Subsection 3.4.1, the gradient evaluation also needs $O(M)$ computations.

3. there is no need for discretisation of a medium into thin layers. This is because the thickness of layers appears directly in the formulation ($\tanh(u_m h_m)$). Not only the electromagnetic parameters (permittivity, conductivity, permeability) but also the thickness of layers are variables in the optimisation process. Consequently, the number of variables in the MSE function is reduced significantly. As an example, to find the permittivity and conductivity profiles of a 3-layer medium (as shown in Fig. 3.3), the MSE is a function of 8 variables in the RMBI. There are however 30 variables in case of employing nonlinear integral equation (3.2.13) when the medium is divided into $M = 15$ thin layers.

Now, the necessary equations are derived. Let $S_1, S_2, \ldots, S_N$ be the reflected fields measured at N frequencies and/or incident angles. Furthermore, let $\mathbf{x}$ be a point in a multi-dimensional space with the dimension given by all constitutive parameters defining a layered medium, e.g. when the medium is non-magnetic, this point can be represented as

$$\begin{aligned} \mathbf{x} &= (x_1, x_2, x_3, \ldots, x_{D-1}, x_D) \\ &= (\sigma_1, \epsilon_1, h_1, \ldots, \sigma_M, \epsilon_M) \end{aligned} \tag{3.4.1}$$

where $D = 3M - 1$. The objective function (MSE) for the inverse method is defined as

$$f(\mathbf{x}) = \frac{1}{2N} \sum_{n=1}^{N} |P_n \, \Gamma_n(\mathbf{x}) - S_n|^2 \tag{3.4.2}$$

where P_n is the incident wave and $\Gamma_n(\mathbf{x})$ denotes the reflection coefficient obtained from the forward model under the same conditions as the observed (measured) data S_n. This equation can also be used when S_n is the reflection

coefficient of the medium by letting P_n be 1. The constitutive parameters are found by minimization of the function $f(\mathbf{x})$. A similar formulation can be applied to the case of non-uniform transmission line.

Due to the nonlinearity of the forward model, $f(\mathbf{x})$ may have several minima. The model-based inversions have the potential to be used in practical applications if they converge to the global minimum (the lowest minimum) of the objective function. Thus, a global optimization method should be used for $f(\mathbf{x})$. In this chapter, a modified-Newton method, being a local optimisation technique, is used to appreciate the importance of employing the global methods. The next chapter will be devoted to an study of global optimisation methods and their application to inverse problems.

Depending on the initial point, the modified-Newton method converges to a minimum that hopefully might be the global minimum. This method requires both the gradient vector and the Hessian matrix (i.e. the matrix of the second derivatives) of a function to find a minimum point. The gradient of the MSE function is herein derived. The Hessian matrix is estimated by finite differences within NAG routine E04KDF [50], which is a realisation of the modified-Newton algorithm and used in the present work.

3.4.1 The closed-form expression for the gradient

Let x_m be one of the parameters (σ_m, ϵ_m, μ_m or h_m) of the mth layer. The derivative of the objective function f given by (3.4.2) with respect to x_m can be written as

$$\frac{\partial f}{\partial x_m} = \frac{1}{N} \mathrm{Re}\left[\sum_{n=1}^{N} P_n \left(P_n \Gamma_n - S_n\right)^* \frac{\partial \Gamma_n}{\partial x_m}\right] \tag{3.4.3}$$

where "Re" and "$*$" denote respectively the real part and complex conjugation. Using Equations (3.3.11), (3.3.12), and (3.3.14), one can derive

$$\frac{\partial \Gamma_n}{\partial x_m} = -2 \frac{Y_0}{(Y_0 + W_1)^2} V_m^1 \,, \; m = 1, 2, \ldots, M \tag{3.4.4}$$

where $V_m^i = \partial W_i / \partial x_m$. The expression for V_m^i depends on the relation between i and m. If $i < m$, we have

$$V_m^i = \left(\frac{Y_i}{Y_i + W_{i+1} T_i} \right)^2 \left(1 - (T_i)^2\right) V_m^{i+1} \tag{3.4.5}$$

where $T_i = \tanh u_i h_i$. For the case of $i = m$, and $x_m = \sigma_m$, ϵ_m or μ_m, V_m^m is given by

$$\begin{aligned} V_m^m = \Big(& T_m \left[(W_{m+1})^2 + (Y_m)^2 + 2 Y_m W_{m+1} T_m \right] \frac{\partial Y_m}{\partial x_m} + \\ & Y_m \left[(Y_m)^2 - (W_{m+1})^2 \right] \frac{\partial T_m}{\partial x_m} \Big) \Big/ (Y_m + W_{m+1} T_m)^2 \end{aligned} \tag{3.4.6}$$

The expression for V_m^m when $x_m = h_m$ is

$$V_m^m = Y_m u_m \left[1 - (T_m)^2\right] \frac{(Y_m)^2 - (W_{m+1})^2}{(Y_m + W_{m+1} T_m)^2} \tag{3.4.7}$$

Finally, for the special case of $m = M$, Equation (3.4.6) is simplified to

$$V_M^M = \frac{\partial Y_M}{\partial x_M} \tag{3.4.8}$$

$\partial Y_m / \partial x_m$ and $\partial T_m / \partial x_m$ in (3.4.6) and (3.4.8) for $x_m = \sigma_m$, ϵ_m and μ_m are

$$\begin{aligned} \frac{\partial Y_m}{\partial \sigma_m} &= \frac{1}{2u_m} & , \quad \frac{\partial T_m}{\partial \sigma_m} &= \frac{\left[1-(T_m)^2\right] h_m}{2Y_m} \\ \frac{\partial Y_m}{\partial \epsilon_m} &= j\omega_n \frac{\partial Y_m}{\partial \sigma_m} & , \quad \frac{\partial T_m}{\partial \epsilon_m} &= j\omega_n \frac{\partial T_m}{\partial \sigma_m} \\ \frac{\partial Y_m}{\partial \mu_m} &= \frac{Y_m}{\mu_m} \left[\frac{1}{2} \left(\frac{\gamma_m}{u_m} \right)^2 - 1 \right] & , \quad \frac{\partial T_m}{\partial \mu_m} &= h_m \left[1 - (T_m)^2\right] \frac{\gamma_m^2}{2\mu_m u_m} \end{aligned} \tag{3.4.9}$$

Due to the similarity between the formulation of the forward problem for a multi-layered medium and that of a non-uniform transmission line, Equations (3.4.3)-(3.4.8) are applicable for the latter case. In addition, $\partial Y_m / \partial x_m$ and $\partial T_m / \partial x_m$ for $x_m = R_m$, L_m, G_m and C_m can be written as

$$\begin{aligned} \frac{\partial Y_m}{\partial R_m} &= -\frac{Y_m^2}{2u_m} & , \quad \frac{\partial T_m}{\partial R_m} &= \frac{Y_m \left[1-(T_m)^2\right] h_m}{2} \\ \frac{\partial Y_m}{\partial L_m} &= j\omega_n \frac{\partial Y_m}{\partial R_m} & , \quad \frac{\partial T_m}{\partial L_m} &= j\omega_n \frac{\partial T_m}{\partial R_m} \\ \frac{\partial Y_m}{\partial G_m} &= \frac{1}{2u_m} & , \quad \frac{\partial T_m}{\partial G_m} &= \frac{\left[1-(T_m)^2\right] h_m}{2Y_m} \\ \frac{\partial Y_m}{\partial C_m} &= j\omega_n \frac{\partial Y_m}{\partial G_m} & , \quad \frac{\partial T_m}{\partial C_m} &= j\omega_n \frac{\partial T_m}{\partial G_m} \end{aligned} \tag{3.4.10}$$

where use has been made of Equations (3.3.15) and (3.3.16).

With regard to the recursive Equation (3.4.5), the number of computations for calculating the gradient is $O(M)$, which is in proportion to that needed for calculating the objective function itself. This makes the RMBI more efficient.

3.4.2 The necessary condition for the unique solution to 1D EIS problems

Two quantities, Y_m (the characteristic admittance) and $X_m = u_m h_m$, of each layer might be obtained at most from the reflection coefficient of a multi-layer medium. This is because the reflection coefficient depends on the constitutive parameters of the medium only through Y_m and X_m. By manipulating (3.3.3) and (3.3.5), we have

$$\frac{a_\mu}{\omega} = \frac{X_m}{j\omega Y_m} = \mu_m h_m \tag{3.4.11}$$

$$a_\sigma + j a_\epsilon = X_m Y_m = \sigma_m h_m + j\omega \left[\epsilon_m - \frac{1}{\mu_m}\left(\frac{\sin\theta}{c}\right)^2\right] h_m \tag{3.4.12}$$

With the known values of X_m and Y_m that give the three quantities a_σ, a_ϵ and a_μ, the following three relations can be derived

$$\begin{cases} \sigma_m h_m = a_\sigma \\ \left[\epsilon_m - \frac{1}{\mu_m}\left(\frac{\sin\theta}{c}\right)^2\right] h_m = a_\epsilon/\omega \\ \mu_m h_m = a_\mu/\omega \end{cases} \tag{3.4.13}$$

According to the above set, one can state:

1. *Let the reflection coefficients (or the scattering data) be given at one incident angle for a multi-layered medium. Then one out of four parameters* $\{\sigma_m, \epsilon_m, \mu_m, h_m\}$ *of each layer, must be known in order to uniquely reconstruct the profile of the medium. If a layer is lossless, one of three*

parameters $\{\epsilon_m, \mu_m, h_m\}$ *of that layer, apart from* $\sigma_m = 0$, *must be known for the unique reconstruction of the multi-layered medium.*

Note that, the two terms a_ϵ/ω and a_μ/ω are frequency independent. Therefore, four parameters cannot uniquely be calculated by taking into account the value of X_m and Y_m at different frequencies.

2. *To obtain all unknown parameters uniquely, it is necessary that the reflection coefficients are available for at least two incident angles, resulting in one extra independent relation in* (3.4.13).

3. *When the data is given for one incident angle excluding* $\theta = 0°$, *the unique determination of all unknown parameters requires that the reflection coefficients are available for both TE and TM wave incidence.*

It should be noted that when a layer is lossless, the equation containing σ_m will be omitted from the set (3.4.13). That is why the first statement includes the lossless condition. The third statement can be achieved by the manipulation of the reflectivity formulation for both TE and TM wave incidence.

Pursuing a similar procedure for the case of a non-uniform transmission line, it can be stated that:

In order to uniquely reconstruct the profile of a non-uniform transmission line from the reflection coefficients of the line, one out of five parameters $\{R_m, L_m, C_m, G_m, h_m\}$ *of each section excluding zero value parameters must be known.*

There is no alternative for this case owing to the only possibility of $\theta = 0°$.

3.4.3 Determining the number of layers of a medium

It was assumed that the number of layers is known in the description of the RMBI. If the number of layers is however unknown, to find the structure of the medium, we could employ the present procedure making use of the

RMBI iteratively. At the kth iteration of this procedure, while the medium is considered to consist of k layers, the constitutive parameters of the medium are reconstructed by the RMBI. The resultant MSE $\tilde{f}_k$, which is viewed as the global minimum of the objective function, is compared with the one from the $(k-1)$th iteration ($\tilde{f}_{k-1}$). If they are sufficiently close, two cases may arise: a) the parameters of two adjacent layers are matched $\sigma_m = \sigma_{m-1}$, $\epsilon_m = \epsilon_{m-1}$ etc.; b) the thickness of a layer converges to zero. For both cases, one layer can be omitted and the reconstructed profile for k-layer medium is the same as that for $(k-1)$-layer medium. This would happen for $k = M+1$, where M is the actual number of layers. When the observed data is free of noise, the global minimum of the objective function for M-layer and $(M+1)$-layer mediums are equal (i.e. $\tilde{f}_M = \tilde{f}_{M+1}$). For the case where the data is corrupted by noise, we generally have $\tilde{f}_{M+1} \leq \tilde{f}_M$. Consequently, the iterative procedure at iteration k is terminated if

$$\left|\tilde{f}_k - \tilde{f}_{k-1}\right| \leq \varrho \tilde{f}_k \tag{3.4.14}$$

where ϱ is a small value less than one. Otherwise, the number of layers is incremented and the process is repeated.

Example 3.2. The profile of the 3-layer medium in Example 3.1 is now reconstructed by the RMBI. The frequency components of the reflected field shown in Fig. 3.5(b) (solid line) in the interval [450 MHz, 850 MHz] are used as the observed data. The magnitudes of the data are maximum in this region resulting in a higher signal-to-noise ratio. This is an example that shows how one can diminish the effect of noise in model-based inverse methods.

The reduction of the MSE versus the number of function evaluations by the modified-Newton method is illustrated in Fig. 3.8. The initial points for the MSE curves are listed in Table 3.1. The computational efficiency of optimisation methods is usually measured in terms of the number of evaluations of the objective function. In order to estimate the computation cost, the time

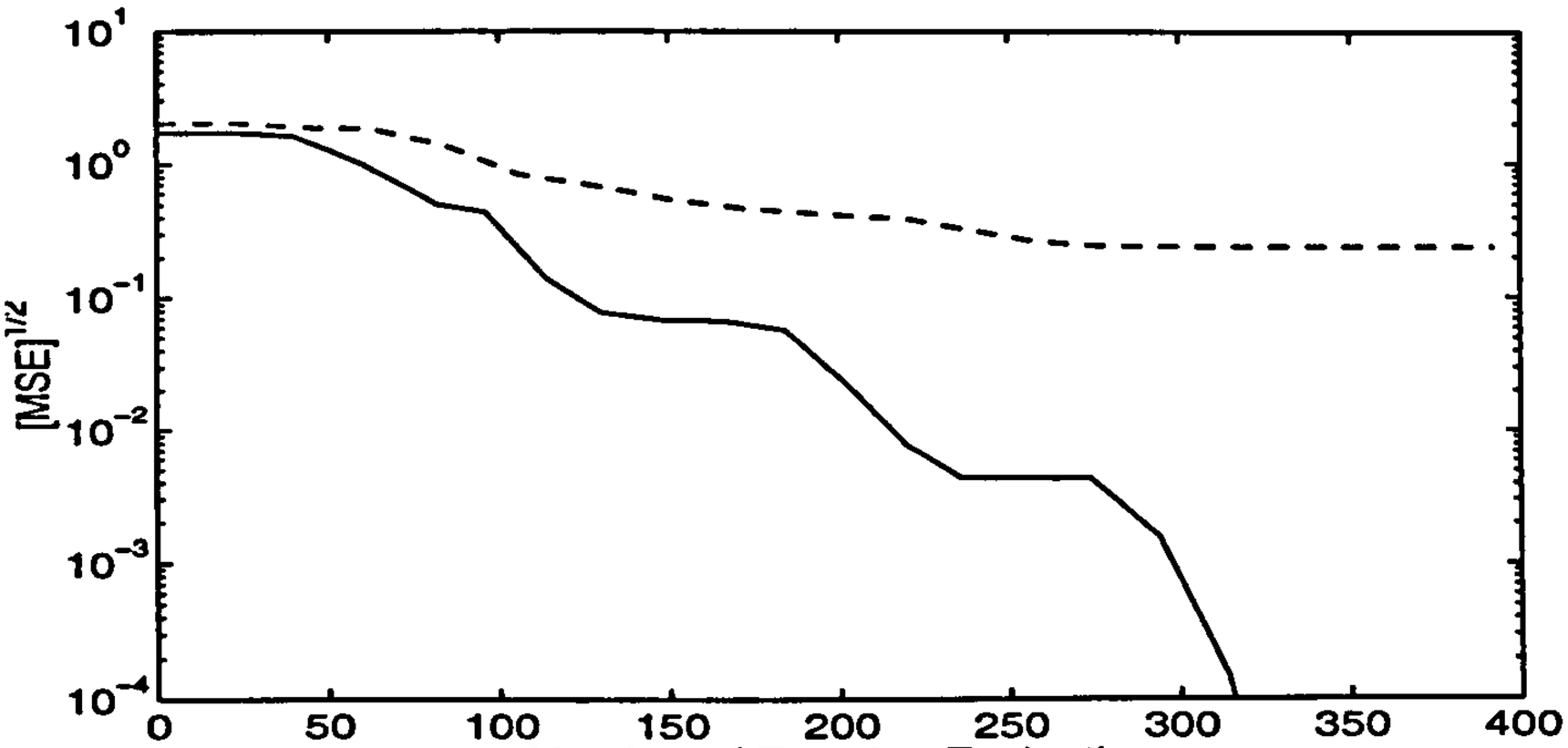

Figure 3.8: Illustration of reducing the MSE function by the modified-Newton method with two different sets of initial parameters given in Table 3.1.

Table 3.1: The initial profiles corresponding to the solid and dashed lines in Fig. 3.8.

		Initial parameters			Final
		σ(S/m)	ϵ_r	h(cm)	MSE
Solid	Layer 1	0.0100	6.0	15.0	
line	Layer 2	0.0030	10.0	12.0	0.0
	Layer 3	0.0400	5.0	–	
Dashed	Layer 1	0.0250	10.0	10.0	
line	Layer 2	0.0100	10.0	10.0	0.0567
	Layer 3	0.1000	10.0	–	

for gradient evaluation is measured in terms of the time for the function evaluation. For this example and all examples given in the next chapter, it has been found that the cost of gradient evaluation is nearly twice that of function evaluation.

The final profiles are shown in Fig. 3.9. It can be concluded that firstly the objective function has several minima and secondly the modified-Newton method provides different solutions for the two initial points. The medium is

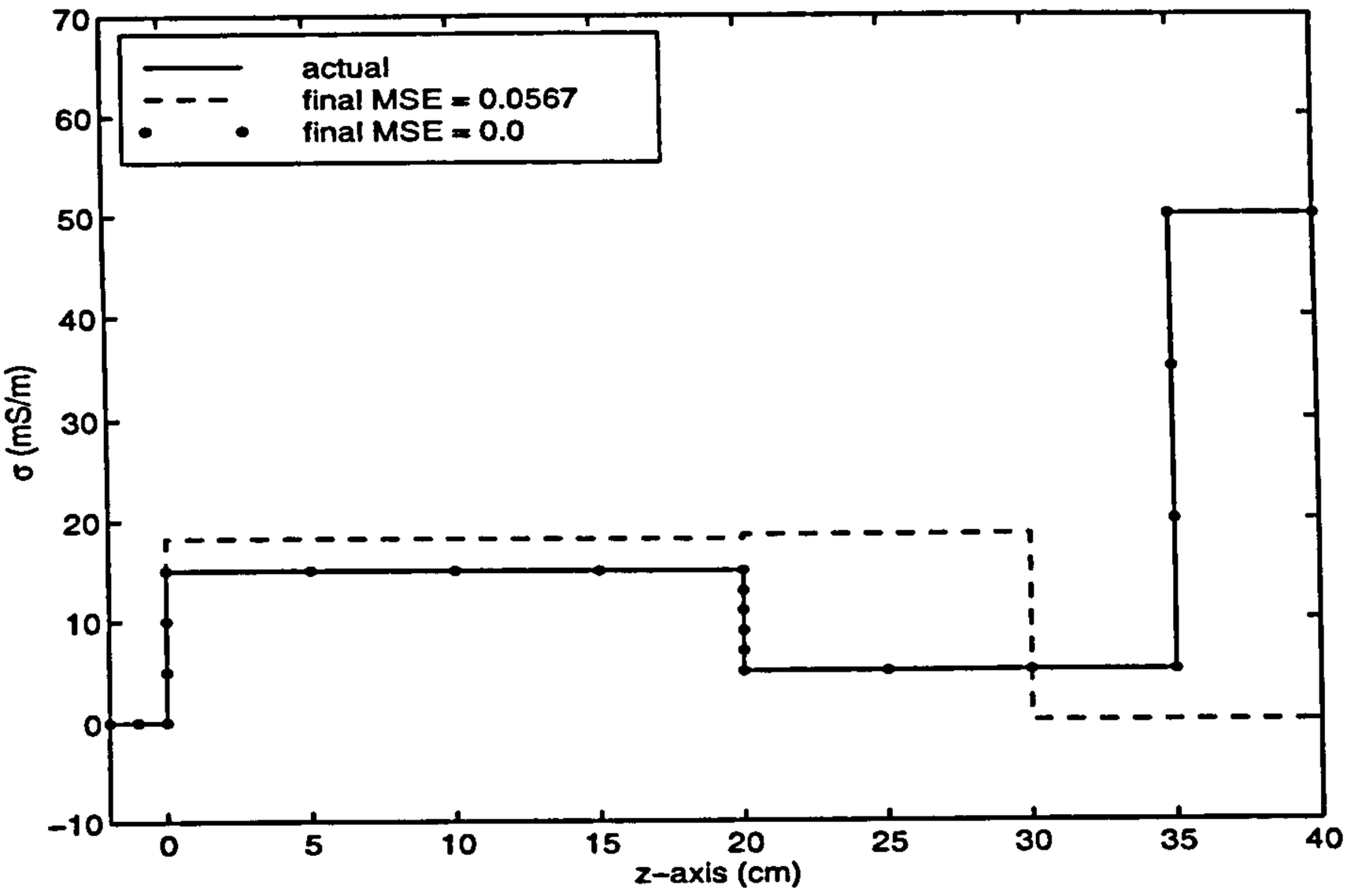

(a)

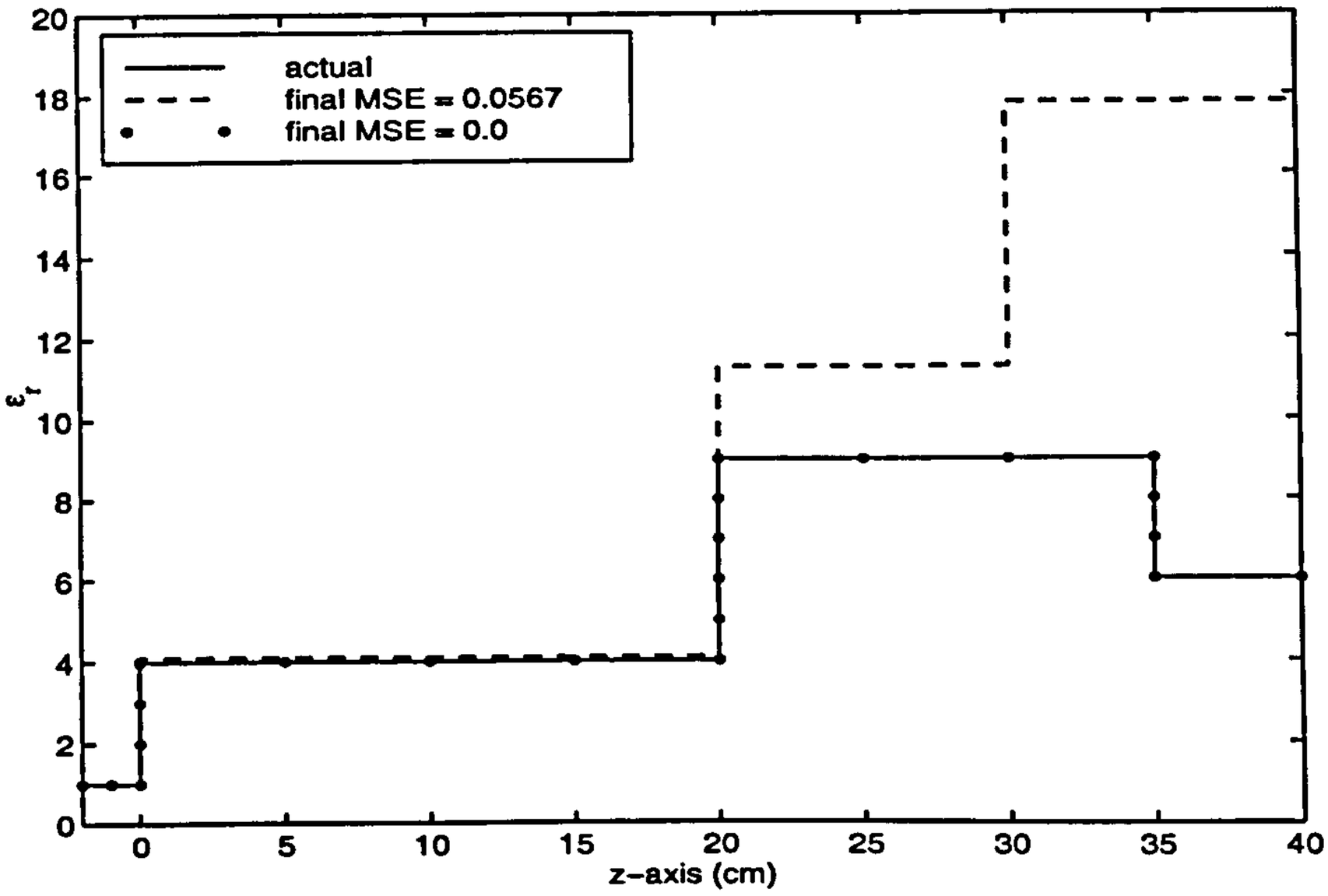

(b)

Figure 3.9: The profiles obtained by employing the modified-Newton method in the RMBI with the initial parameters given in Table 3.1.

fully reconstructed for the first selected initial profile, but not for the second one.

In addition to the modified-Newton method, the conjugate gradient and quasi-Newton methods were also tested using a number of multi-layered media. The conclusion was that none of these local optimisation techniques are reliable.

THE APPLICATION OF GPR

Chapter 4

Global Optimisation Methods

4.1 Introduction

Local optimisation methods have often been used for IS problems [12], [29], [30], [49], [64]. The convergence of local optimisation methods to the global optimum can only be assured if *a priori* information is incorporated in the definition of the objective function as well as in the selection of the initial guess. There is however no certainty that the method finds the global minimum in a case with a lack of sufficient prior knowledge, as it was seen from Example 3.2 given in the previous chapter. Such a situation often arises in practical applications. Therefore, a global optimisation technique should be used in a model-based inversion [23], [57]. In global optimization methods, it is no longer necessary to specify the initial guess although the bounds of the parameters have to be defined. Any prior knowledge of the parameters can help to narrow the parameter bounds and results in a faster convergence to the true profile (the global minimum).

The global optimisation problem is to find a solution in a feasible set of solutions, for which the objective function attains the smallest value. The feasible set might be discrete containing a finite but very large number of

solutions. In that case, the problem is referred as a combinatorial problem. The number of solutions will be infinite for an objective function with continuous variables, as it is the case for electromagnetic inverse problems. A continuous global optimisation problem for an objective function $f(\mathbf{x})$ can be defined by

Definition 4.1. Given $f(\mathbf{x}) : \mathbb{R}^D \longrightarrow \mathbb{R}$ and $S \subseteq \mathbb{R}^D$ ($\mathbb{R}$ denotes the set of real numbers) then find $\mathbf{x}^{**} \in S$ for which $f(\mathbf{x}^{**}) \leq f(\mathbf{x})$ for all $\mathbf{x} \in S$. $\mathbf{x}^{**}$ is referred as the *global minimizer* (or the *global minimum point*) of the objective function and $f(\mathbf{x}^{**})$ is referred as the *global minimum* . The feasible region S is usually given by

$$S = \{x \mid L_i \leq x_i \leq U_i \,,\; i = 1, \ldots, D\} \tag{4.1.1}$$

where L_i and U_i are respectively the lower and upper bounds of the variable x_i.

The theory of finding a minimizer in the neighbourhood of an initial solution (i.e. finding a local minimum) is well developed [19], [25]. Classical hill-climbing methods, such as steepest decent, conjugate gradient, quasi-Newton and modified-Newton methods, are among those, which efficiently find a local optimum. The final solution of these methods is determined by the starting point as illustrated in Fig. 4.1. Commencing from any point in the region $S_1 = [x_1, x_2]$, hill-climbing algorithms give the same solution x_1^* for the 1D function $f(x)$ shown Fig. 4.1. Region S_1 is called the *attraction region* of the minimum $f(x_1^*)$, generally defined as

Definition 4.2. The attraction region (or the basin) of a local minimum $f(x^*)$ is the set of points in the feasible region S starting from which a given local search procedure converges to $f(x^*)$.

Multistart was one of the early methods to tackle the global optimisation problems. This algorithm uses a local procedure that starts from different

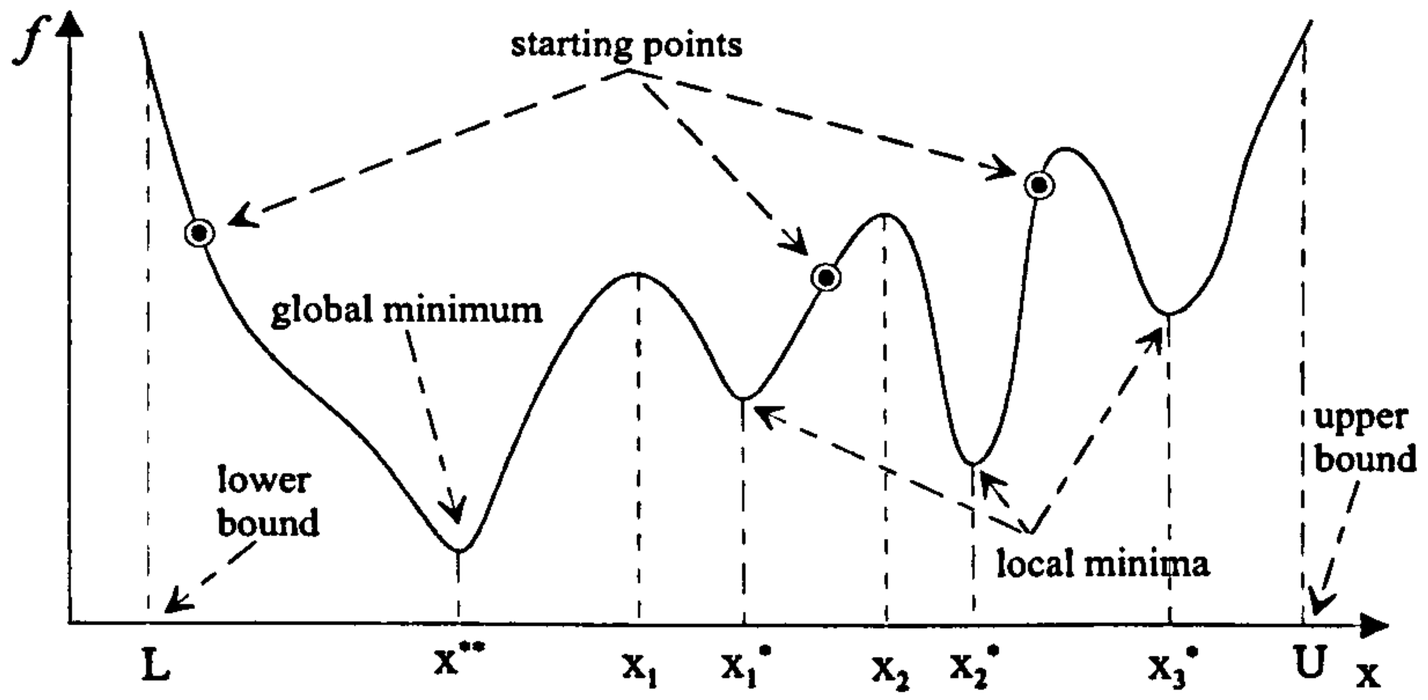

Figure 4.1: A function in 1-dimensional space having several minima.

points sampled in the whole optimisation region. The main drawback of Multistart is that when many starting points are used, the same minimum may be found several times. Various methods with better efficiency have been proposed since then. They can broadly be classified into two classes: the deterministic and the stochastic approaches, as recognised by Dixon and Szego [18].

Included in the class of deterministic approaches are space covering and trajectory methods. Most of these techniques do not provide a guarantee that the global minimum will be found. Such a guarantee is provided under additional assumptions about the objective function f, which are difficult to verify in practice [11]. Furthermore, large computational effort is required in many deterministic methods in order to find the global minimum. The methods in the second group incorporate stochastic features in the search procedure, generally the sampling of $f(\mathbf{x})$ at randomly distributed points over the feasible region. This allows a probabilistic guarantee that the methods converge to the global optimum. The stochastic methods are therefore investigated for application in the RMBI. It is not possible to conduct a thorough investigation of the relative merits of various stochastic approaches in this thesis. Instead, we consider genetic algorithms (GA) and simulated annealing (SA) that have already been used in the inverse problems [23],[57] together with the multi-level

single-linkage (MLSL) method known as an efficient technique for the optimisation of continuous functions [11]. A comparative study of GA, SA and MLSL will be carried out in order to identify the most efficient and reliable algorithm for our application.

Genetic algorithms optimise a function using processes inspired from the mechanics of natural selection and genetics (crossover and mutation) [44]. The optimisation is accomplished by evolving a population of candidate solutions and improving incrementally the individuals forming the population. The convergency of GA and its variants to the global optimum is only guaranteed in a weak probabilistic sense, whereas it has been proved for SA and MLSL. A comparison between GA and MLSL has been performed by Renders and Flasse [56]. They have proposed a hybrid version of genetic algorithms combining principles from GA and hill-climbing techniques in order to improve the computing time and the accuracy of GA. The conclusion was that the hybrid method is superior to the standard GA but it produces the same results as those of MLSL.

Consequently, the attention is paid to SA and MLSL in this work. Due to the stochastic nature of these algorithms, it is required to run them many times for a specific objective function in order to compare the general performance of the two methods. The performance is evaluated in terms of efficiency (the computation time) and reliability (the probability of finding the global minimum within a finite computing time). In the examples presented in this chapter, every algorithm is tried 10 times for the minimization of each objective function. Because the computational cost is dominated by the evaluation of the MSE function, the efficiency of the algorithms is compared in terms of the number of evaluating the MSE function. Nevertheless, the running time is given in some examples for comparison of the algorithms. An intrinsic FORTRAN function (dtime) is used to obtain the running time.

This chapter is organised into 5 sections: Section 4.2 is devoted to a brief

formulation of the modified-Newton method used as the local procedure in MLSL. Section 4.3 deals with the description of the standard SA algorithm and adaptive SA (a faster version of SA). The multi-level single-linkage method is detailed in Section 4.4 where several examples are presented in order to compare its performance with that of the standard SA and adaptive SA methods for 1D inverse problems. In Section 4.5, a novel optimisation algorithm, adaptive random search, is introduced. The employment of this method in conjunction with MLSL forms a hybrid method, which improves the reliability and efficiency. The improvement is verified by various minimization examples.

4.2 Modified-Newton Method

Hill-climbing algorithms generate an iterative sequence $\mathbf{x}(k)$ that might converge to a local or global minimizer. Most of them construct a sequence of $\mathbf{x}$ which satisfies [19, Chapter 2]

$$\mathbf{x}(k+1) = \mathbf{x}(k) + \zeta(k)\,\mathbf{q}(k) \tag{4.2.1}$$

where $\zeta(k)$ is the step length and the vector $\mathbf{q}(k)$ is called the search direction. The computation of $\zeta(k)$ involves a line search, the purpose of which is to find a particular value of ζ for which the function $f[\mathbf{x}(k) + \zeta(k)\,\mathbf{q}(k)]$ is minimized.

The distinction between hill-climbing methods lies with the definition of the search direction. Of the hill-climbing techniques, Newton's methods minimize an objective function, which is approximated at each iteration k by a quadratic function. The methods use both the gradient and the Hessian matrix of the objective function to define the search direction. Let $\mathbf{g}(\mathbf{x})$ denote the gradient and $\mathbf{H}(\mathbf{x})$ the Hessian matrix of the function f. Then

$$\mathbf{g}(\mathbf{x}) = \left[\frac{\partial f}{\partial x_1}, \frac{\partial f}{\partial x_2}, \cdots, \frac{\partial f}{\partial x_D}\right]^T \tag{4.2.2}$$

$$\mathbf{H}(\mathbf{x}) = \begin{bmatrix} \frac{\partial^2 f}{\partial x_1^2} & \cdots & \frac{\partial^2 f}{\partial x_1 \partial x_D} \\ \vdots & \ddots & \vdots \\ \frac{\partial^2 f}{\partial x_D \partial x_1} & \cdots & \frac{\partial^2 f}{\partial x_D^2} \end{bmatrix} \tag{4.2.3}$$

where T stands for matrix transpose. Note that $\mathbf{H}$ is symmetric, i.e. $\mathbf{H} = \mathbf{H}^T$. The quadratic model of f is obtained by truncating the Taylor series expansion of the function about $\mathbf{x}(k)$, i.e.

$$f[\mathbf{x}(k) + \Delta\mathbf{x}(k)] = f[\mathbf{x}(k)] + \mathbf{g}^T[\mathbf{x}(k)]\,\Delta\mathbf{x}(k) + \frac{1}{2}\,\Delta\mathbf{x}^T(k)\,\mathbf{H}[\mathbf{x}(k)]\,\Delta\mathbf{x}(k) \tag{4.2.4}$$

If the Hessian matrix is positive definite (i.e. if all its eigenvalues are positive), the quadratic model has a unique minimum at $\Delta\mathbf{x}(k) = \mathbf{q}(k)$ that satisfies

$$\mathbf{H}[\mathbf{x}(k)]\,\mathbf{q}(k) = -\mathbf{g}[\mathbf{x}(k)] \tag{4.2.5}$$

Thus, the solution of this equation gives the search direction $\mathbf{q}(k)$. Equation (4.2.5) can be derived by setting the gradient of the quadratic function to zero.

The quadratic model need not have a minimum when $\mathbf{H}[\mathbf{x}(k)]$ is not positive definite. In this case, the search direction is obtained by modifying the Hessian matrix to a positive-definite one. Several strategies have been developed for this [25]; the methods, which do not use the Newton direction when the Hessian matrix is indefinite, are termed modified-Newton methods. The NAG routine E04KDF [50], adopted in this research, determines the search direction using

$$\{\mathbf{H}[\mathbf{x}(k)] + \mathbf{A}\}\,\mathbf{q}(k) = -\mathbf{g}[\mathbf{x}(k)] \tag{4.2.6}$$

where the non-negative diagonal matrix $\mathbf{A}$ is chosen so that $\mathbf{H}[\mathbf{x}(k)] + \mathbf{A}$ is a positive-definite matrix. More details of the algorithm can be found in [25, Chapter 4].

4.3 Simulated Annealing

Simulated annealing is based on the analogy between the physical annealing process of solids and the problem of finding the minimum of an objective function [1]. In an annealing process the temperature of a solid in a heat bath is initially increased to a maximum value at which the solid melts and becomes disordered. The temperature is then lowered slowly so that the system at any time is approximately in thermal equilibrium. As cooling proceeds, the system becomes more ordered and approaches a frozen ground state at temperature zero. It is presumed that the initial temperature of the solid is sufficiently high and the cooling is carried out adequately slow; Otherwise the system may become quenched forming defects or freezing out in meta-stable states (i.e. trapped in a local energy state).

Metropolis algorithm [1] provides a simple method for simulating the evolution of a solid in a heat bath to thermal equilibrium. In each step of the algorithm, the current state is perturbed slightly to generate a new state. If the resulting change in the energy of the system $\Delta E \leq 0$, the new state is accepted as the current state. If the energy difference is positive ($\Delta E > 0$), the new state is accepted with a probability given by

$$P(\Delta E) = \exp\left(-\frac{\Delta E}{k_B T}\right) \tag{4.3.1}$$

where k_B is the *Boltzmann constant* and T denotes the temperature. This process is repeated a sufficient number of times to give a good sampling statistics for the current temperature until thermal equilibrium is reached. The temperature is then decremented and the entire process repeated until a frozen state is achieved ($T = 0$). Thermal equilibrium is characterized by the *Boltzmann distribution* . According to this distribution, the probability of a physical system being in a state i with energy E_i at temperature T is given by

$$P_i = \frac{1}{Z} \exp\left(-\frac{E_i}{k_B T}\right) \tag{4.3.2}$$

where Z is the partition function defined as

$$Z = \sum_j \exp\left(-\frac{E_j}{k_B T}\right) \tag{4.3.3}$$

The summation is taken over all possible states.

Making an analogy between the system energy and the value of a function, SA algorithm can be viewed as Metropolis algorithm, applied for minimization of a function. This algorithm and its numerous variants have been widely used in actual large-scale optimisation problems ranging from VLSI circuitry to image analysis [4]. Two kinds of SA methods are described herein: the standard SA and adaptive SA. Before proceeding with the detailed discussion of the methods, we define the necessary terms to be used later.

Definition 4.3. $S_{\mathbf{x}}$ is called a neighbourhood region of a point $\mathbf{x}$ if $S_{\mathbf{x}} \subseteq S$ and $\mathbf{x} \in S_{\mathbf{x}}$. The neighbourhood region is mostly chosen to be a hypercube in the D-dimensional space. In accordance with (4.1.1), $S_{\mathbf{x}}$ is given by

$$S_{\mathbf{x}} = \{\mathbf{y} \mid L_{\mathbf{x}i} \leq y_i \leq U_{\mathbf{x}i}\ ,\ i = 1, \ldots, D\} \tag{4.3.4}$$

where $L_{\mathbf{x}i}$ and $U_{\mathbf{x}i}$ are determined by

$$\begin{aligned}
L_{\mathbf{x}i} = U_i - \beta_i \quad &, \quad U_{\mathbf{x}i} = U_i \qquad \text{if} \quad x_i^c + \tfrac{\beta_i}{2} > U_i \\
L_{\mathbf{x}i} = L_i \quad &, \quad U_{\mathbf{x}i} = L_i + \beta_i \quad \text{if} \quad x_i^c - \tfrac{\beta_i}{2} < L_i \\
L_{\mathbf{x}i} = x_i^c - \tfrac{\beta_i}{2} \quad &, \quad U_{\mathbf{x}i} = x_i^c + \tfrac{\beta_i}{2} \qquad \text{otherwise}
\end{aligned} \tag{4.3.5}$$

providing that $\beta_i \leq U_i - L_i$. The point $\mathbf{x}^c = [x_1^c, x_2^c, \ldots, x_D^c]$ is the central point of $S_{\mathbf{x}}$ and the elements of the vector $\beta = [\beta_1, \beta_2, \ldots, \beta_D]$ correspond to the lengths of the sides of $S_{\mathbf{x}}$.

Definition 4.4. The generation probability density function $g_{\mathbf{x}}(\mathbf{y})$ determines the probability of generating a point $\mathbf{y}$ in the region $S_{\mathbf{x}}$.

Definition 4.5. The acceptance probability is defined as the chance of accepting a point $\mathbf{y}$ for an objective function f in the neighbourhood region of the

current point $\mathbf{x}$. It is given by

$$A_{\mathbf{x}}(\mathbf{y}) = \begin{cases} 1 & , \quad f(\mathbf{y}) \leq f(\mathbf{x}) \\ \exp\left(-\frac{f(\mathbf{y})-f(\mathbf{x})}{T_c}\right) & , \quad f(\mathbf{y}) > f(\mathbf{x}) \end{cases} \tag{4.3.6}$$

where the control parameter T_c plays the role of the temperature in Metropolis algorithm.

4.3.1 Standard simulated annealing

In standard SA, the generation probability is uniform over a neighbourhood region $S_{\mathbf{x}}$, i.e.

$$g_{\mathbf{x}}(\mathbf{y}) = \begin{cases} \frac{1}{|S_{\mathbf{x}}|} & , \quad \mathbf{y} \in S_{\mathbf{x}} \\ 0 & , \quad \mathbf{y} \notin S_{\mathbf{x}} \end{cases} \tag{4.3.7}$$

where $|S_{\mathbf{x}}|$ is called the Lebesgue measure of $S_{\mathbf{x}}$. With regard to (4.3.5), we have

$$|S_{\mathbf{x}}| = \prod_{i=1}^{D} \beta_i \tag{4.3.8}$$

Considering $U[0,1]$ as a uniform random number in the interval $[0,1]$, the standard SA can be described in pseudo English as follows [1]:

1. Initialise the control parameter ($T_c(0)$), choose an initial point ($\mathbf{x}(0)$) uniformly over S and set the current iteration to 1 ($k = 1$).

2. Generate a sample point $\mathbf{y}$ and its function value $f(\mathbf{y})$.

3. Select the new point $\mathbf{x}(k)$. Acceptance probability of $\mathbf{y}$ is calculated. If $A_{\mathbf{x}(k-1)}(\mathbf{y}) \geq U[0,1]$ then $\mathbf{x}(k) = \mathbf{y}$; otherwise $\mathbf{x}(k) = \mathbf{x}(k-1)$.

4. Decide whether to update the control parameter. Go to Step 2 if not.

5. Decrease the control parameter $T_c(k)$ slightly.

THE APPLICATION OF GPR

6. Decide whether to stop. If stopping rule is satisfied, the algorithm is terminated; otherwise it is repeated from Step 2.

At each iteration, the solution that gives the lowest value for f is viewed to be the minimum point found so far.

Generating a number of points uniformly over the feasible region at the beginning, the initial value of the control parameter $T_c(0)$ is usually set to the mean or standard deviation of the function values at these points. For employing the standard SA in the RMBI, we choose $T_c(0)$ to be the maximum of the MSE function at these generated points. Since the MSE is a positive value, this selection provides a larger value than the former ones ensuring that most of transitions are initially accepted by the algorithm. $\mathbf{x}(0)$ will be the last generated point in this category.

It has been proven [1, Chapter 3] that if the control parameter satisfies

$$T_c(k) \geq \frac{T_c(0)}{\ln(k+2)} \tag{4.3.9}$$

for every k, where $T_c(0)$ is a sufficiently large constant, then with probability one the algorithm will converge to the global minimum of the objective function. The annealing schedule specified by (4.3.9) is extremely slow for practical use. A finite-time approximation of SA [1, Chapter 4], frequently used for empirical situations, is

$$T_c(k) = \kappa\, T_c(k-1) \tag{4.3.10}$$

where κ is a constant smaller but close to unity. Typical values of κ lie between 0.8 and 0.99. At each temperature, enough transitions (say N_T) are attempted as indicated in Step 4 so that thermal equilibrium is roughly achieved.

The price paid for this approximation is that the algorithm is no longer guaranteed to find the global minimum with probability 1. Nevertheless, the resulting approximate form of the algorithm is capable of producing near-optimum solution for many practical applications.

THE APPLICATION OF GPR

It has been suggested [4, Chapter 5] that the initial search region should be large in order to ensure the computation efficiency at the beginning. The algorithm used herein to obtain $S_{\mathbf{x}}$ is that initially $S_{\mathbf{x}}(0) = S$. Then every time the control parameter T_c is updated, each side of $S_{\mathbf{x}}$ is reduced according to

$$\beta_i(k) = \kappa\, \beta_i(k-1)\ ,\ i = 1, \ldots, D \tag{4.3.11}$$

The reduction will be continued until the limit β_i^{min} is reached.

Example 4.1. This example demonstrates the performance of the standard SA in minimizing the MSE function in the RMBI. The medium is a one-layer slab shown in Fig. 4.2. The parameters of the slab correspond to the

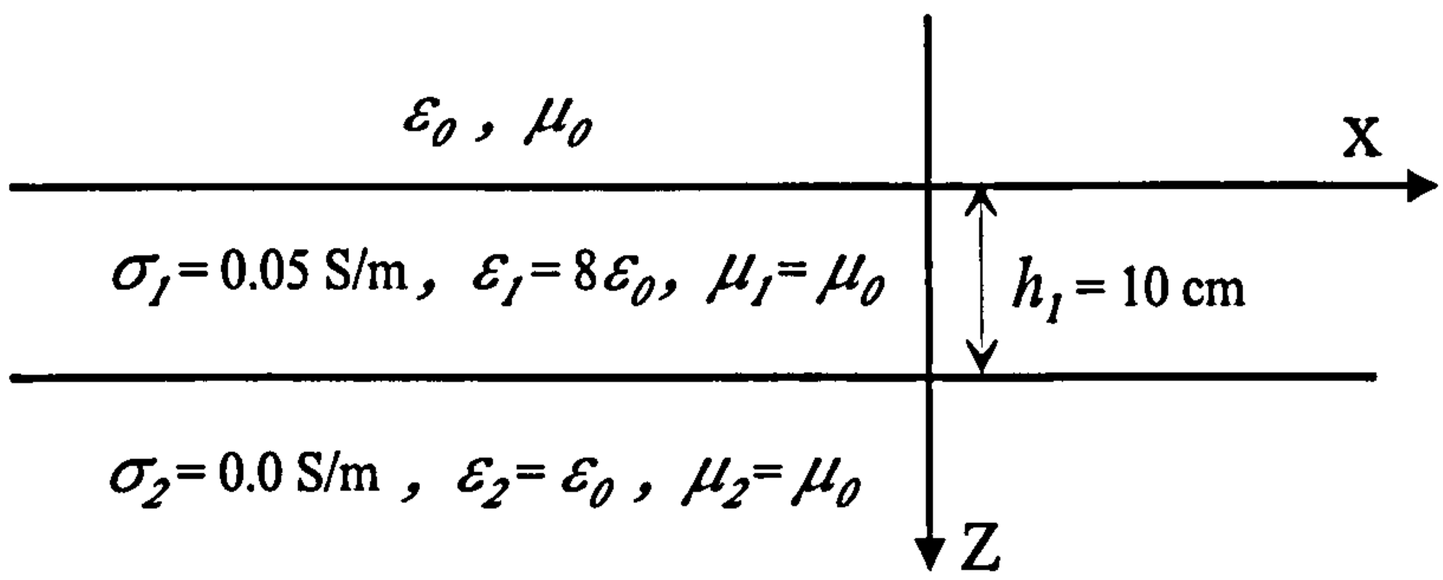

Figure 4.2: A concrete slab placed in free space.

parameters of a concrete wall surrounded by air. Indicated in Fig. 4.3, the reflection coefficients of the medium for the normal incidence are obtained from the simulation of the reflective formulation. It is assumed that the parameters of the second layer (σ_2, ϵ_2) are not known, i.e. the MSE function has 5 variables. The feasible region S is set to

$$\begin{aligned} &0 \le \sigma_1 \le 0.5\ \text{S/m}\ ,\ 1 \le \epsilon_{r1} \le 50\ ,\ 1 \le h_1 \le 50\ \text{cm} \\ &0 \le \sigma_2 \le 0.5\ \text{S/m}\ ,\ 1 \le \epsilon_{r2} \le 50 \end{aligned} \tag{4.3.12}$$

The parameters of the SA algorithm (κ, N_T) are determined empirically for a specified function. There is a direct dependency between their values and the number of minima of the function as well as the extensions of the feasible

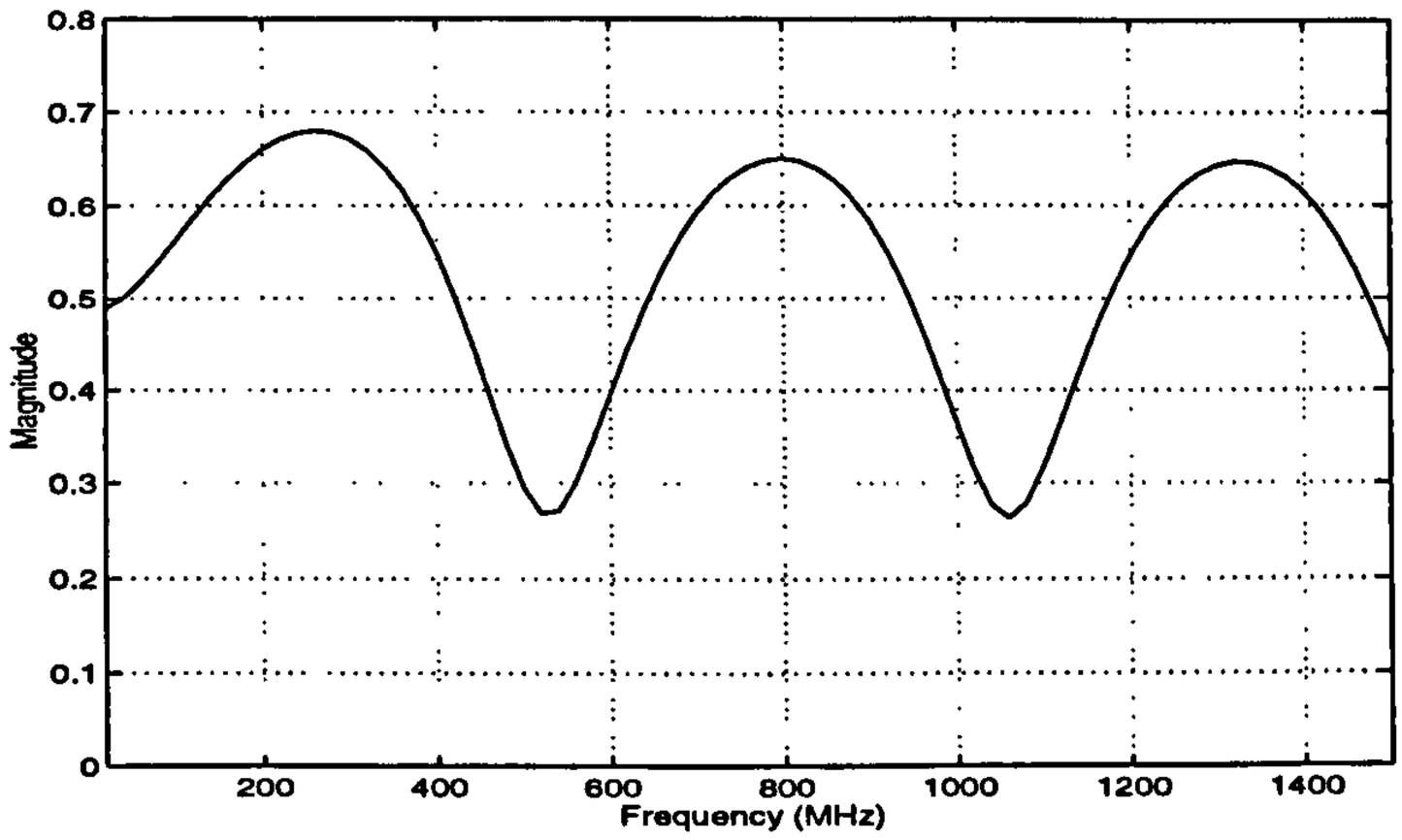

(a)

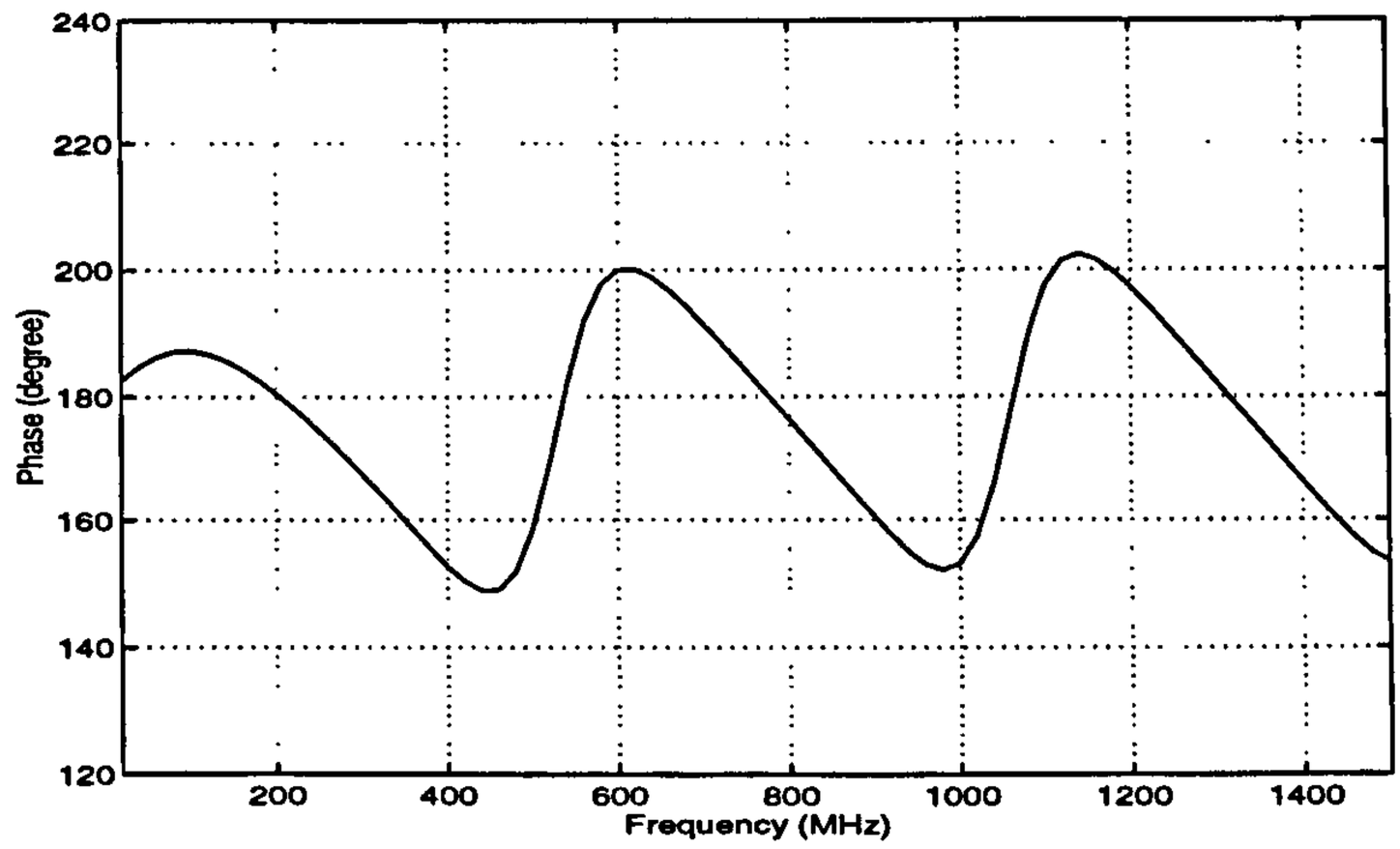

(b)

Figure 4.3: The reflection coefficients of the medium shown in Fig. 4.2 for normal incidence.

region. The minimization of a function with a big feasible region and/or many minima needs large values for κ and N_T. Otherwise, the algorithm is most likely to get stuck in a local minimum. In this example, κ is fixed at 0.99 and two values, 100 and 500, are tried for N_T.

Using the reflection coefficients at 25 frequencies equally spaced in the in-

Table 4.1: The resultant MSE for 10 runs of the standard SA algorithm. The feasible region for the first and second sets of runs is (4.3.12) and for the third one is (4.3.13).

Feasible region	Number of function evaluation	N_T	Final MSE values for 10 runs				
(4.3.12)	500000	100	8.0e-7	0.0029	0.0029	4.0e-7	0.0037
			9.0e-7	0.0038	0.0038	0.0030	0.0042
		500	0.0029	3.4e-6	9.2e-4	2.5e-5	1.6e-6
			0.0028	2.3e-6	0.0027	7.2e-6	6.5e-6
(4.3.13)	100000	100	1.2e-5	2.4e-5	8.7e-6	1.4e-5	5.1e-6
			7.2e-6	5.4e-6	1.2e-5	6.2e-6	5.2e-6

terval [500 MHz, 1000 MHz] as the observed scattering data, Table 4.1 shows the final MSE values for 10 runs of the algorithm. The corresponding convergence curves and final resulting profiles for the best and worst cases (i.e. for the lowest and highest resultant MSE in Table 4.1) among the 10 attempts are demonstrated in Fig. 4.4, 4.5 and 4.6.

It can be seen that the selection $N_T = 100$ does not provide appropriate reliability and the algorithm behaves more like a local method. One hundred transitions ($N_T = 100$) are not sufficient for this problem in order to reach thermal equilibrium at each temperature. In other words, the cooling is not carried out adequately slow. The increase in N_T enhances the reliability as the average of 10 MSE values for $N_T = 500$ is smaller than that for $N_T = 100$. Enlarging N_T (and/or κ) provides a reliable SA; but excessive increase in these parameters makes the algorithm inefficient. We can achieve a good efficiency while maintaining reliability by using some prior information to reduce the size of the feasible region. For this example, one may speculate that the conductivity and relative permittivity of concrete, even wet concrete, are not greater than 0.2 S/m and 20 respectively. Furthermore, considering the medium is a slab placed in free space, the number of variables of MSE function might be reduced to three that decreases the feasible region size substantially. It should be

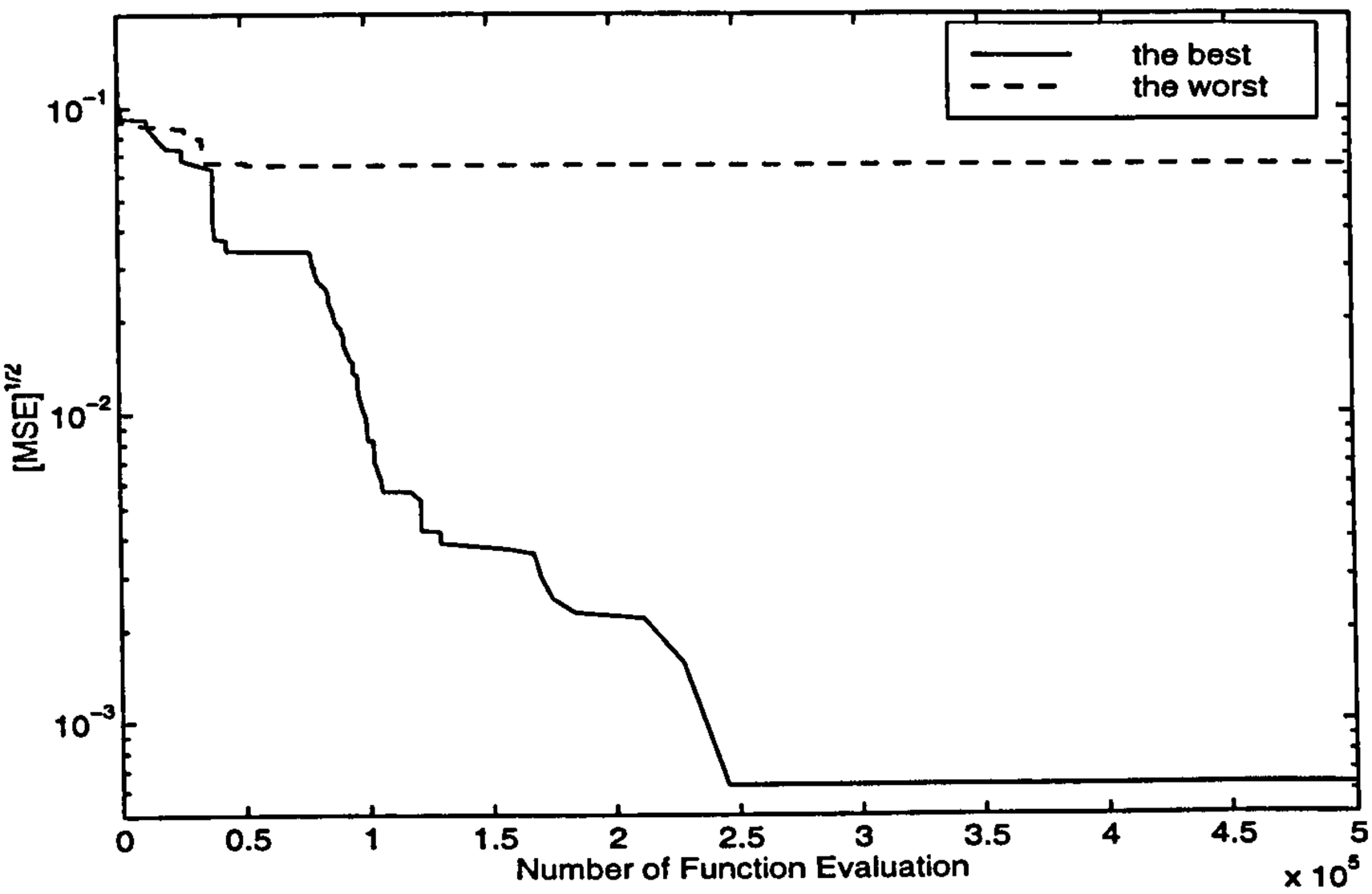

(a)

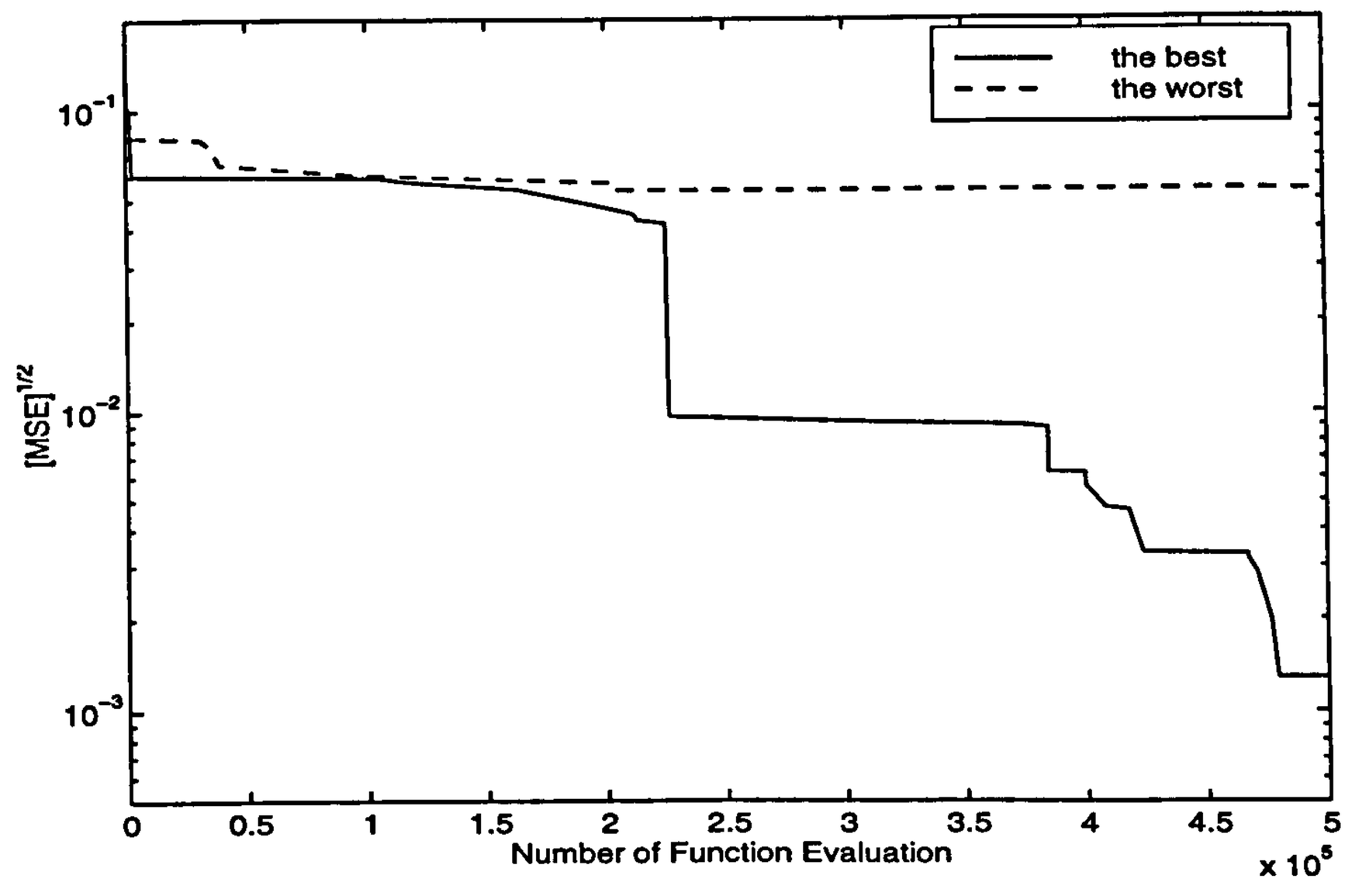

(b)

Figure 4.4: Illustration of the performance of the standard SA in minimizing the MSE function for the concrete slab when the feasible region is (4.3.12). (a) $N_T = 100$ (b) $N_T = 500$

THE APPLICATION OF GPR

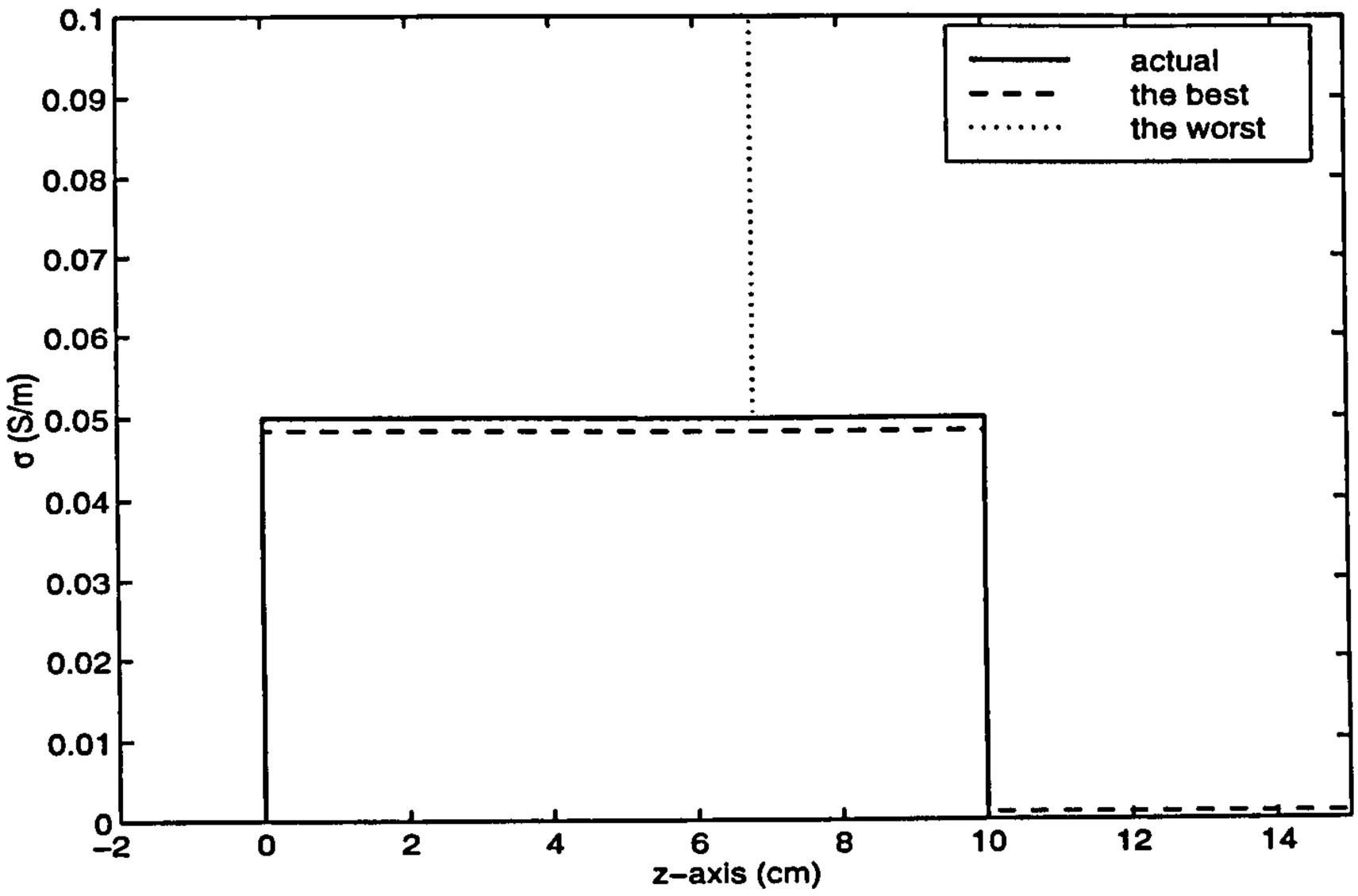

(a)

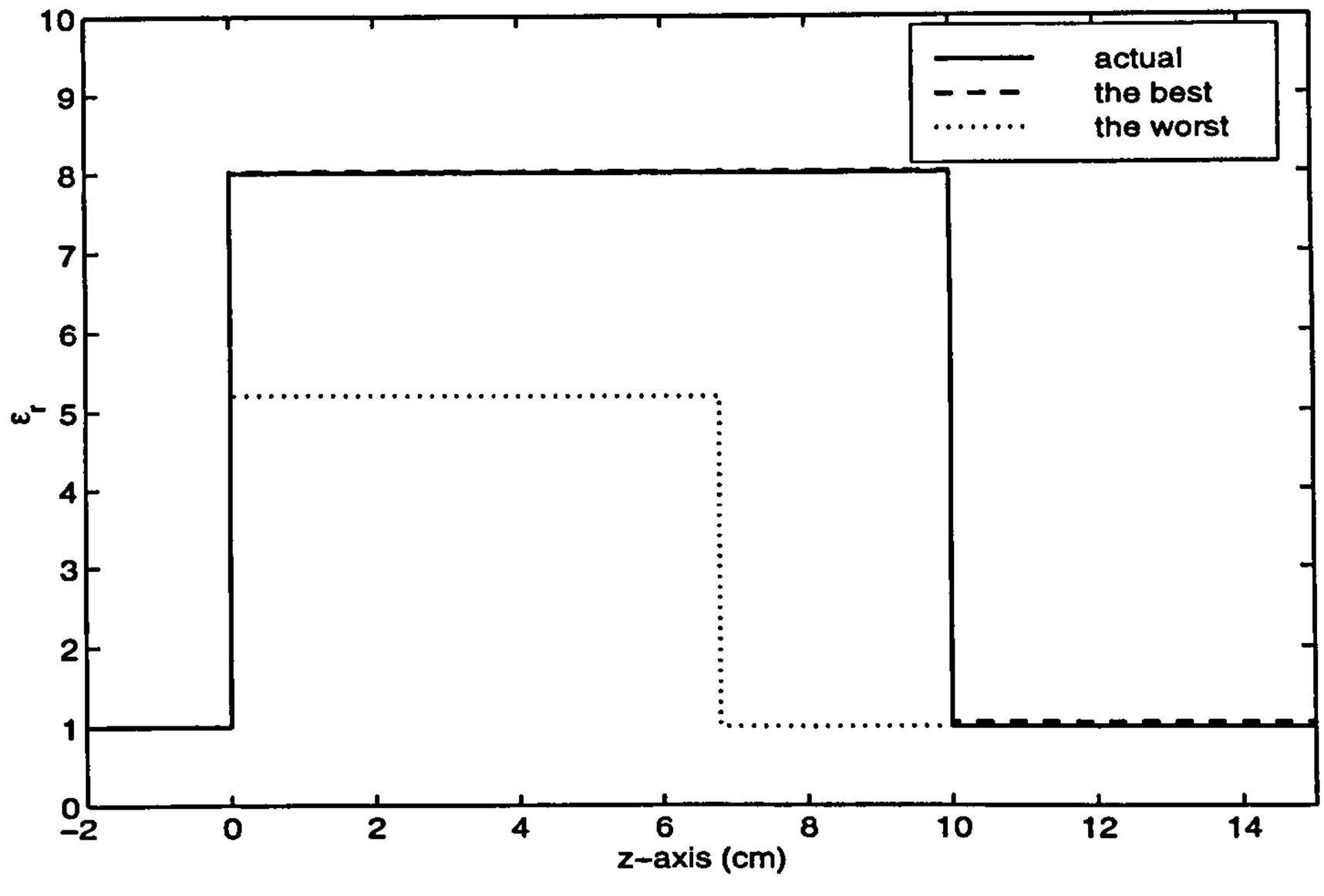

(b)

Figure 4.5: The reconstructed profiles using the standard SA with the bounds (4.3.12) and $N_T = 100$.

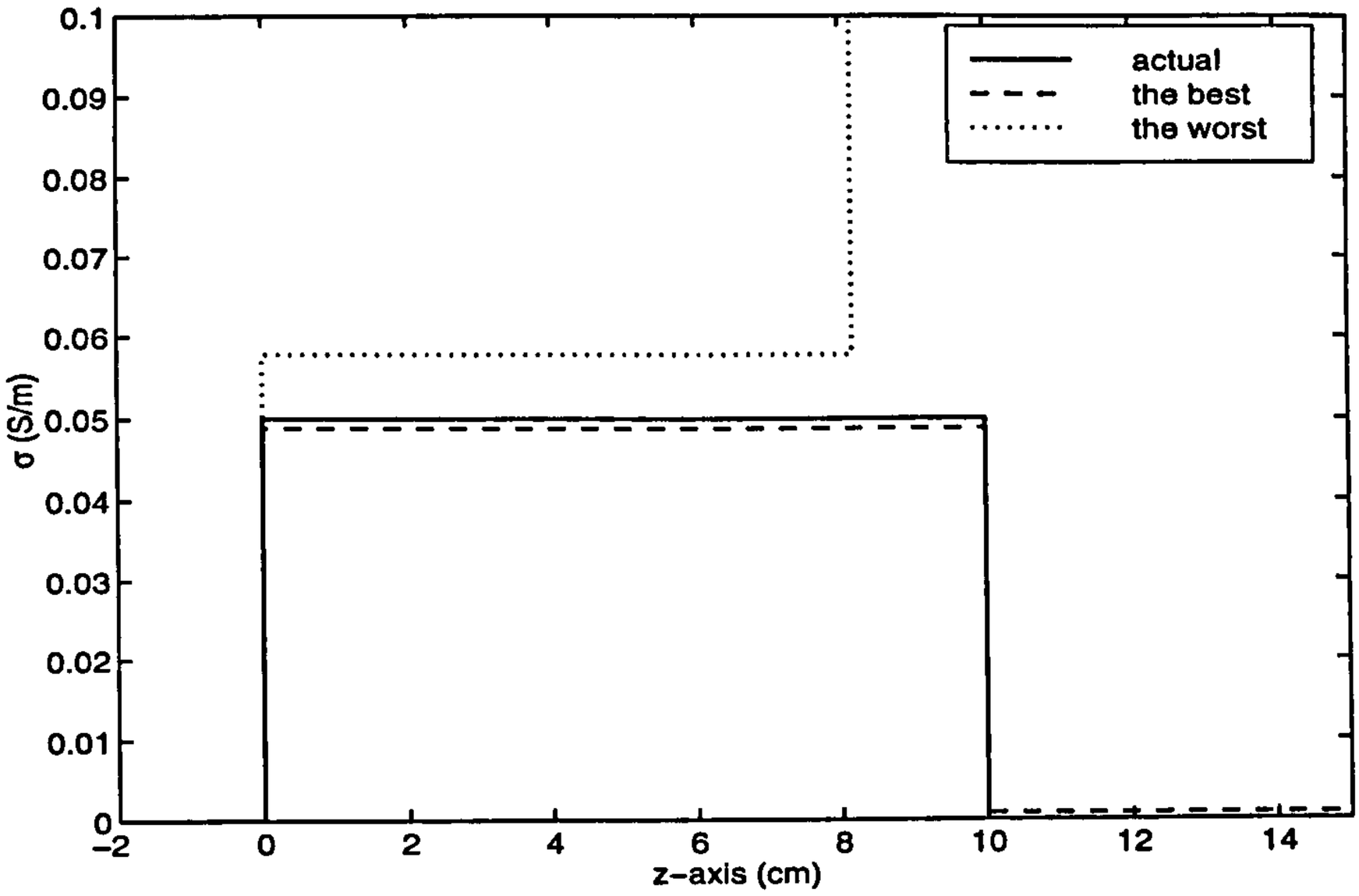

(a)

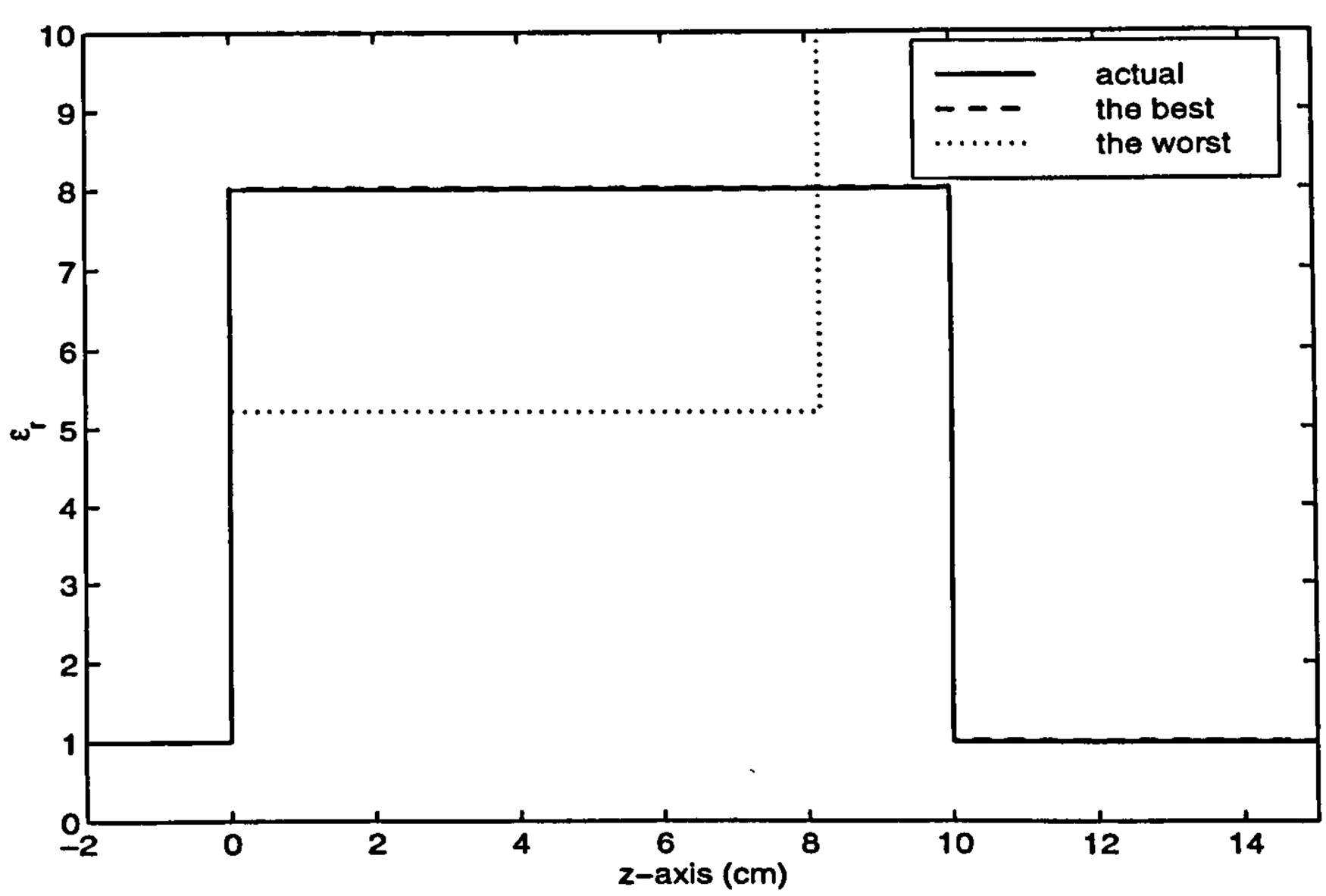

(b)

Figure 4.6: The reconstructed profiles using the standard SA with the bounds (4.3.12) and $N_T = 500$

however noted that the bottom layer is not known for most GPR applications. Setting S as

$$\begin{aligned} &0 \leq \sigma_1 \leq 0.2 \text{ S/m} \,,\; 1 \leq \epsilon_{r1} \leq 20 \,,\; 1 \leq h_1 \leq 30 \text{ cm} \\ &0 \leq \sigma_2 \leq 0.05 \text{ S/m} \,,\; 1 \leq \epsilon_{r2} \leq 5 \end{aligned} \tag{4.3.13}$$

the results are depicted in the third row of Table 4.1 and Fig. 4.7.

As expected, better results are obtained. However, generally speaking, the standard SA is slow. Several variants of SA have been proposed [5], [33] to improve the efficiency. Of these variants, the adaptive simulated annealing has been used in inverse problems of layered-media [57]. The next subsection deals with the mathematical description of this algorithm.

4.3.2 Adaptive simulated annealing

Ingber [32] proposed a modified version of SA known as the Adaptive Simulated Annealing (ASA). It is mainly different from the standard SA in the generation function used to introduce a new point. Consider the optimisation of a function in D-dimensional space with the feasible region given by (4.1.1). The ith variable of the objective function (x_i) at iteration k is updated using

$$x_i(k) = x_i(k-1) + y_i \,(U_i - L_i) \tag{4.3.14}$$

where the random variable $y_i \in [-1, 1]$ has the following probability density function

$$g_T(\mathbf{y}) = \prod_{i=1}^{D} \frac{1}{2\,(|y_i| + T_{ci})\,\ln\left(1 + \frac{1}{T_{ci}}\right)} \tag{4.3.15}$$

y_i can be generated from a uniform random number $r_i \in U[0, 1]$ by

$$y_i = \text{sgn}\left(r_i - \frac{1}{2}\right) T_{ci} \left[\left(1 + \frac{1}{T_{ci}}\right)^{|2r_i - 1|} - 1\right] \tag{4.3.16}$$

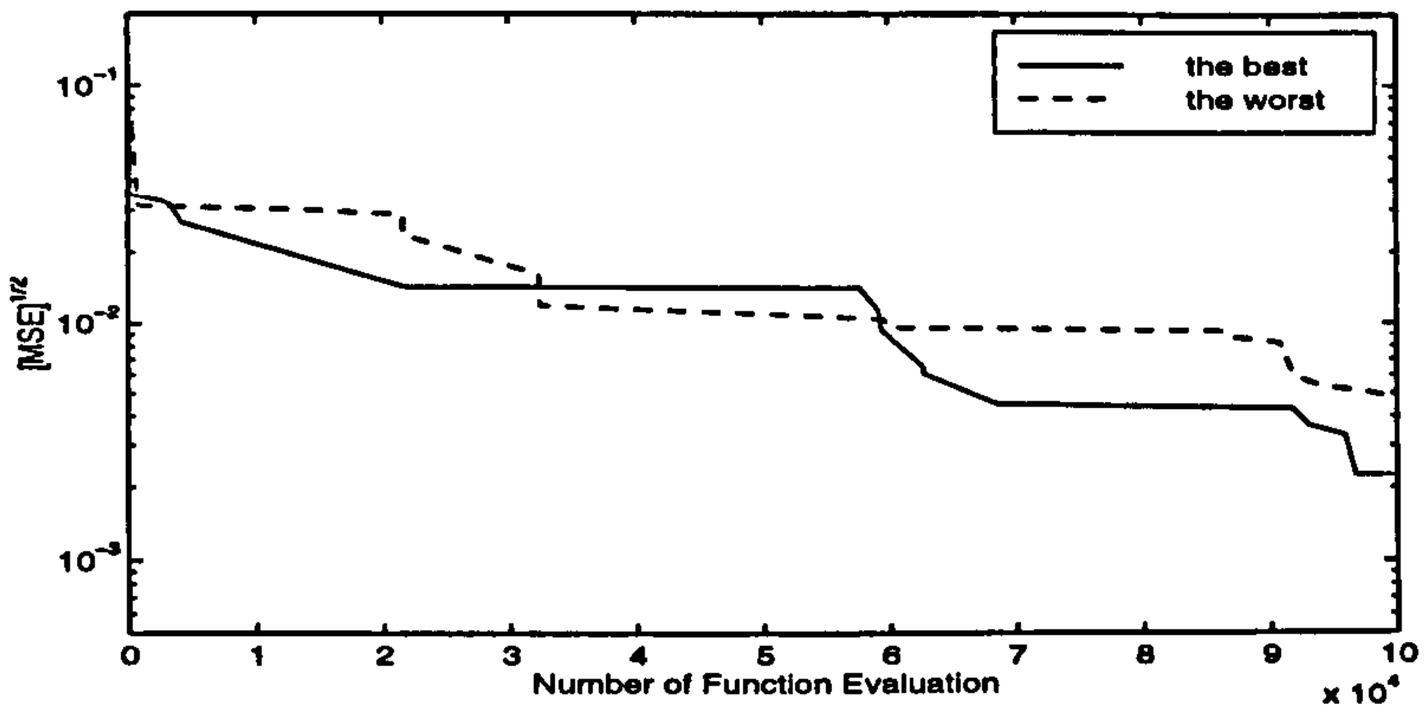

(a)

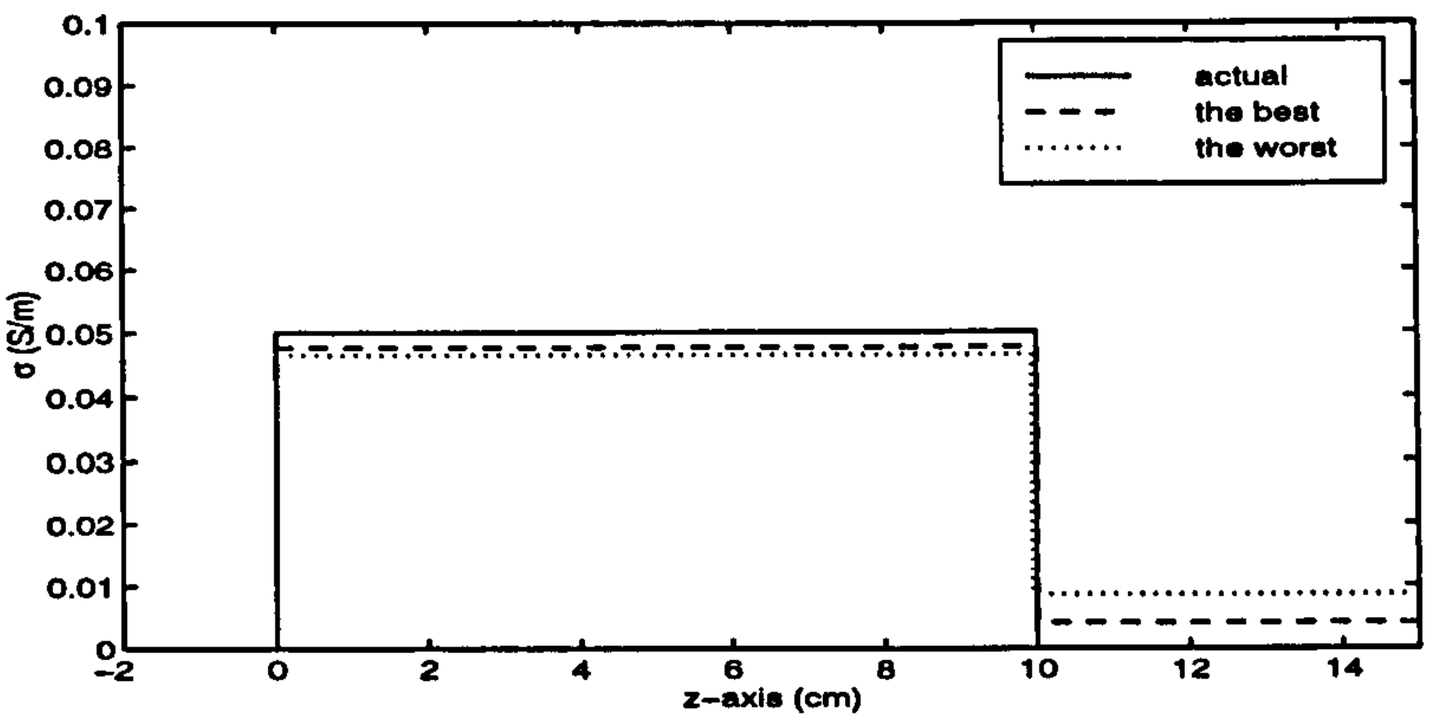

(b)

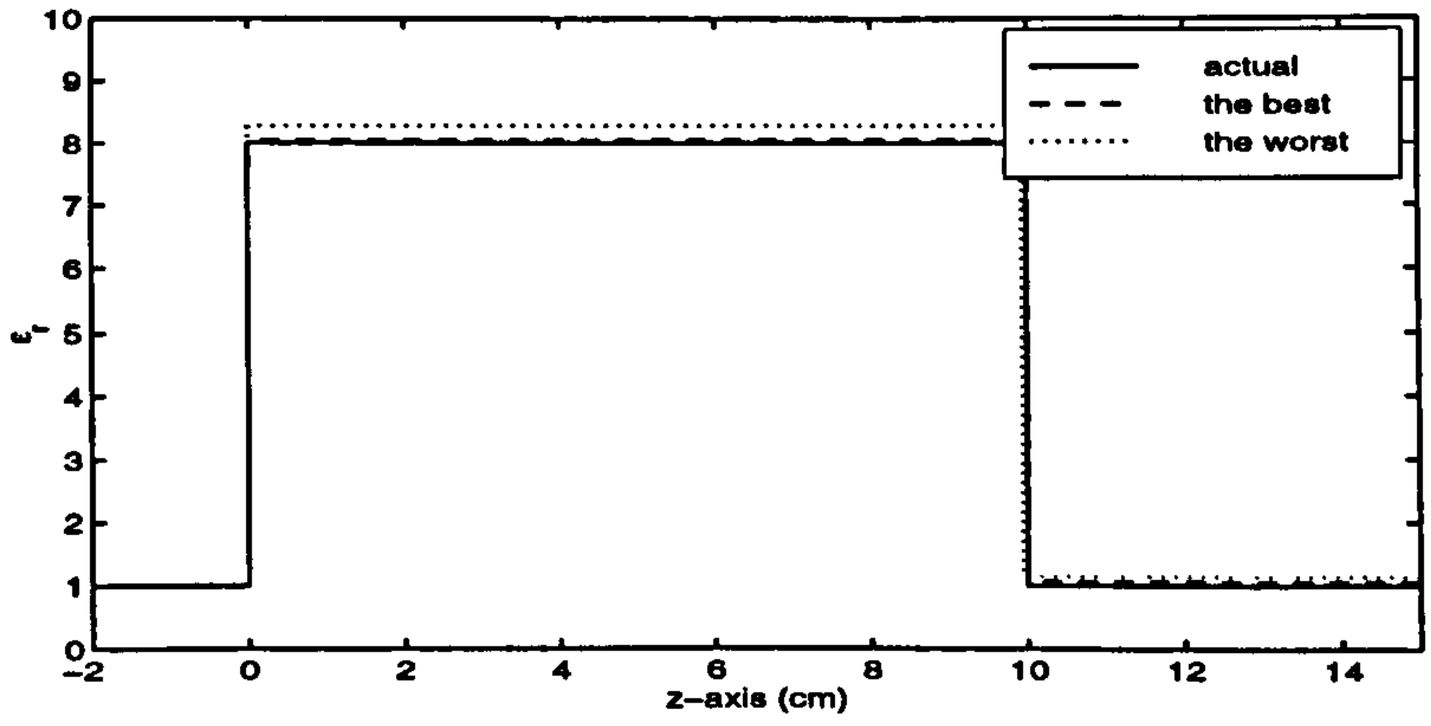

(c)

Figure 4.7: The results of using the standard SA with the feasible region (4.3.13) and $N_T = 100$

It can be understood from these equations that the generation probability function $g_{\mathbf{x}}$ is defined over the entire feasible region S for all iterations, i.e. the neighbourhood region for all points is fixed to S and it does not change during the procedure. Nevertheless, $g_{\mathbf{x}}$ depends on D control parameters T_{ci} specified for each function variable x_i, thus the generation function shape is allowed to be updated within the procedure.

The control parameters are lowered with regard to annealing schedules by

$$T_{ci}(k) = T_{ci}(0) \exp\left(-c_i k^{1/D}\right) \tag{4.3.17}$$

where c_i is a parameter used to control the schedule and to tune the algorithm to specific problems. $g_{\mathbf{x}}$ permits for the generation of points far away from the current position at high temperatures (T_{ci}), whereas it prefers points in the close proximity of the current location at low temperatures . This is actually in accordance with the idea of choosing initially a large neighbourhood region and then reducing its size in the standard SA to speed up the algorithm. For both cases (the standard SA and ASA), the probability of selection of far points is decreased as the algorithm proceeds. Nevertheless, this reduction in ASA is different for each function variable. The reason for such a modification is that each function variable owns a different finite range of variations and the objective function has different sensitivity to each variable. Consequently, they should individually be assigned different degrees of perturbations from their current position. It has been shown [32] that ASA algorithm converges to the global minimum with probability 1 using annealing schedule (4.3.17). The cooling schedule for the acceptance probability is same as the standard SA (i.e. (4.3.10)).

Another feature included in ASA [32] is to occasionally rescale the annealing schedule for a variable in terms of the sensitivity of the function f to that

---

THE APPLICATION OF GPR

variable. The sensitivity is defined as

$$s_i = \frac{\partial f}{\partial x_i} \tag{4.3.18}$$

Suppose that T_{ci}^k denotes the control parameter for x_i at annealing time k. The rescaling is performed according to

$$T_{ci}^{k'} = T_{ci}^k \left(\frac{s_{max}}{s_i} \right) \tag{4.3.19}$$

where s_{max} is the largest value of s_i. In this way, the algorithm is allowed to stretch out the ranges over which relatively insensitive variables are being searched comparative to the ranges of more sensitive ones. This new feature is termed reannealing.

A program in C for the ASA algorithm is publicly available from its inventor (Ingber). We employ this program to minimize the MSE function in the RMBI. The MSE function written in a FORTRAN subroutine is introduced to the algorithm by linking the subroutine to the ASA program. There are many parameters in ASA that ought to be tuned to a specific problem. Two examples provided next were examined with several changes in the most influential ASA parameters. The results presented are those achieved with the most efficiency and reliability.

Example 4.2. The reconstruction of the medium in Example 4.1 is also considered here in order to compare the performance of ASA with the standard SA. The bounds of the parameters are given in (4.3.12) and the same reflection coefficients over the frequency range [500 MHz, 1000 MHz]) are used.

The final MSE values are summarised in the first row of Table 4.2. Figure 4.8 illustrates the convergence of the MSE value and the profiles obtained. The comparison of these results with those obtained by the standard SA for the same feasible region (4.3.12) indicates that ASA offers an improvement in the efficiency and reliability. This efficiency can also be confirmed by comparing the running times. The times elapsed for running the standard SA and ASA are

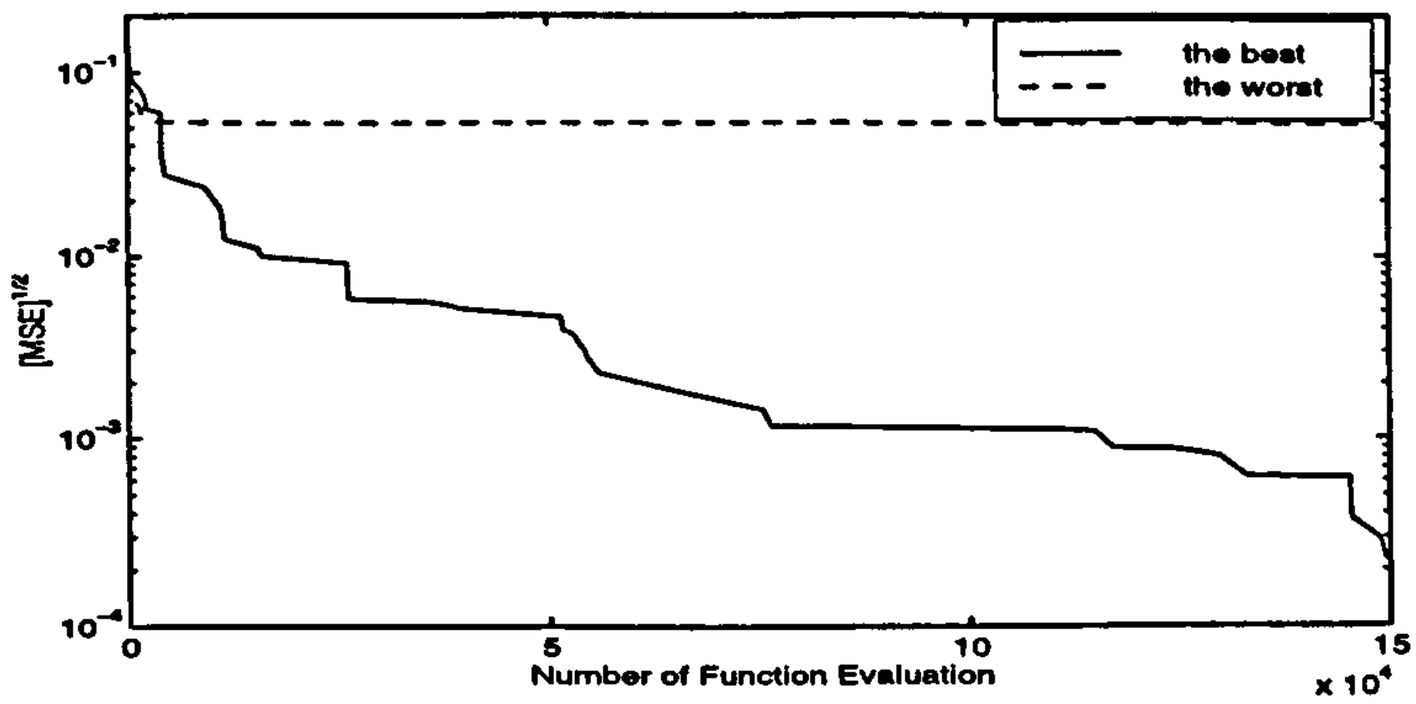

(a)

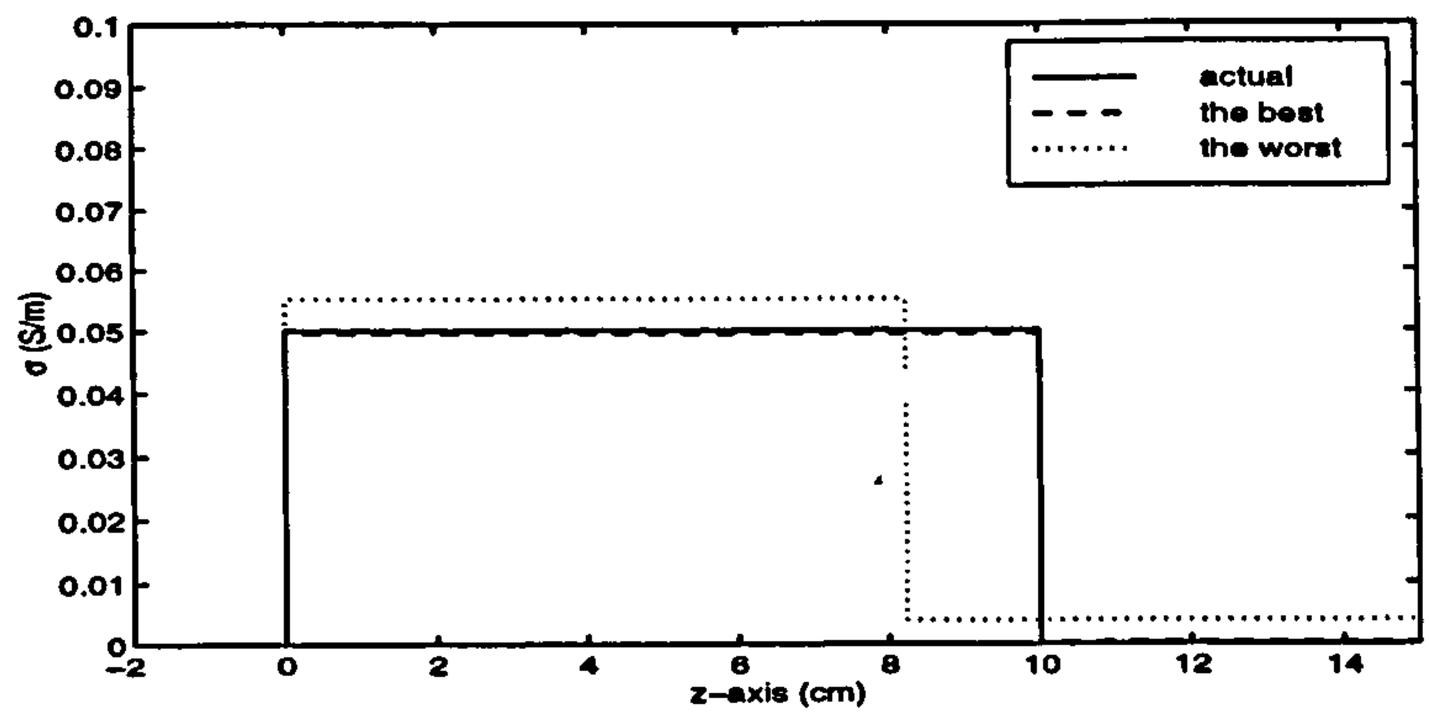

(b)

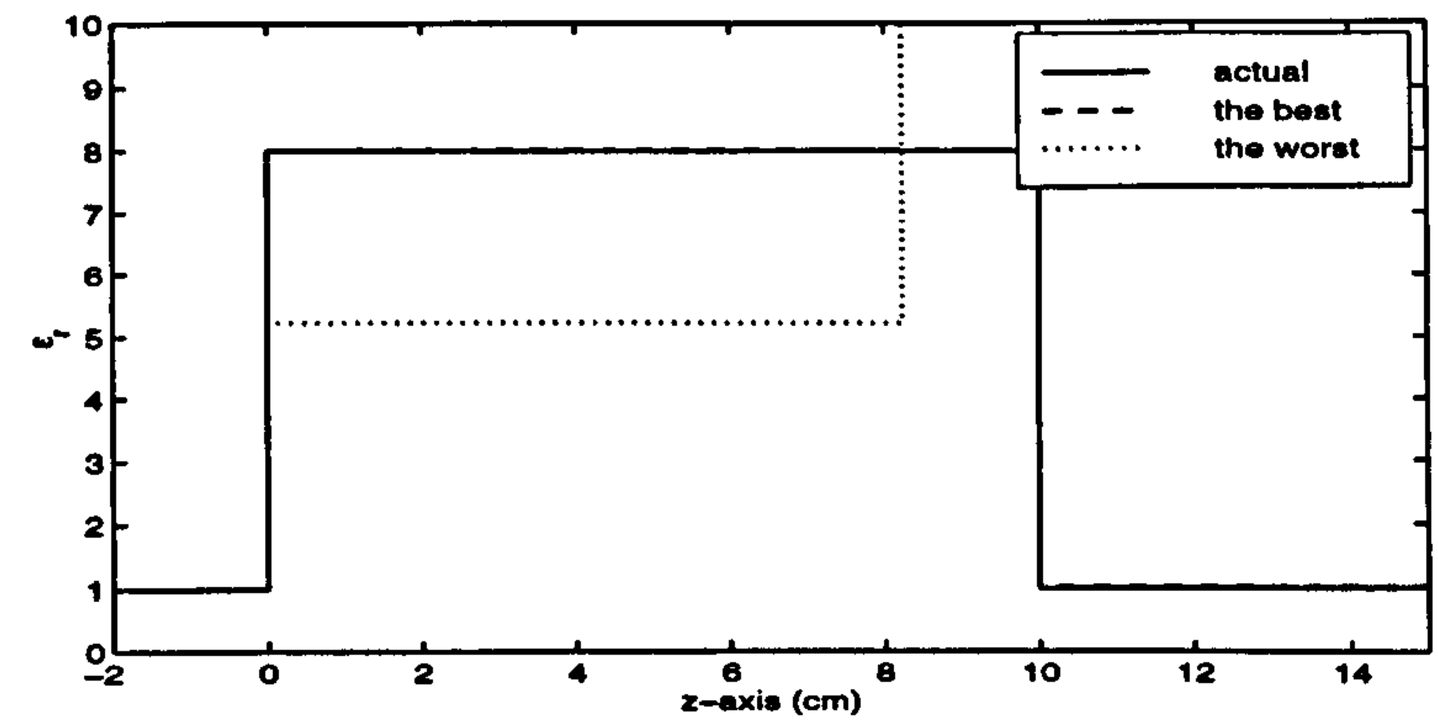

(c)

Figure 4.8: (a) The convergence curves, the (b) conductivity and (c) permittivity profiles yielded by employing the ASA algorithm for the inverse problem given in Example 4.1 with the feasible region (4.3.12). The best and worst results correspond respectively to the lowest and highest final MSE values given in the first row of Table 4.2

respectively measured to be 522 and 185 second in this reconstruction example. The ratio of the running times (522/185) is close to the ratio of the number of function evaluations (500000/150000). This points out that the computational cost is dominated by the evaluation of the MSE function.

Example 4.3. This example deals with the reconstruction of the 3-layer medium introduced in Example 3.1 but the observed data is that used in Example 3.2 (Chapter 3). The eight parameters are constrained by

$$\begin{aligned} &0 \le \sigma_1 \le 0.5 \text{ S/m} \,,\; 1 \le \epsilon_{r1} \le 50 \,,\; 1 \le h_1 \le 50 \text{ cm} \\ &0 \le \sigma_2 \le 0.5 \text{ S/m} \,,\; 1 \le \epsilon_{r2} \le 50 \,,\; 1 \le h_2 \le 50 \text{ cm} \\ &0 \le \sigma_3 \le 0.5 \text{ S/m} \,,\; 1 \le \epsilon_{r3} \le 50 \end{aligned} \tag{4.3.20}$$

Applying the ASA algorithm in the RMBI for this problem, the results are shown in the second row of Table 4.2 and Fig. 4.9. Overall, the algorithm has failed to find the profile of the medium even with a large number of evaluations. The ASA algorithm has been reported to be faster than genetic algorithms as well as the standard SA [33]. The results of application of ASA in geophysical inverse problems [57] have also drawn the same conclusion. Unfortunately, it is not sufficiently fast for our purpose, especially when a medium consists of several layers and the bounds of parameters have to be wide. This situation can arise in GPR applications where a layer might be a water table ($\epsilon_r = 80$) or a metal plate, and the bounds must therefore be extended.

Table 4.2: The resultant MSE for 10 runs of ASA.

Number of function evaluation	medium	Final MSE values				
150000	Fig.	7.2e-7	8.1e-7	0.0028	2.3e-6	0.0027
	4.2	7.4e-6	8.4e-7	6.9e-5	5.1e-8	9.8e-7
500000	Fig.	0.0147	0.0238	0.0242	0.0098	0.0181
	3.3	0.0245	0.0249	0.0158	0.0137	0.0139

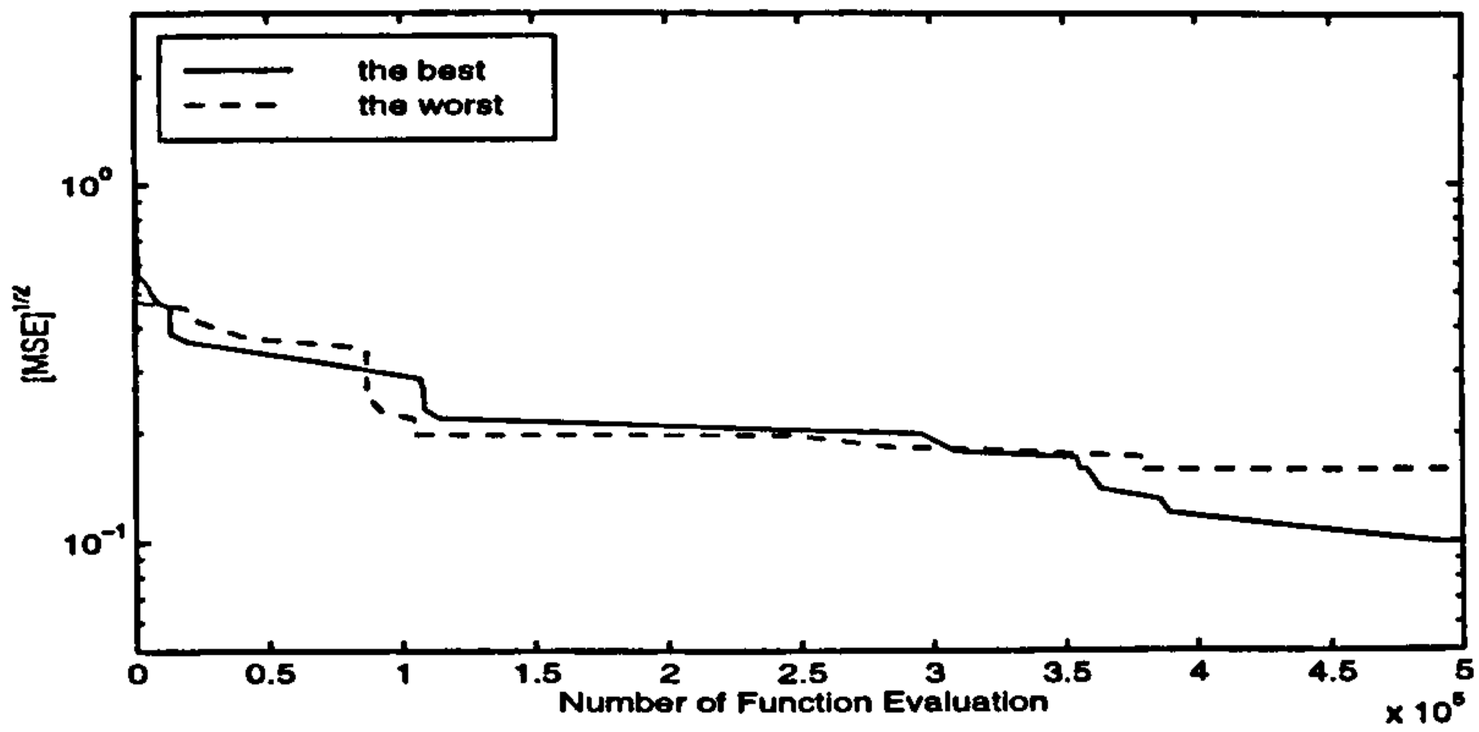

(a)

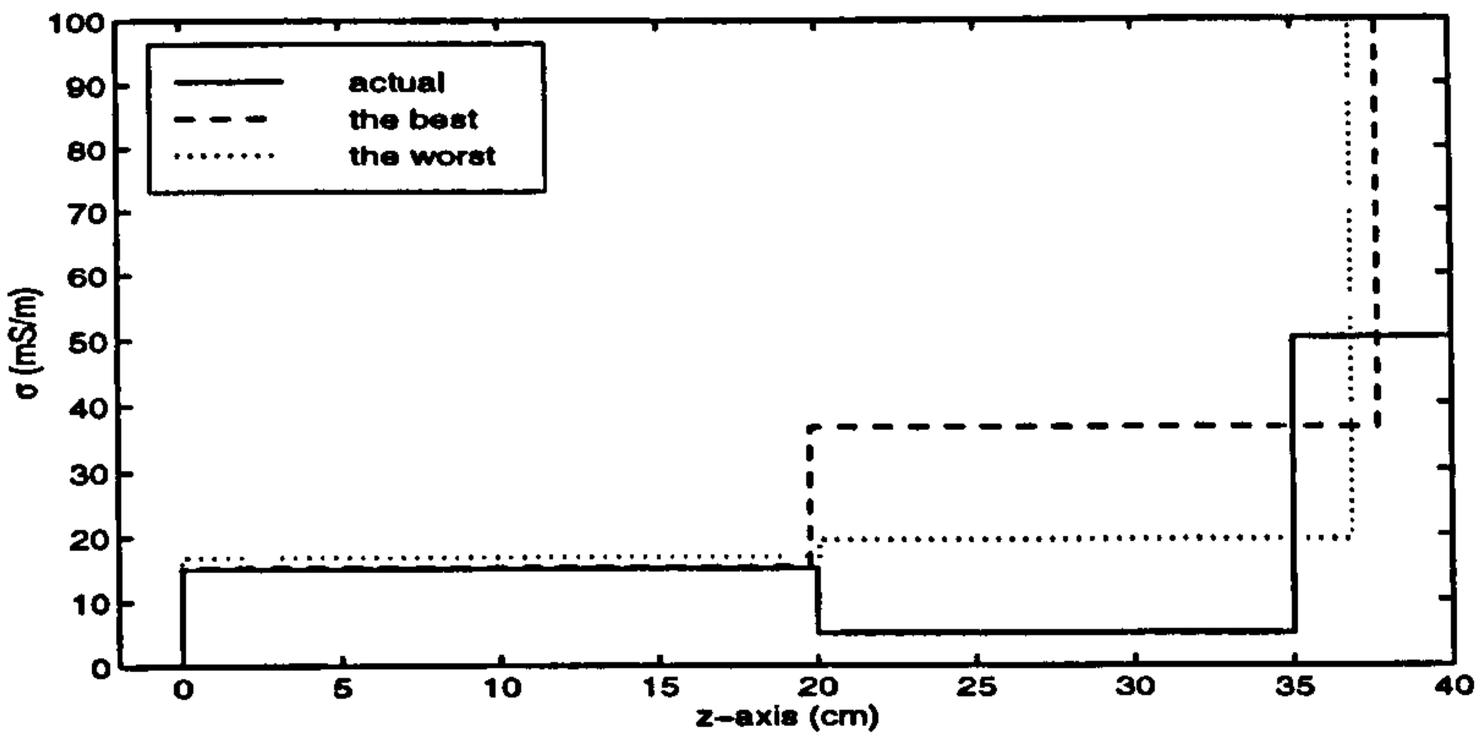

(b)

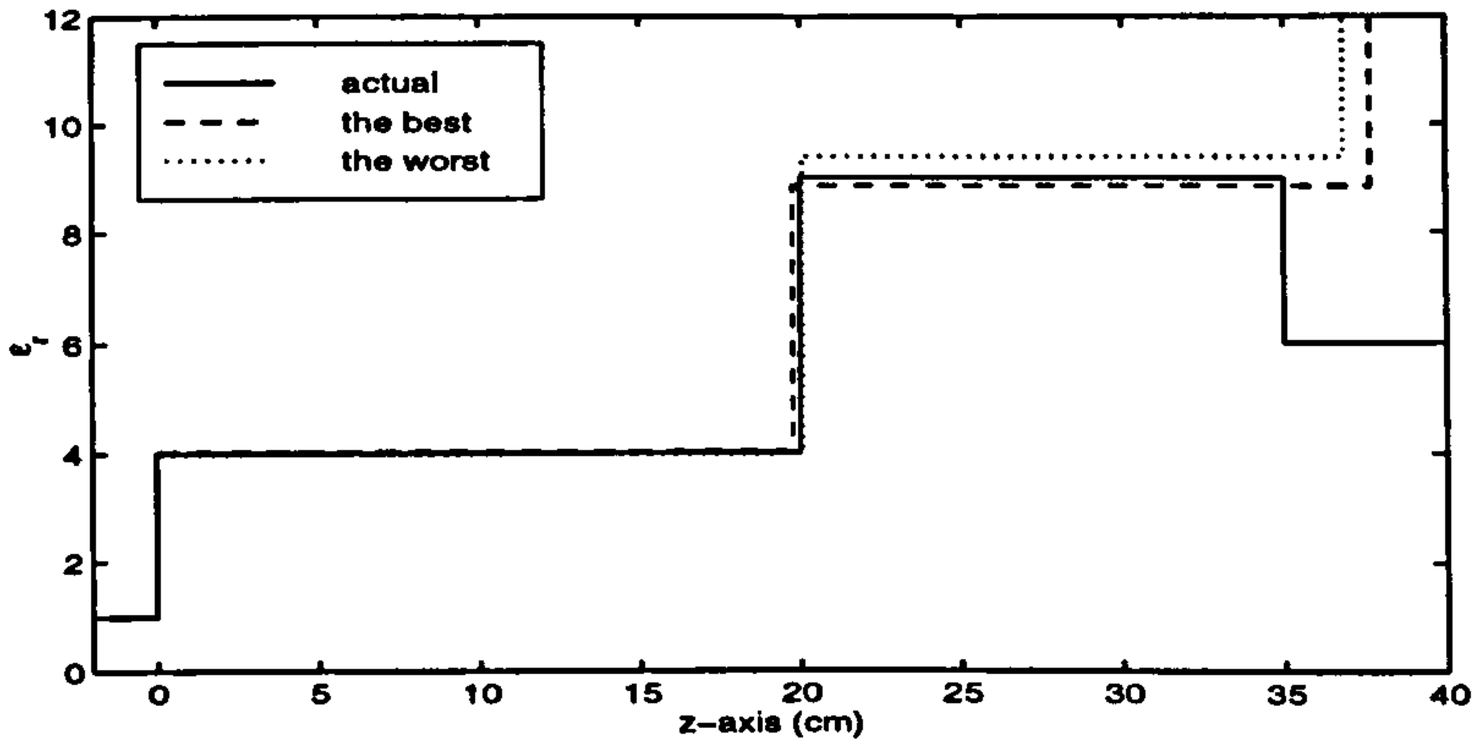

(c)

Figure 4.9: The results of using ASA algorithm for the 3-layer medium.

4.4 Multi-Level Single-Linkage Method

Simulated annealing (and also GA) algorithms suffer from slow convergence due to using only the value of the objective function and not exploiting local information. In addition, they are not sufficiently accurate in terms of locating the exact solution, as was seen from the examples of the previous section. On the other hand, local optimisation methods reach an optimum efficiently and accurately using local information such as the gradient and the Hessian matrix. Local algorithms should therefore be incorporated within a global search so as to benefit from their advantages. A simple search procedure, Multistart, uses a local algorithm starting from several points distributed over the feasible region. One disadvantage of Multistart is that the same minimizer may be found several times. Clustering methods provide more adaptation of Multistart to avoid the repeated determination of local minimizers [38]. This is realised by grouping (clustering) the sample points around the local minimizers and starting a single local optimisation from each group. In fact, the formed clusters accord to the attraction regions of the minima.

The multi-level single-linkage method, proposed by Rinnooy Kan and Timmer [38], [39] is a clustering method that appears to be efficient as shown by computational experiments. It also has probabilistic guarantees of computational efficiency. The kth iteration of the algorithm outlined by Byrd *et.al* [11] is as follows:

1. Generate N_p sample points, drawn from a uniform distribution over S, and calculate the corresponding functional values at these points. Add N_p points to the (initially empty) set of sample points.

2. Determine a set of the reduced sample points by taking $\xi k N_p$ points with the smallest function values, where ξ is any fixed number in (0, 1].

3. Select start points from the reduced sample points for local searches. The

selection procedure will be discussed later.

4. Perform local minimization from the selected start points.

5. If the stopping rule is satisfied, the lowest local minimum is taken as the global minimum, otherwise go to Step 1.

In Step 3, at the kth iteration, each reduced sample point $\mathbf{x}$ is selected as a start point for a local minimization provided that the start point has not been used at a previous iteration, and that there is no sample point $\mathbf{y}$ within the critical distance $d(k)$ of $\mathbf{x}$ with $f(\mathbf{y}) < f(\mathbf{x})$. Considering the definition 4.1, the critical distance is given by [39]

$$d(k) = \pi^{-1/2} \left[GF\left(1 + \frac{D}{2}\right) |S| \, \rho \, \frac{\ln kN_p}{kN_p} \right]^{1/D} \tag{4.4.1}$$

where GF denotes the gamma function, $|S|$ denotes the Lebesque measure of S and ρ is a positive constant. In fact, the distance $d(k)$ defines the boundary of the attraction region for every local minimum. Rinnooy Kan and Timmer [39] have proven that if the critical distance is determined by (4.4.1) with $\rho > 0$, all local minimizers of $f(\mathbf{x})$ will be found within a finite number of iterations with probability 1. Moreover, when $\rho > 4$, the total number of local searches started by the MLSL method will be finite with probability 1 even if the sampling continues forever. ρ is set to 4 in our reconstruction examples.

A Bayesian stopping rule is applied in Step 5. Let w denote the number of local minimizers found after k iterations. A Bayesian estimate of the total number of local minimizers is given by

$$\frac{w\,(\xi kN_p - 1)}{\xi kN_p - w - 2} \tag{4.4.2}$$

In addition, a Bayesian estimate of the portion of S covered by the attraction region of the local minima found so far is given by

$$\frac{(\xi kN_p - w - 1)(\xi kN_p + w)}{\xi kN_p(\xi kN_p - 1)} \tag{4.4.3}$$

The algorithm is terminated after the kth iteration if the estimate given by (4.4.2) is greater than w by less than 0.5, and the estimate given by (4.4.3) is greater than a value near but less than 1 such as 0.999.

Any standard optimisation algorithm can be used to perform the local minimization task. The modified-Newton method is adopted within this research.

The selection of the values for the two parameters N_p and ξ are problem dependent. A decrease in ξ reduces the number of local searches, which involves several function as well as gradient evaluations. Thus, small values for ξ ought to be chosen for the minimization of a function whose minima have relatively big attraction regions. In this way, the repeated findings of local minima are more likely avoided. This actually enhances the computational performance of the MLSL method. No procedure can be established for the exact selection of the parameters N_p and ξ; they can only be determined empirically for a specific problem.

Three examples from [47] and two other examples are provided in the following to demonstrate the effectiveness of the MLSL method for the reconstruction of different multi-layered media in the presence of noise from the simulated and experimental data. The method is run 10 times for the first two examples in order to compare the MLSL method with the standard SA and ASA algorithms. It is run once for the final three examples but with enough iterations to make sure that the global minimum is found. The validity of the procedure, described in Subsection 3.4.3 (Chapter 3), for finding the structure of a medium (i.e. determining the number of layers) will also be tested in Examples 4.6 and 4.7. More examples of applying the MLSL method to the inverse problem of non-uniform transmission lines can be found in [45].

Example 4.4. The MLSL method is applied to the reconstruction of the medium described in Example 4.1 with the same observed data and the feasible region given by (4.3.12). The final MSE and the number of minima found for

---

10 runs and three sets of the two parameters N_p and ξ are listed in Table 4.3. The number of function evaluations is fixed to 10000 for each run, which takes about 11.5 s. A comparison between these results and those of the standard

Table 4.3: The final MSE for 10 runs of the MLSL algorithm for the medium introduced in Example 4.1. Each run involves 10000 function evaluations.

$N_p = 100$ $\xi = 0.1$	Final MSE	0.0	0.0	0.0	0.0	0.0
		0.0	0.0	0.0	0.0	0.0
	No. of Minima found	7	7	8	8	8
		8	8	7	8	6
$N_p = 100$ $\xi = 0.2$	Final MSE	0.0	0.0	0.0	0.0	0.0
		0.0	0.0	0.0	0.0	0.0
	No. of Minima found	6	7	6	7	8
		8	7	6	8	7
$N_p = 100$ $\xi = 0.5$	Final MSE	0.0	0.0	0.0	0.0	0.0
		0.0	0.0	0.0	0.0	0.0
	No. of Minima found	6	7	7	7	7
		7	7	8	7	8

SA and ASA shows that the MLSL method is undoubtedly more reliable and efficient than the standard SA and ASA. Furthermore, it can be seen that the MLSL algorithm locates the exact solution, as it has reached zero value (10^{-18}) for the MSE function. Figure 4.10 shows the corresponding convergence curves.

Example 4.5. This example is aimed at comparing the performance of MLSL with that of ASA for the inverse problem posed in Example 4.3. Table 4.4 and Fig. 4.11 give the results. While ASA did not find the global minimizer after 500000 function evaluations, the MLSL method found it several times within only 50000 function evaluations. The running time is respectively 700 s and 51 s for ASA and MLSL. Again, it is evident that the MLSL method is superior to the ASA and to the standard SA.

It can be concluded from Table 4.3 and 4.4 that the performance of the MLSL for each particular problem is insensitive to and optimal within a range

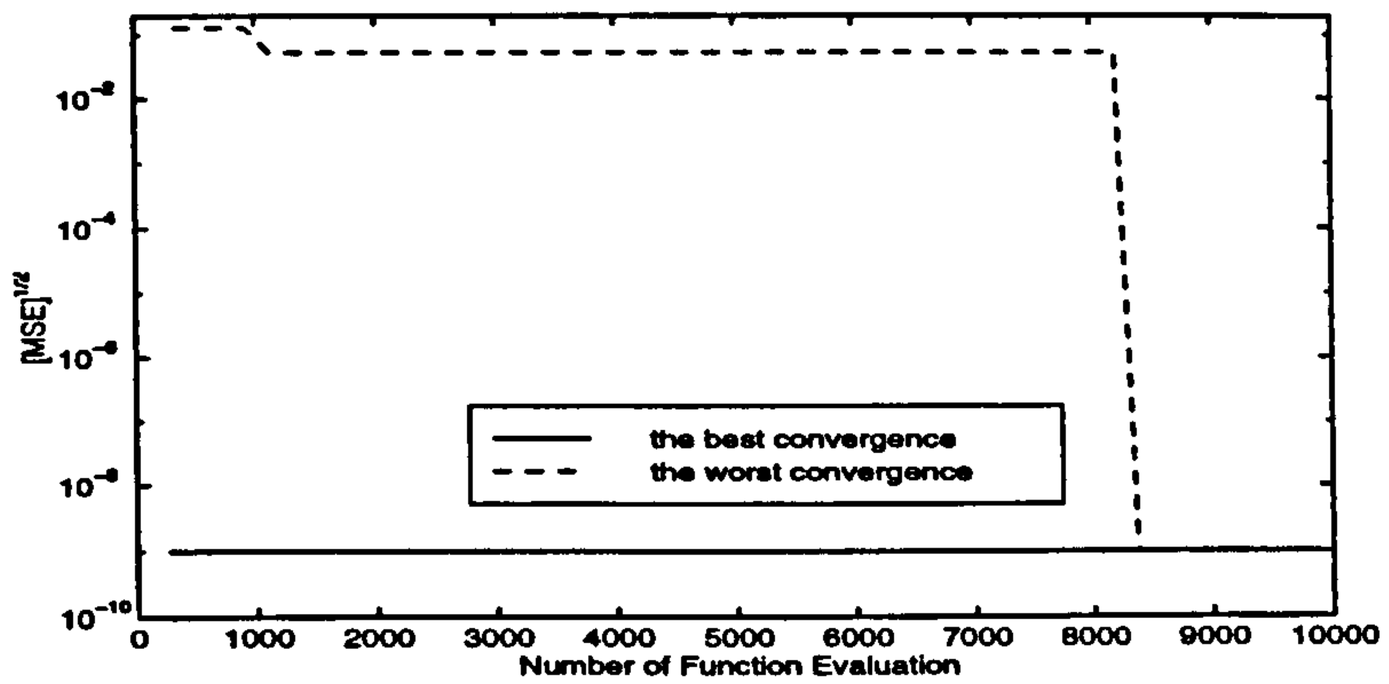

(a)

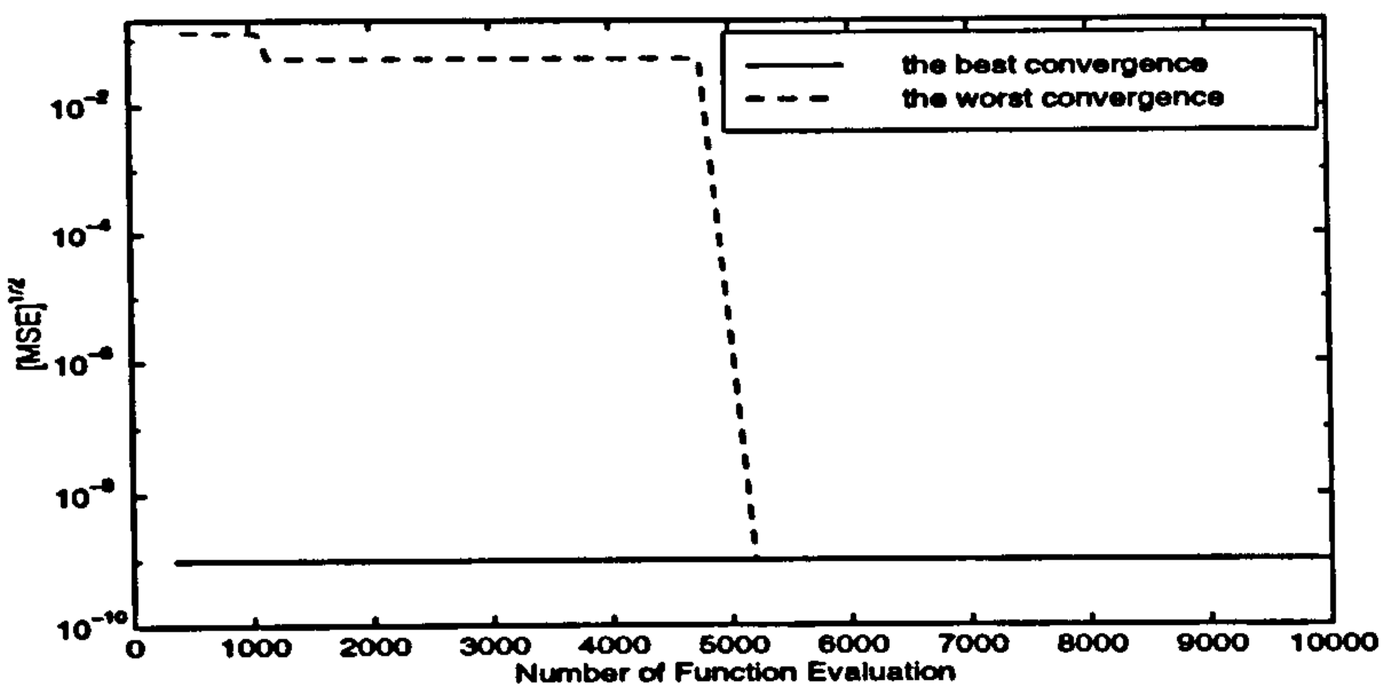

(b)

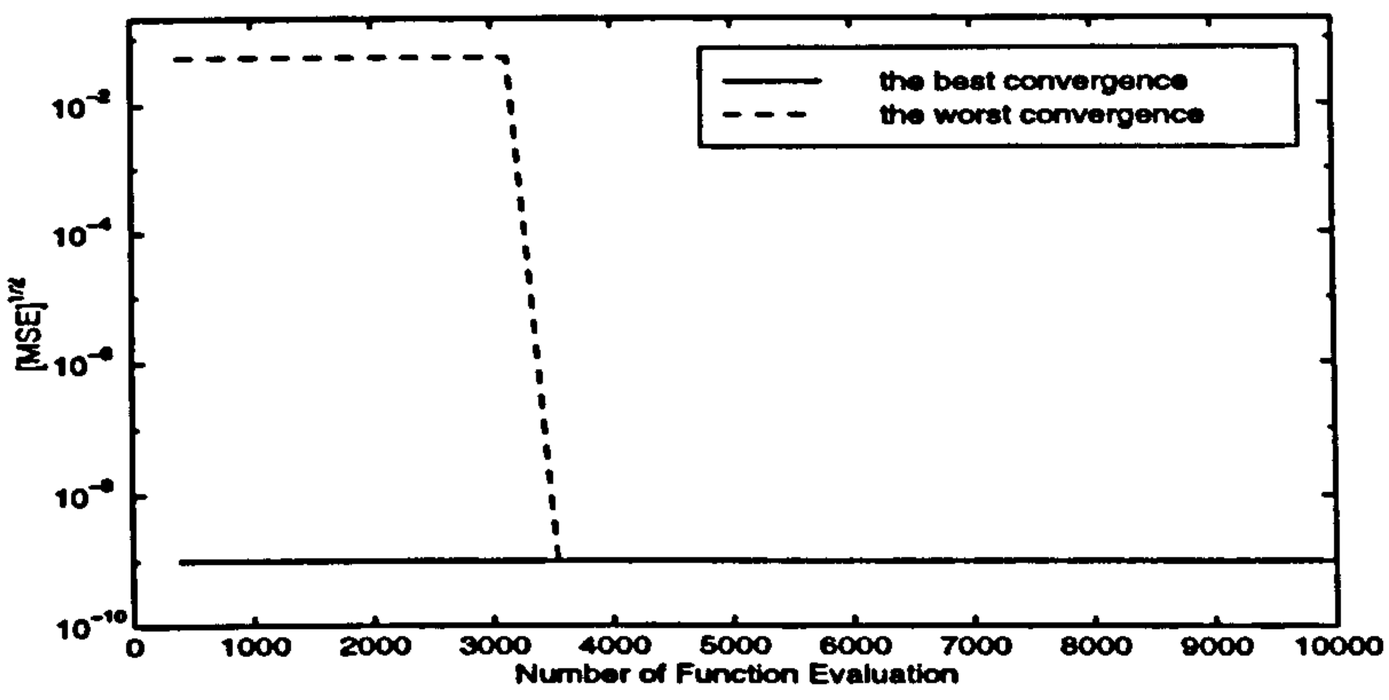

(c)

Figure 4.10: The performance of the MLSL method in reducing the MSE value for the reconstruction of the medium introduced in Example 4.1. (a) $N_p = 100$, $\xi = 0.1$ (b) $N_p = 100$, $\xi = 0.2$ (c) $N_p = 100$, $\xi = 0.5$

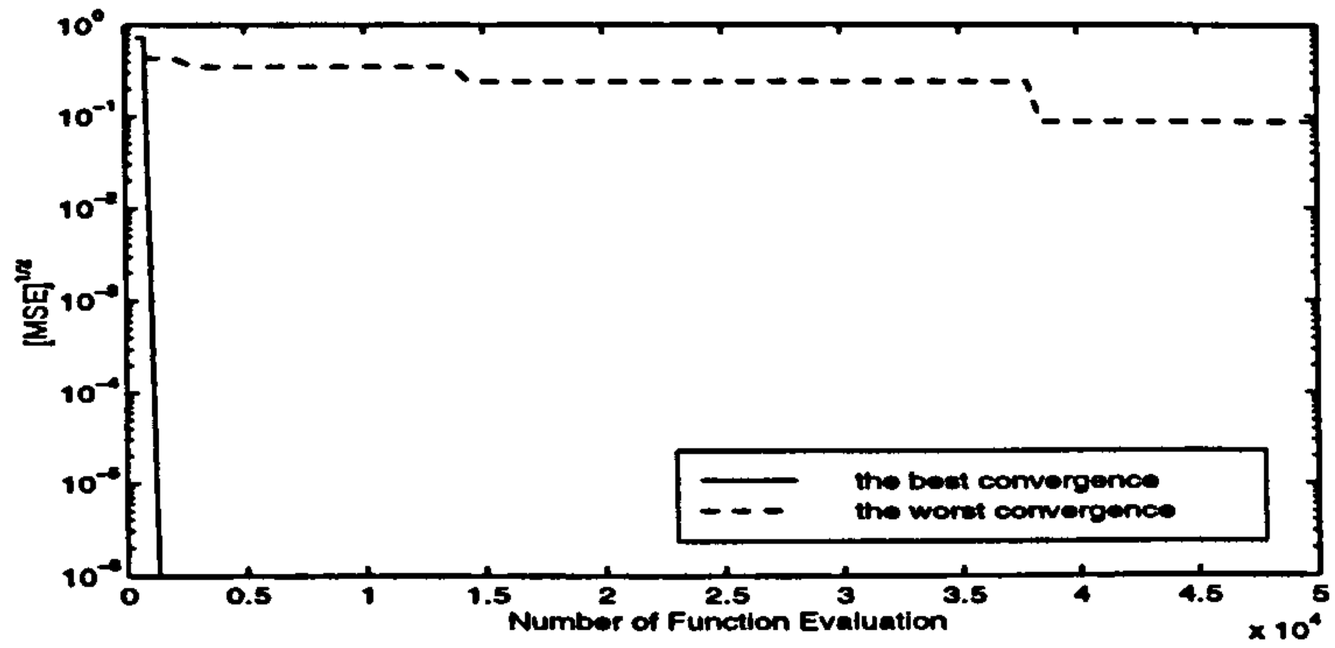

(a)

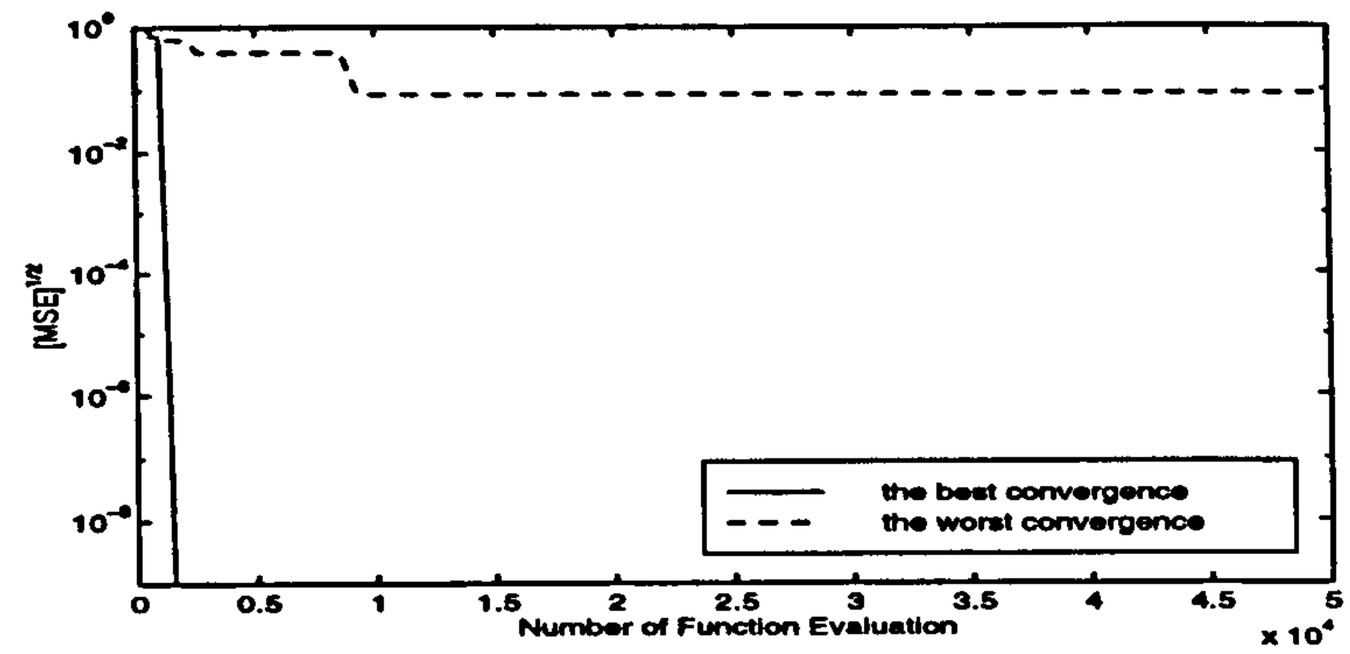

(b)

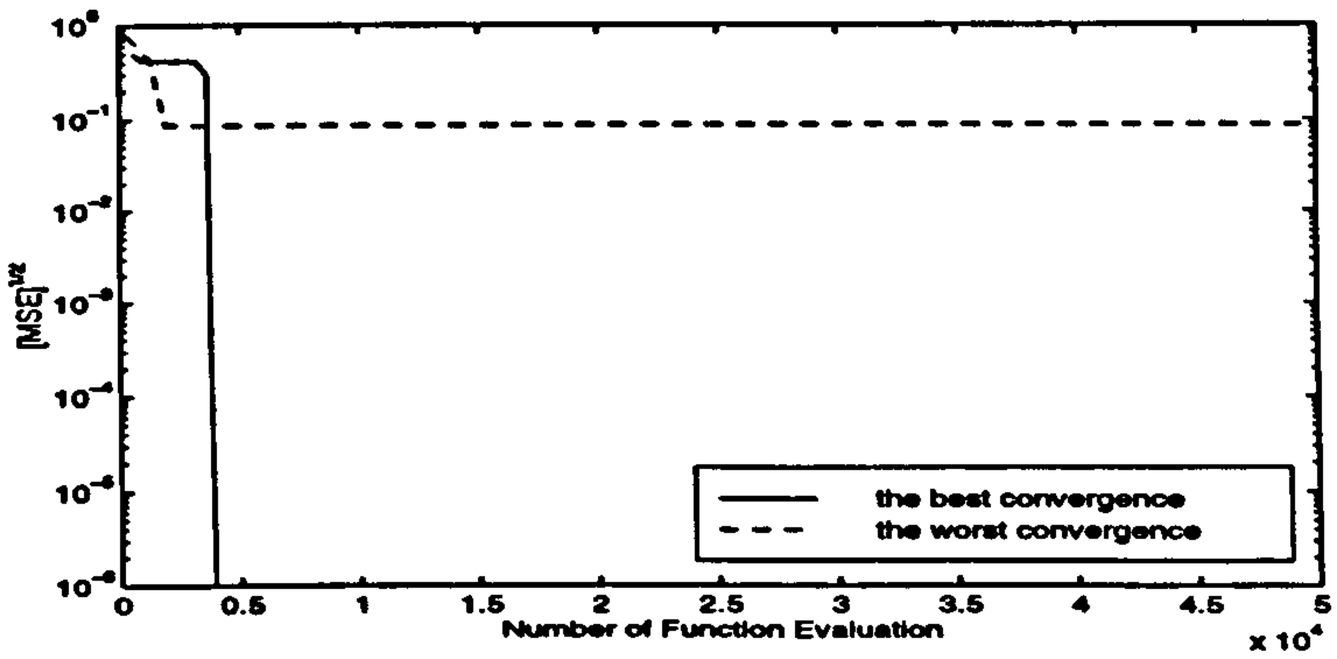

(c)

Figure 4.11: The square root of the MSE function versus the number of function evaluation when MLSL is used in the RMBI to solve the inverse problem presented in Example 4.3. (a) $N_p = 100$, $\xi = 0.02$ (b) $N_p = 100$, $\xi = 0.05$ (c) $N_p = 100$, $\xi = 0.1$

Table 4.4: The resultant MSE for 10 runs of the MLSL method for the inverse problem posed in Example 4.3. Each run involves 50000 function evaluations.

$N_p = 100$ $\xi = 0.02$	Final	0.0	0.0073	0.0	0.0	0.0
	MSE	0.0	0.0	0.0	0.0	0.0
	No. of	25	21	23	21	27
	Minima found	26	28	24	21	26
$N_p = 100$ $\xi = 0.05$	Final	0.0	0.0	0.0	0.0	0.0
	MSE	0.0	0.0073	0.0	0.0	0.0
	No. of	27	26	25	27	27
	Minima found	25	24	22	29	26
$N_p = 100$ $\xi = 0.1$	Final	0.0	0.0073	0.0073	0.0	0.0
	MSE	0.0	0.0	0.0	0.0	0.0
	No. of	26	24	28	26	28
	Minima found	28	27	27	27	25

of values of its parameters, N_p and ξ. $N_p = 100$ and $0.02 \leq \xi \leq 0.05$ gives better results for this inverse problem. Numerical reconstructions of layered media show the values of N_p and ξ should be selected in the ranges given in Table 4.5.

Table 4.5: The recommended values for the parameters of the MLSL method.

	2-layer medium	3-layer medium	4-layer medium	5(6 or 7)-layer medium
N_p	100	100	500-1000	1000-2000
ξ	0.1-0.5	0.02-0.05	0.01-0.005	0.002-0.001

Example 4.6. This example is the one considered in [64]. The goal is to reconstruct the permittivity and conductivity profiles of a three-layer slab placed in free space as shown in Fig. 4.12. The thickness of the whole ensemble together with the permittivity and conductivity of the bottom half-space are assumed known in [64]. In contrast, we only assume that the bottom layer is free space. The observed data is generated by using the reflectivity formulation presented in Chapter 3.

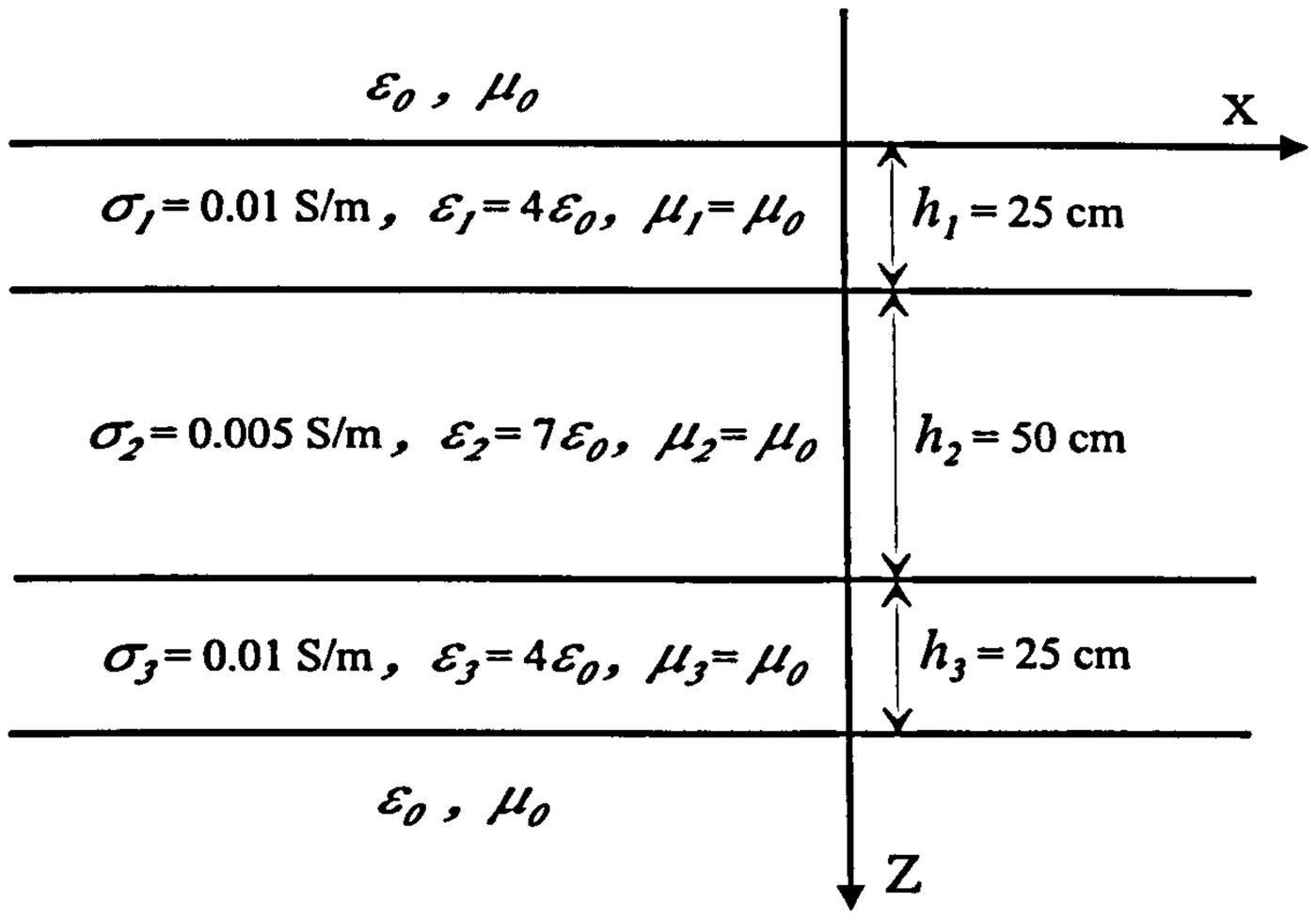

Figure 4.12: A 3-layer slab placed in free space.

To simulate the presence of the noise in the observed data, Gaussian noise is added. The noise is a complex random variable whose real and imaginary parts are independent Gaussian random variables with zero mean and standard deviation $\bar{\sigma}$. The parameters of N_p and ξ in the MLSL method are set to 500 and 0.01 respectively. In addition, the feasible region S is given by

$$0 \leq \sigma_m \leq 0.5 \text{ S/m} , \; 1 \leq \epsilon_{rm} \leq 100 , \quad 0 \leq h_m \leq 100 \text{ cm} \qquad m = 1, 2, 3 \tag{4.4.4}$$

The above bounds on permittivity and conductivity are sufficiently wide such that they cover the dielectric parameters of most materials which may be found in an environment.

As shown in Fig. 4.13, the reflection coefficients are obtained for a TE wave incidence at 15 frequencies equally spaced in the interval [5 MHz, 75 MHz] and at two incident angles, $\theta = 0°$ and 45°. Gaussian noise with different standard deviations is introduced to simulate the effect of noise.

The profile is first reconstructed from noise-free data at incident angle $\theta = 0°$. Figure 4.14(a) illustrates that how the objective function (MSE function) is reduced by the MLSL method under the assumptions that the number

of layers of the slab is 2, 3 and 4 respectively. The conductivity and permittivity profiles derived from the inverse method are shown in Fig. 4.14(b) and 4.14(c). The results show that the procedure of determining the structure of a medium (Subsection 3.4.3, Chapter 3) is successful. It can be seen that identical profiles are obtained for 3-layer and 4-layer structures. For the 4-layer case,

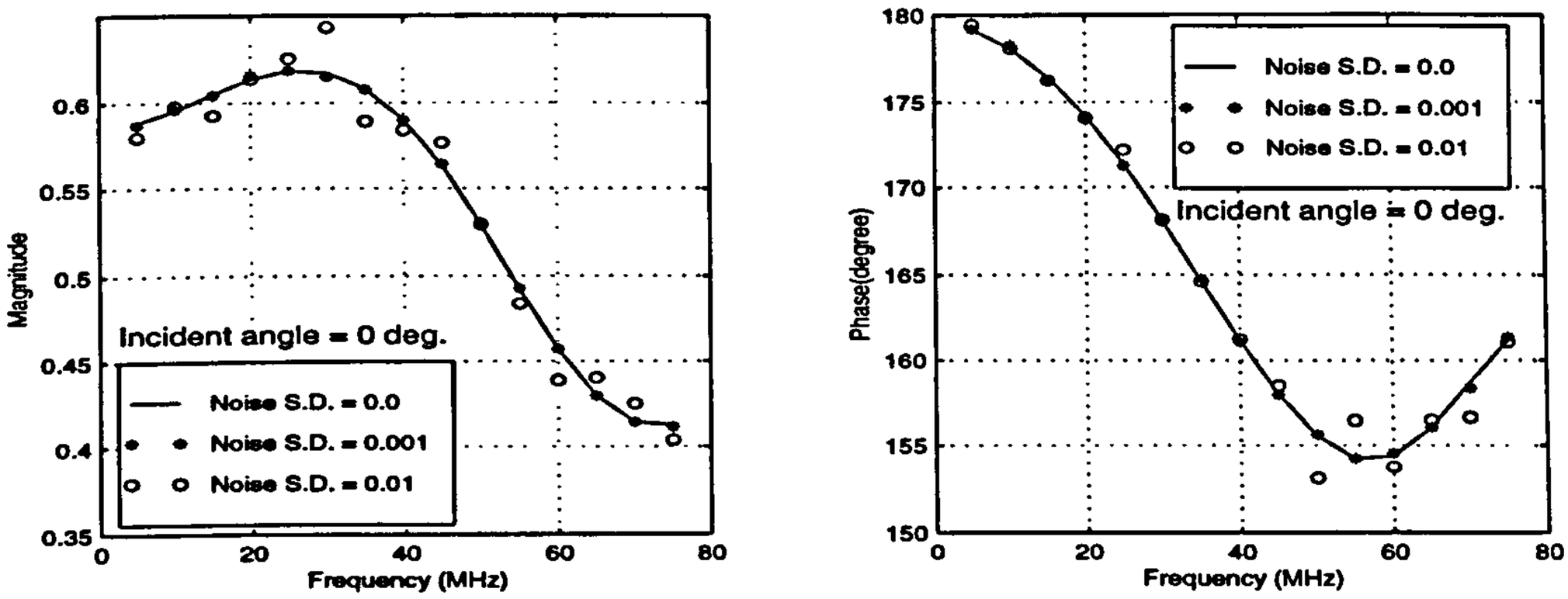

(a)

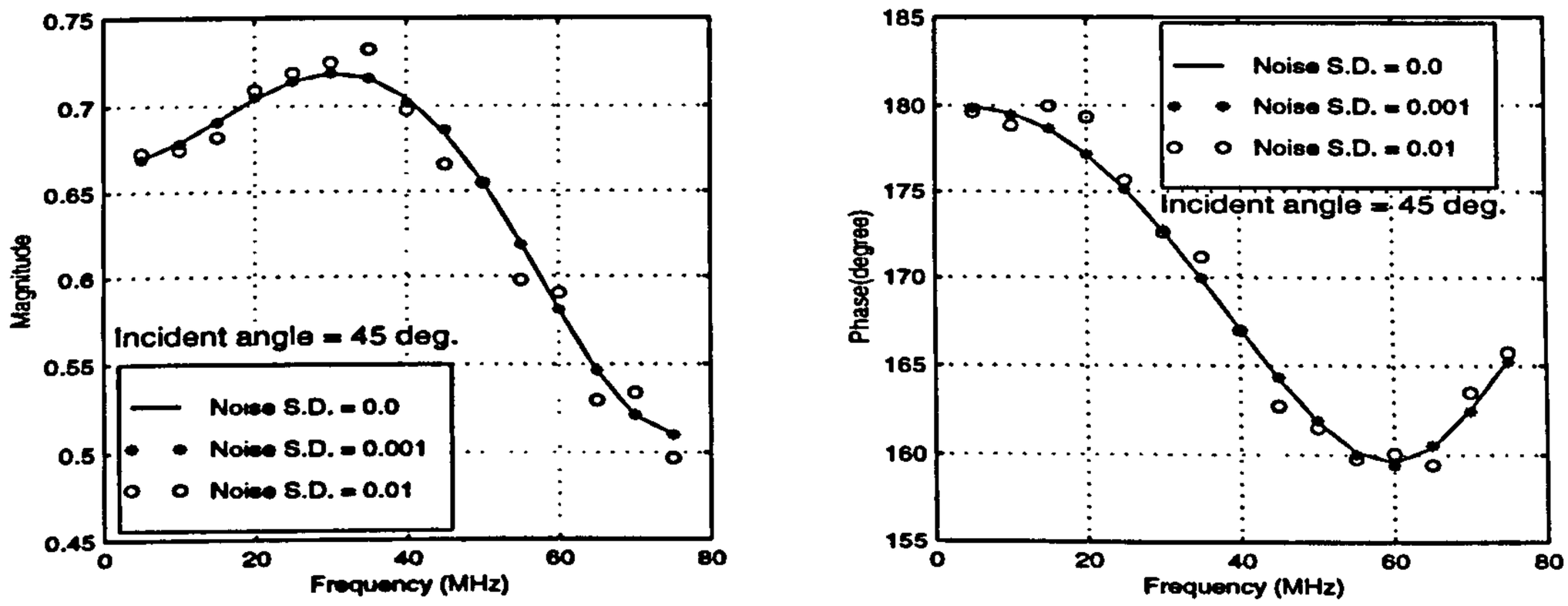

(b)

Figure 4.13: The reflection coefficients of the 3-layer slab obtained for a TE wave incidence at 15 frequencies equally spaced in the interval (5 MHz, 75 MHz). (a) Incident angle $\theta = 0°$. (b) Incident angle $\theta = 45°$.

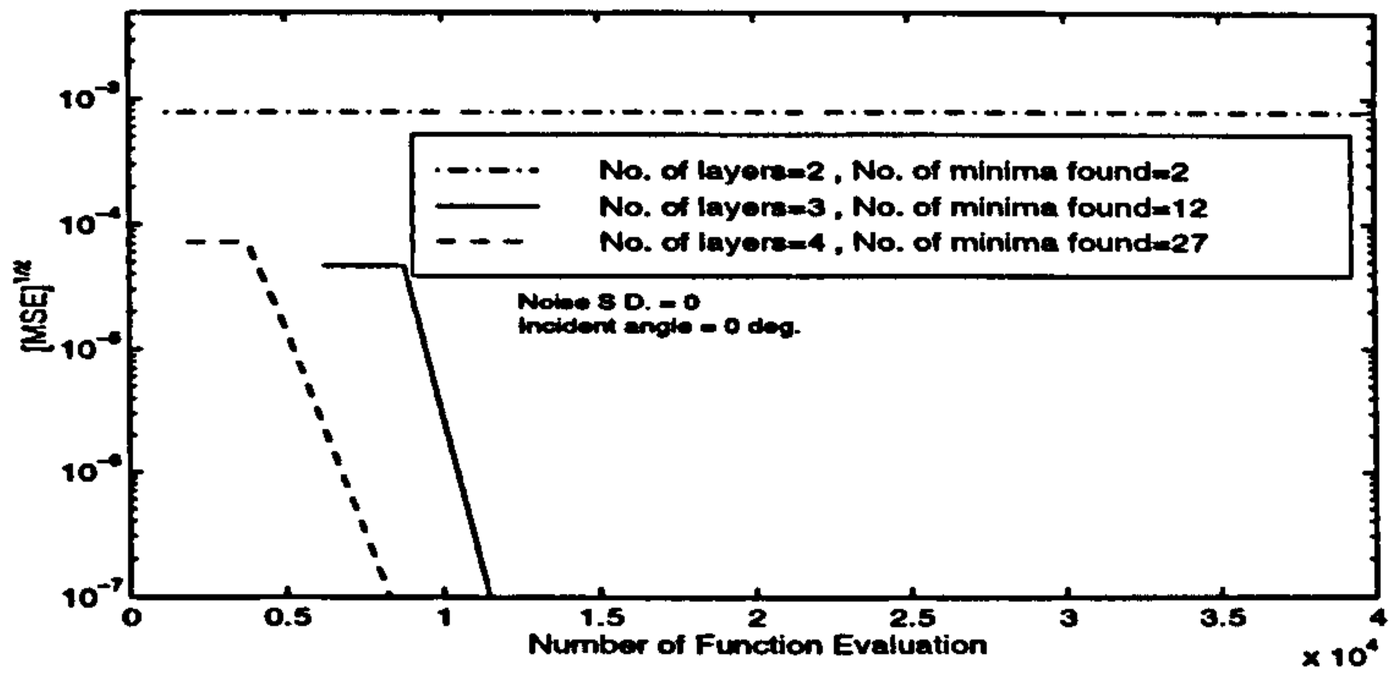

(a)

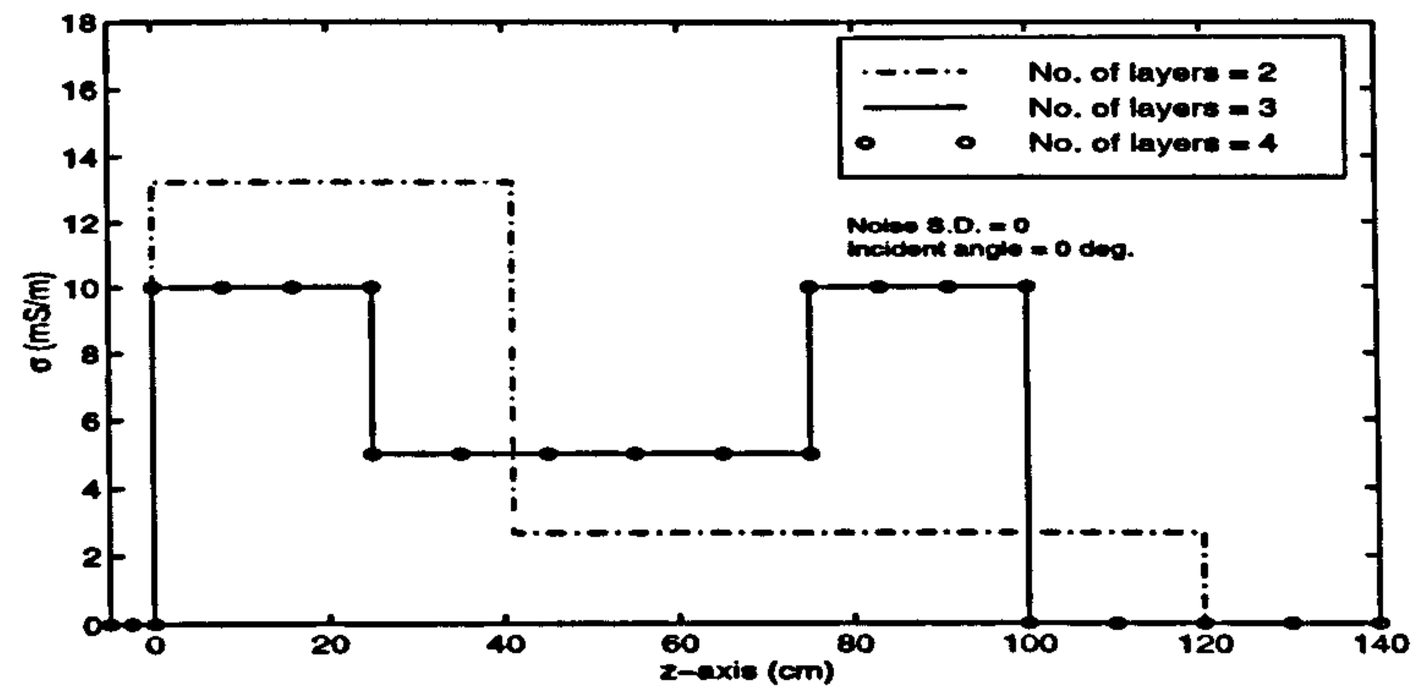

(b)

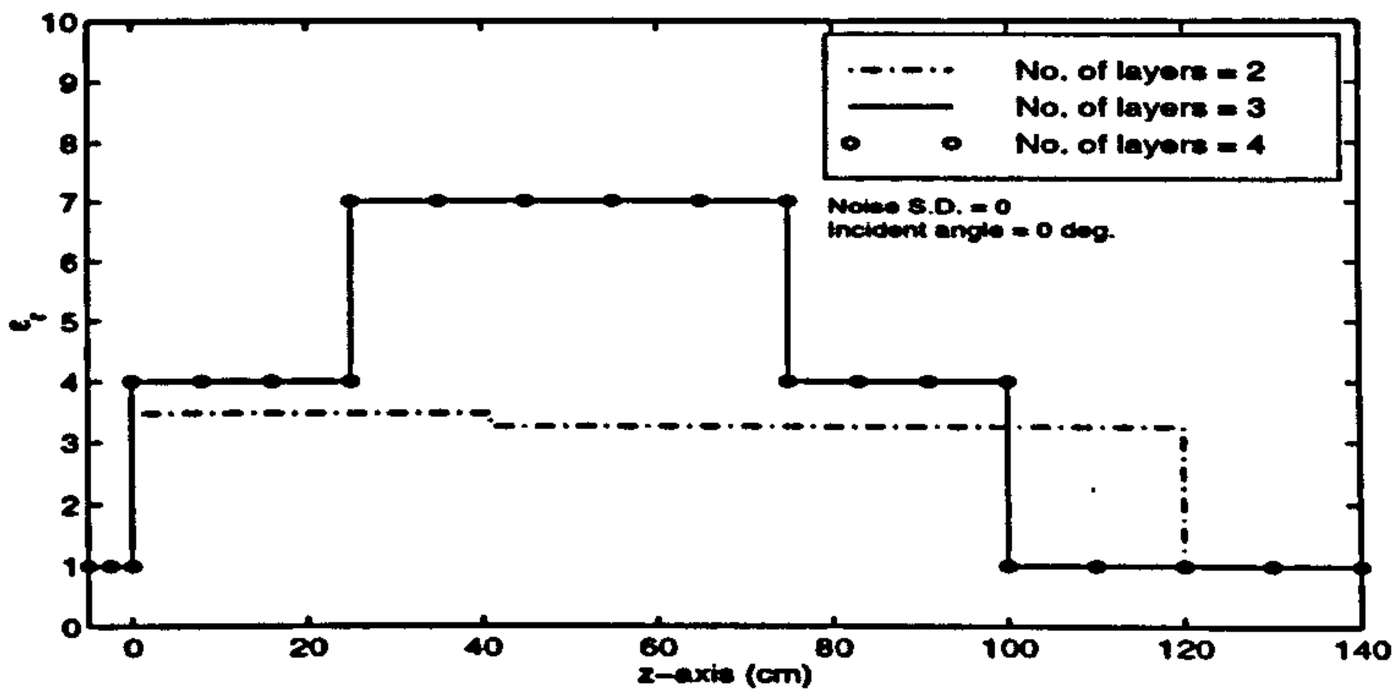

(c)

Figure 4.14: (a) Illustration of the performance of the MLSL method in minimizing the objective function for the 3-layer slab. The number of layers assumed is 2, 3 and 4. The observed data at $\theta = 0°$ is free of noise. The reconstructed (b) conductivity (c) and permittivity profiles

The results in the presence of a Gaussian noise with a standard deviation $\bar{\sigma} = 10^{-3}$ are shown in Fig. 4.15, where the influence of the noise is clearly visible. Nevertheless, this influence can be reduced by extending the data to include more frequencies and incident angles. In Fig. 4.16, the data at 15 frequencies over the range of [5 MHz, 75 MHz] and at two incident angles $\theta = 0°, 45°$ have been used. The improvement is apparent. Further improvement can be achieved by doubling the frequency points (Fig. 4.17). An important consequence of the successful convergence to the global minimum is that the inverse method can reconstruct the profile of a layered medium even if the wavelengths of the scattering data are greater than the thickness of the layers. For the first reconstruction, the smallest wavelength in the layer 1 of the medium is 2 metre, eight times of the thickness of the layer. This cannot be done using the layer-stripping method.

Example 4.7. This example aims at testing the inverse method with experimental data. A non-uniform transmission line, which consists of four coaxial sections as shown in Fig. 4.18, is investigated. The coaxial cables are connected to each other via SMA 50 Ω connectors. An HP-8753B network analyzer with an output impedance of 50 Ω is used to measure the reflection coefficients. The lines are standard 50 Ω and 75 Ω coaxial cables, which have negligible series resistance and shunt conductance. The nominal value of the shunt capacitance per unit length, C_m, provided by the manufacturer, is 100 pF/meter for 50 Ω line and 56 pF/meter for 75 Ω line. The series inductance L_m, given in Fig. 4.18, are calculated by using

$$Z_m = \left(L_m/C_m\right)^{1/2} \tag{4.4.5}$$

where Z_m is the characteristic impedance of the mth section. The fourth line is terminated by a 50 Ω load so that it can be considered as an infinitely long transmission line.

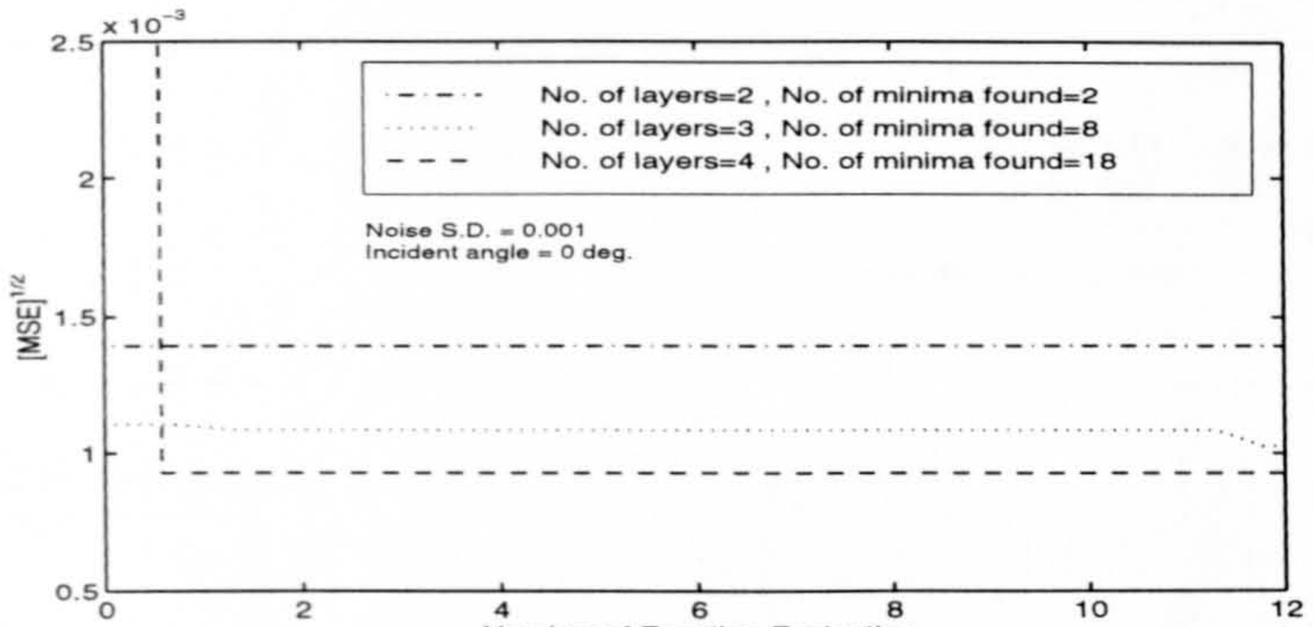

(a)

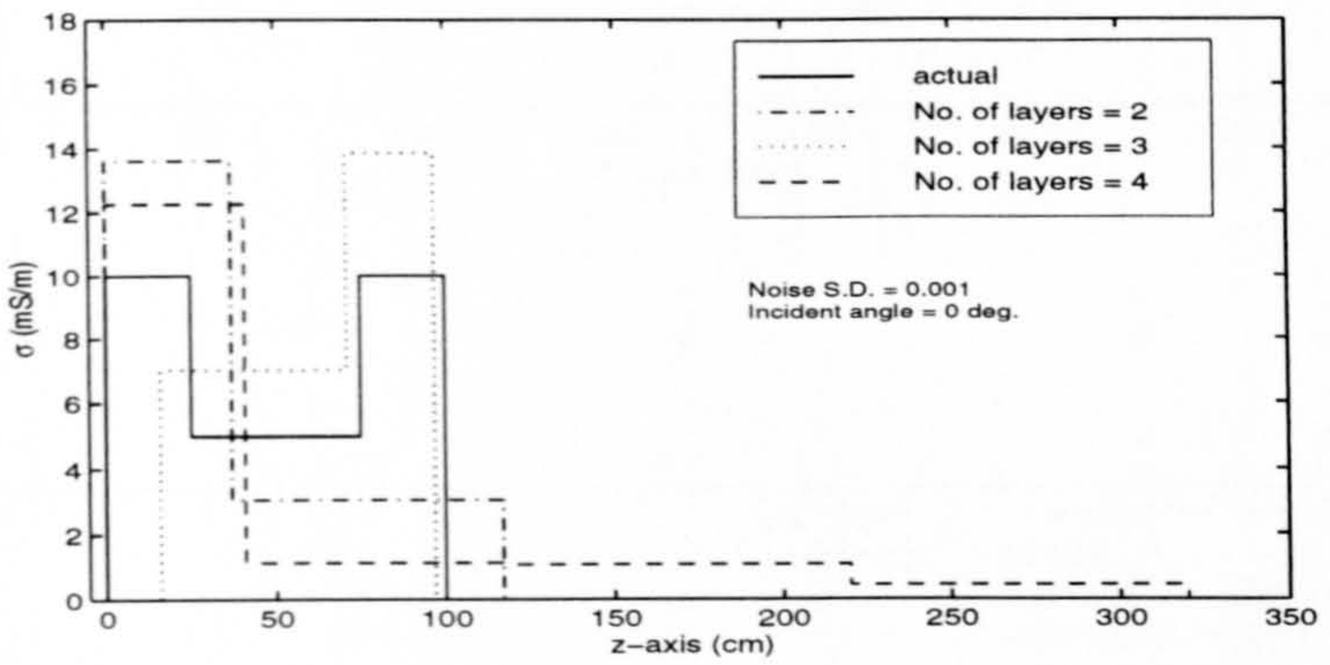

(b)

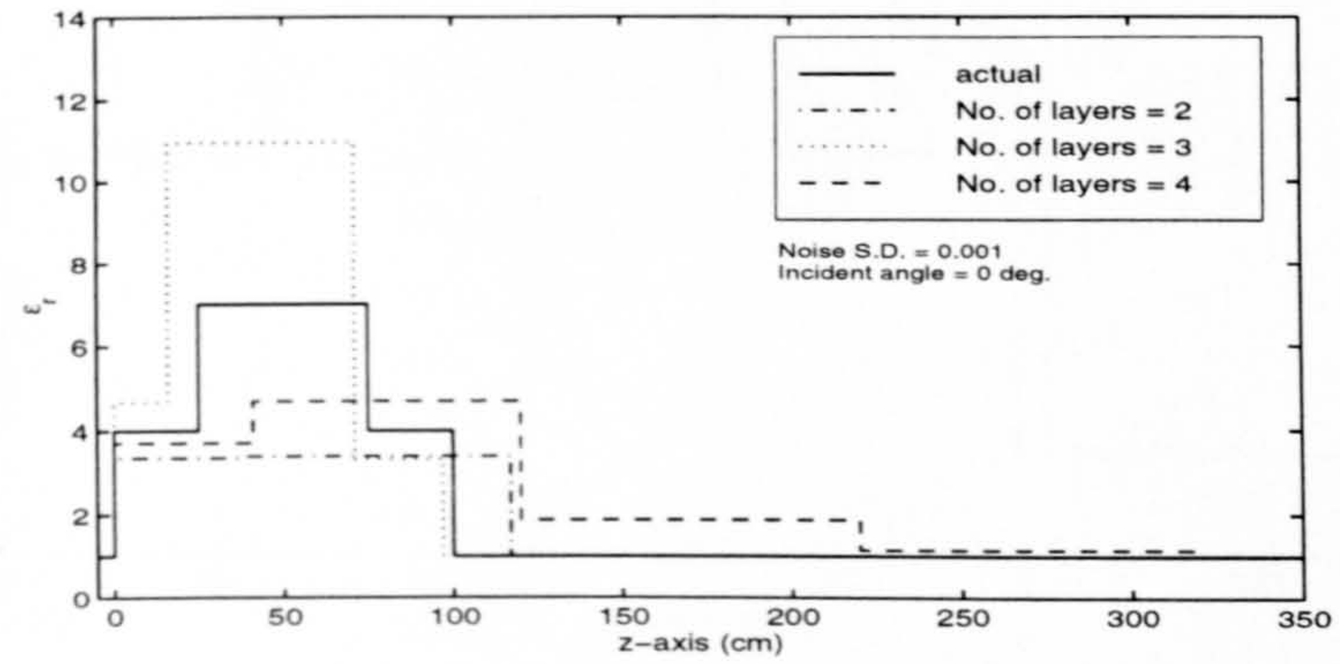

(c)

Figure 4.15: The results of using MLSL in the RMBI for reconstruction of profile of the 3-layer slab when the observed data at normal incidence is corrupted by a Gaussian noise with $\bar{\sigma} = 10^{-3}$.

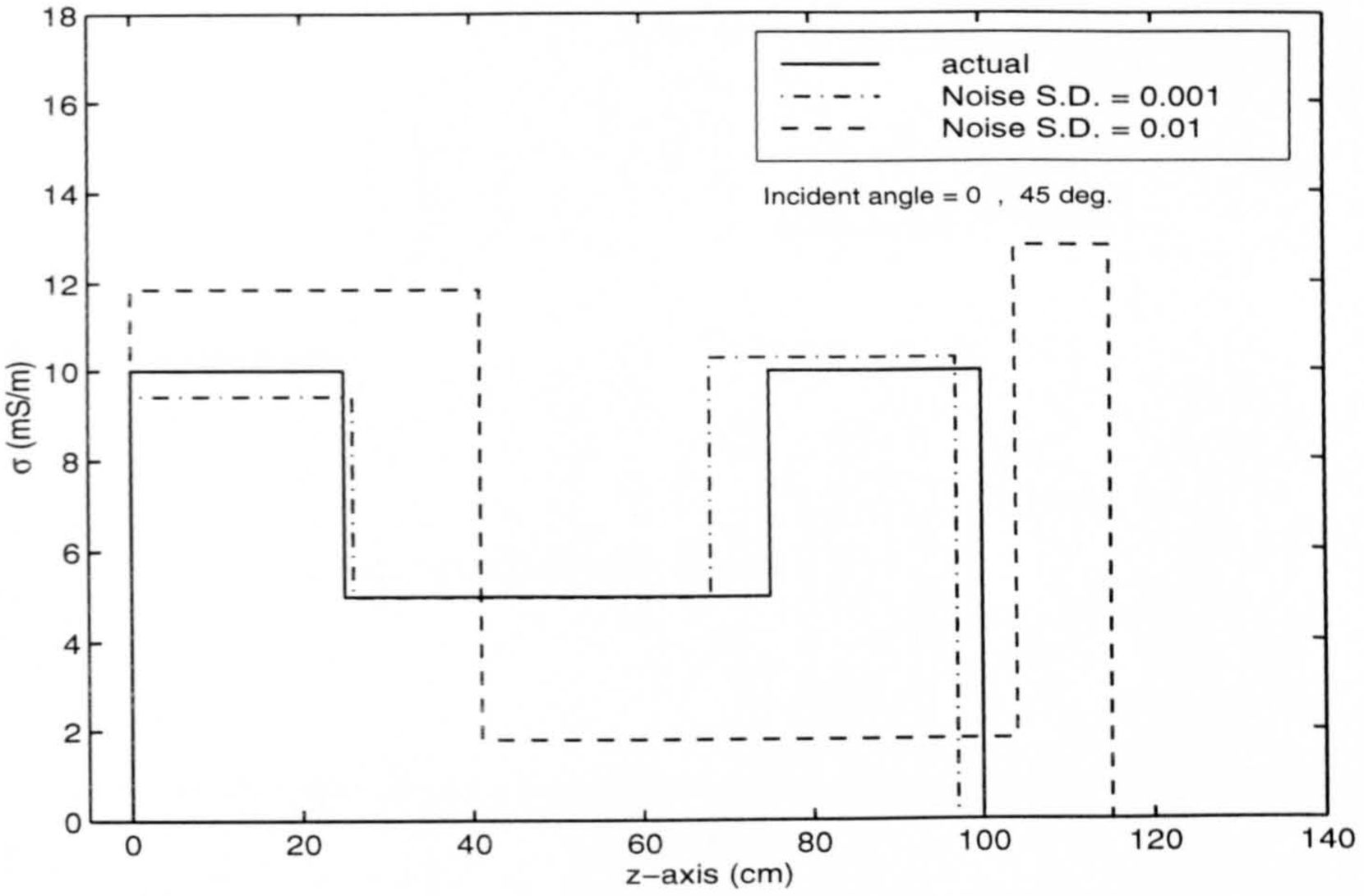

(a)

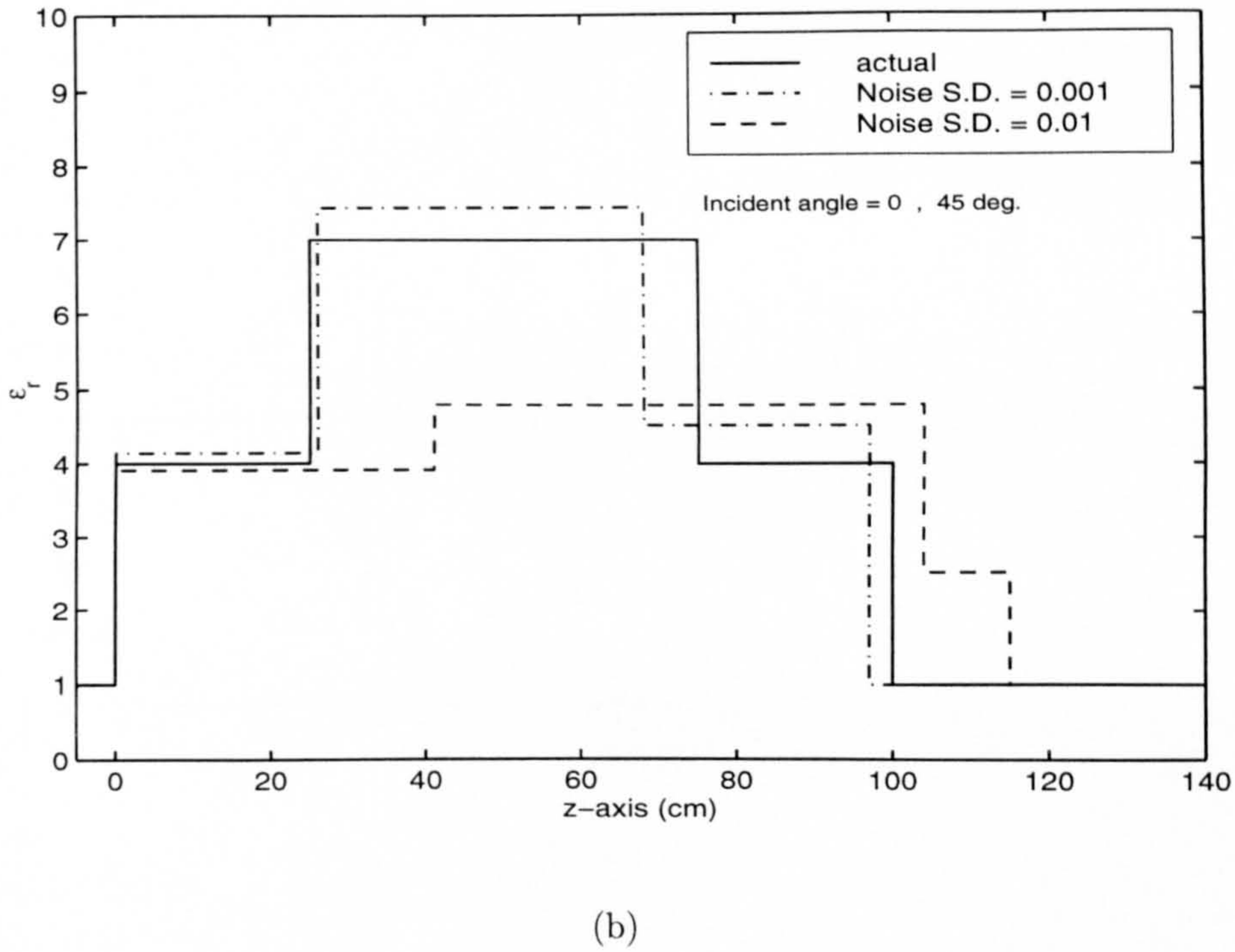

(b)

Figure 4.16: Illustration of the improvement of the reconstructed profile for 3-layer slab using more observed data. The results are based on the observed data at 15 frequencies and two incident angles (0° and 45°).

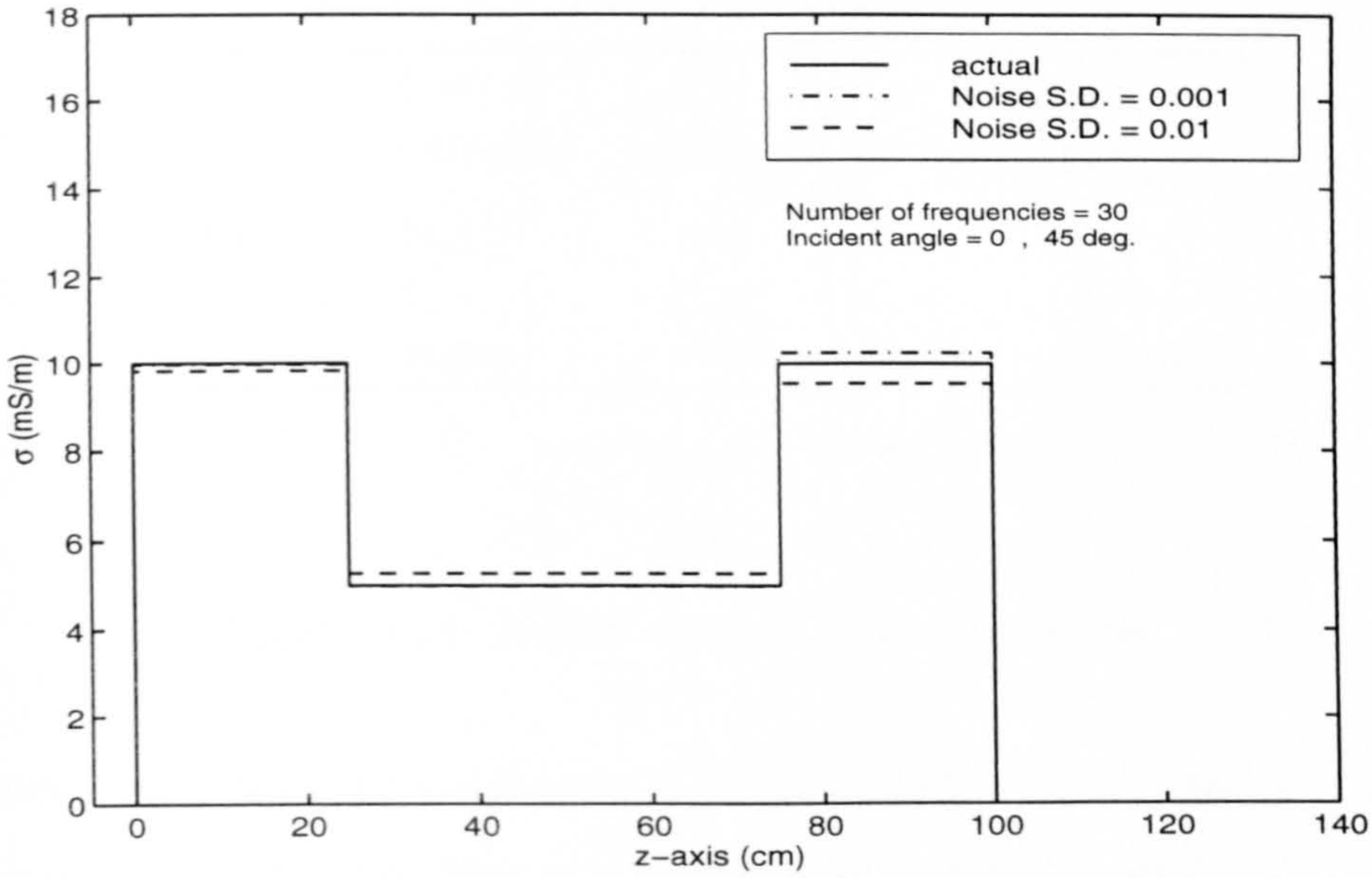

(a)

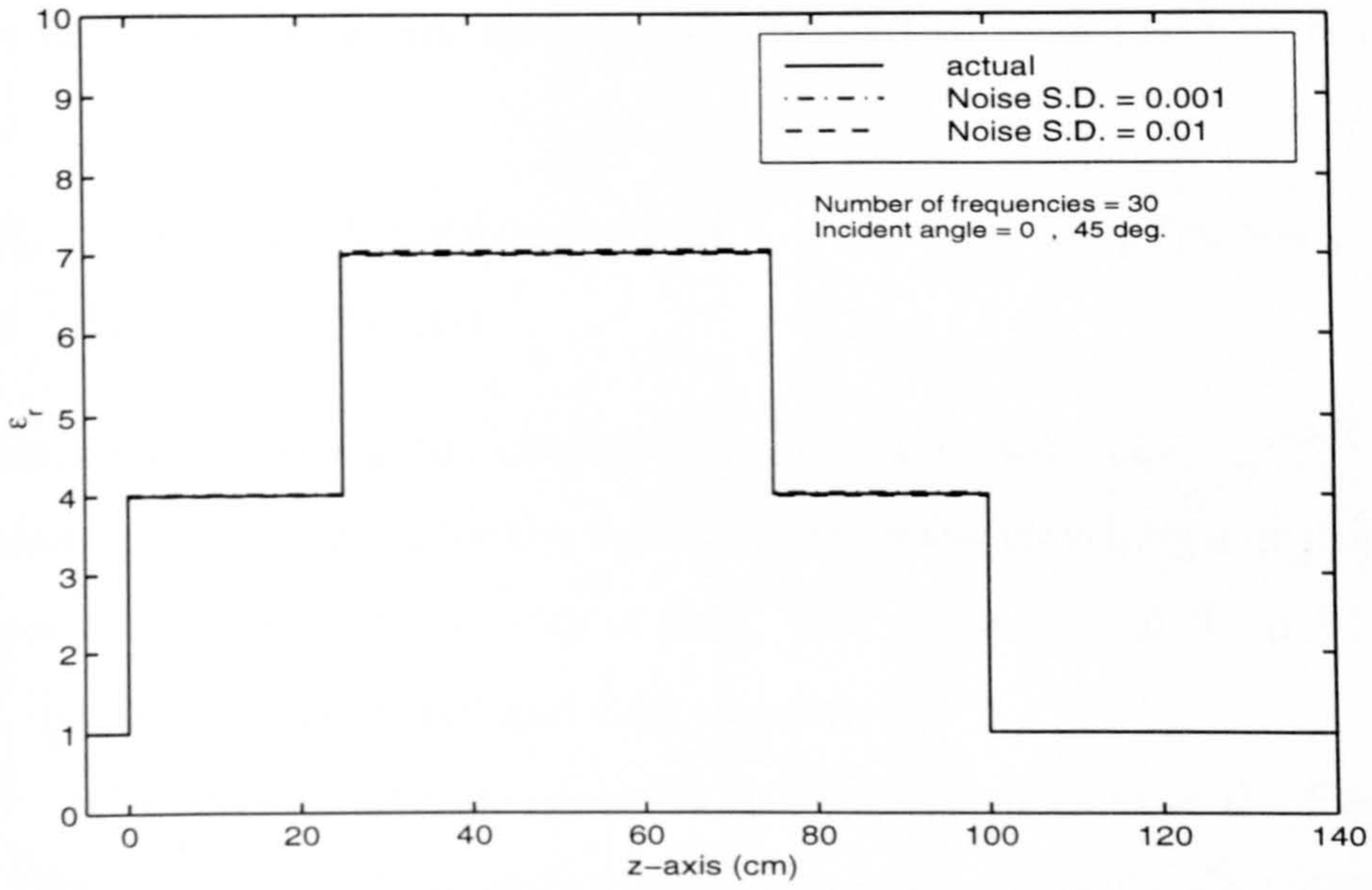

(b)

Figure 4.17: The conductivity (a) and permittivity (b) profiles of the 3-layer slab reconstructed from the reflection coefficients obtained at two incident angles (0° and 45°) and at 30 frequencies over the range of [5 MHz, 150 MHz] with linear spacing.

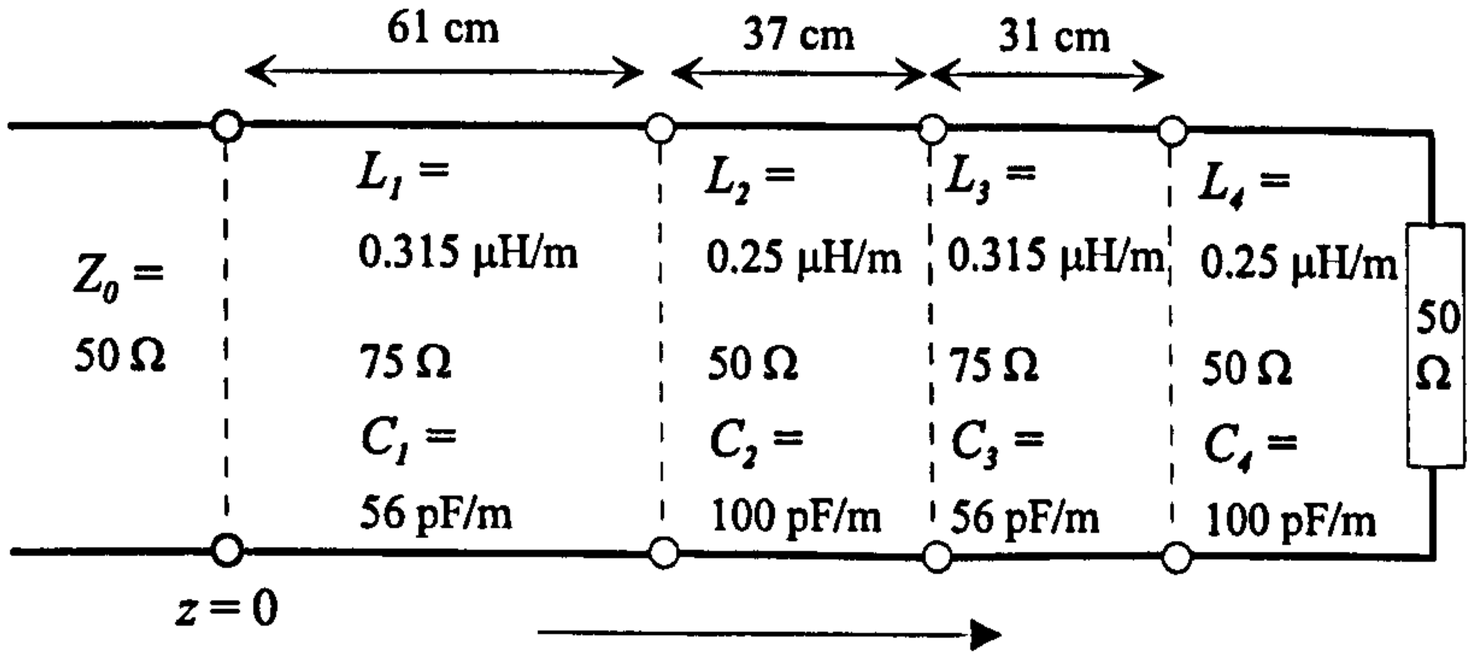

Figure 4.18: A non-uniform transmission line.

Since the value of the series resistance R_m and shunt conductance G_m of the lines are nearly zero, the value of one of the three parameters L_m, C_m and h_m (the thickness) has to be known according to the necessary condition (Chapter 3). In this example, the value of L_m is assumed known and C_m and h_m are reconstructed by the inverse method. The bounds of these parameters are set to

$$\begin{aligned} &35.3 \leq C_1, C_3 \leq 200 \text{ pF/meter}, \ 44.5 \leq C_2, C_4 \leq 200 \text{ pF/meter}, \\ &0 \leq h_1, h_2, h_3 \leq 2 \text{ metre} \end{aligned} \tag{4.4.6}$$

The lower bounds of C_m are obtained in accordance with $(L_m C_m)^{-1/2} \leq 3 \times 10^8$ meter/sec which indicates the velocity of the wave travelling along the lines cannot be in excess of the velocity of light. The parameters of N_p and ξ in the MLSL method are set to 100 and 0.05 respectively.

The reflection coefficients measured at 16 frequencies over the frequency range [100 MHz, 250 MHz] with linear spacing are shown in Fig. 4.19. The objective function during minimization and the reconstructed profiles are illustrated in Fig. 4.20. The characteristic impedance shown in Fig. 4.20(c) is obtained from the capacitance per unit length by using equation (4.4.5). There is an error in the reconstructed profile for the true structure (i.e. 4-section structure). Although the measurement noise can be considered having

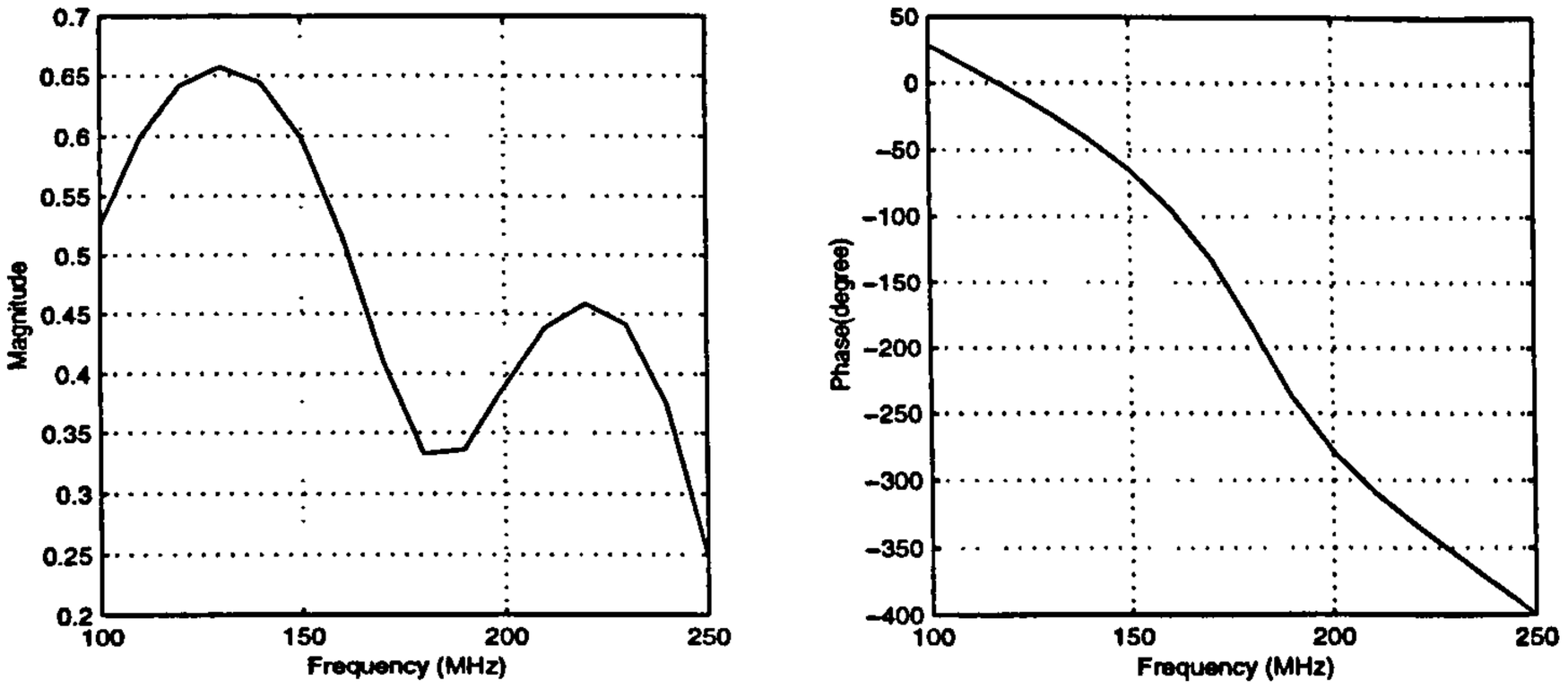

Figure 4.19: The reflection coefficients of the transmission line shown in Fig. 4.18. The data is measured by an HP-8753B network analyzer at 16 frequencies equally spaced in the interval [100 MHz, 250 MHz].

contributed in generating this error, we think the dominant sources of this error are:

1. The SMA connectors introduce local capacitances that are not taken into account in the modelling.

2. The value of the capacitance per unit length is a nominal value and the actual value can be different from the nominal one.

3. The series resistance is neglected whereas its value for 50 Ω cables at 100 MHz is nearly 2 Ω/meter which is considerable.

Example 4.8. This example is concerned with the simultaneous reconstruction of four parameters R, L, G and C of a non-uniform transmission line from simulated data, assuming that the lengths of the sections are known. In practice, these parameters vary with frequency: the variations of L, G and C are small whereas that of R is considerable. The frequency dependence of R_m can be modelled by $R_m = Q_m\sqrt{\omega}$ [55, Chapter 3]. Thus, Q_m is to be reconstructed. Consequently, the expression (3.4.10) (Chapter 3) for R_m is replaced with the

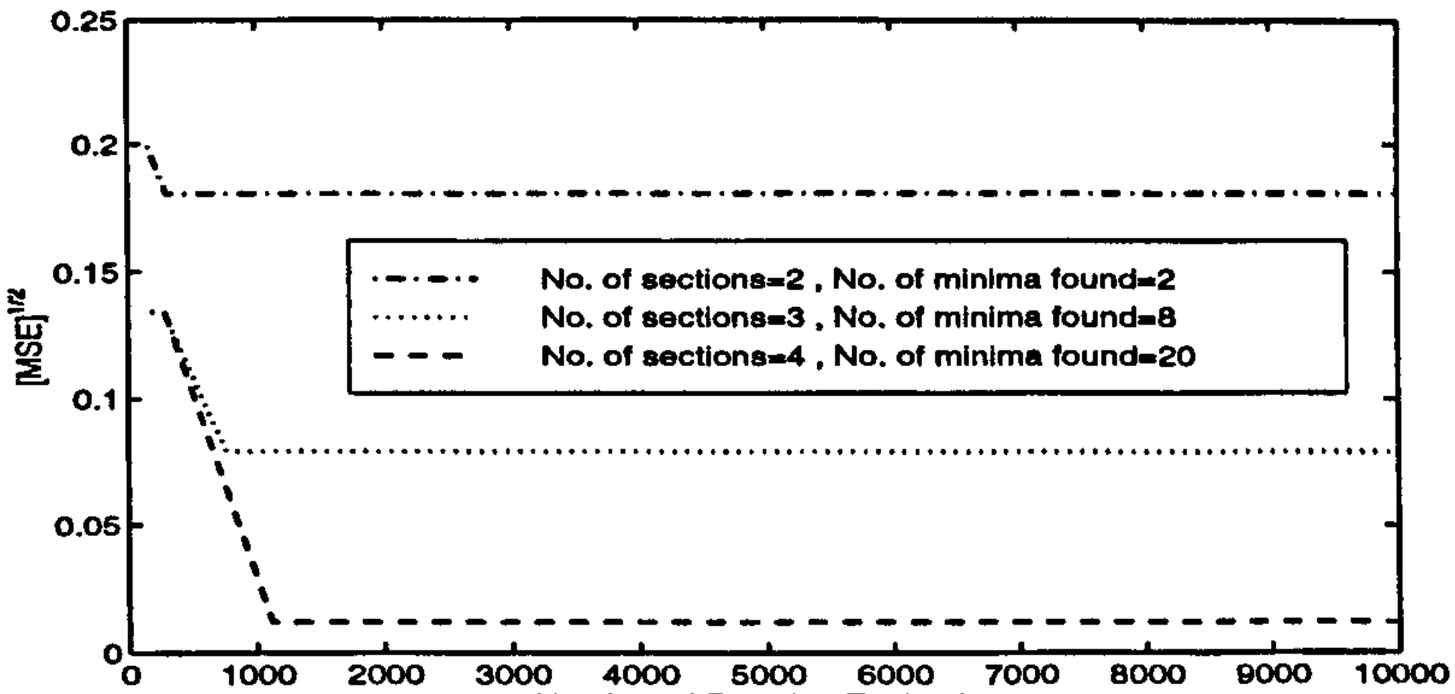

(a)

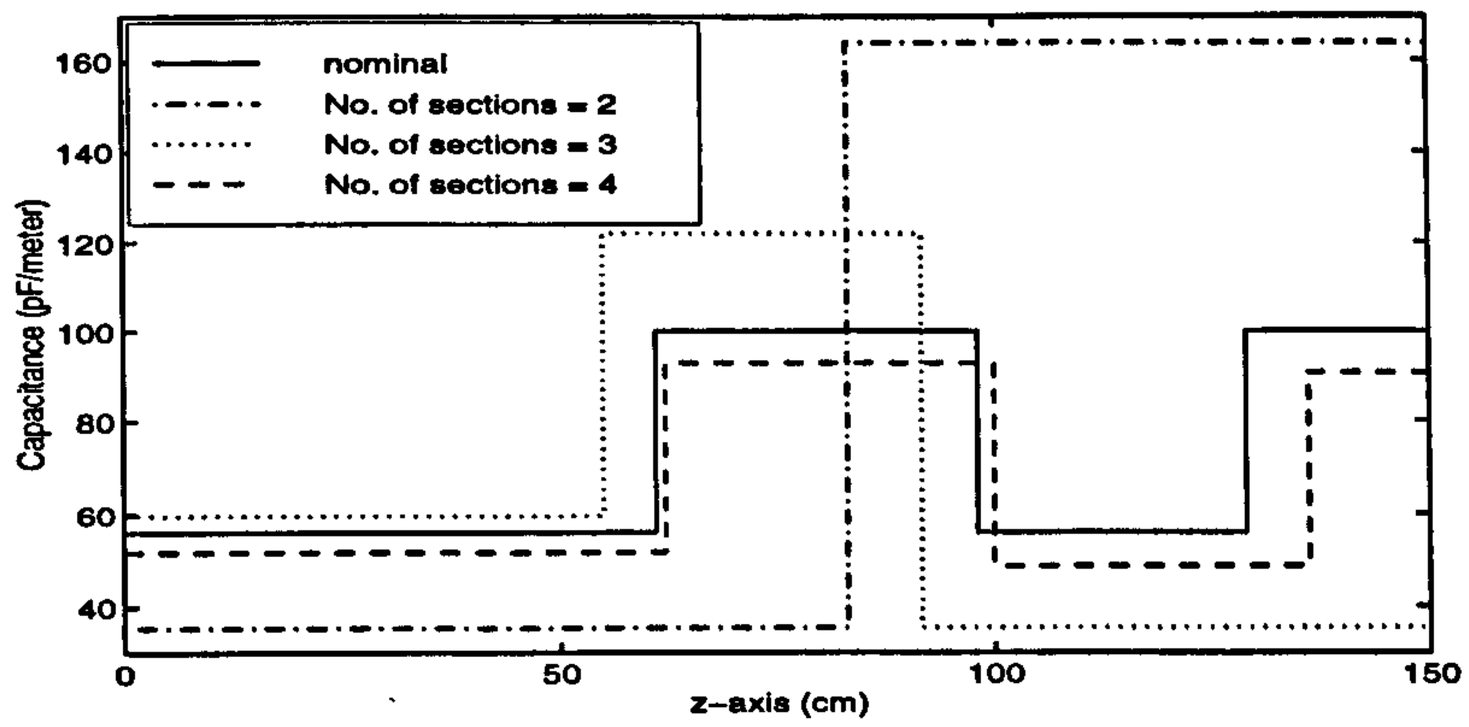

(b)

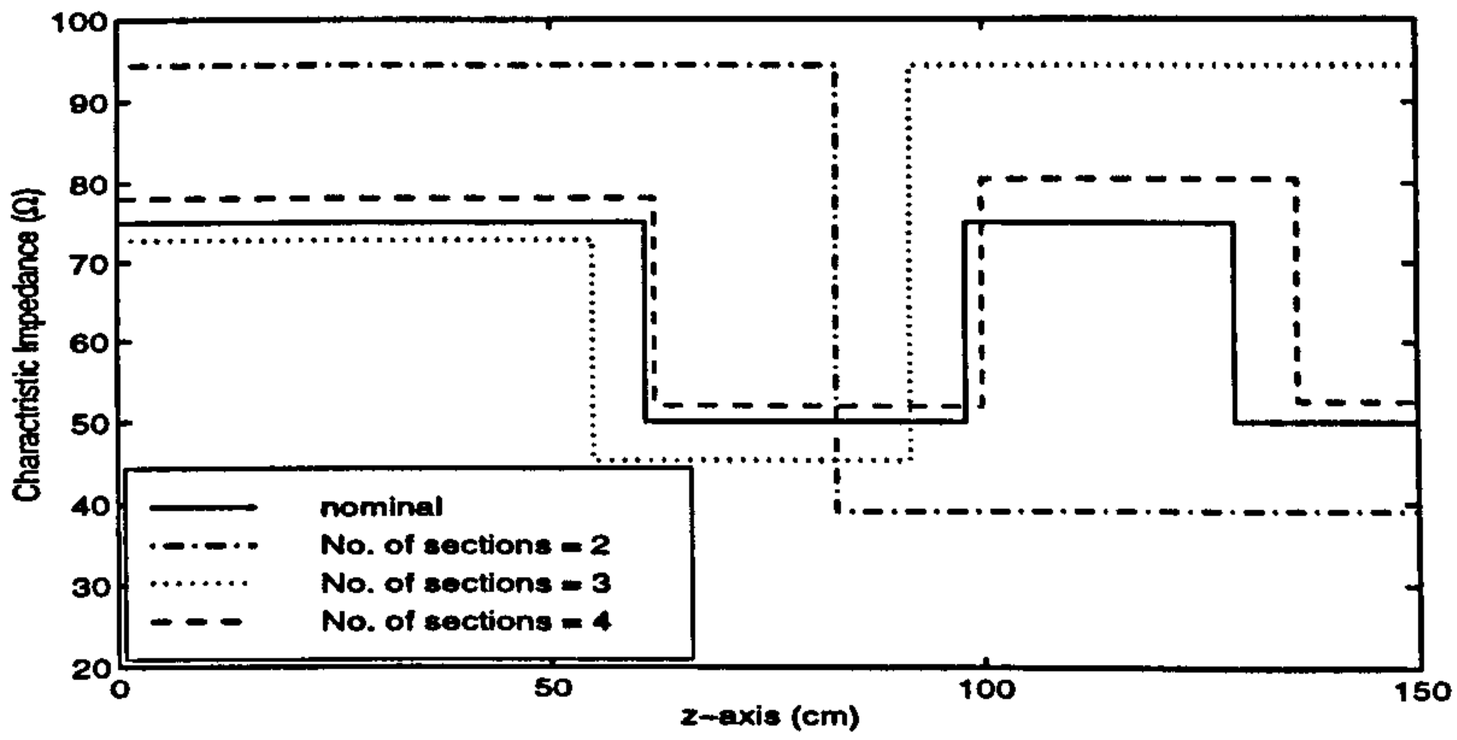

(c)

Figure 4.20: (a) Illustration of the performance of the MLSL method in minimizing the objective function for the transmission line shown in Fig. 4.18 when the number of sections are 2, 3 and 4. The reconstructed (b) capacitance and (c) characteristic impedance.

following expression

$$\frac{\partial Y_m}{\partial Q_m} = -\sqrt{\omega_n}\,\frac{Y_m^2}{2u_m} \quad , \quad \frac{\partial T_m}{\partial Q_m} = \sqrt{\omega_n}\,\frac{Y_m\,[1-(T_m)^2]\,h_m}{2} \tag{4.4.7}$$

The line parameters chosen for this example are shown by the solid lines in Fig. 4.22. The corresponding values for the parameter Q are

$$Q_1 = 0\,,\; Q_2 = 2\times 10^{-4}\,,\; Q_3 = 5\times 10^{-4}\,,\; Q_4 = 0$$

The line is excited from a uniform line with a characteristic admittance $Y_0 = 0.02\,\mathrm{S}$. The other side is left open, i.e. $Y_M = 0$. The parameters of N_p and ξ in the MLSL method are set to 1000 and 0.005 respectively. The search region is selected as:

$$\begin{aligned} &0 \le G_m \le 1000\ \mathrm{mS/meter} \quad , \; 10 \le C_m \le 200\ \mathrm{pF/meter} \\ &0 \le Q_m \le 0.01 \qquad\qquad\quad , \; 1/(0.09C_m) \le L_m \le 0.55\ \mu\mathrm{H/meter} \\ &\qquad\qquad\qquad\qquad\qquad\quad \text{for } m = 1,2,3,4 \end{aligned} \tag{4.4.8}$$

Figures 4.21 and 4.22 show respectively the graph of $[MSE]^{\frac{1}{2}}$ and the reconstructed profiles, making use of the observed data shown in Fig. 4.23. For the noise-free data, the objective function approached zero and therefore the profiles were precisely reconstructed.

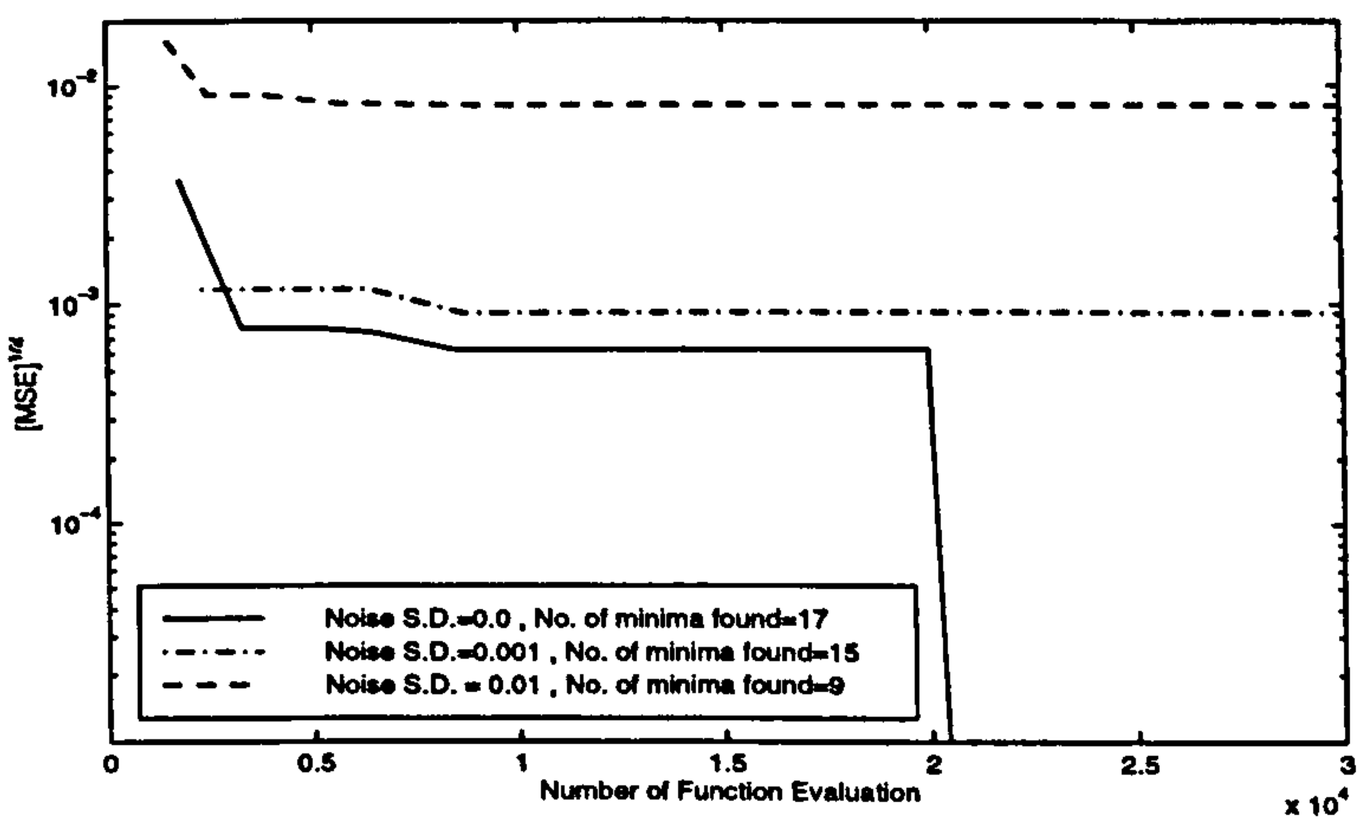

Figure 4.21: The square root of the objective function versus the number of function evaluation.

The Application of GPR

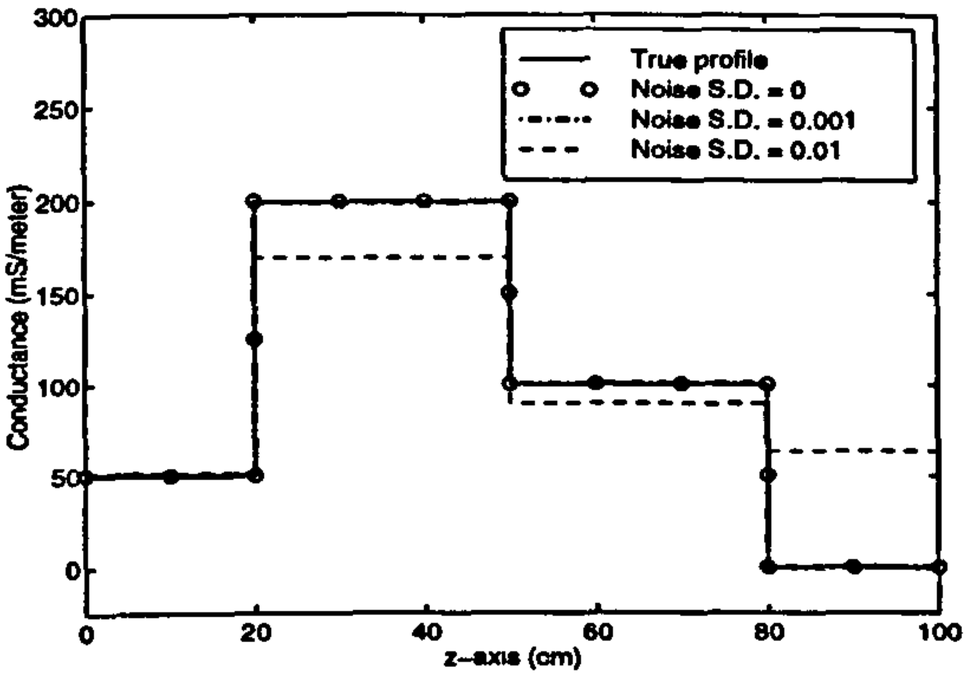

(a)

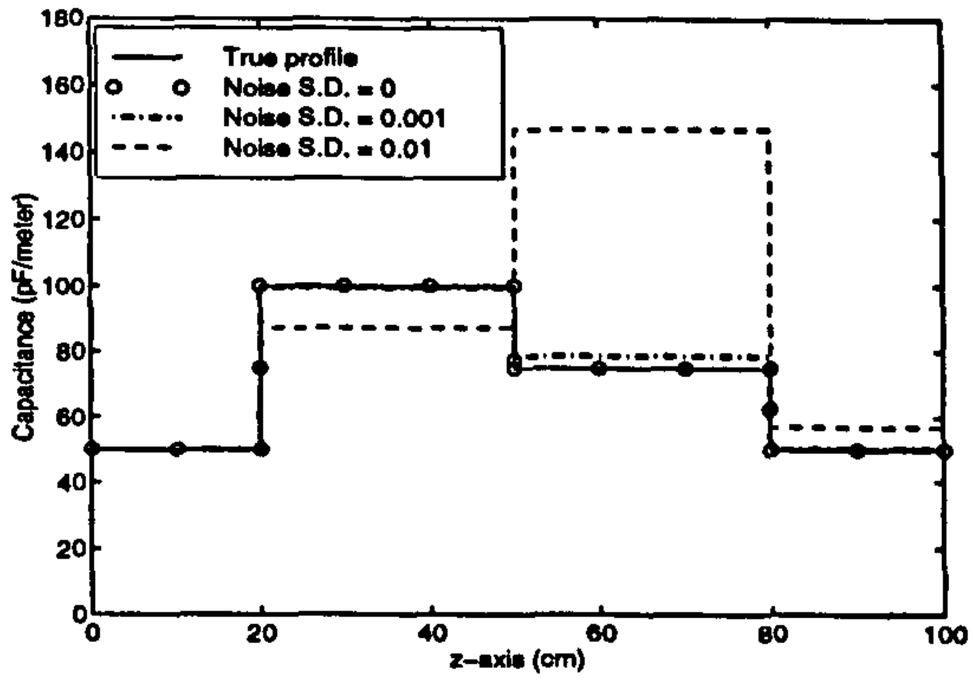

(b)

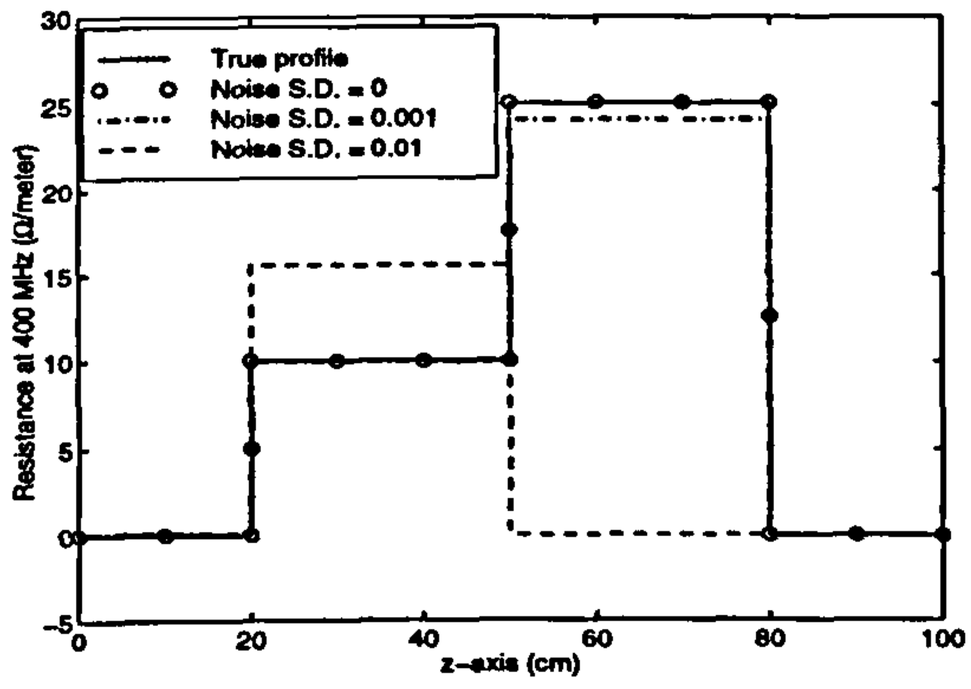

(c)

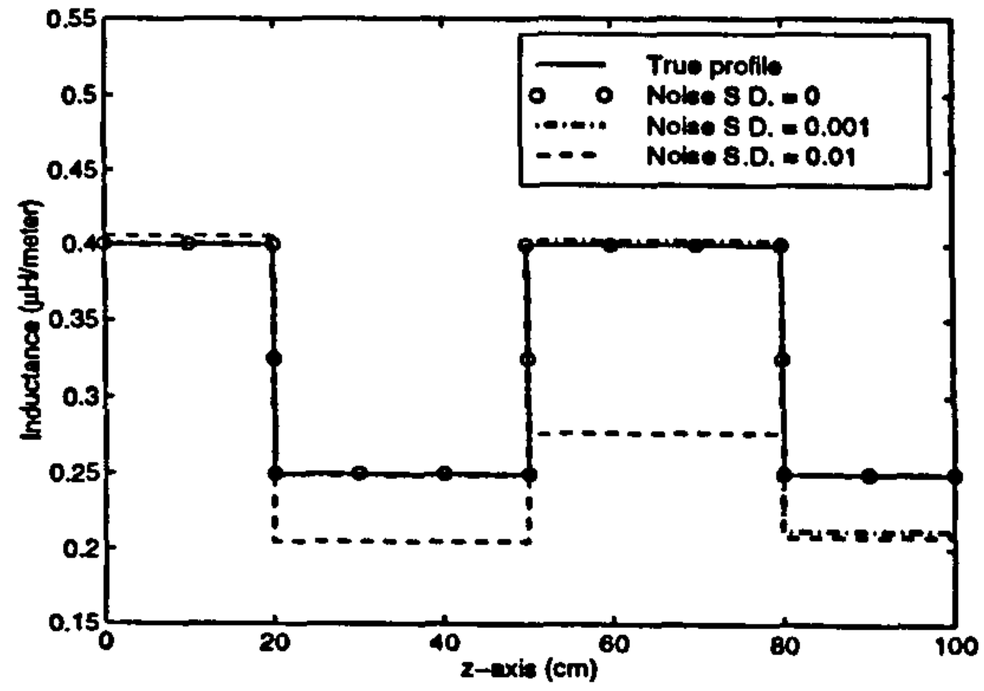

(d)

Figure 4.22: Simultaneous reconstruction of the (a) conductance G, (b) capacitance C, (c) resistance R and (d) inductance L.

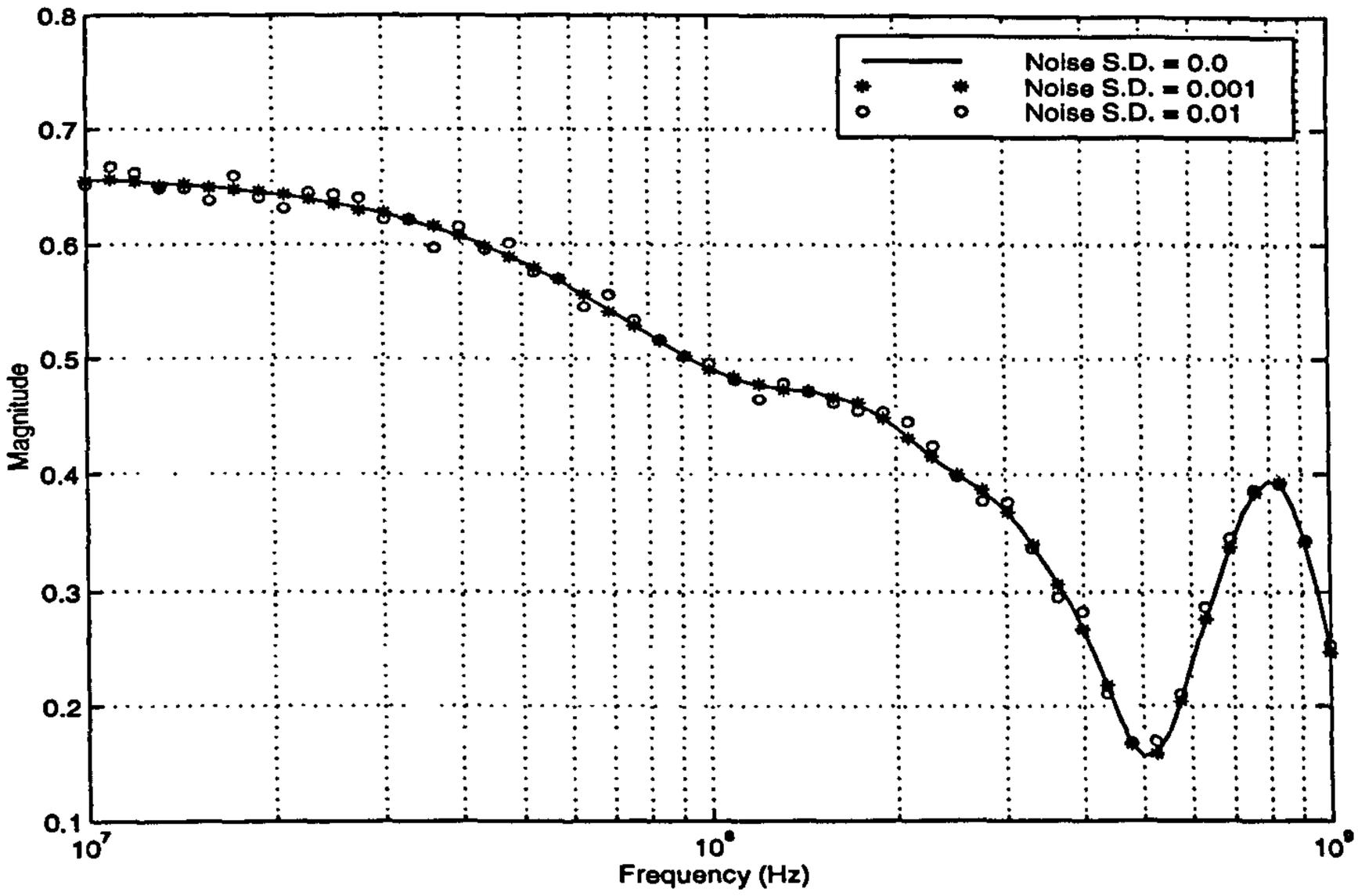

(a)

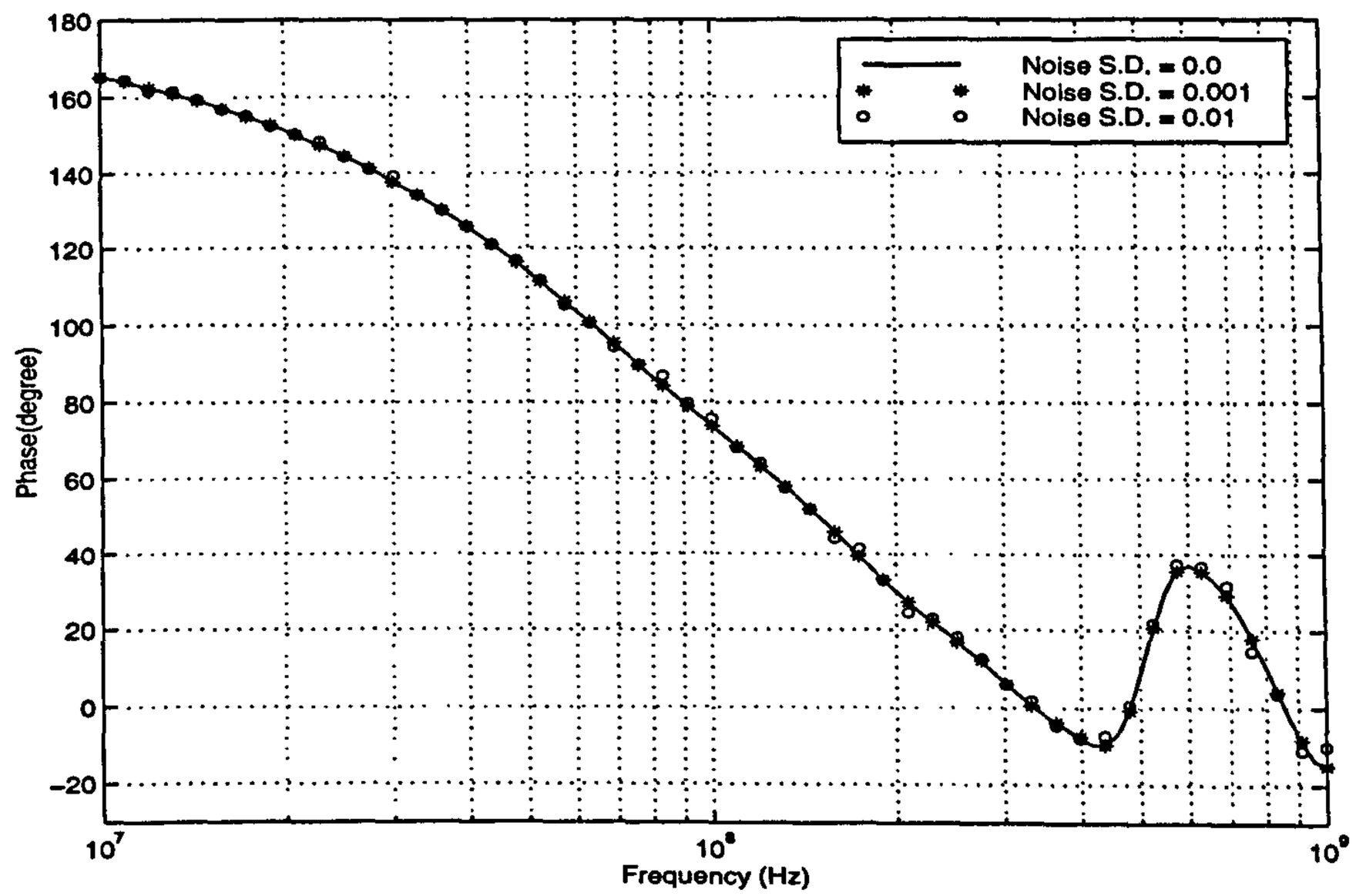

(b)

Figure 4.23: The reflection coefficients of the transmission line whose profile is shown by the solid lines in Fig. 4.22. The data is obtained at 101 frequencies with logarithmic spacing in the interval (10 MHz, 1 GHz).

4.5 A Hybrid Optimisation Algorithm

In spite of the good performance of the MLSL method, it has been recognised that the method may fail to find the true profile of some media with a relatively large number of layers (more than three layers). This happens especially when the deepest layer is unknown, the observed data is rather incomplete and/or there are wide bounds on the parameters. In an attempt to improve the efficiency and reliability of this approach, we have developed a hybrid method, which is the combination of the MLSL and a novel optimisation algorithm-the Adaptive Random Search (ARS). The hybrid method is referred as the MLSLARS and is based on heuristic reasoning. All examples attempted by us have demonstrated the superiority of the MLSLARS to the MLSL method.

4.5.1 Adaptive random search

The idea behind the ARS algorithm is to minimize a function derived from the transformation of the objective function f instead of minimizing f directly. Let g denote the transformed version of f. The value of $g(\mathbf{x})$ is the minimum obtained if a local optimisation method with initial point $\mathbf{x}$ is applied to the objective function f. The function g therefore acquires constant values in the attraction regions of the minima of f. Considering that the transformation Tr indicates the act of the local optimisation algorithm on function f and S_i^* denotes the attraction region of the minimum $f(\mathbf{x}_i^*)$, one can write

$$Tr : \mathbb{R} \to \mathbb{R} \text{ such that } Tr[f(\mathbf{x})] = g(\mathbf{x}) = f(\mathbf{x}_i^*) \quad , \mathbf{x} \in S_i^* \quad i = 1, \ldots, N_{min} \tag{4.5.1}$$

where N_{min} is the number of minima of f inside the feasible region. The regions $\{S_i^* \ , \ i = 1, \ldots, N_{min}\}$ are called the plateaus of the function $g(\mathbf{x})$.

Figure 4.24 illustrates the transformation for the function shown in Fig. 4.1. Another example is concerned with a function of two variables as shown

in Fig. 4.25(a) where three minima, $f(2,8) = 0$, $f(5,2) = 3$, $f(8,6) = 6$ are recognisable in the feasible region $\{(x_1, x_2) \mid 0 \leq x_1 \leq 10 \, , \, 0 \leq x_2 \leq 10\}$. Applying the modified-Newton method to $f(x_1, x_2)$, the function $g(x_1, x_2)$ is shown in Fig. 4.25(b).

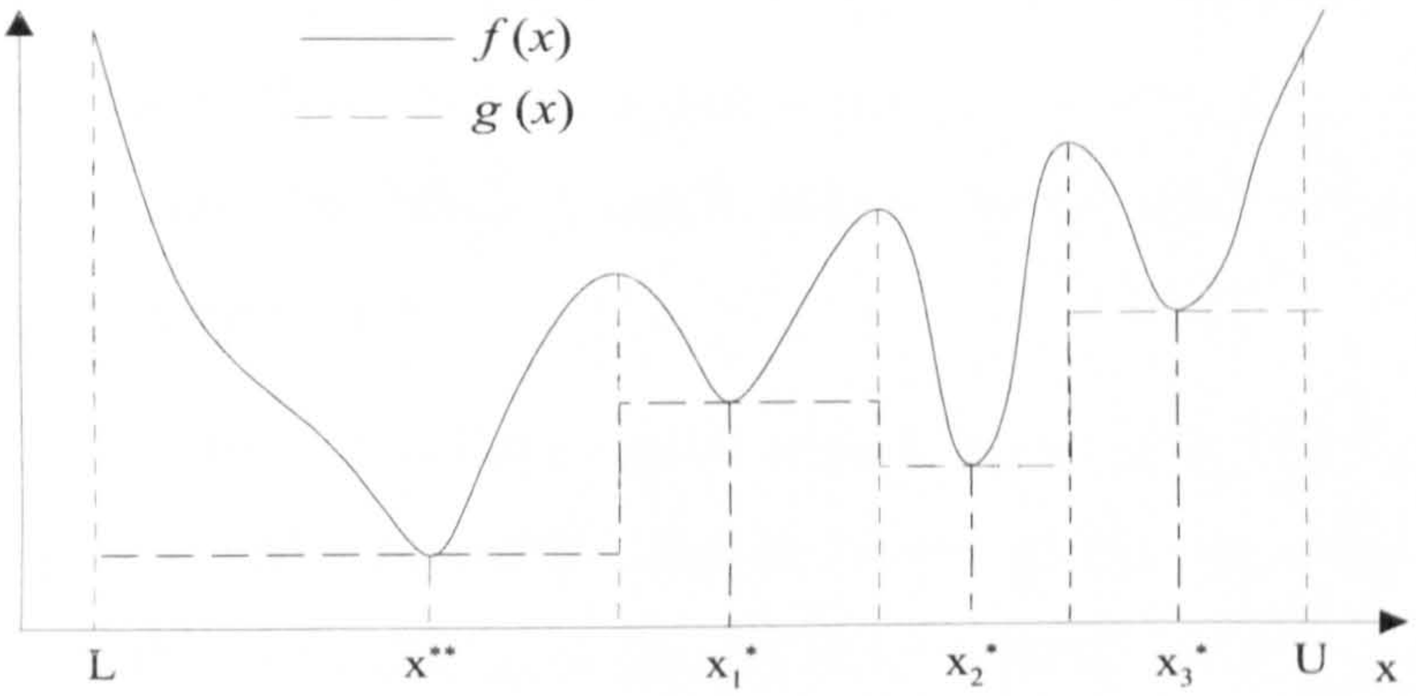

Figure 4.24: Transformation of a function in 1-dimensional space by a local optimisation algorithm.

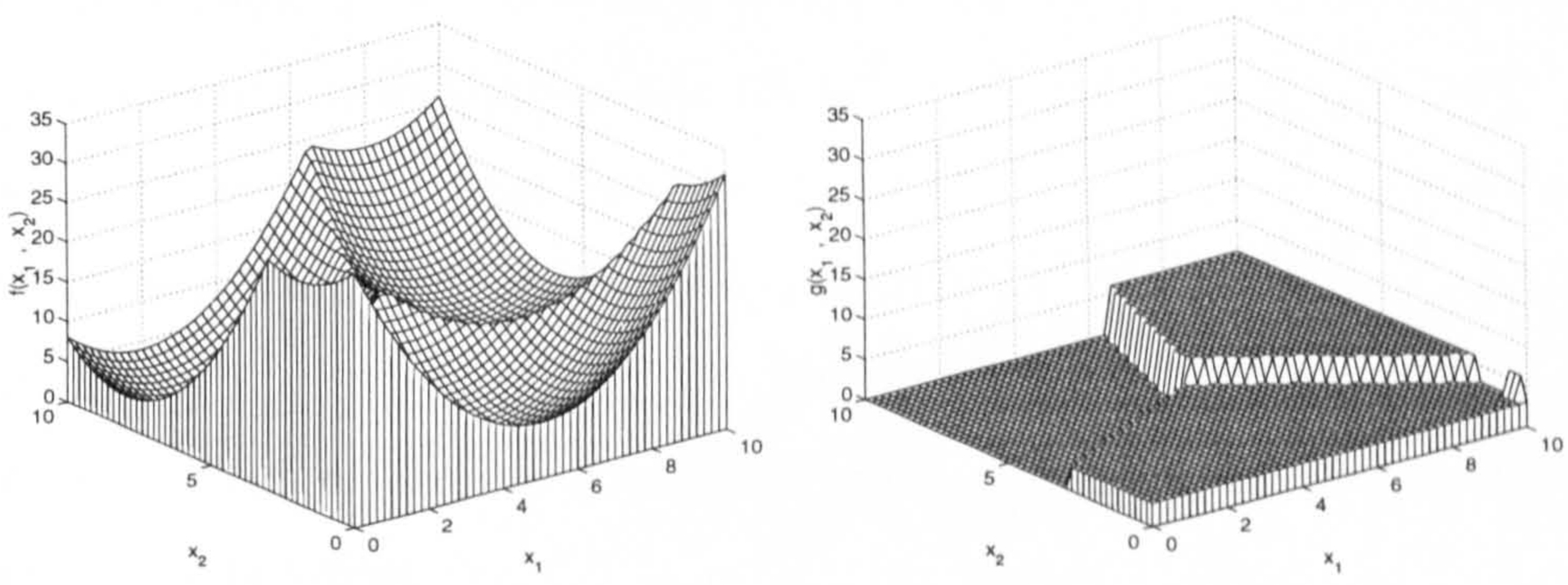

(a) (b)

Figure 4.25: (a) a function in 2-dimensional space. (b) The function g derived from that shown in part (a) using the modified-Newton method

Four properties can be summarised for the function g from these examples:

1. The number of the values of g is finite (N_{min}). For the second example, function g has three values $\{0, 3, 6\}$ corresponding to the minima of f.

---

2. The gradient of g is either zero or does not exist.

3. Function g has fewer local minima than f. Figure 4.24 shows that g has two local minima whereas f has four.

4. The attraction regions of g are wider than or equal to those of f. Figure 4.25 indicates that there is a single attraction region for the function g which covers the whole feasible region, being much wider than each attraction region of f.

The ARS algorithm is a local search aimed at reaching the lowest plateau of function g. The wider attraction region for the global minimum of g would result in the higher probability of finding it by a local search procedure. For a class of the objective functions, whose derived functions (g) possess one minimum (such as the second example), performing just one local search gives the global minimum. In general, the ARS method is required to be combined with a global search so that it does not get stuck in the basin of local minima. The global search actually explores the entire feasible region and provides an initial point (hopefully being in the attraction region of the global minimum of the function g) for the ARS algorithm. The global search can be accomplished by any global method like SA or GA. Nevertheless, MLSL is chosen due to its better performance. The interaction between ARS and MLSL will be discussed in the next subsection.

The ARS method is inspired from SA algorithms in which the control parameter is zero. With $T_c = 0$ in Equation (4.3.6), a movement in SA will be accepted only if the value of the objective function is lowered or unchanged. That is that the method always seeks the lower function values. To speed up the finding of a local minimum, ARS includes a new feature that makes it different from the SA with $T_c = 0$. The new feature is to modify adaptively the neighbourhood region. In order to describe under what conditions and how the modification will be carried out, we need to define the state of the ARS

THE APPLICATION OF GPR

algorithm at kth iteration as

$\mathbf{x}(k)$: the current point.

$\mathbf{x}^*(k)$: the minimizer of the objective function in the plateau that contains $\mathbf{x}(k)$.

$S_{\mathbf{x}(k)}$: the neighbourhood region of $\mathbf{x}(k)$. It is a hypercube specified by a central point $\mathbf{x}^c$ and a vector β (Equation (4.3.5)).

$B(k)$: the set of the eligible sides of $S_{\mathbf{x}(k)}$. The concept of the eligible sides will be discussed later on.

Suppose that the search is performed on a plateau $S^*(k)$ (current plateau) of the function g. The updating of $S_{\mathbf{x}(k)}$ has to satisfy the following three requirements:

1. A few samples (ideally one) are taken from each plateau. Searching on a plateau more than once does not offer any new information.

2. The probability of sampling a neighbourhood plateau of $S^*(k)$ with higher function value is reduced after detecting such a plateau.

3. Having transferred to a lower plateau, the neighbourhood plateaus of $S^*(k)$ are initially explored with equal probability.

To satisfy the first requirement, the size of $S_{\mathbf{x}(k)}$ is expanded while the new sample point is found to be on the current plateau. The expansion of $S_{\mathbf{x}(k)}$ is accomplished by increasing the length of its sides ($\beta(k)$). Not all sides are eligible to be updated at every iteration and only the selected sides will be expanded. If $\mathbf{y}$ denotes the new generated point that is on the current plateau at the kth iteration, the length of the eligible sides are increased as

$$\beta_i(k) = \left[1 + \frac{|y_i - x_i(k-1)|}{d_B\left(\mathbf{y}, \mathbf{x}(k-1)\right)}\right] \beta_i(k-1) \quad \text{if} \quad i \in B(k-1) \tag{4.5.2}$$

where d_B is the Euclidean distance in the subspace spanned by $B(k-1)$.

The eligible sides are determined in accordance with requirement 2. Initially containing all sides, the set of the eligible sides $B(k)$ is changed only when the

search finds a higher plateau. Suppose $\mathbf{y}$ is a new sample point on the higher plateau, i.e. $g(\mathbf{y}) > g(\mathbf{x}(k-1))$. Furthermore, suppose the jth side satisfies

$$|y_j - x_j(k-1)| \geq |y_i - x_i(k-1)| \quad , \quad i \in B(k-1) \tag{4.5.3}$$

Considering B^D denotes the set of all sides of $S_{\mathbf{x}(k)}$ (the objective function is defined in a D-dimensional space), the set of the eligible sides is updated by

$$B(k) = \begin{cases} B^D & \text{if the number of members of } B(k-1) \text{ is one} \\ B^e & \text{otherwise} \end{cases} \tag{4.5.4}$$

where B^e is a new set obtained by rejecting the jth side from $B(k-1)$. According to (4.5.4), when $B(k)$ is about to become empty, it will be set to B^D so that the process can be repeated.

Having detected a higher plateau, the neighbourhood region is also moved away from this plateau. The movement is in the opposite direction of vector $\mathbf{y} - \mathbf{x}(k-1)$ so that the generated point $\mathbf{y}$ is located at the boundary of the displaced neighbourhood region. Suppose $d_{\mathbf{y}}$ denotes the length of the line that connects point $\mathbf{y}$ to the boundary of the neighbourhood region $S_{\mathbf{x}(k-1)}$ in the direction of vector $\mathbf{y} - \mathbf{x}(k-1)$. The movement of the neighbourhood region is performed by updating its central point as

$$\mathbf{x}^c(k) = \mathbf{x}^c(k-1) - \frac{\mathbf{y} - \mathbf{x}(k-1)}{|\mathbf{y} - \mathbf{x}(k-1)|}\, d_{\mathbf{y}} \tag{4.5.5}$$

where $|\mathbf{y} - \mathbf{x}(k-1)|$ is the length of the vector $\mathbf{y} - \mathbf{x}(k-1)$.

Once a lower plateau is found, the search will be transferred to this plateau. The neighbourhood region should be resized with respect to the extensions of the lower plateau in different dimensions so as to satisfy the third requirement. These extensions are roughly proportional to the inverse of the derivative (sensitivity) of the objective function f. This can be understood from figure 4.25 by considering the plateau $g(x_1, x_2) = 3$. The function $f(x_1, x_2)$ in this plateau has less sensitivity to x_1 that corresponds to the dimension in which $g(x_1, x_2)$

has more extension. Let ν_i represent the relative extension of the lower plateau in the ith dimension. An estimate of ν_i is given by

$$\nu_i = \left[\frac{1}{N_\nu} \sum_{j=1}^{N_\nu} \left| \frac{\partial f(\mathbf{x}_j)}{\partial x_i} \right| \right]^{-1} \quad , \qquad i = 1, \ldots, D \tag{4.5.6}$$

where $\mathbf{x}_j$ is a randomly selected point in the vicinity of the minimum point of the lower plateau and N_ν is the number of these points. Assuming ν_{max} denotes the maximum relative extension, the size of $S_{\mathbf{x}(k)}$ is determined by

$$\beta_i(k) = \widehat{sf} \, \frac{\nu_i}{\nu_{max}} \quad , \qquad i = 1, \ldots, D \tag{4.5.7}$$

where $\widehat{sf}$ is a scaling factor. In the implementation of the ARS, $\beta_i(k)$ satisfies a minimum limit, i.e. $\beta_i(k) \geq \beta_i^{min}$. Thus, if the value provided by (4.5.7) is less than this limit, $\beta_i(k) = \beta_i^{min}$.

For the case of the 1D EIS problem, one can notice that the scaling factor should be different for the permittivity, conductivity, permeability and thickness of layers. In addition, the scaling factor of a parameter ought to be chosen with respect to the value of that parameter. Suppose sf_p is the scaling factor of a parameter p where $p = \sigma$, ϵ, μ or h. In the ARS algorithm, $\widehat{sf}_p$ is determined by

$$\widehat{sf}_p = c_p \, p \tag{4.5.8}$$

c_p is a constant set to:

$$c_\sigma = 0.4 \, , \; c_\epsilon = 0.25 \, , \; c_\mu = 0.25 \, , \; c_h = 0.5$$

in our reconstruction examples. The scaling factor in (4.5.7) is calculated from (4.5.8) for the parameter corresponding to ν_{max}.

According to these explanations, the kth iteration of the ARS algorithm can be implemented as follows:

1. Generate a sample point $\mathbf{y}$ and obtain $g(\mathbf{y})$.

---

2. Determine the new state of the algorithm. There are three cases:

   i) If $g[\mathbf{x}(k-1)] = g(\mathbf{y})$ then $\mathbf{x}(k) = \mathbf{y}$, $\mathbf{x}^*(k) = \mathbf{x}^*(k-1)$, $B(k) = B(k-1)$, $\mathbf{x}^c(k) = \mathbf{y}$ and the neighbourhood region is expanded in terms of Equation (4.5.2).

   ii) If $g[\mathbf{x}(k-1)] < g(\mathbf{y})$ then $\mathbf{x}(k) = \mathbf{x}(k-1)$, $\mathbf{x}^*(k) = \mathbf{x}^*(k-1)$, $B(k)$ is updated using (4.5.4), and $\mathbf{x}^c(k)$ is determined by (4.5.5) (i.e. the neighbourhood region is moved but its size remains unchanged).

   iii) If $g[\mathbf{x}(k-1)] > g(\mathbf{y})$ then $\mathbf{x}(k) = \mathbf{x}^*$, $\mathbf{x}^*(k) = \mathbf{x}^*$, $B(k) = B^D$, $\mathbf{x}^c(k) = \mathbf{x}^*$ and the size of the neighbourhood region is obtained using (4.5.7). Note that $\mathbf{x}^*$ is the minimum point of the new lower plateau specified by $g(\mathbf{y})$.

Under condition that the ARS algorithm does not find any lower plateau (for instance, gets stuck in a local minimum of g), the neighbourhood region is gradually expanded, approaching to cover the entire feasible region. In this case, the algorithm is converted to Multistart.

4.5.2 The MLSLARS method

As mentioned before, the ARS method can be combined with the MLSL to prevent the ARS from getting stuck in a local minimum of function g. The resultant method, the MLSLARS, consists of three stages distinguishable by the Bayesian estimate (4.4.3). This estimation gives the portion of the feasible region covered by the basins of the local minima found by the MLSL. Let x^* be the minimizer obtained by the MLSL algorithm. The Bayesian estimate (4.4.3) can be used to assess the level of the certainty that x^* lies inside the attraction region of the global minimum of function g. One can therefore decide whether to start the ARS algorithm from x^* using this estimation.

The MLSLARS method includes the following stages:

STAGE 1:

THE APPLICATION OF GPR

1. Initialise the MLSL algorithm.

2. Run MLSL until the Bayesian estimate (4.4.3) is less than a constant value α_1

STAGE 2:

3. Initialise the state of the ARS algorithm. Consider $\mathbf{x}^*$ is the minimum solution provided by the MLSL algorithm and $k = 0$. The state of the ARS is determined by: $\mathbf{x}(k) = \mathbf{x}^*$, $\mathbf{x}^*(k) = \mathbf{x}^*$, $B(k) = B^D$, $\mathbf{x}^c(k) = \mathbf{x}^*$ and β_k is obtained using (4.5.7).

4. Perform one iteration of the ARS.

5. Perform one iteration of the MLSL algorithm.

6. If the minimum value yielded from the MLSL algorithm is less than that of the ARS, go to step 3.

7. GO to step 4 if the estimate (4.4.3) is less than another constant α_2.

STAGE 3:

8. Run the ARS algorithm until the stop condition is satisfied.

Stage 2 may be removed; but the reconstruction examples showed that the inclusion of this stage enhances the efficiency of the algorithm.

In order to compare the performance of the MLSLARS with the MLSL, two examples are given. The constants α_1 and α_2 are selected to be 0.75 and 0.95 respectively.

Example 4.9. The comparison of the MLSL with the MLSLARS for the simultaneous reconstruction of the permittivity, conductivity and permeability profiles are considered in this example. As shown in Fig. 4.26(a), the medium is the same as the one in Example 4.6 except that the layers are magnetic. It

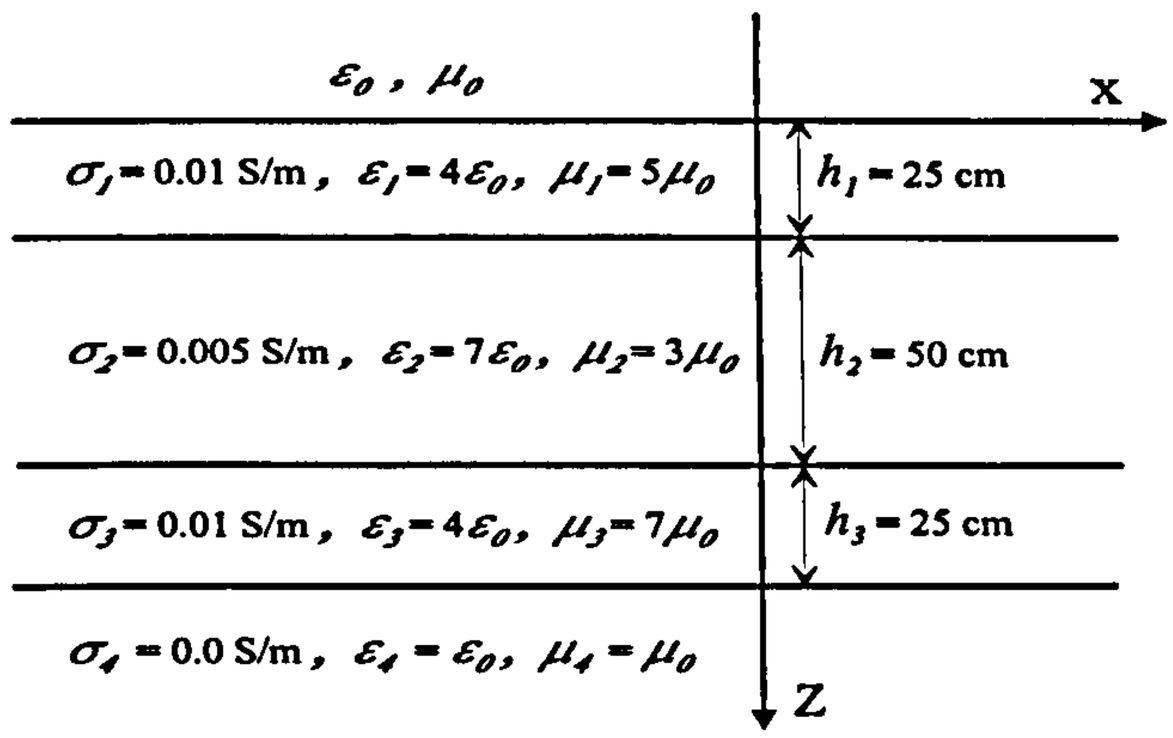

(a)

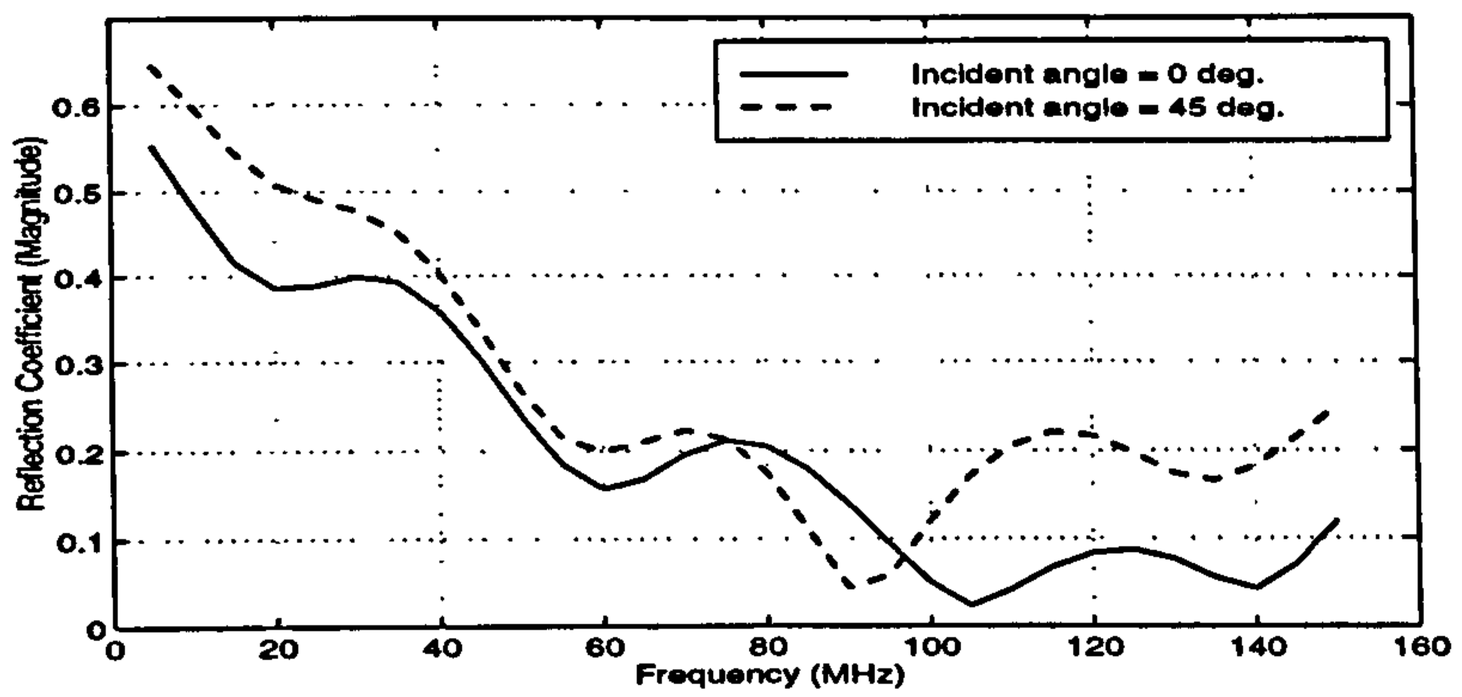

(b)

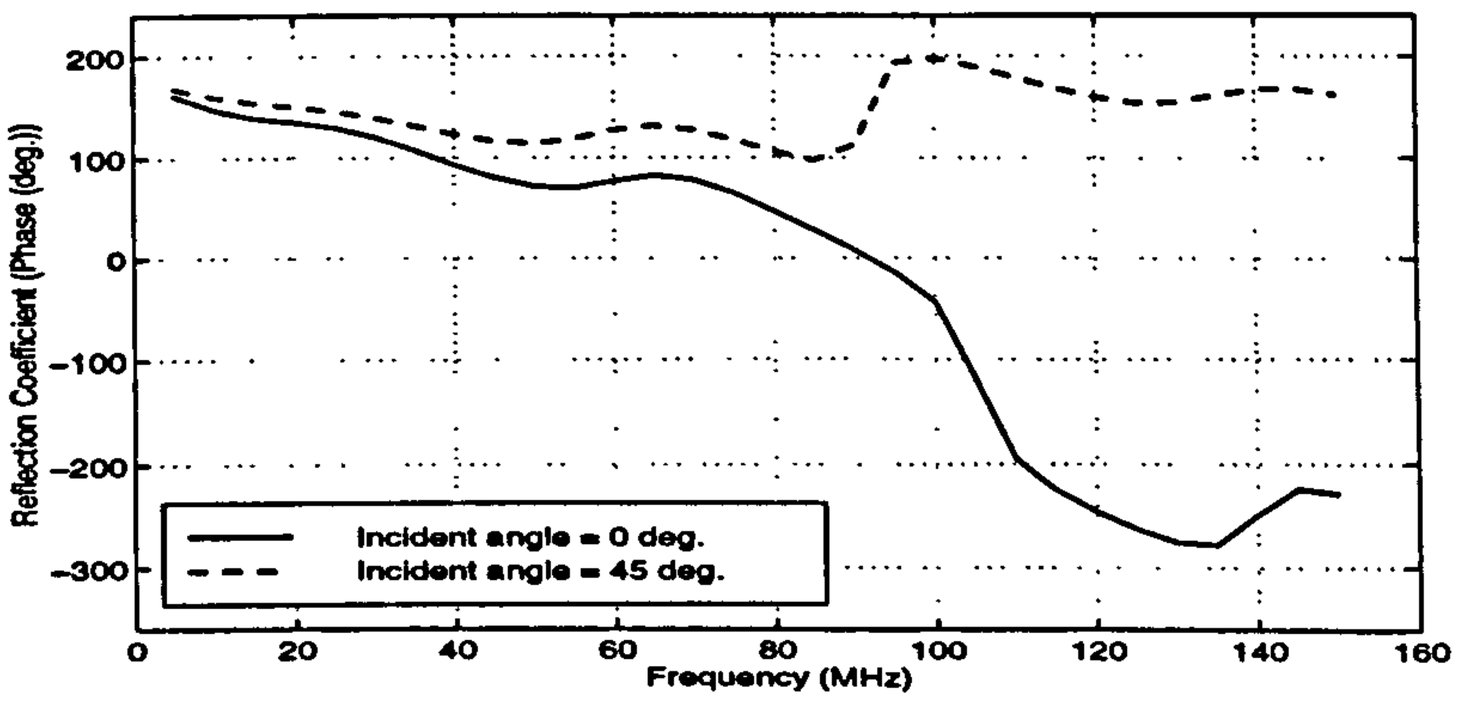

(c)

Figure 4.26: (a) A 4-layer magnetic medium and (b), (c) its reflection coefficients synthesised for a TE wave incidence at 30 frequencies equally spaced in the interval [5 MHz, 150 MHz] and at two incident angles $\theta = 0°$ and $\theta = 45°$.

is also assumed that the properties of the last layer are unknown; thus, the MSE function has 15 variables. According to the necessary condition (Chapter 3), the scattering data has to be obtained at two incident angles. The data generated by the simulation of the reflectivity formulation are illustrated in Fig. 4.26(b) and 4.26(c).

The parameters of N_p and ξ in the MLSL method are set to 1000 and 0.002 respectively and the search region S is selected as

$$\begin{aligned} &0 \leq \sigma_m \leq 0.5 \text{ S/m} , \ 1 \leq \epsilon_{rm} \leq 50 , \quad 1 \leq \mu_{rm} \leq 20 \\ &0 \leq h_m \leq 100 \text{ cm} \qquad\qquad\qquad\qquad\quad m = 1, 2, 3, 4 \end{aligned} \tag{4.5.9}$$

Ten runs were conducted and the final value of the MSE obtained by the MLSL and the MLSLARS are given in Table 4.6 after 200000 function evaluations. The MLSL method found the global minimum just once, whereas the

Table 4.6: The final MSE values attained for 10 runs of the MLSL and MLSLARS methods when reconstructing the profile of the magnetic medium. Each run involves 200000 function evaluations.

MLSL	Final MSE	1.6e-4	0.0002	1.8e-5	0.0017	0.0017
		0.0002	0.0	0.0002	0.0002	2.3e-4
	No. of Minima found	12	13	15	8	11
		12	12	14	13	13
MLSLARS	Final MSE	0.0	8.3e-4	6.9e-5	0.0	1.5e-4
		0.0	7.5e-5	0.0	0.0	1.9e-4
	No. of Minima found	18	16	19	27	15
		20	20	25	27	20

MLSLARS found it 5 times. A considerable improvement in the reliability has therefore been achieved. Moreover, Fig. 4.27 shows that the efficiency is improved, as the MLSLARS method found the global minimum with fewer function evaluations for the best convergence. The resultant profiles are illustrated in Fig. 4.28 where the simultaneous reconstruction of all electromagnetic parameters is demonstrated. It is noteworthy that this simultaneous

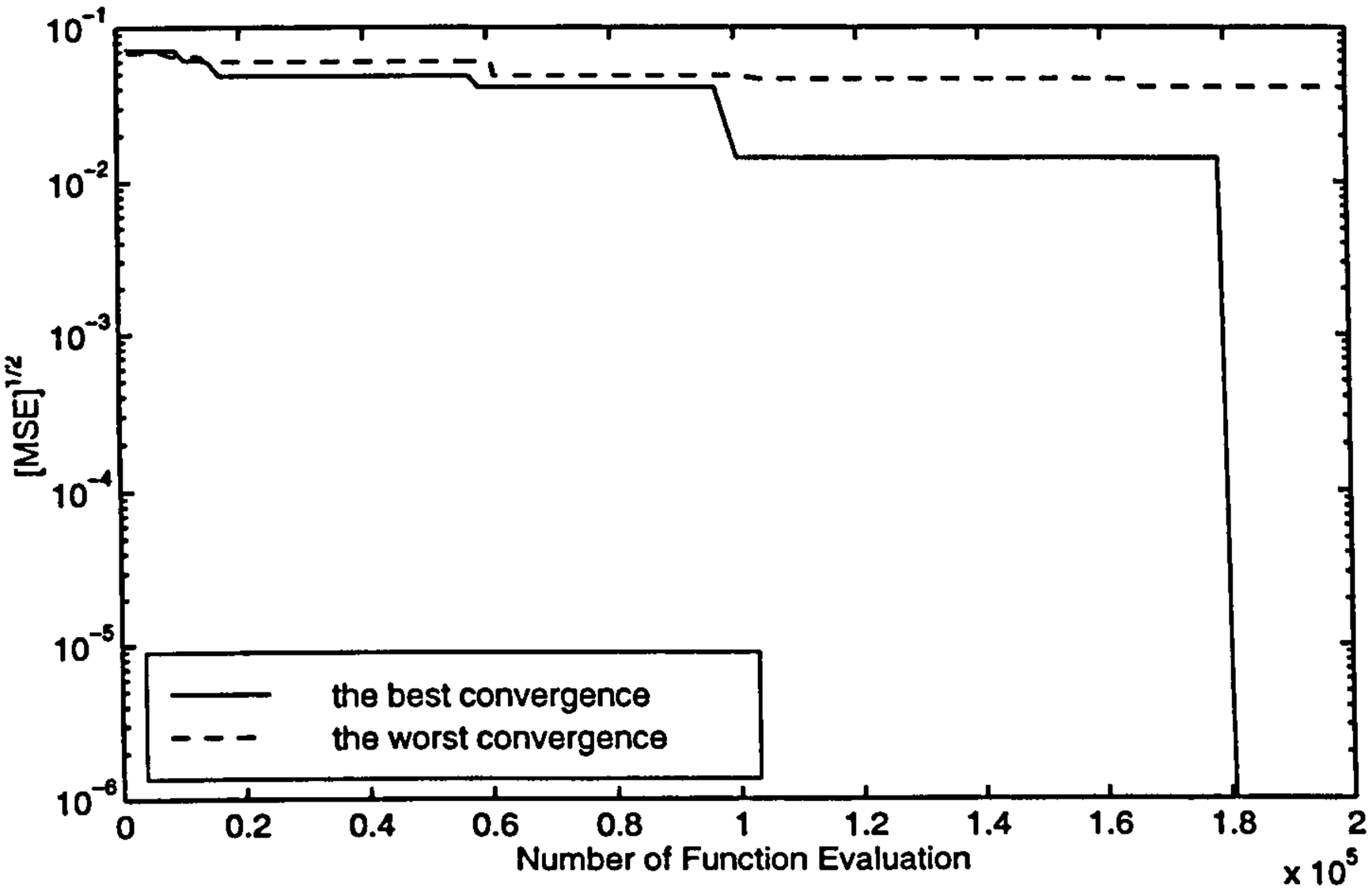

(a)

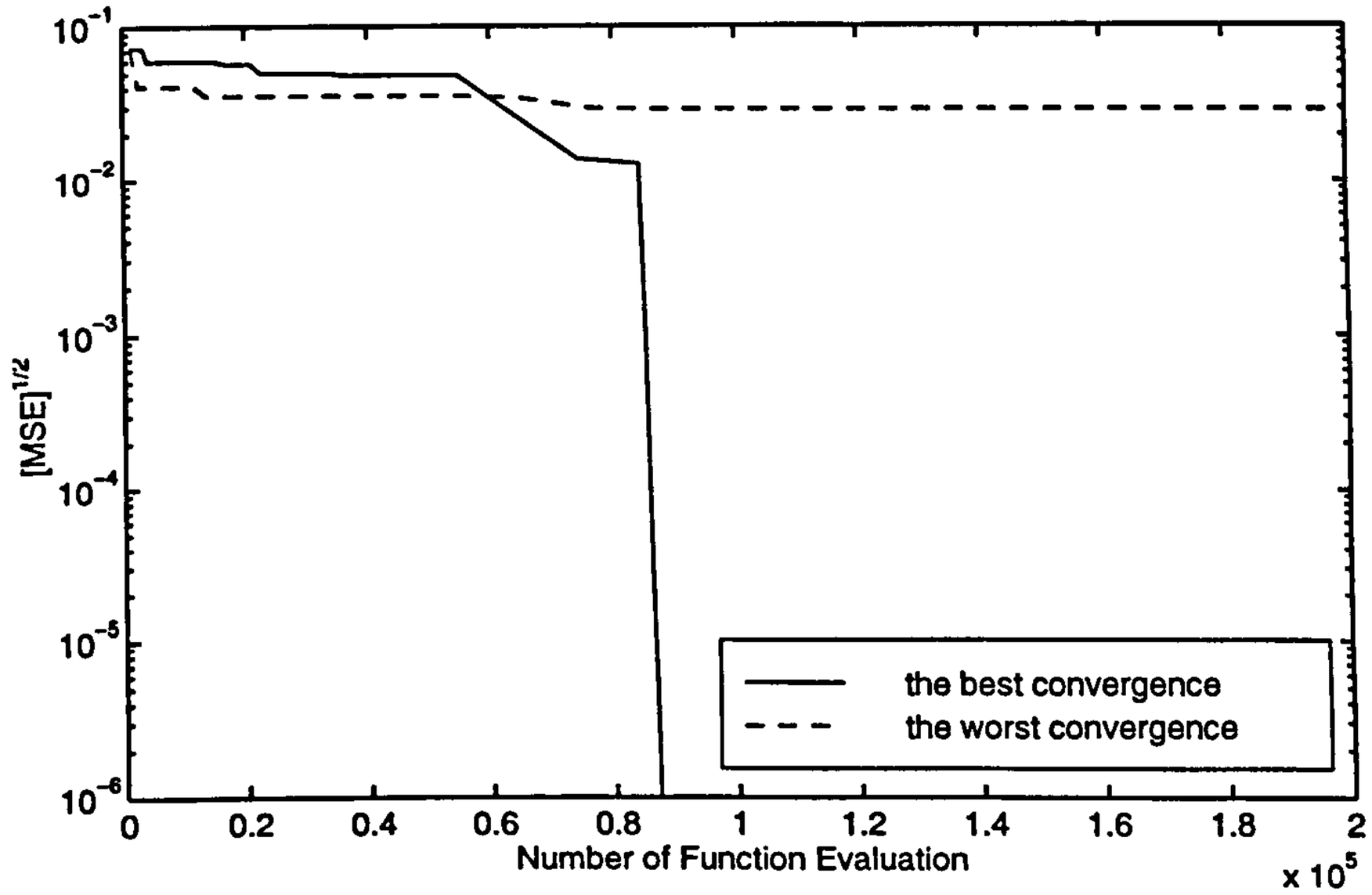

(b)

Figure 4.27: The minimization of the MSE function by (a) MLSL and (b) MLSLARS for the best and worst convergence within 10 runs. The medium and the used scattering data are depicted in Fig. 4.26.

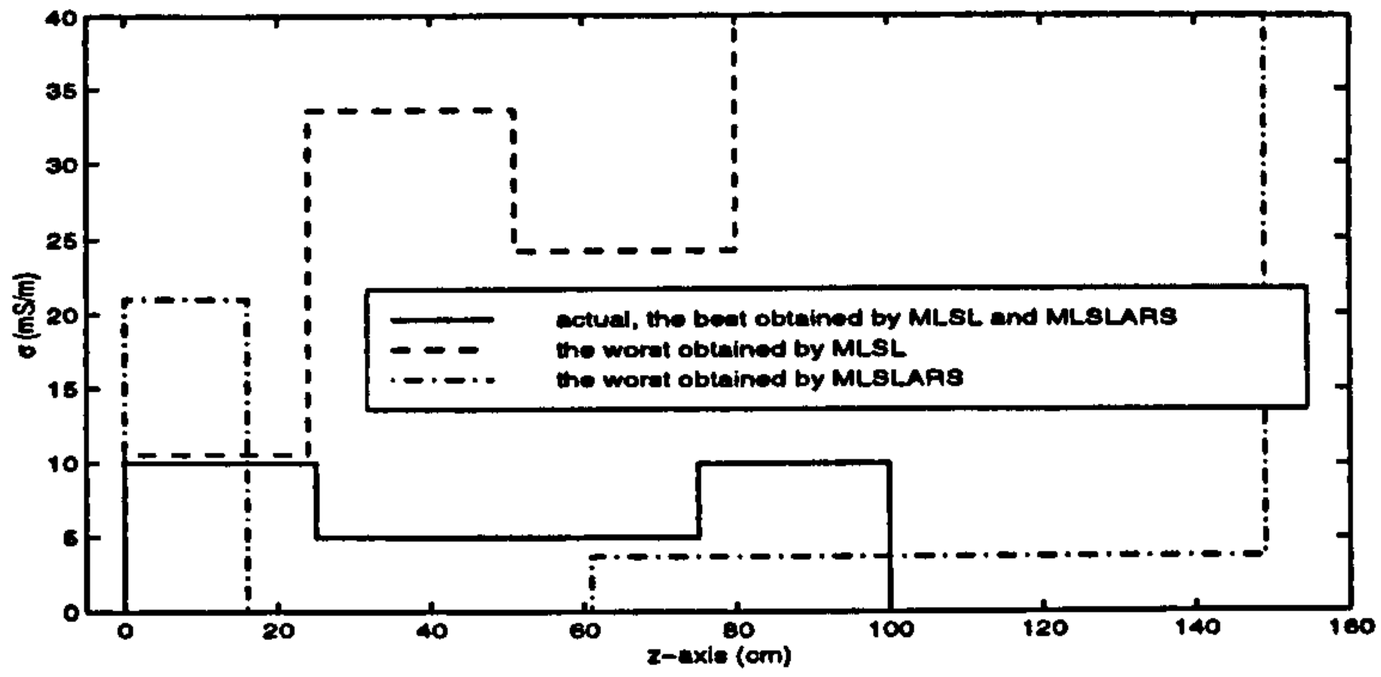

(a)

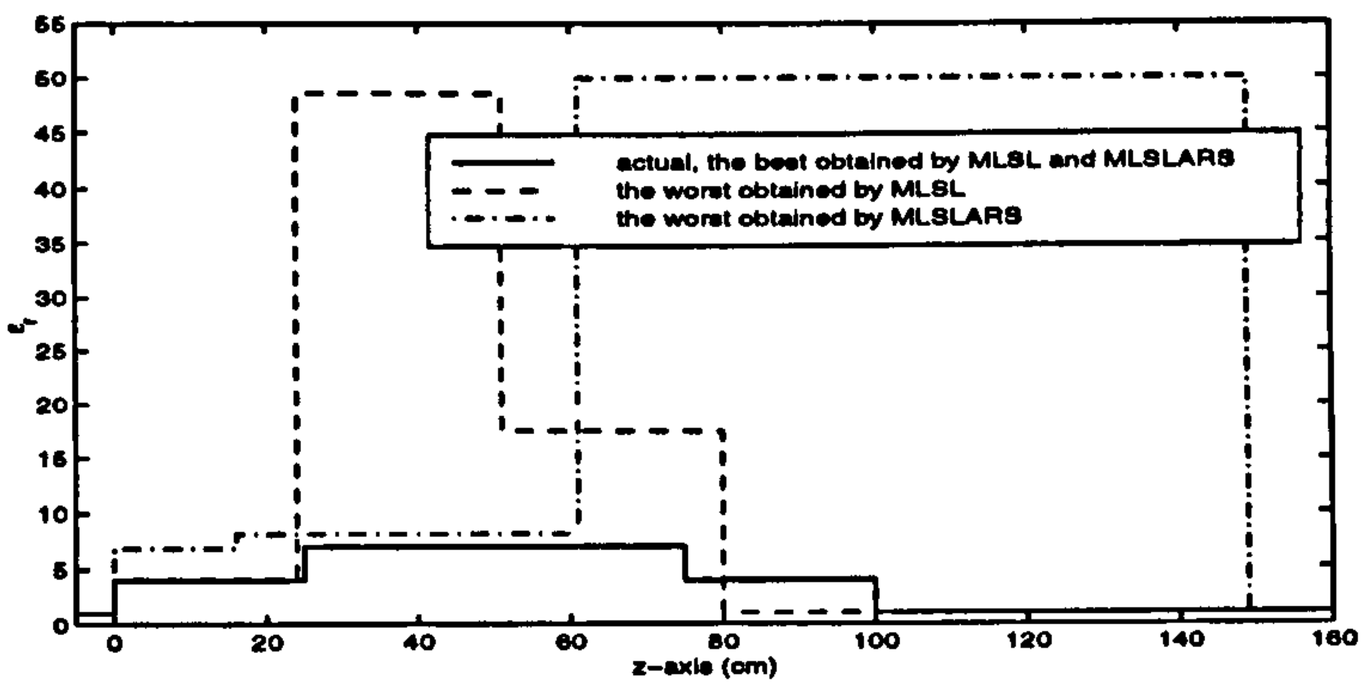

(b)

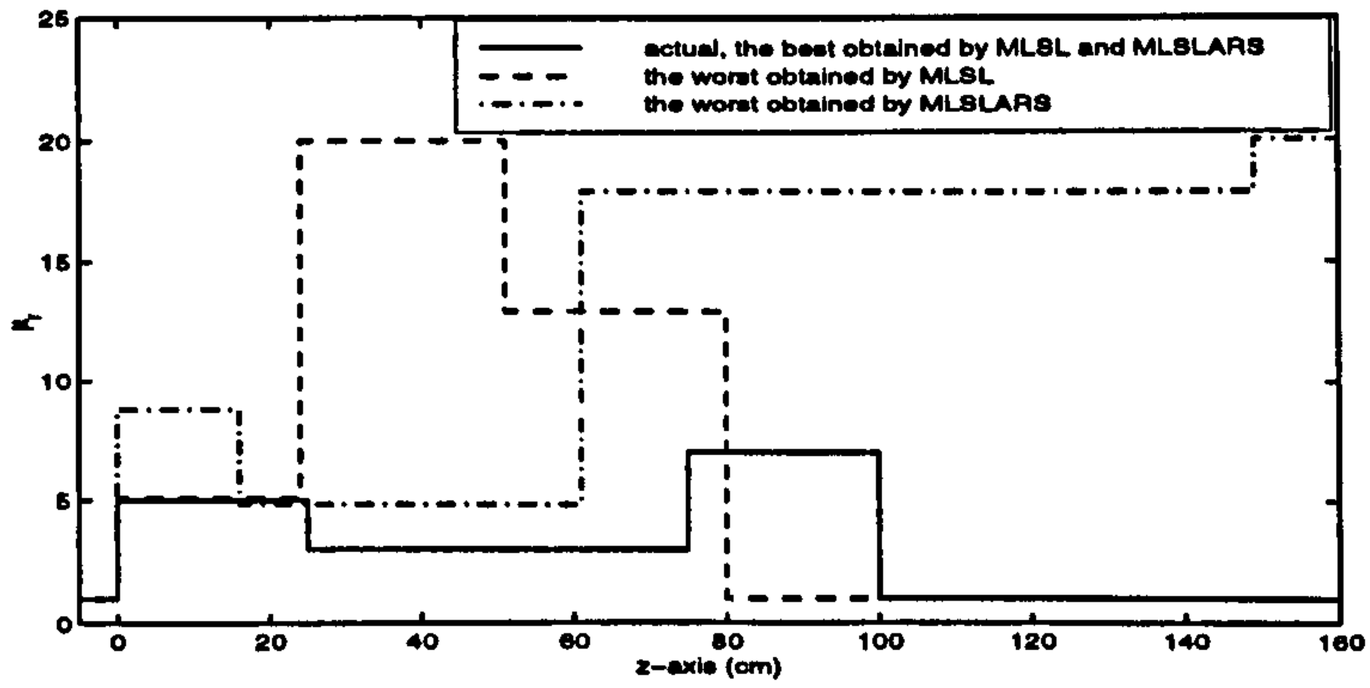

(c)

Figure 4.28: The simultaneous reconstruction of the (a) conductivity, (b) permittivity and (c) permeability profiles of the 4-layer magnetic medium by the MLSL and MLSLARS using the reflection coefficients at two incident angles. The best profiles obtained by the MLSL and MLSLARS coincide with the actual ones.

reconstruction has not been dealt with before in any other work. Using the data for both TE wave and TM wave incidences or using the data at two incident angles, some authors [21], [22], [30], [63], [64] have only considered the simultaneous reconstruction of the permittivity and conductivity.

Example 4.10. This example deals with finding the parameters of a continuous medium, the profile of which is shown by the solid line in Fig. 4.29. It is the profile of a road pavement. The permittivity of the pavement has been experimentally measured [61] and its conductivity is taken from measurements for asphalt and concrete. The two transition regions, that between asphalt1 and asphalt2, and that between asphalt2 and concrete, have properties described by a linear function of depth. This linear function gives a good approximation to the real situation. The line stared in Fig. 4.29 shows a discontinuous 3-layer version of this profile. As illustrated in Fig. 4.30, the reflection coefficients of the 3-layer medium and the continuous medium are obtained for the normal incidence by dividing the transition parts into 20 steps. The scattering data for the 3-layer medium is not used for the reconstruction and it is referred to later to justify some facts.

At first, the reconstruction is carried out by using the data at 21 frequencies over the band [250 MHz, 450 MHz] with linear spacing. The feasible region is set to

$$0 \le \sigma_m \le 0.2 \text{ S/m}\,,\ 1 \le \epsilon_{rm} \le 25\,,\quad 0 \le h_m \le 25 \text{ cm} \qquad m = 1, 2, \ldots, M \tag{4.5.10}$$

Assuming the number of layers (M) is 3, the results are given in Table 4.7. An identical performance can be seen for the MLSL and the MLSLARS in this example. Note that the value of the MSE function at the global minimum point is unknown. In other words, the value 3.5e-11 is not guaranteed to be the global minimum. However, since both algorithms have reached this value in all 10 runs, it is likely to be the global minimum. The profiles obtained are

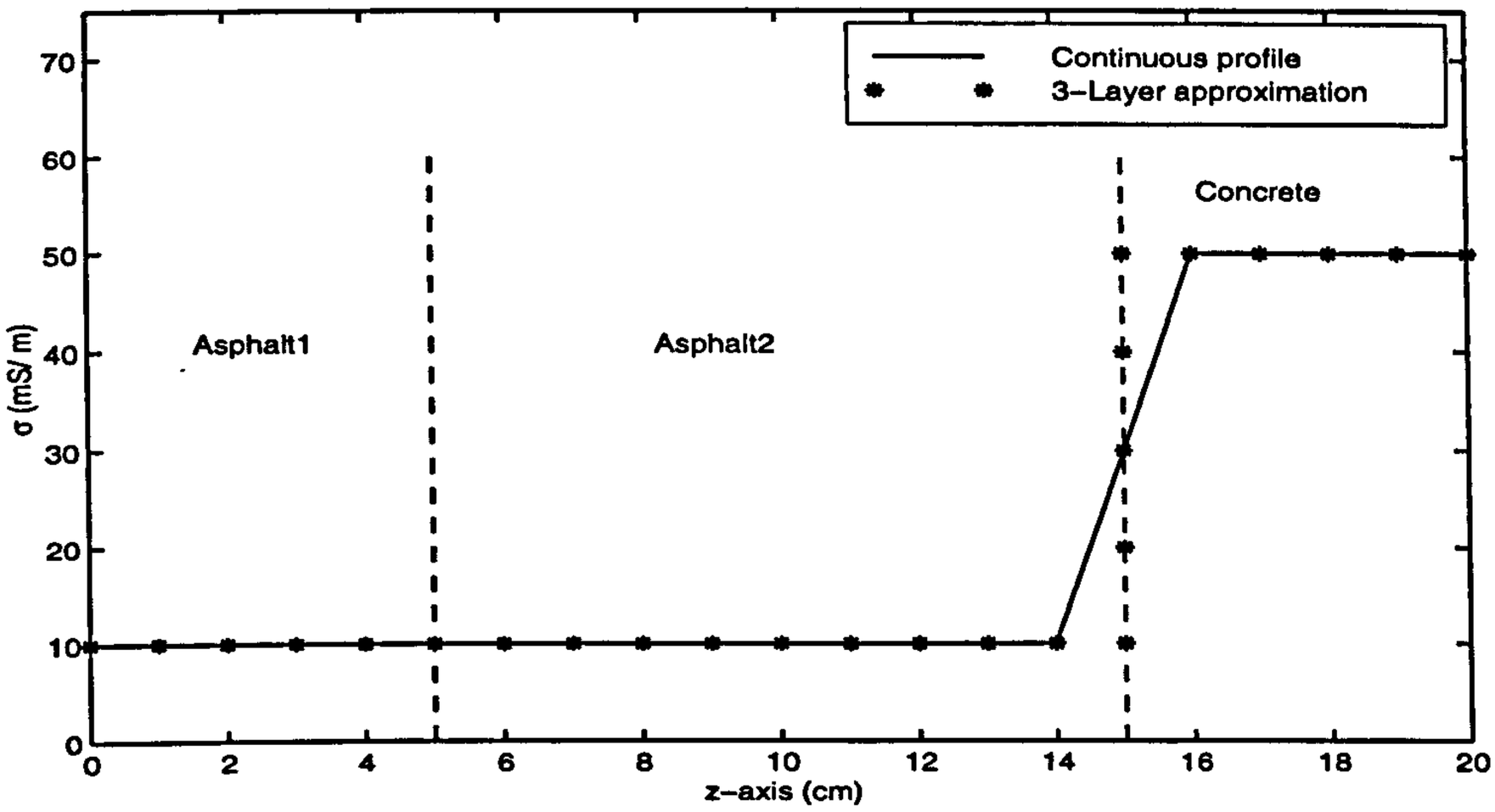

(a)

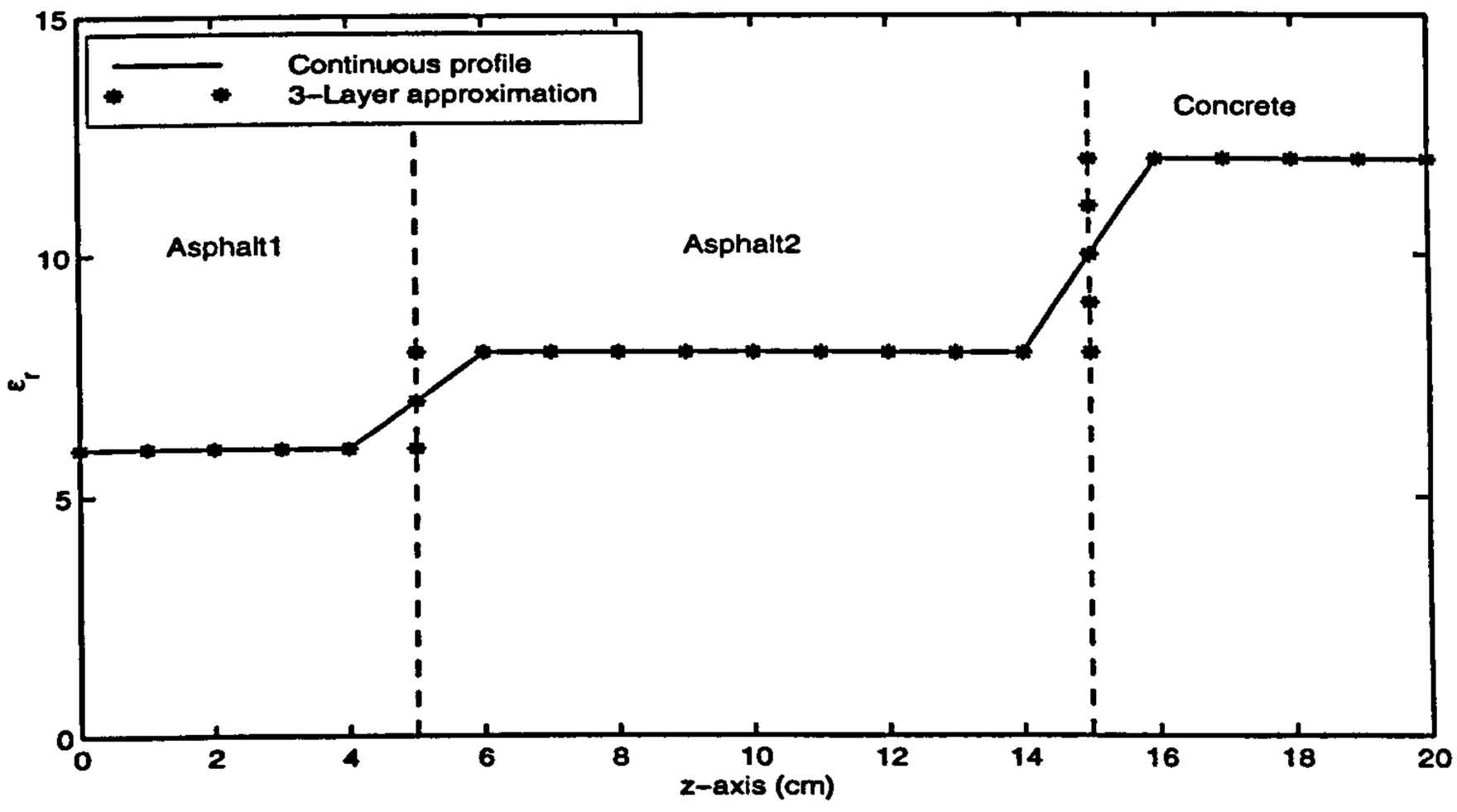

(b)

Figure 4.29: The (a) conductivity and (b) permittivity profile of a typical 3-layer road pavement.

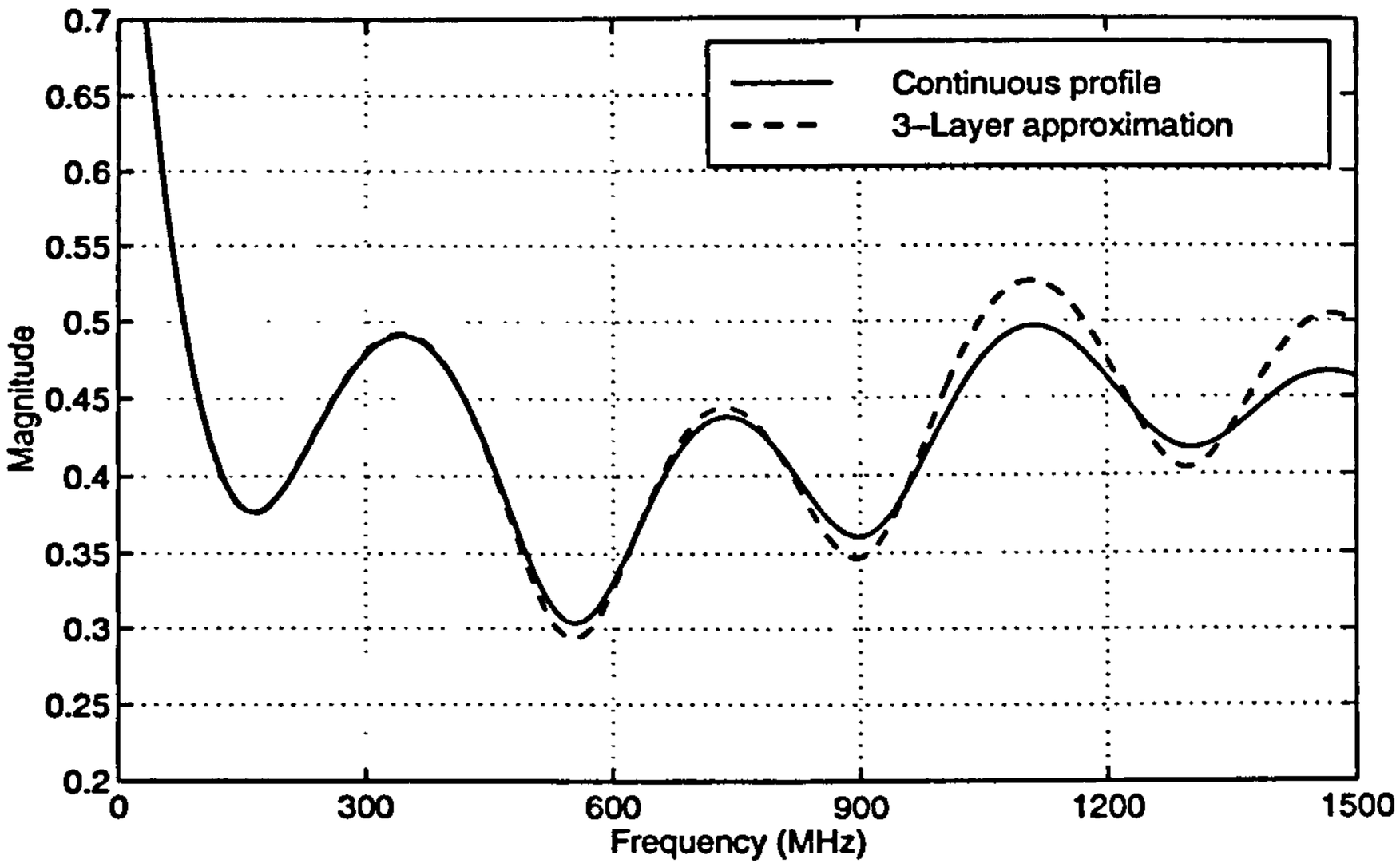

(a)

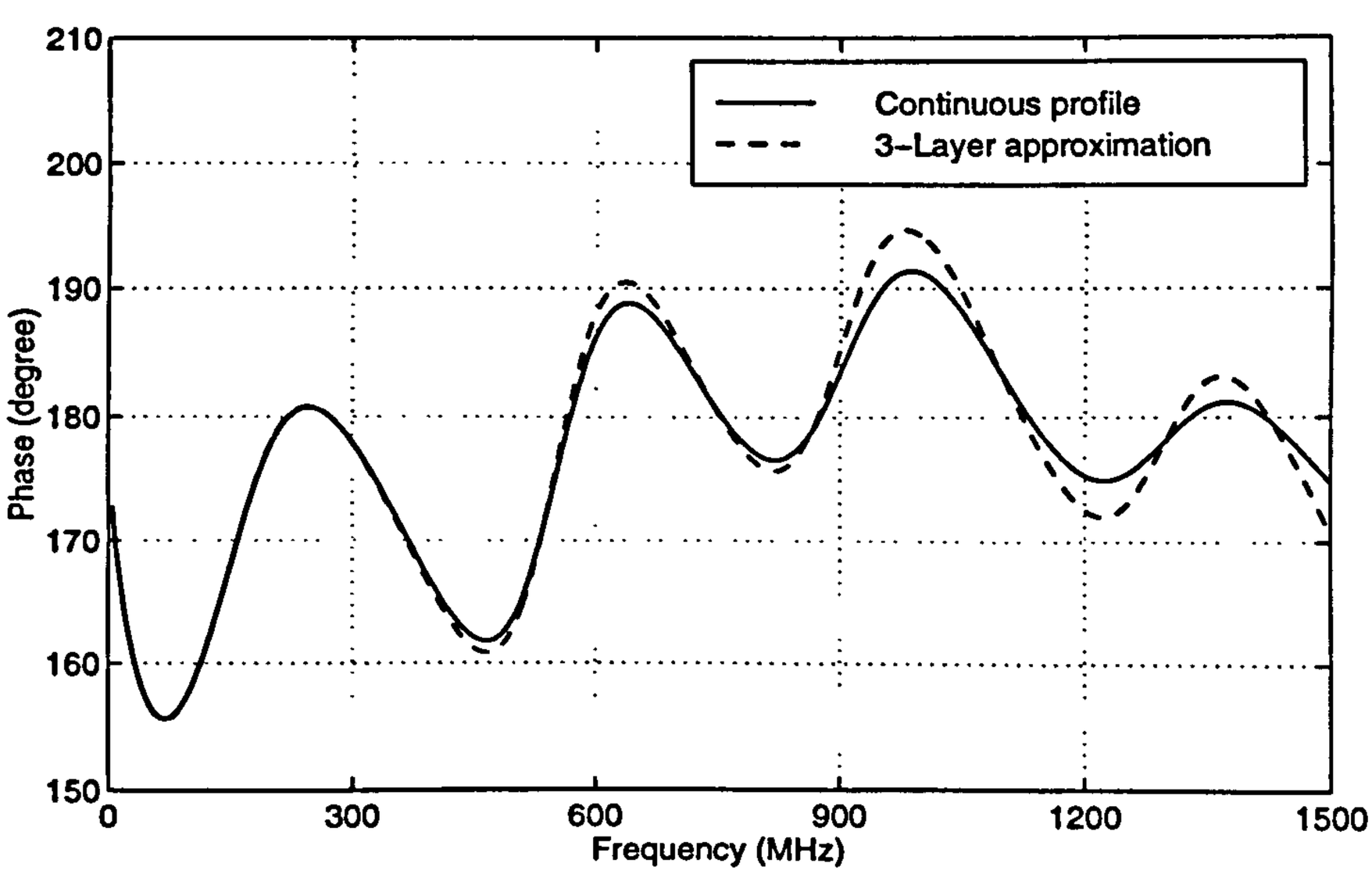

(b)

Figure 4.30: The reflection coefficients of the profiles shown in Fig. 4.29 for the normal incidence.

Table 4.7: The resultant MSE using the MLSL and MLSLARS methods for reconstructing the profile of the continuous medium from the reflection coefficients obtained in the interval [250 MHz, 450 MHz] when $M = 3$.

Number of function eval. = 25000, $N_p = 100$, $\xi = 0.05$						
MLSL	Final MSE	3.5e-11	3.5e-11	3.5e-11	3.5e-11	3.5e-11
		3.5e-11	3.5e-11	3.5e-11	3.5e-11	3.5e-11
	No. of Minima found	17	15	16	14	13
		15	20	18	18	14
MLSLARS	Final MSE	3.5e-11	3.5e-11	3.5e-11	3.5e-11	3.5e-11
		3.5e-11	3.5e-11	3.5e-11	3.5e-11	3.5e-11
	No. of Minima found	12	15	16	15	13
		15	15	17	15	15

shown in Fig. 4.31.

It can be demonstrated that the data in the frequency range [250 MHz, 450 MHz] is not adequate to approximate the continuous profile with a 5-layer medium. This can be justified from Fig. 4.30 where there exist slight differences between the reflection coefficients of the 3-layer and continuous mediums over the frequency band [250 MHz, 450 MHz]. The data at large wavelengths offers low resolution, which means the detailed variations of a medium in spatial dimensions cannot be extracted using the low frequency data. When the medium is assumed to have 5 layers and the data in the interval [250 MHz, 450 MHz] is used, it has been found that the MSE function has several well-separated minimizers with the MSE values close to the global minimum. This implies an instability that means large changes in the parameters of the 5-layer medium can correspond to very small changes in the reflection coefficients over the band [250 MHz, 450 MHz]. As a result, the inverse problem is nearly ill-posed in such a circumstance.

The reconstruction for $M = 5$ with the bounds (4.5.10) are therefore performed employing the reflection coefficients at 21 frequencies equally spaced in the interval [650 MHz, 1150 MHz]. The resultant MSE are given in Table 4.8

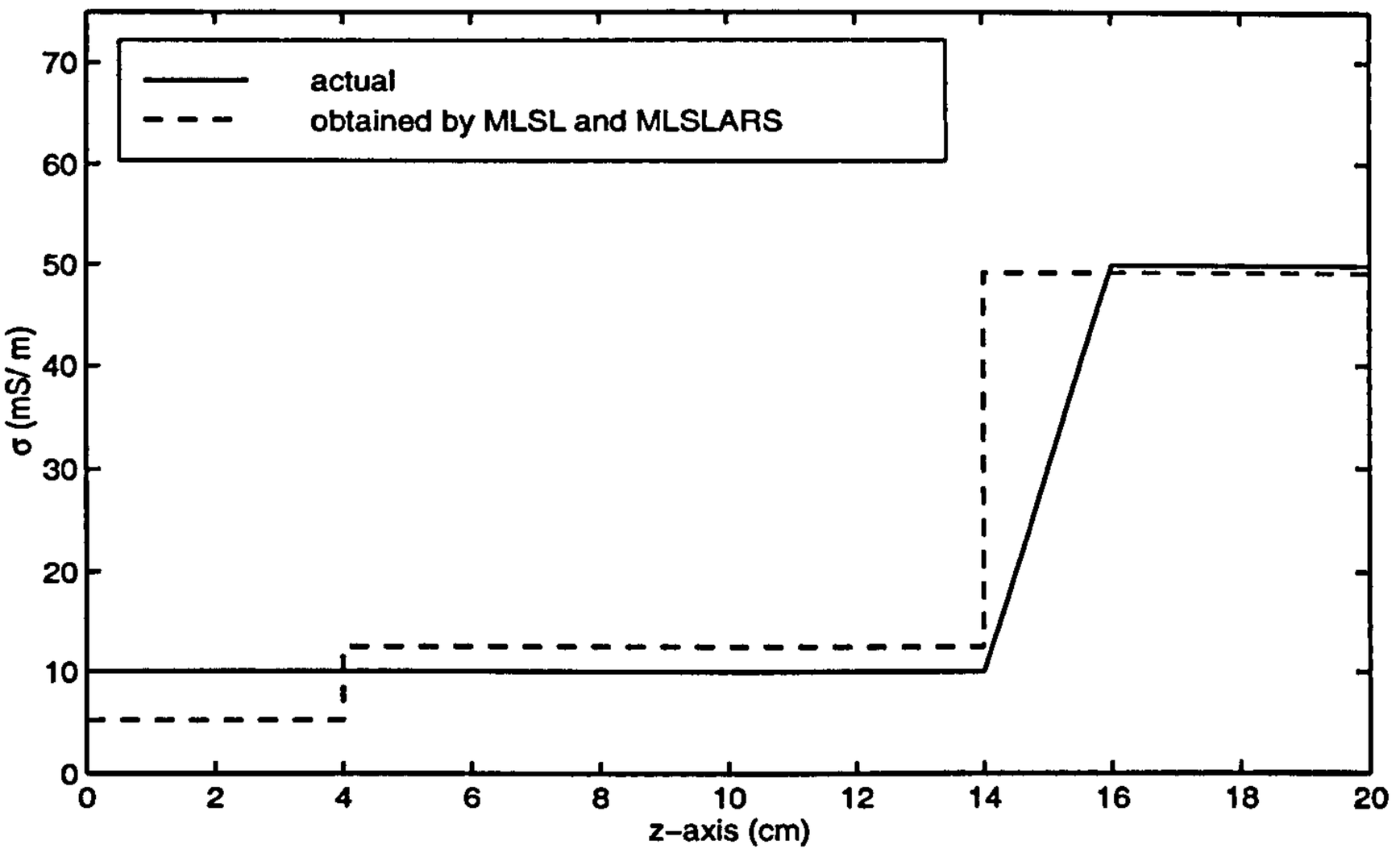

(a)

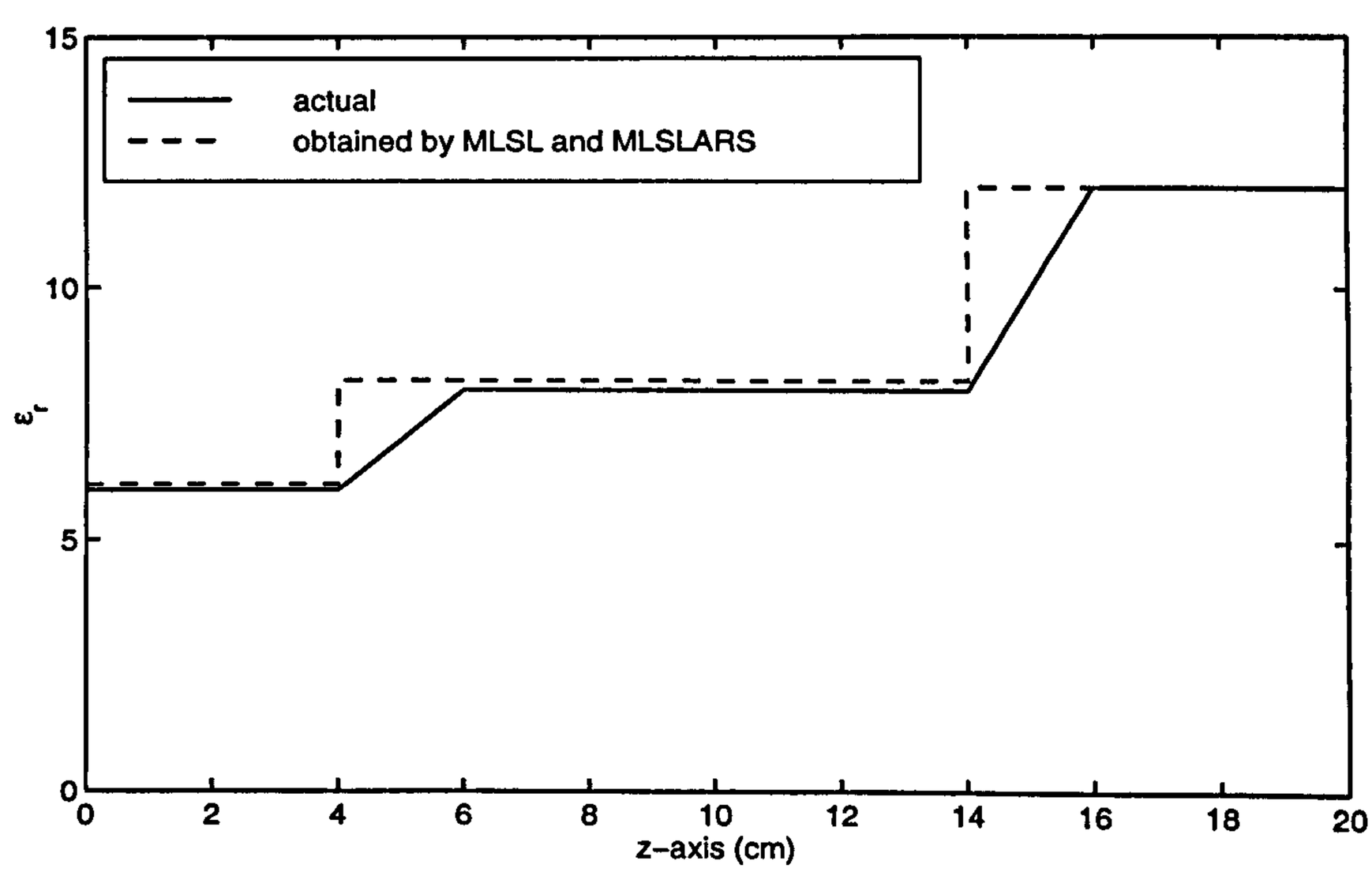

(b)

Figure 4.31: The 3-layer profiles reconstructed using the reflection coefficients in the interval [250 MHz, 450 MHz].

and the reconstructed profiles are illustrated in Fig. 4.32. It is evident that the MLSLARS gives the better results than the MLSL for this case. and appears to be more successful for the media with a large number of layers.

Table 4.8: The final MSE values using the MLSL and MLSLARS methods for reconstructing the profile of the continuous medium from the reflection coefficients obtained in the interval [650 MHz, 1150 MHz] when $M = 5$.

Number of function eval. = 500000, $N_p = 1000$, $\xi = 0.002$						
MLSL	Final MSE	3.5e-8	1.3e-8	1.4e-8	3.7e-9	2.3e-9
		1.8e-9	4.4e-8	3.7e-9	8.2e-9	1.7e-9
	No. of Minima found	89	86	84	92	87
		84	89	80	82	92
MLSLARS	Final MSE	2.6e-10	4.8e-11	2.7e-9	4.8e-11	5.3e-11
		2.8e-10	2.6e-10	4.6e-12	6.8e-12	4.6e-12
	No. of Minima found	85	83	94	82	78
		74	70	70	78	97

The profile obtained for $M = 5$ is still not satisfactory. This is because the lowest value 4.6e-12 found by the MLSLARS is not necessarily the global minimum. To show this, the reconstruction is carried out in a reduced feasible region given by

$$\begin{aligned}
&0 \le \sigma_1 \le 0.02 \text{ S/m}\,,\ 4 \le \epsilon_{r1} \le 8\,,\ 2 \le h_1 \le 6 \text{ cm}\\
&0.005 \le \sigma_2 \le 0.015 \text{ S/m}\,,\ 6 \le \epsilon_{r2} \le 8\,,\ 1 \le h_2 \le 5 \text{ cm}\\
&0.005 \le \sigma_3 \le 0.05 \text{ S/m}\,,\ 6 \le \epsilon_{r3} \le 12\,,\ 5 \le h_3 \le 15 \text{ cm}\\
&0.01 \le \sigma_4 \le 0.05 \text{ S/m}\,,\ 8 \le \epsilon_{r4} \le 12\,,\ 1 \le h_4 \le 10 \text{ cm}\\
&0.01 \le \sigma_5 \le 0.1 \text{ S/m}\,,\ 8 \le \epsilon_{r5} \le 16
\end{aligned} \tag{4.5.11}$$

Running the MLSLARS algorithm 10 times with 500000 function evaluations, we found that MSE attains a final value of 1.9e-12 for all 10 runs. Figure 4.33 illustrates the obtained profile, which is acceptable. It is seen that even the MLSLARS fails to find the global minimum within the bounds of (4.5.10). If the number of iterations is increased, a lower minimum could be found within

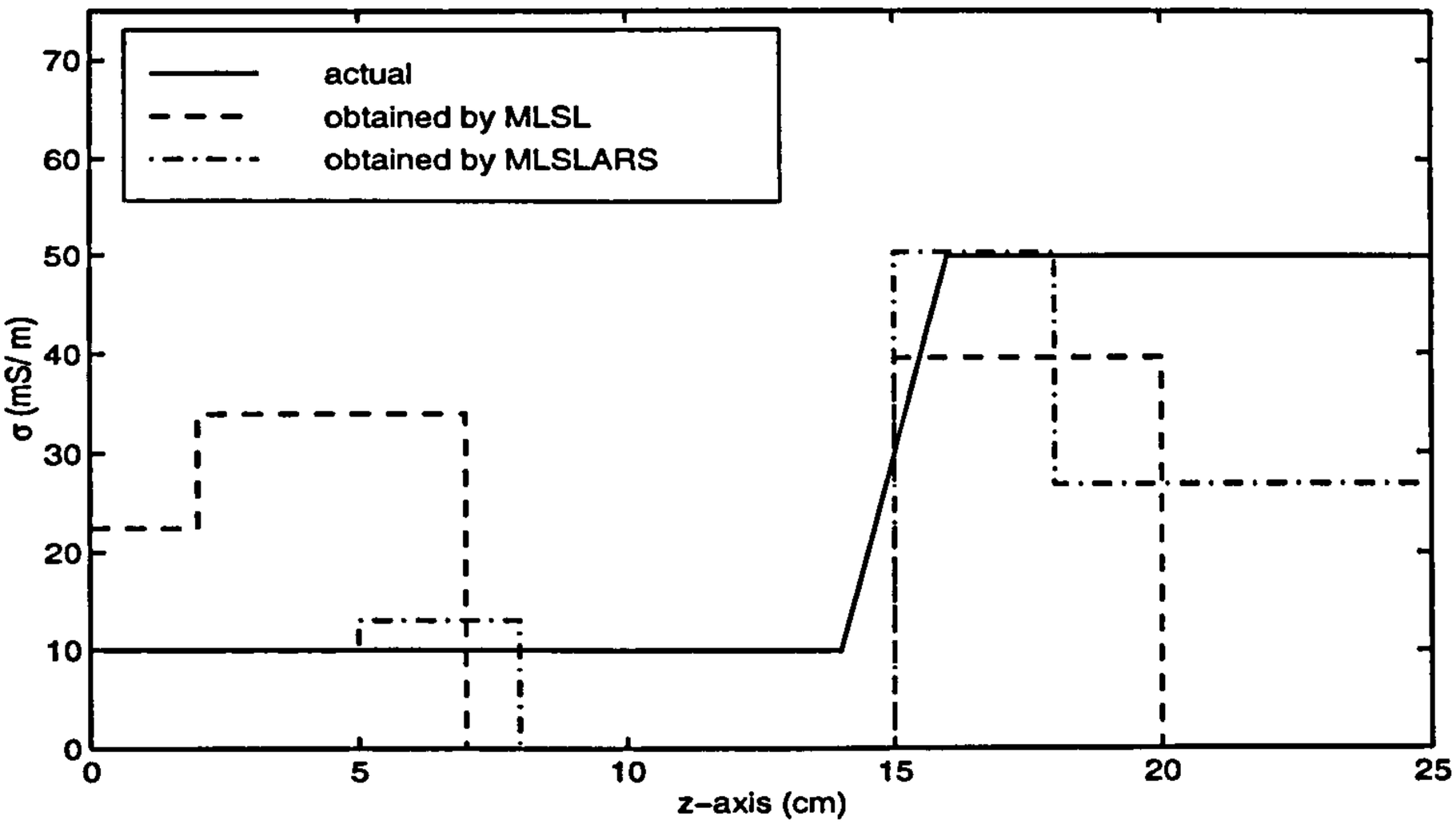

(a)

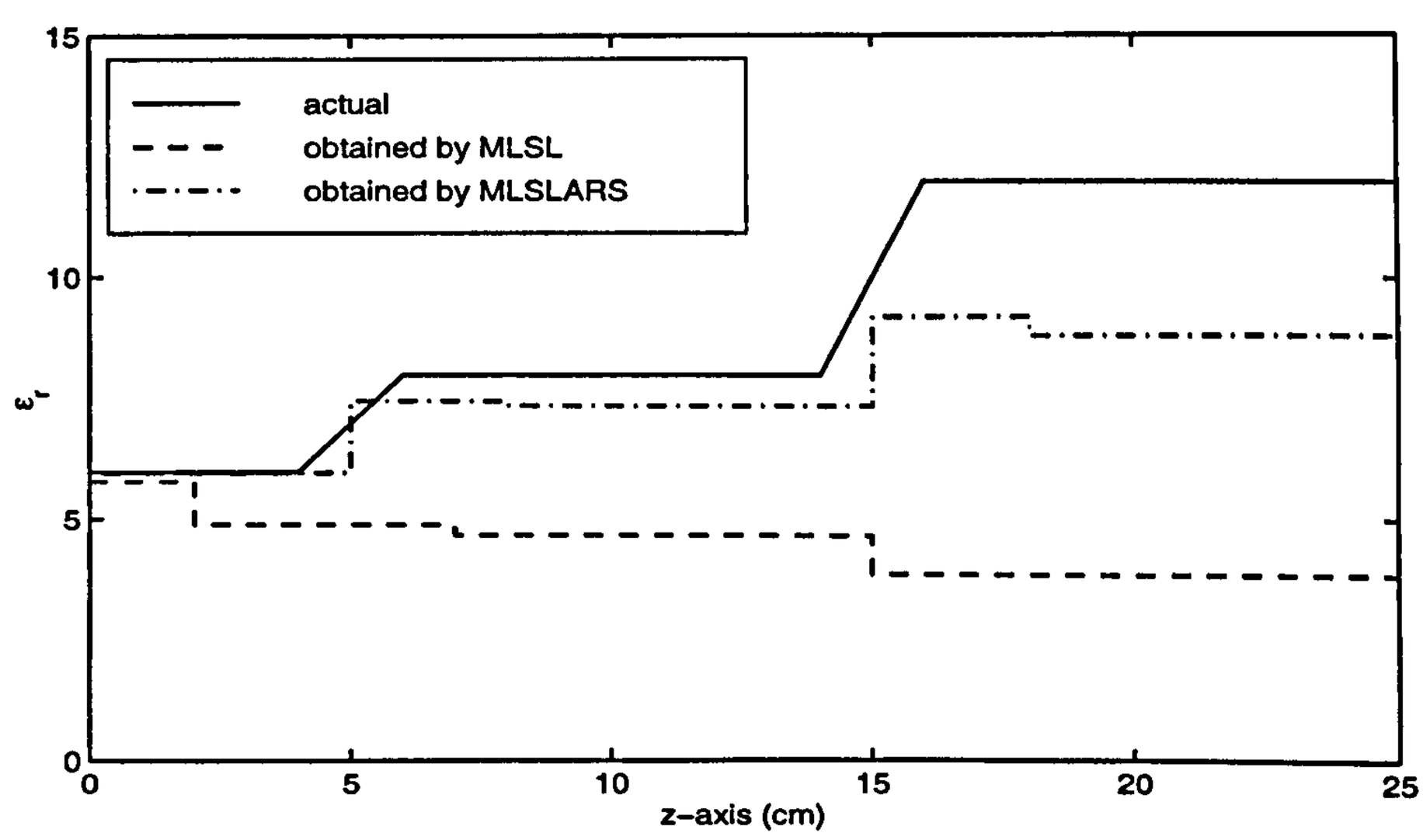

(b)

Figure 4.32: The profiles correspond to the lowest values in Table 4.8 with $M = 5$.

---

the bounds of (4.5.10). This can however be avoided in some practical applications where the feasible region may be shrunk with respect to the profile

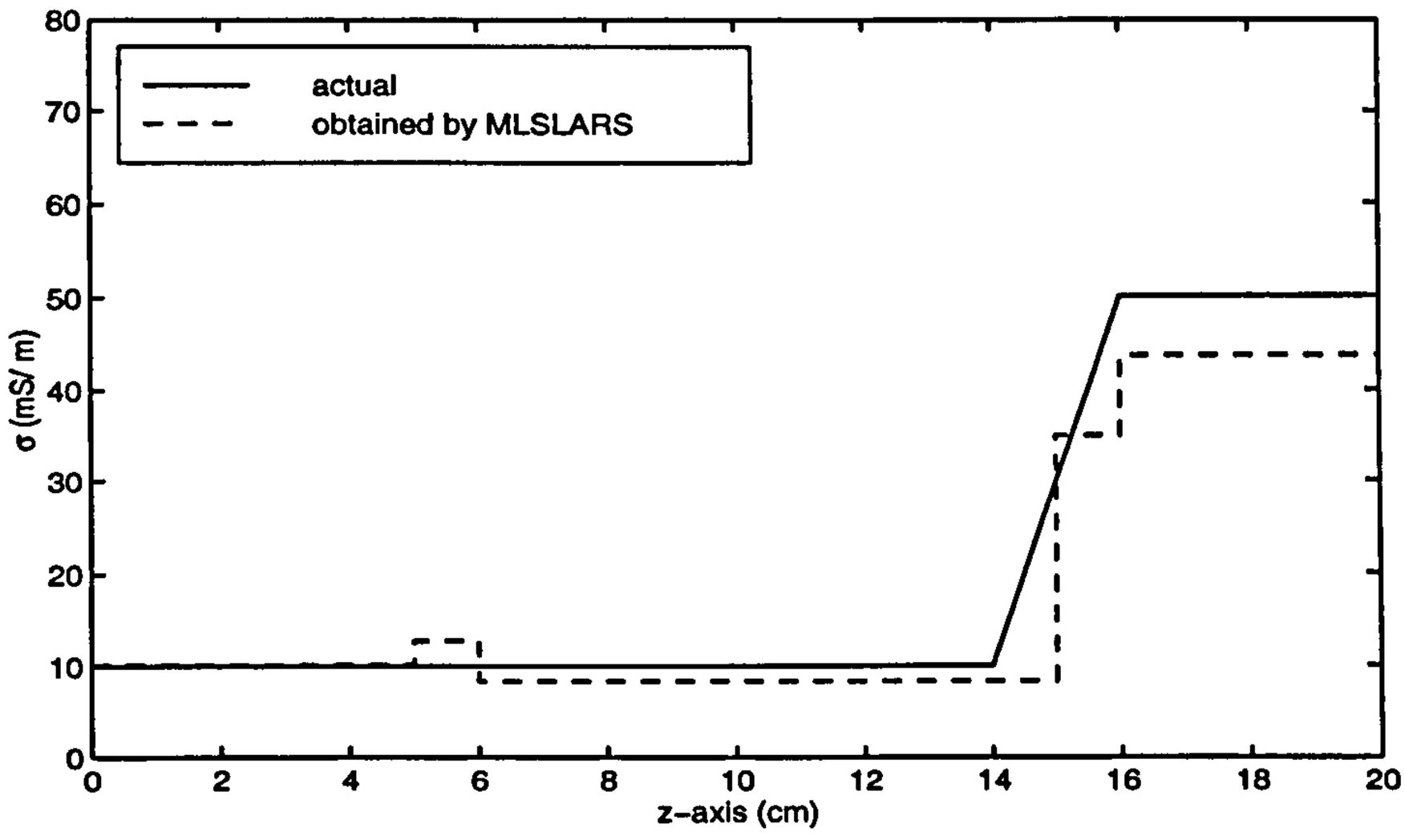

(a)

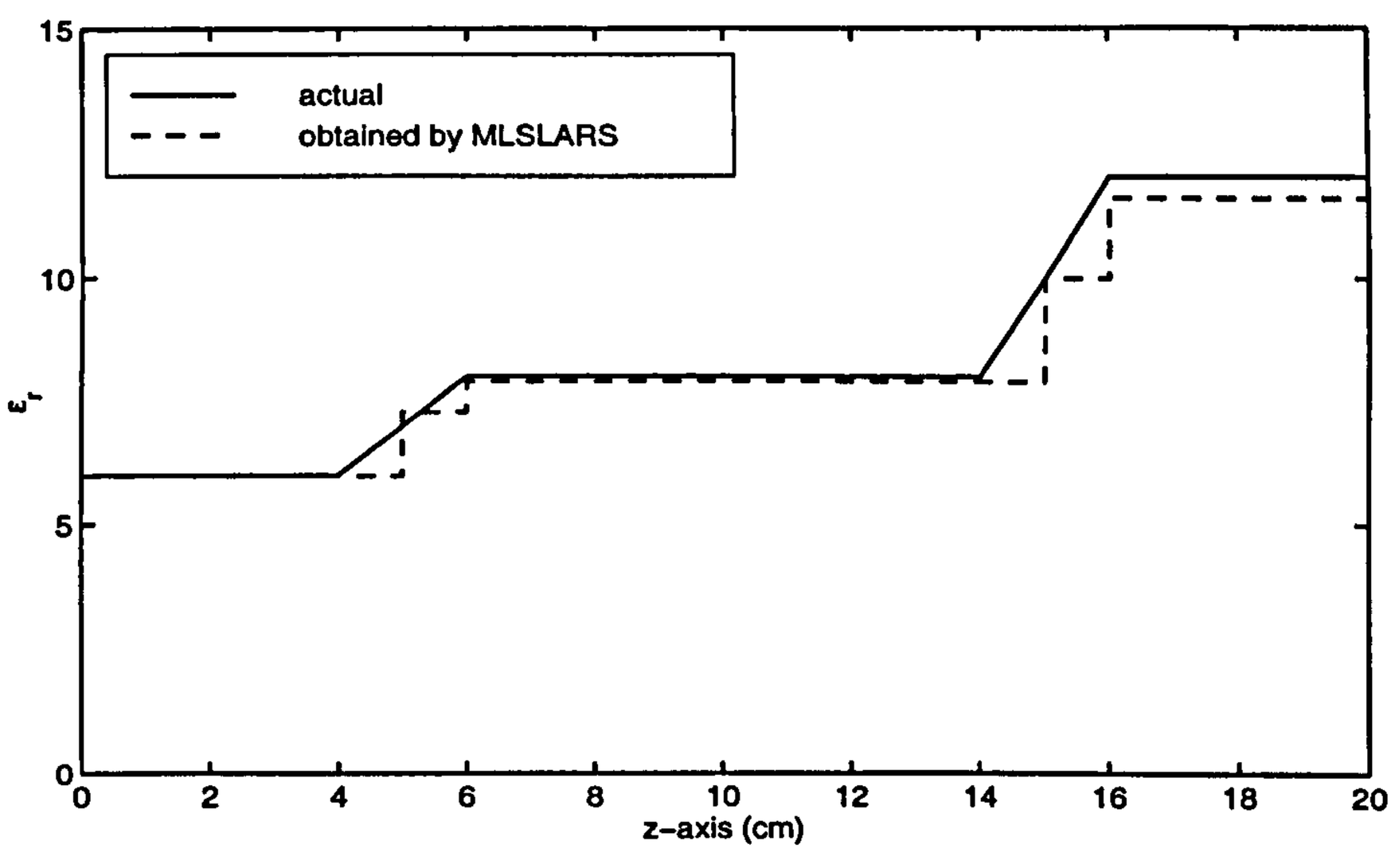

(b)

Figure 4.33: The profile corresponds to the value 1.9e-12 for the MSE function with $M = 5$.

---

found from the low frequency data. Having the profile derived from the low frequency data for $M = 3$ (Fig. 4.31), one can suggest bounds like (4.5.11). Alternatively, it may be suggested to employ the low and high frequency data simultaneously. Nonetheless, this is not preferable for the following reasons:

1. The more data used, the more computation cost.
2. The electromagnetic parameters of many materials, especially those concerned with the GPR application, depend on frequency. Thus, since the RMBI presents a unique value for each parameter for the frequency band used, the error in the parameters will be substantial if the data is distributed over a wide range of frequency.

One can observe from the reconstruction examples of this chapter that the largest error occurs in the conductivity profile. This can be explained by Equation (3.4.9), which shows that the MSE function is more sensitive to the permittivity than the conductivity especially at high frequencies. In fact, low frequency data provides higher accuracy in the reconstruction of the conductivity profile. In addition, it can be seen that the error is greater for the parameters of the deeper layers. This is because the reflections from the shallow layers are stronger than those from the deeper ones and contribute more to the MSE. Consequently, the MSE function is less sensitive to variations of the parameters of the deeper layers. The solution to such problems needs further consideration that is left for future research.

Chapter 5

Modelling of Ground Penetrating Radar

5.1 Introduction

In order to use GPR data to determine the profile of a multi-layered medium by the RMBI, a model that relates the GPR data to the reflection coefficients of the medium is needed. King *et al* [40] have solved Maxwell's equations for horizontal and vertical dipole antennas, facing a layered medium. Several equations are derived under different conditions, which enable some simplifications to be made. Such conditions are not generally satisfied for GPR applications. Besides, antenna configurations for GPR are not as simple as a dipole. The system can be monostatic or bistatic composed of dipole, bow-tie or horn antennas. There is usually a metallic shield, and the whole ensemble is put into a plastic case. Due to the complexity and the operation of GPR in the close proximity of the ground, it is not possible to analytically solve Maxwell's equations for GPR. 3-dimensional numerical methods can be used for the modelling, but require intensive computation time (Chapter 2).

One way to approximately model a GPR antenna above the surface of a

multi-layered medium is to maintain a separation distance between the antenna and the medium. This idea is inspired by free-space methods used to measure the electromagnetic properties of materials [2], [36], [37]. There exist several GPR applications in which the antenna is inevitably separated from the ground. Such applications include ice thickness profiling [28], bridge deck inspection and pavement profiling [61] where the surveys are continuously made at high speed (50km/h). The parameters of the host medium in GPR applications can also be identified by using the data collected when the GPR antenna is separated from the medium.

Being among non-destructive techniques, free-space methods are based on the approximation of the radiated field as a plane wave at the surface of the sample under test. It is therefore required that the sample is a flat large-aperture medium placed far enough from the antenna. In this way, material properties are obtained from the measured reflection and/or transmission coefficients. The dimensions of the sample and its separation from the antenna are of the order of several wavelengths. An acceptable accuracy can be achieved for large sample aperture with large separation. Consequently, free-space methods have mostly been adopted in centimeter-wave and millimetre-wave regions (3-300 GHz).

GPR systems often operate at UHF frequencies. For a deep penetration, some systems may operate at lower frequencies (VHF) as well. Thus, the separation distance ought to be around a few metres so that the model employed in free-space methods can be used for GPR systems. Large separations are not practical since this causes the reduction in the electromagnetic power penetrating into the ground together with the introduction of higher clutter into the received signal. In order to decrease the separation distance while maintaining the accuracy, the effects of the antenna-medium coupling has to be taken into account in the modelling. Thus, a new formulation that relates the received signal to the reflection coefficient of the medium is proposed in this chapter.

Using the new model, experimental and numerical examples demonstrate that the separation between the medium and the antenna could be of the order of a wavelength or less. In addition to the GPR application, the model enables free-space measurement techniques to be used not only for the frequency range [3 GHz, 300 GHz] but also for the UHF and VHF ranges. The closeness between the sample and transmitting-receiving apertures provides higher signal to noise ratio, lower diffraction around the edges of the sample and lower extraneous reflections into the measurement path. As a result, a better accuracy in the measurements is achieved.

To validate the proposed model and compare it with the conventional free-space model, several experiments were carried out by using a commercial GPR in the Department of Civil Engineering (University of Liverpool). The experiments involved the collection of data from a metal plate, a tank of water and a concrete block at different separations. The results confirm the superiority of the new model to the conventional one. Unfortunately, due to the lack of facilities, it was not possible to extend the experiment to more complicated layered media such as road basements. Thus, computer simulations were conducted using the 3-dimensional Finite-Difference Time-Domain (FDTD) method.

A similar idea was pursued by Spagnolini [61], but no mathematical formulation is given for the modelling of the GPR system in that paper. Hamran *et al* [28] have also considered the application of the conventional model to the estimation of the dielectric constants of an ice shelf using GPR data.

This chapter is organised into four sections. In Section 5.2, the formulation of the conventional modelling and the new modelling are detailed. A commercial GPR antenna is simulated by the FDTD method in section 5.3. The final section is devoted to the experimental and numerical examples and the analysis of the results.

5.2 Problem Formulation

The geometry of the problem is shown in Fig. 5.1 where a transmitting-receiving aperture is illuminating a flat-surface medium through an air gap. It is a bistatic configuration, which consists of a transmitting antenna and a

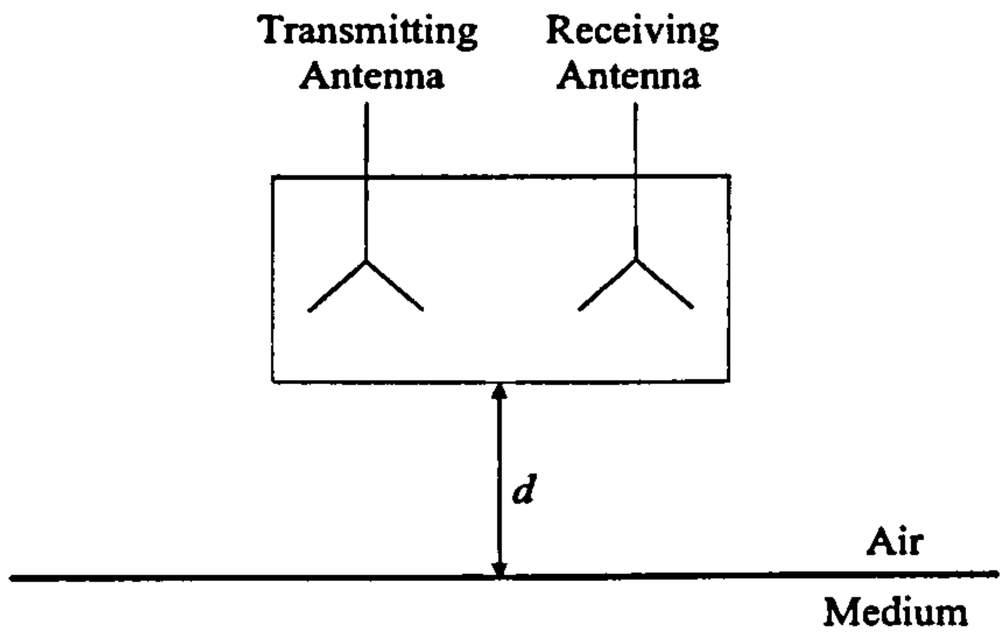

Figure 5.1: Schematic diagram of a GPR antenna facing a multi-layered medium.

receiving antenna both mounted inside a common box a finite distant apart. Such a system can be considered as a monostatic configuration where the same antenna is used for transmission and reception. The formulations presented in this section are for the monostatic system. As shown in the figure, d denotes the separation between the antenna and the medium. Under the assumption that the transmitting-receiving aperture is parallel to the surface of the medium and d is large enough, the incident wave can be treated as being normal to the medium. The problem is to relate the received signal to the reflection coefficient of the medium.

The voltage incident on the terminal of the transmitting antenna induces an electric current in the transmitting-receiving aperture. This current radiates a wave that is partially reflected from the medium. The reflected wave returns to the aperture where it generates an output signal at the terminal of the receiving antenna. In addition, it influences the distribution of the current in the transmitting-receiving aperture. This influence is the source of a secondary

wave, which in turn is reflected from the medium, generates another received signal and changes the distribution of the current. Thus, there are multiple reflections between the transmitting-receiving aperture and the medium, i.e. antenna-medium coupling.

Let E_n^i and E_n^r denote respectively the nth incident and reflected electric fields defined at the air-medium interface. E_n^r is related to E_n^i through the reflection coefficient of the medium, i.e. $E_n^r = \Gamma E_n^i$. Suppose H_r represents the transfer function that relates E_n^r to the signal $S(\omega)$ received by the receiving antenna (note that H does not denote the magnetic field). Conventional free-space methods are based on the following equation

$$S(\omega) = E_1^i \Gamma H_r = U \Gamma \quad , \quad U = E_1^i H_r \tag{5.2.1}$$

In fact, only the first reflection from the medium is considered in the modelling. The quantity U is obtained through a calibration procedure by replacing the medium with a good conductor, i.e. $\Gamma = -1$. The reflection coefficient of an unknown medium is calculated from $S(\omega)$ using $\Gamma = \frac{S}{U}$.

In order to consider the contribution of the multiple reflections, let us define the transfer function H as the ratio of E_{n+1}^i to E_n^r. The received signal can be written as

$$\begin{aligned} S &= E_1^i \Gamma H_r + E_1^i \Gamma H \Gamma H_r + E_1^i \Gamma H \Gamma H \Gamma H_r + \ldots \\ &= U \Gamma \left[1 + \Gamma H + (\Gamma H)^2 + \ldots\right] \end{aligned} \tag{5.2.2}$$

Equation (5.2.2) is a geometric infinite series with the factor $|\Gamma H| < 1$ and can be simplified as

$$S = \frac{U \Gamma}{1 - \Gamma H} \tag{5.2.3}$$

It should be noted that the mismatch losses (i.e. losses due to mismatch between the antenna and feeding transmission line), antenna responses and the spreading losses in the air gap are included in U and H. These two quantities

are determined by the geometry of the transmitting-receiving aperture as well as the distance d. Moreover, the interaction between the electromagnetic field and the medium is only considered through the parameter Γ (the reflection coefficient). Nevertheless, when the antenna is close to the medium, the near-field effect contributes to the received signal as well. Consequently, the decrease in d will increase the error in both models, i.e. Equations (5.2.1) and (5.2.3). It is important to note that S in (5.2.3) is the signal received owing to the presence of the medium. The actual GPR data includes a background signal that results from the interaction between the antenna, case and other parts such as the metallic shield. For the bistatic configuration, the direct coupling between transmit and receive antennas also contributes to the background signal.

U and H can be obtained by using the received signals from any two known media [46]. The first medium should be a metal plate whose reflection coefficient is -1 over a wide range of frequencies. The reflection coefficients of other materials, including fresh water, are frequency dependant. However, since the permittivity of fresh water ($\epsilon_r \in [77, 81]$) is very high, its reflection coefficient is nearly constant versus frequency. Furthermore, the imaginary part of the reflection coefficient is negligible compared to the real part. Hence, fresh water is an appropriate candidate for the second known medium.

Alternatively, the quantities U and H may be calculated by utilizing the signals received from a single known medium with two different separations. The known medium should be a metal plate. The formulations for both approaches are given in the following sections.

THE APPLICATION OF GPR

5.2.1 Metal-Water approach

Let S^{Met} and S^{Wat} denote the signal received when the medium is a metal plate and a pool of water respectively. These signals are given by

$$S^{Met} = \frac{-U}{1+H} \tag{5.2.4}$$

$$S^{Wat} = \frac{U\,\Gamma^{Wat}}{1-\Gamma^{Wat}\,H} \tag{5.2.5}$$

where Γ^{Wat} is the reflection coefficient of fresh water. Solving (5.2.4) and (5.2.5) for U and H, one can derive

$$U = \frac{1+\Gamma^{Wat}}{\Gamma^{Wat}} \left(\frac{S^{Met}\,S^{Wat}}{S^{Met}-S^{Wat}} \right) \tag{5.2.6}$$

$$H = -\frac{1}{\Gamma^{Wat}} \left(\frac{\Gamma^{Wat}\,S^{Met}+S^{Wat}}{S^{Met}-S^{Wat}} \right) \tag{5.2.7}$$

The reported values for the relative permittivity of fresh water are within $\epsilon_r \in [77, 81]$. In this investigation, Γ^{Wat} is set to -0.797, which is the mean of two extreme values: $\Gamma^{Wat} = -0.795$ for $\epsilon_r = 77$ and $\Gamma^{Wat} = -0.8$ for $\epsilon_r = 81$. Accordingly, substitution of (5.2.6) and (5.2.7) into (5.2.3) yields

$$S = \frac{0.254\,S^{Met}\,S^{Wat}\,\Gamma}{S^{Wat}-S^{Met}-\Gamma\,(S^{Met}-1.254\,S^{Wat})} \tag{5.2.8}$$

Rearranging (5.2.8), we have

$$\Gamma = \frac{S\,(S^{Wat}-S^{Met})}{0.254\,S^{Met}\,S^{Wat}+S\,(S^{Met}-1.254\,S^{Wat})} \tag{5.2.9}$$

The proposed model is given by Equation (5.2.8) or (5.2.9), which relates the received signal to the reflection coefficient of an unknown medium.

5.2.2 Metal-Metal approach

In this approach, the values of U and H are calculated from the measurements carried out on a metal plate with two different distances d. It is

well-known that the radiated field E in the far-field zone of an antenna is given by

$$E = F \frac{e^{-\frac{j\omega r}{c}}}{r} \tag{5.2.10}$$

where F is a proportional factor, c is the velocity of the wave in air and r is the distance from the antenna to the observation point. Consider two rays radiated from and returned to the transmitting-receiving aperture for two different separations and let E_a and E_b be the field strengths of the returned rays at the receiving antenna with separations $d = d_a$ and d_b respectively. The following equation can be obtained from (5.2.10)

$$E_b = \frac{d_a}{d_b} e^{-2j\omega \frac{d_b - d_a}{c}} E_a = V_{ab} E_a \tag{5.2.11}$$

Let S_a, U_a and H_a denote the corresponding quantities in (5.2.2) when $d = d_a$. Observing that the first term in the series (5.2.2) involves one radiated ray, the second term involves two radiated rays and so forth, one can write the relation

$$S_b = U_a V_{ab} \Gamma + U_a V_{ab}^2 \Gamma^2 H_a + U_a V_{ab}^3 \Gamma^3 H_a^2 + \ldots \tag{5.2.12}$$

where S_b is the received signal for $d = d_b$. Equation (5.2.12) can be simplified to

$$S_b = \frac{V_{ab} U_a \Gamma}{1 - V_{ab} \Gamma H_a} \tag{5.2.13}$$

From (5.2.3), we have

$$S_a = \frac{U_a \Gamma}{1 - \Gamma H_a} \tag{5.2.14}$$

Solving (5.2.13) and (5.2.14) for U_a and H_a, one can derive

$$U_a = S_a S_b \frac{1 - V_{ab}}{\Gamma V_{ab} (S_a - S_b)} \tag{5.2.15}$$

$$H_a = \frac{V_{ab}\, S_a - S_b}{\Gamma\, V_{ab}\, (S_a - S_b)} \tag{5.2.16}$$

If a metal plate ($\Gamma = -1$) is used to obtain U_a and H_a, the equations can be rewritten as

$$U_a = S_a^{Met}\, S_b^{Met}\, \frac{1 - V_{ab}}{V_{ab}\, (S_b^{Met} - S_a^{Met})} \tag{5.2.17}$$

$$H_a = \frac{V_{ab}\, S_a^{Met} - S_b^{Met}}{V_{ab}\, (S_b^{Met} - S_a^{Met})} \tag{5.2.18}$$

where S_a^{Met} and S_b^{Met} are the measured signals using the metal plate. The substitution of (5.2.17) and (5.2.18) into (5.2.14) yields

$$S_a = S_a^{Met}\, S_b^{Met}\, \frac{(1 - V_{ab})\, \Gamma}{V_{ab}\, (S_b^{Met} - S_a^{Met}) - \Gamma\, (V_{ab}\, S_a^{Met} - S_b^{Met})} \tag{5.2.19}$$

Rearranging (5.2.19), we have

$$\Gamma = V_{ab}\, S_a\, \frac{S_b^{Met} - S_a^{Met}}{S_a^{Met}\, S_b^{Met}\, (1 - V_{ab}) + S_a\, (V_{ab}\, S_a^{Met} - S_b^{Met})} \tag{5.2.20}$$

Equation (5.2.19) or (5.2.20) gives another version of the proposed model that relates the received signal to the reflection coefficient of an unknown medium placed at a distance d_a from the transmitting-receiving aperture.

5.2.3 Application

According to the proposed models, a GPR antenna at a specific separation can be characterised by two measured signals (S^{Met}, S^{Wat}) or (S_a^{Met}, S_b^{Met}). These calibration measurements just need to be conducted once and the results can be used afterwards for the measurement of the parameters of a layered media. It is necessary to identify suitable separations that offer a satisfactory accuracy for an given GPR antenna. This can be done by conducting some experiments at different separations on a known medium or alternatively by 3-dimensional simulation of the antenna. Further discussion is provided in

Section 5.4. It should be mentioned that such experiments or simulations are also required to be done once for an antenna.

Using (5.2.9) or (5.2.20), the reflection coefficient can be computed from the measured data (e.g. $S_a, S^{Wat}, \ldots$) and then employed in the RMBI to derive the profile of multi-layered media. Owing to the multiplication of two measured signals in the denominator of these equations, the noise will be amplified at the frequencies that bear less power. Hence, it is preferable to use Equations (5.2.8) or (5.2.19) directly in the inversion. To do so, some modifications are required in a few expressions derived for the RMBI.

With regard to Equation (3.4.2) (Chapter 3), let the MSE function be rewritten as

$$f(\mathbf{x}) = \frac{1}{2N} \sum_{n=1}^{N} \left| S_n^{Model} - S_n \right|^2 \tag{5.2.21}$$

where S_n is the observed (measured) signal and S_n^{Model} is the model signal obtained from either (5.2.8) or (5.2.19). The derivative of the MSE function f in terms of a parameter x_m is given by

$$\frac{\partial f}{\partial x_m} = \frac{1}{N} \mathrm{Re} \left[\sum_{n=1}^{N} (S_n^{Model} - S_n)^* \ \frac{\partial S_n^{Model}}{\partial x_m} \right] \tag{5.2.22}$$

For the Metal-Water approach, we have

$$\frac{\partial S^{Model}}{\partial x_m} = \frac{0.254\, S^{Met}\, S^{Wat}\, (S^{Wat} - S^{Met})}{[S^{Wat} - S^{Met} - \Gamma\, (S^{Met} - 1.254\, S^{Wat})]^2} \times \frac{\partial \Gamma}{\partial x_m} \tag{5.2.23}$$

and for the Metal-Metal approach, one can derive

$$\frac{\partial S^{Model}}{\partial x_m} = \frac{V_{ab}\, (1 - V_{ab})\, S_a^{Met}\, S_b^{Met}\, (S_b^{Met} - S_a^{Met})}{[\, V_{ab}\ (S_b^{Met} - S_a^{Met}) - \Gamma\ (V_{ab}\, S_a^{Met} - S_b^{Met})]^2} \times \frac{\partial \Gamma}{\partial x_m} \tag{5.2.24}$$

The derivations for $\frac{\partial \Gamma}{\partial x_m}$ given in Chapter 3 are applicable here.

5.3 The FDTD Simulation of a GPR Antenna

The finite-difference time-domain (FDTD) method has been used successfully to analyse antennas and solve scattering problems. The FDTD technique

utilizes a central difference scheme to discretise Maxwell's curl equations in space-time. Electric and magnetic fields are evaluated alternately at half-time step intervals in closely-spaced computation cells typically having dimensions less than $\lambda/20$, where λ denotes the wavelength in the medium of interest. The technique involves a time marching procedure, which is followed until the desired response is reached.

The results of the simulation of GPR by the FDTD method show a good agreement with measured ones [7], [8], [48]. The FDTD analysis of an antenna, which is similar to that used in a commercial GPR system (Model 3101 of GSSI Inc.), is discussed in this section. The simulation is carried out by LC, a user-friendly software package developed by Silicon Graphics Inc. [58]. The software provides many facilities such as parallel processing, defining the material parameters, selecting different absorbing boundary conditions and introducing voltage and/or current sources at any location. LC allows the user to record the electromagnetic fields, voltage, current, charge density etc. at the positions of interest. The software is run on Silicon Graphics computer (model SGI Power Challenge) having fourteen R10000 processors and 1.768 GB memory. We tested LC by comparing the experimental results, given in [42] for a monopole antenna, with those yielded from the simulation of that antenna by LC. A good agreement was achieved.

The antenna of the commercial GPR is nominally 900 MHz with an aperture of 18 cm $\times$ 33 cm. To simulate this radar, the details of the antenna dimensions and materials are required. Since the antenna is sealed off, we are not allowed to open the antenna case. Using information supplied by the manufacturer, the FDTD model shown in Fig. 5.2 is used for simulation.

The device contains two metallic bow-tie antennas (bistatic configuration) with similar design (Fig. 5.2(b)). The terminals of the antennas are connected to transmission lines consisting of two parallel cylindrical wires. The simulation of cylindrical shapes needs very fine cells, which will substantially increase

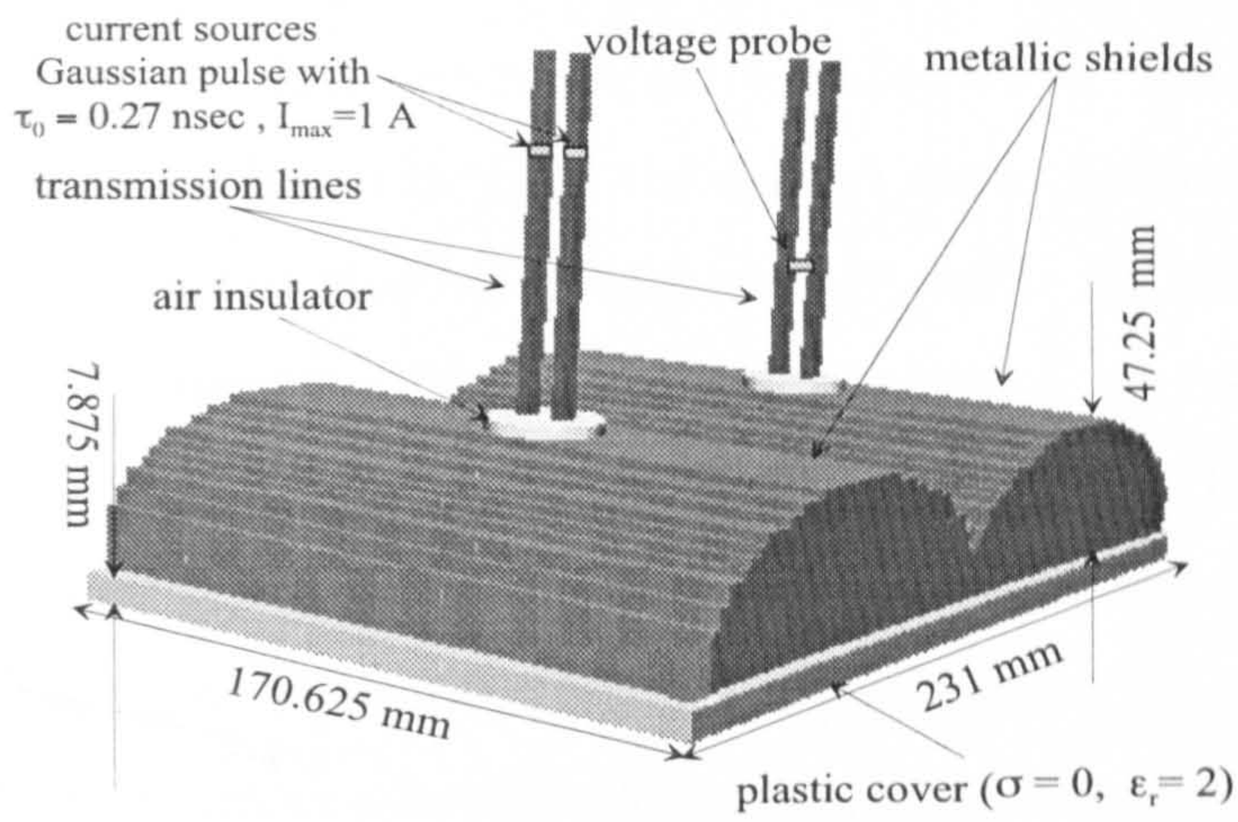

(a)

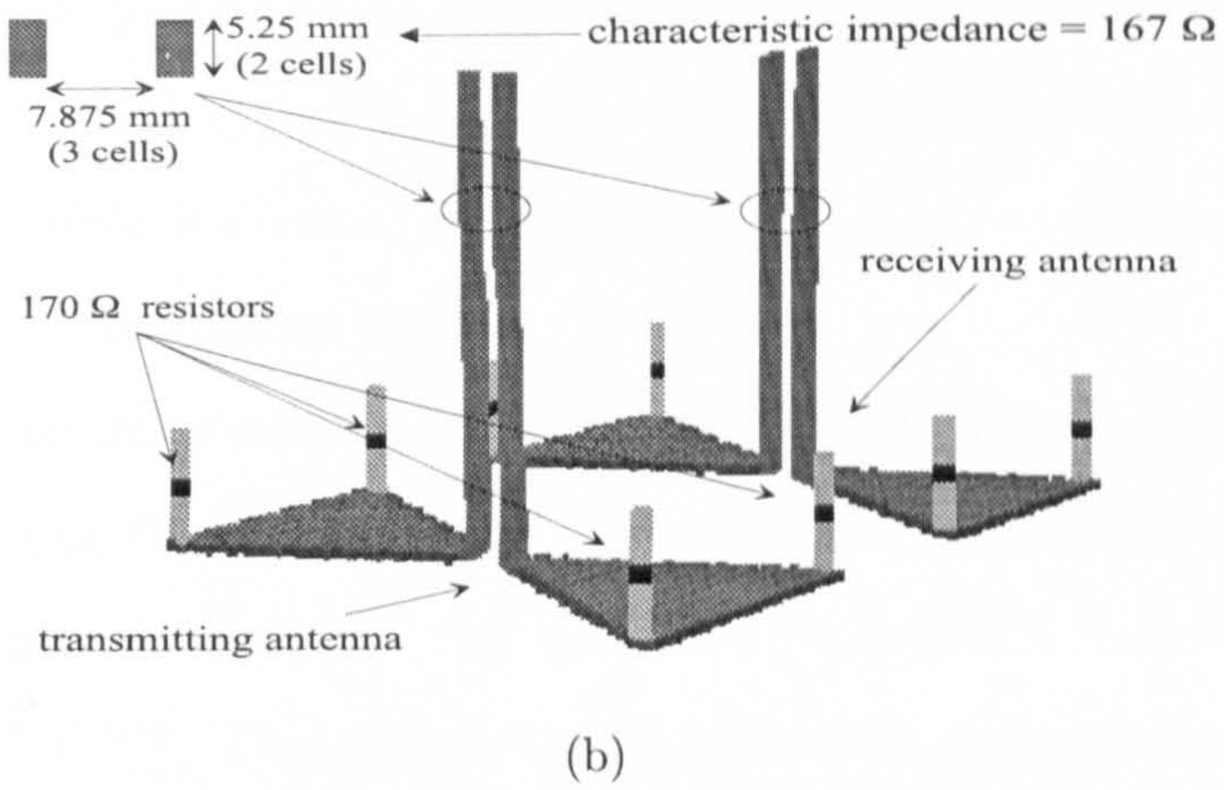

(b)

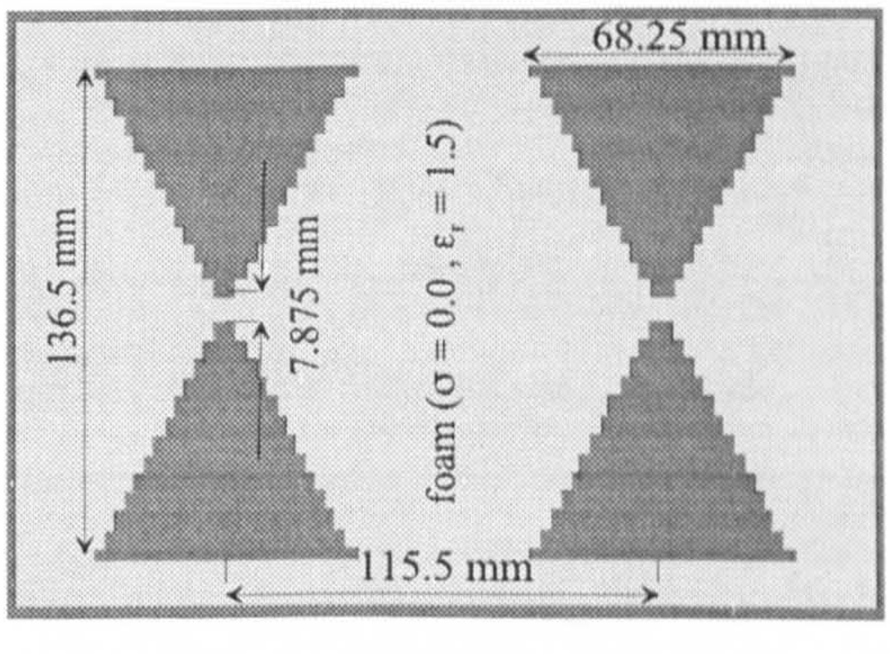

(c)

Figure 5.2: The FDTD model of a GPR antenna. (a) the complete antenna. (b) The bow-tie antennas with the metallic shield, foam packing and plastic cover stripped away. (c) Bottom view with the plastic cover removed.

the amount of memory required and exceed the computer memory available; hence, the transmission lines are modelled as cubic wires. The dimensions of transmission lines are chosen to yield the desired characteristic impedance of 167 Ω. Note that it is not possible to achieve every value for the characteristic impedance. This is because the dimensions of the lines are required to be a multiple of the cell size. Each antenna is loaded with four 170 Ω resistors, giving an equivalent 170 Ω value which is nearly matched to the characteristic impedance of the lines. These resistors make the antennas broadband.

The device incorporates a metallic shield that minimizes the radiation from top and sides of the antennas and directs the radiation toward the ground. The antennas are held by foam, which fills the space inside the shield. An air insulator protects the transmission line from touching to the metallic shield. The whole ensemble is covered by a plastic case, the bottom section of which is considered in the antenna model.

Two Gaussian pulse current sources with opposite direction are placed along the wires to excite the transmitting antenna. The characteristics of the excitation pulse, such as rise time, fall time and pulsewidth, were not known for the commercial GPR. The parameter τ_0 of the Gaussian pulse (Fig. 2.3) is experimentally set to 0.27 ns, which gives an acceptable match between the background GPR and FDTD signals (i.e. the signals are obtained from the GPR measurement and the FDTD simulation without the presence of any obstruction). The signals are shown in Fig. 5.3 where the GPR signal is scaled in amplitude and offset in time with respect to the FDTD signal. Note that scaling and time offsetting are necessary so that one can easily compare the signals. The received signal is recorded by a voltage probe located between the wires of the receiving transmission line as indicated in Fig. 5.2(a).

The cell size in all FDTD simulation is set to 2.625 mm that is a compromise between the requirement for shortest wavelength (cell size should be $\leq \lambda_{min}/20$), the maximum computer memory available, and the need to achieve

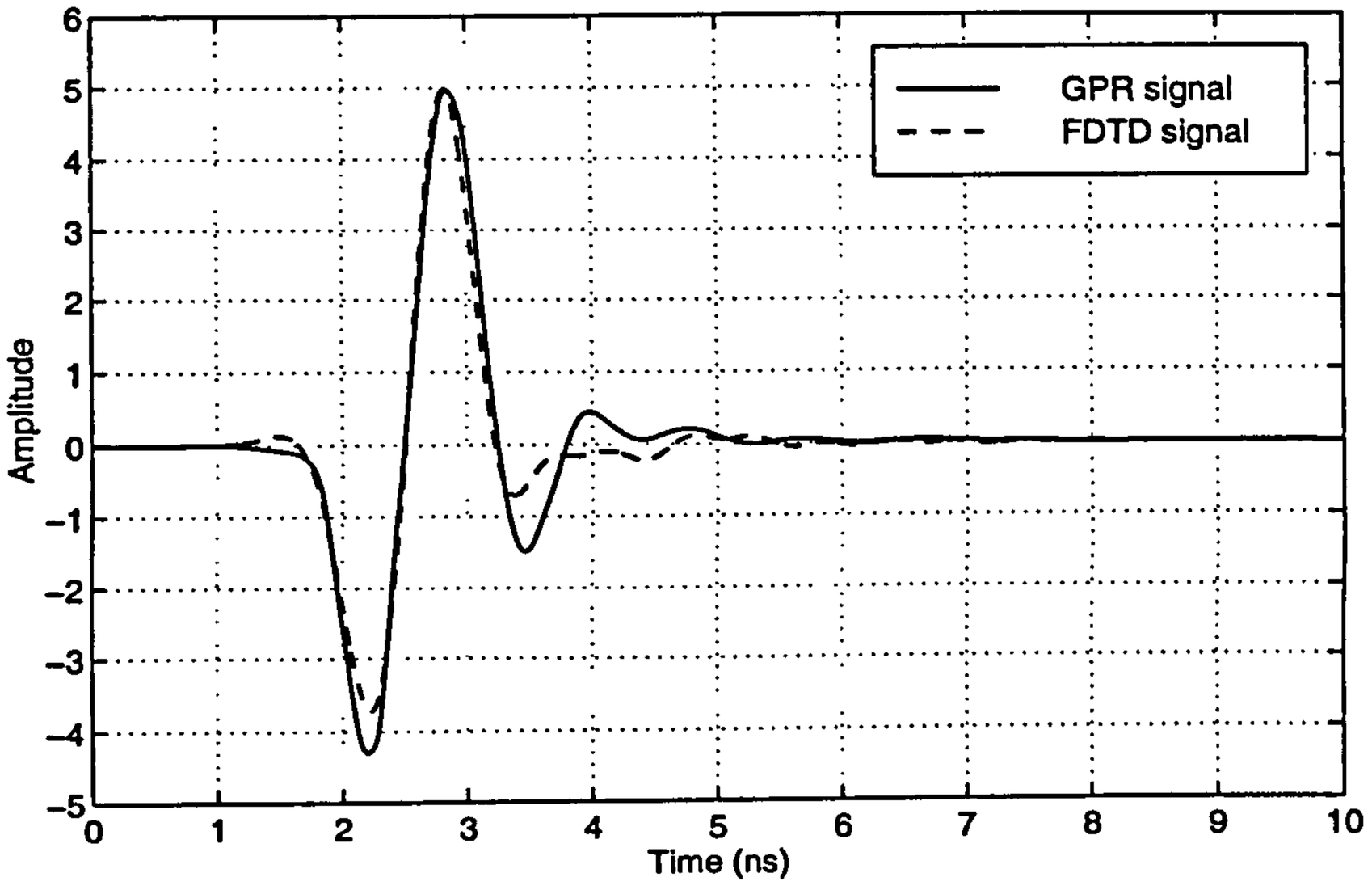

(a)

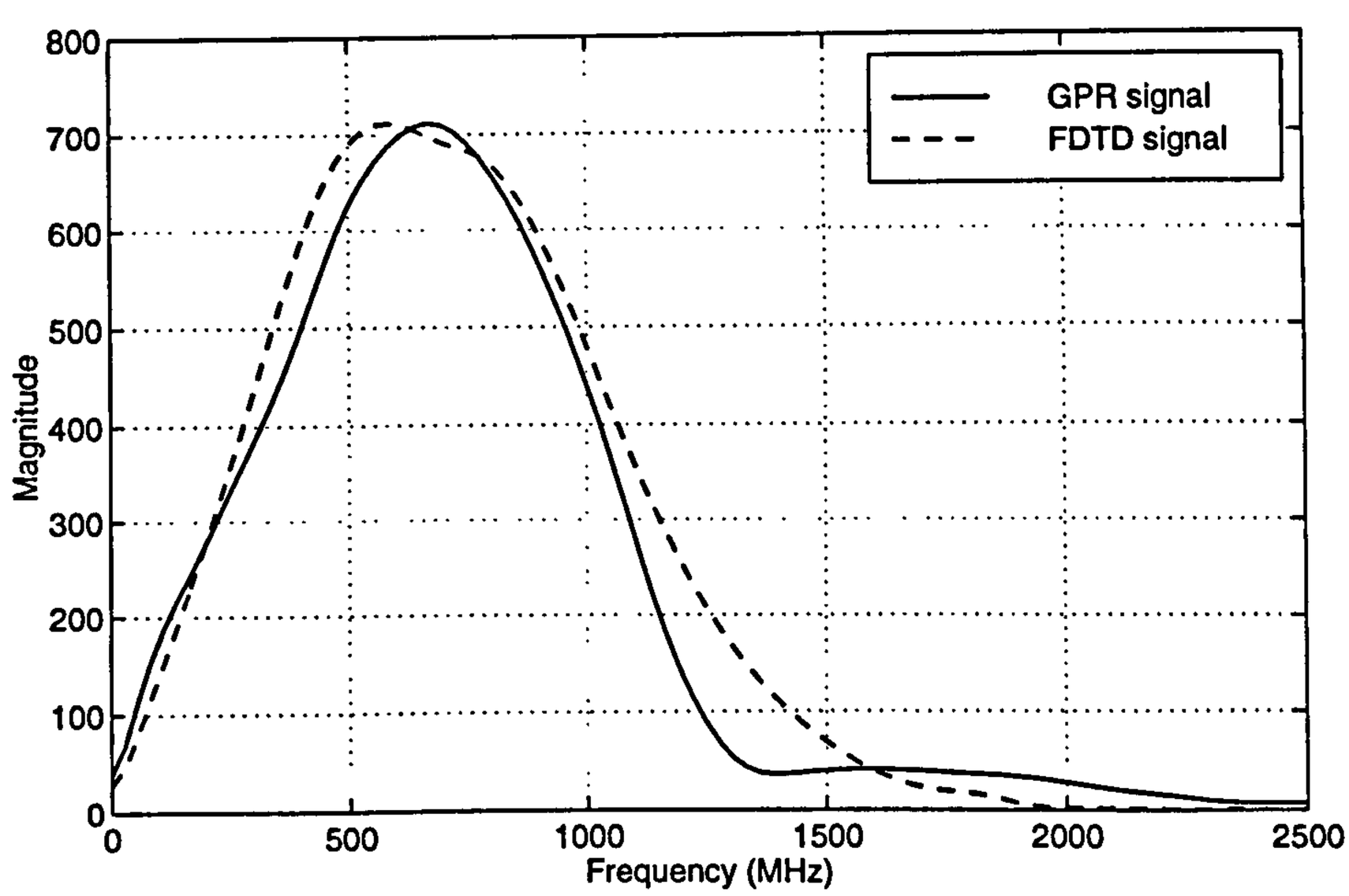

(b)

Figure 5.3: The background GPR and FDTD signals in (a) time domain and (b) frequency domain when there is no medium in front of the antenna.

a certain value for the characteristic impedance of the transmission lines. It is noteworthy that all dimensions of the elements in the model (Fig. 5.2) are chosen as multiples of the cell size so that no part is missed during the discretisation. Once the cell size is selected, LC automatically assigns a value to the time step, which for the present size is equal to 4.378 ps.

A comparison between the experimental and simulated data is provided here for the case when the GPR antenna is above a concrete block illustrated in Fig. 5.4(a). As it can be seen, a metal bar is embedded in the block. To minimize the effect of this bar, the polarization of the antenna is orthogonal to the bar. In addition, the top surface (80 cm × 120 cm) of the block, which is 15 cm away from the metal bar, is below the GPR antenna. The age of the block is two years and so it is dry. The relative permittivity and conductivity of dry concrete were measured by the transmission-line method and are shown in Fig. 5.4(b) and 5.4(c) as a function of frequency. The parameters with frequency dependency cannot be accommodated in LC. Thus, a medium with $\epsilon_r = 6$ and $\sigma = 0.04$ S/m, being roughly the average of the parameters of the concrete block, is used in the FDTD simulation.

Figures 5.5 and 5.6 illustrate the resultant signals in the time and the frequency domains respectively. These signals are obtained after deducting the background signals of Fig. 5.3 from the original ones. They are therefore the result of the presence of the concrete block and the medium with $\epsilon_r = 6$ and $\sigma = 0.04$ S/m. It can be observed that the rate of attenuation of the GPR and FDTD signals in terms of the separation distance is almost the same. Furthermore, a similar shift in the centre frequency of the signals occurs at different separations for the both signal sets. Overall, the FDTD simulation agrees well with the real signal. Thus, the FDTD method can be a useful tool for analysing and designing GPR antennas.

With regard to the cost of the simulation, Table 5.1 summarises the corresponding minimum and maximum limits.

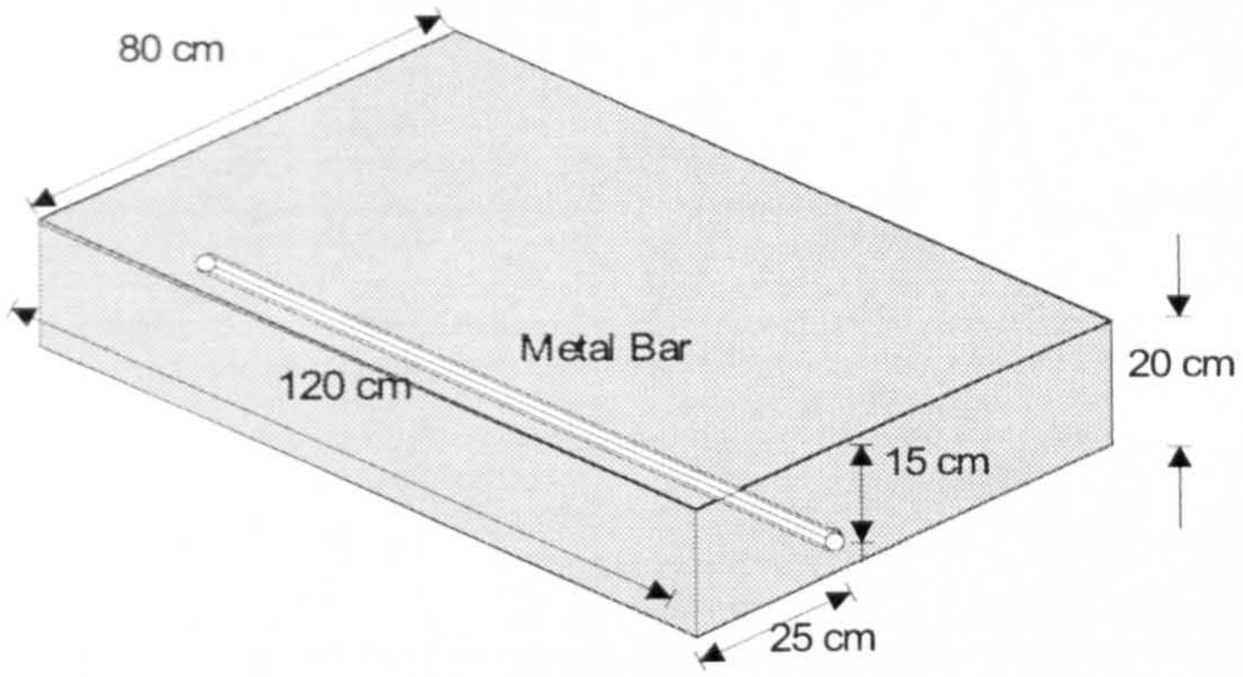

(a)

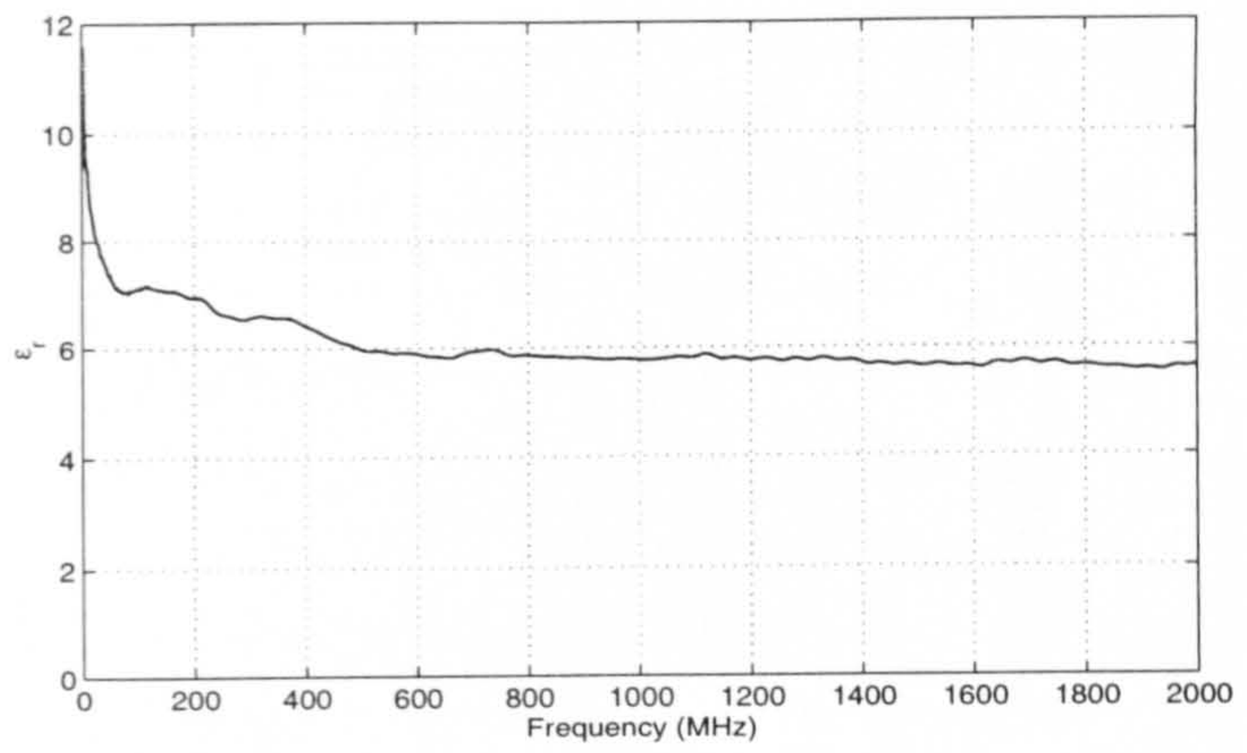

(b)

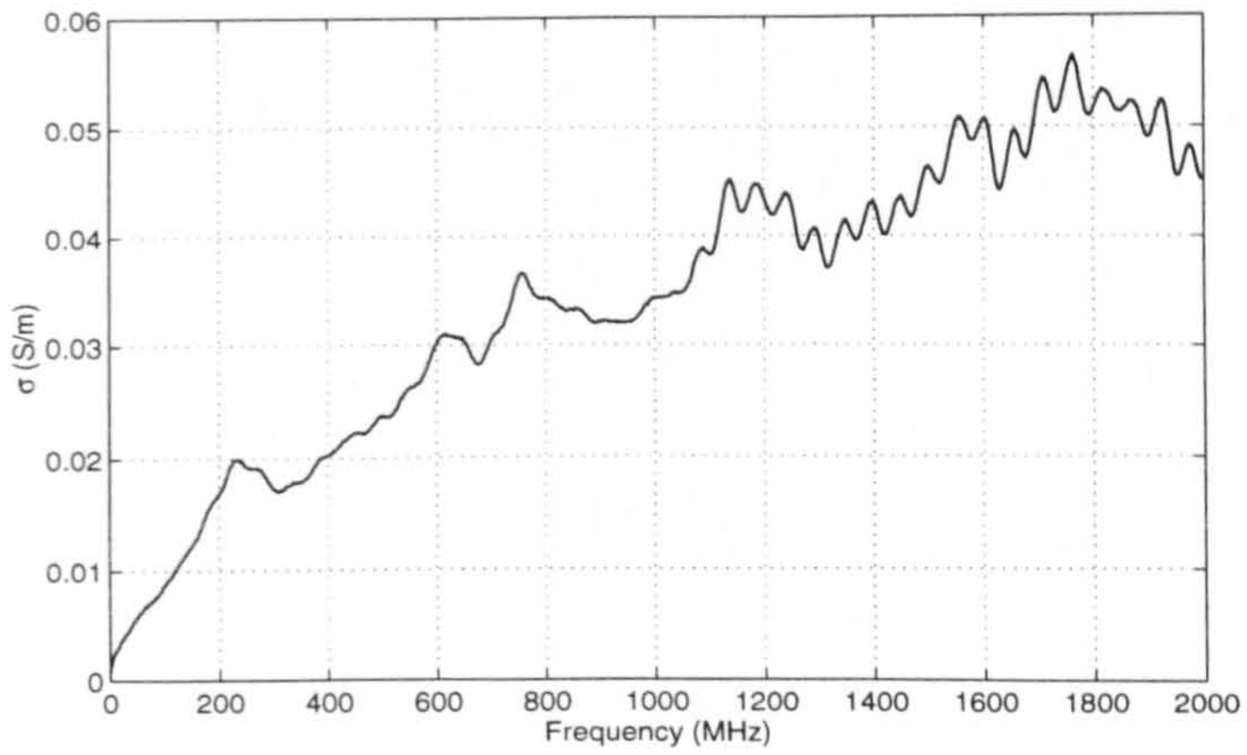

(c)

Figure 5.4: (a) A two years old concrete block. (b) The permittivity and (c) conductivity of dry concrete measured by the transmission-line method.

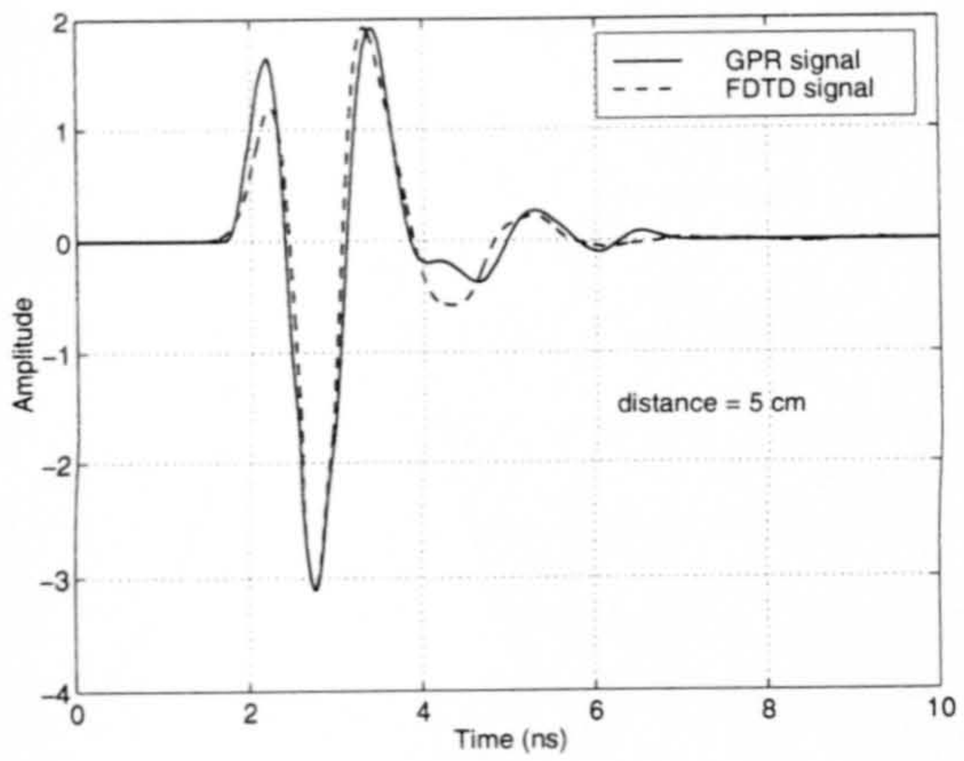

(a)

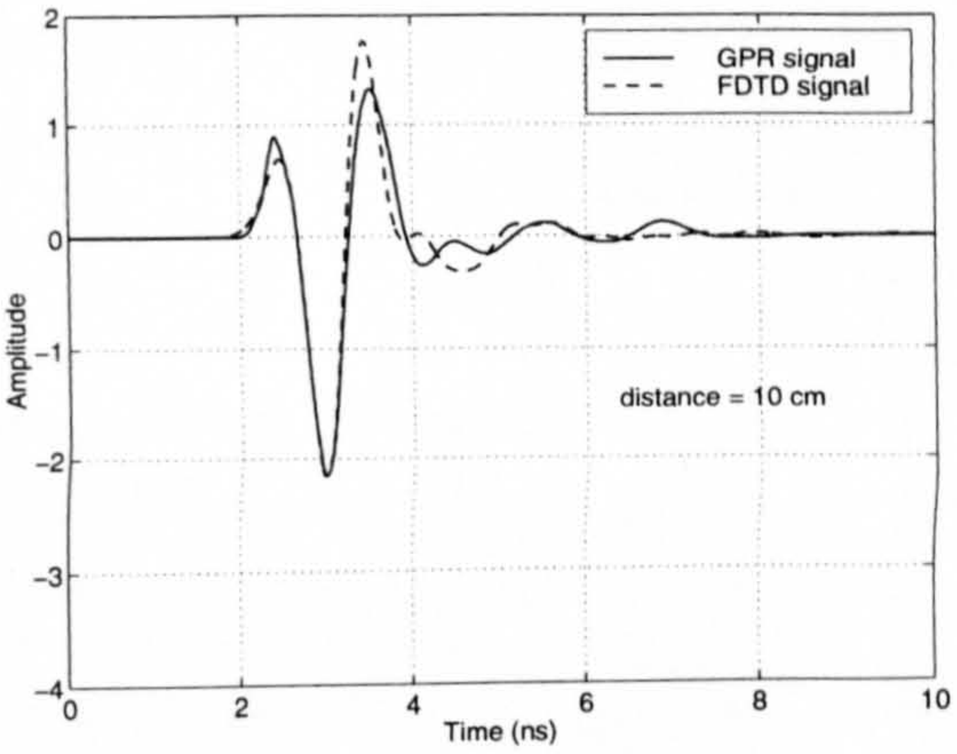

(b)

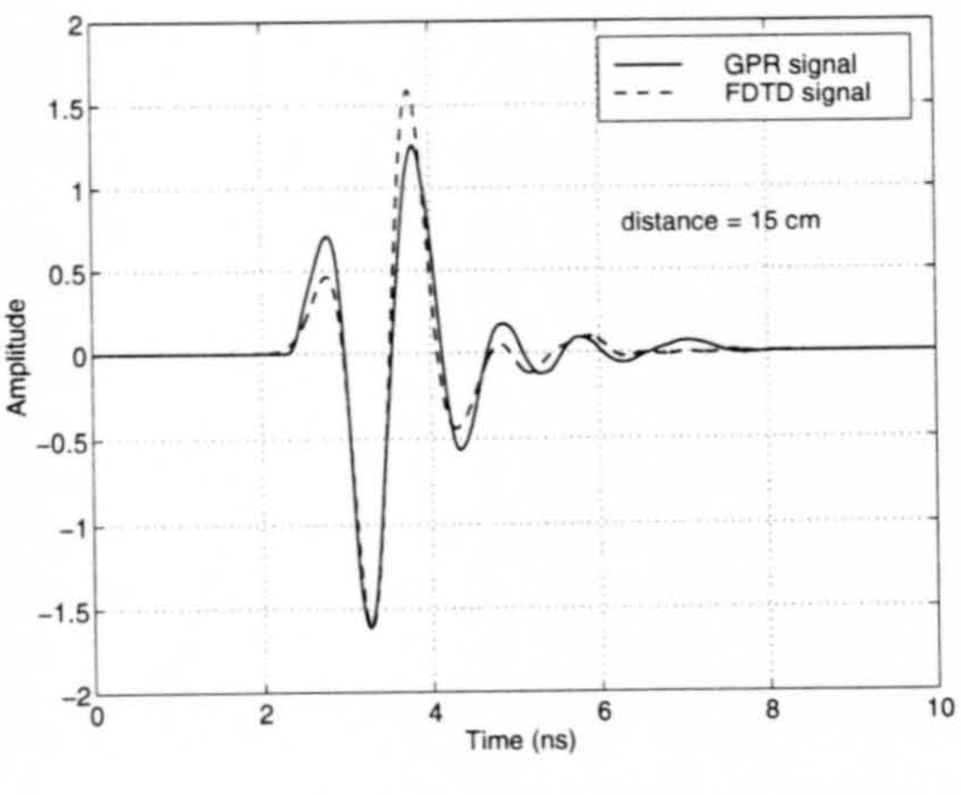

(c)

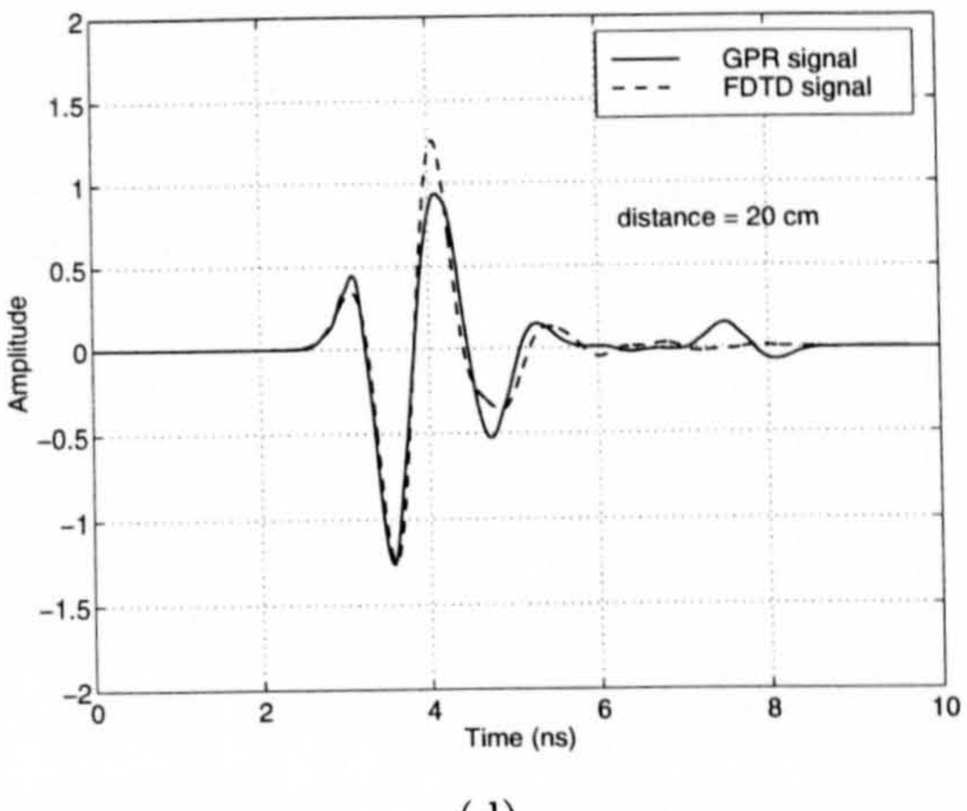

(d)

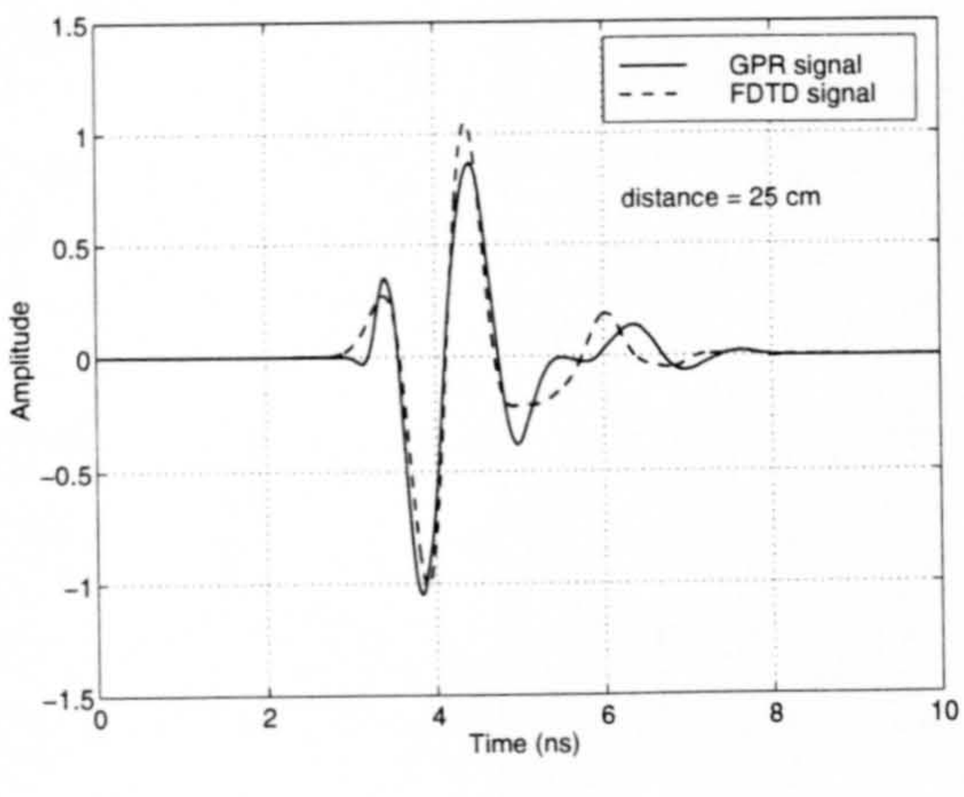

(e)

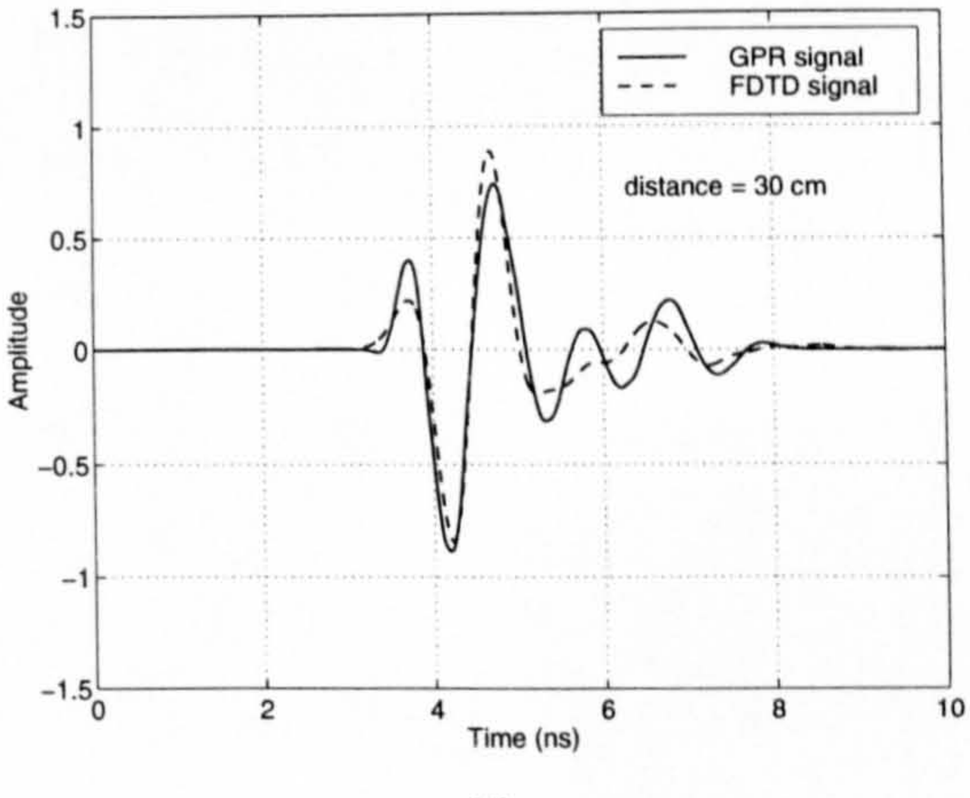

(f)

Figure 5.5: The measured and simulated GPR signals with different antenna to concrete separations.

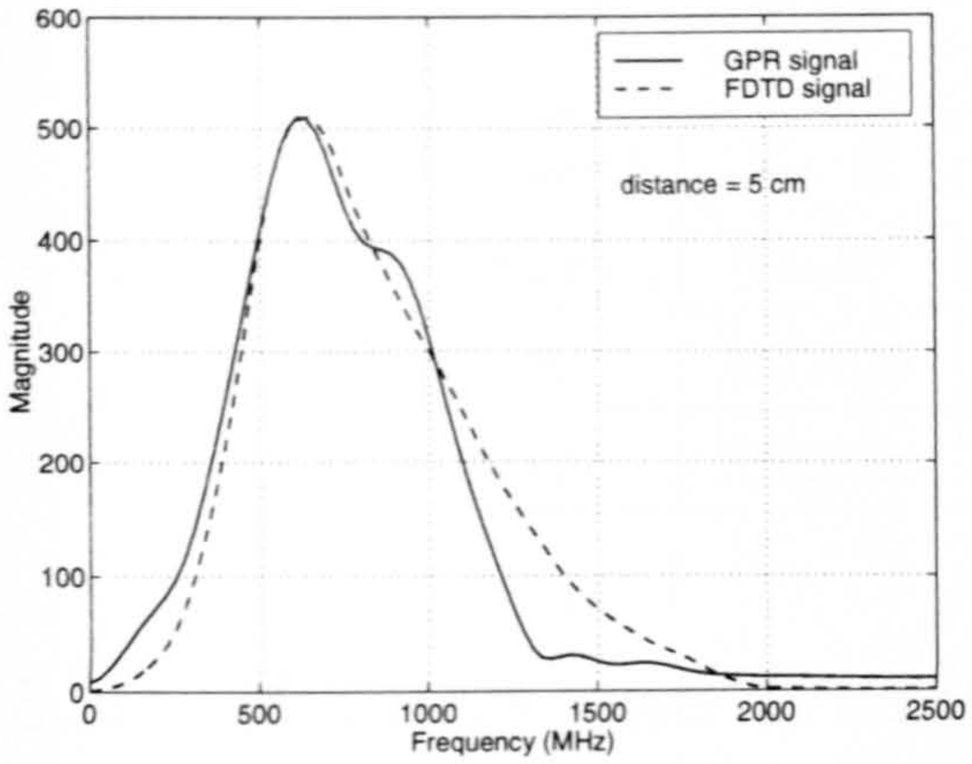

(a)

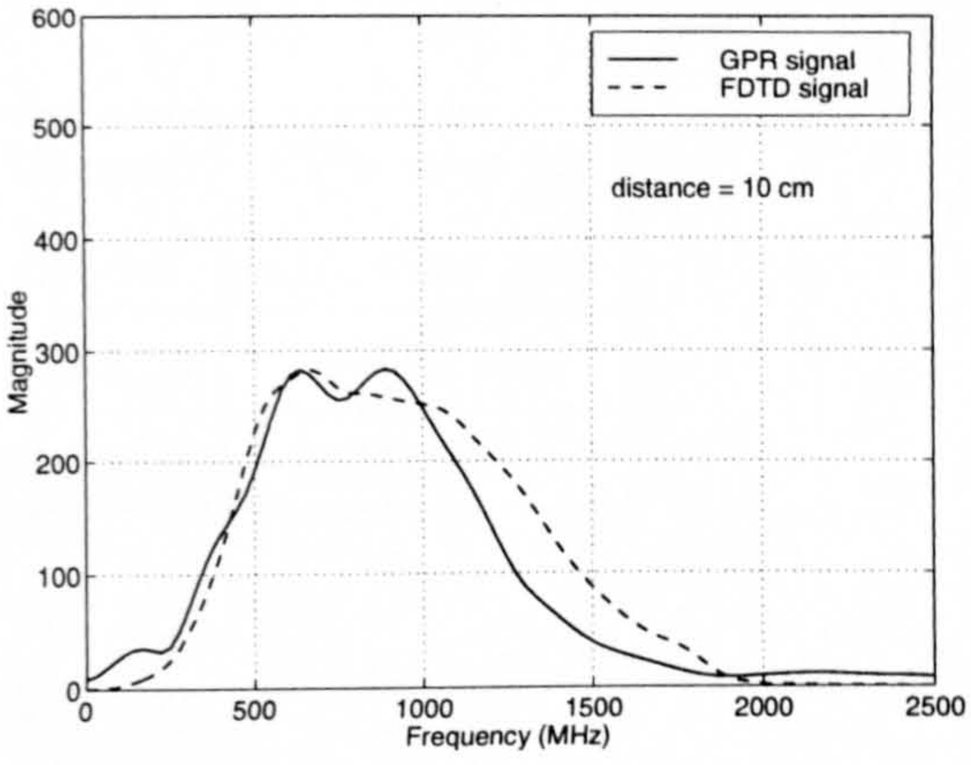

(b)

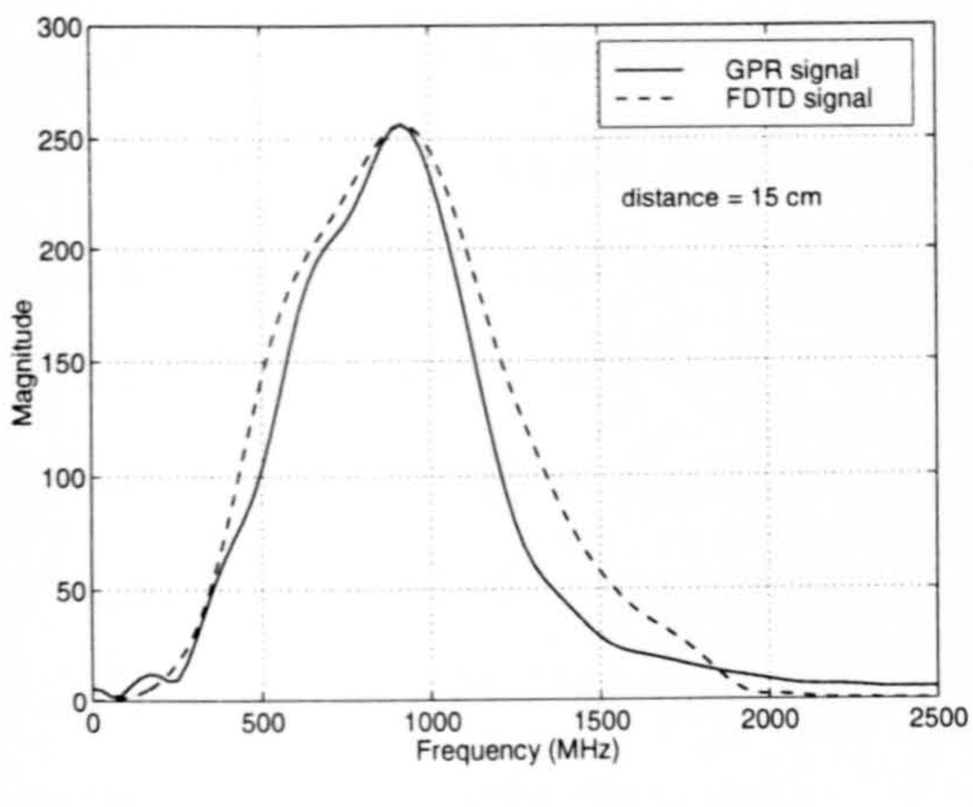

(c)

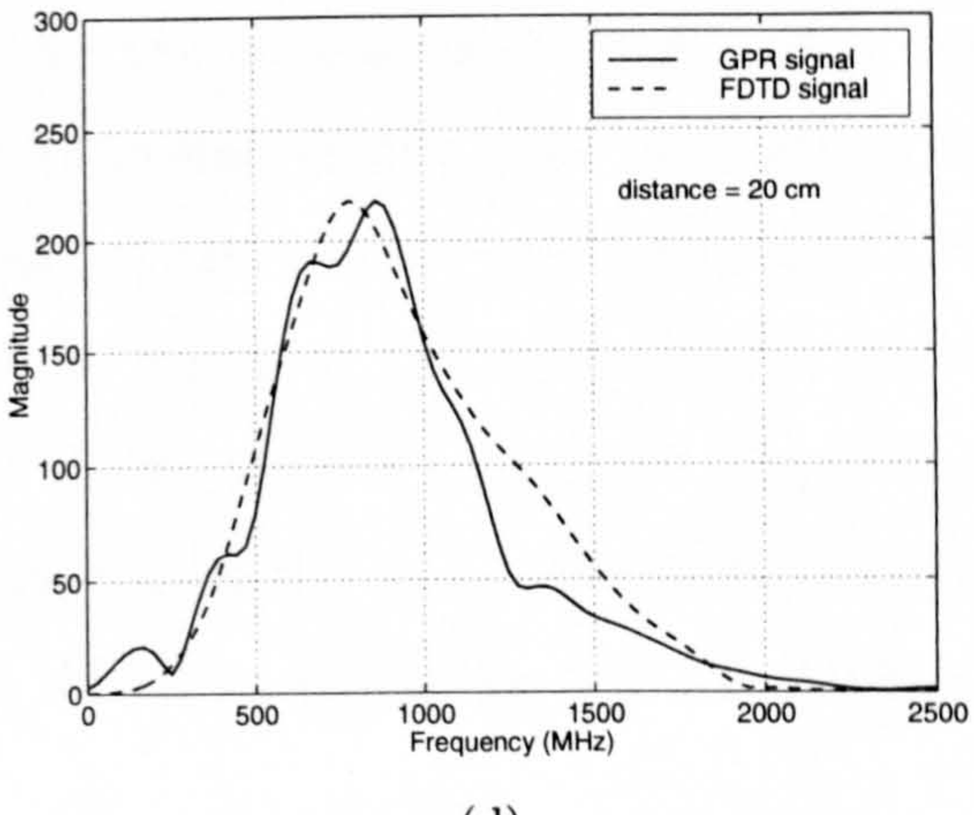

(d)

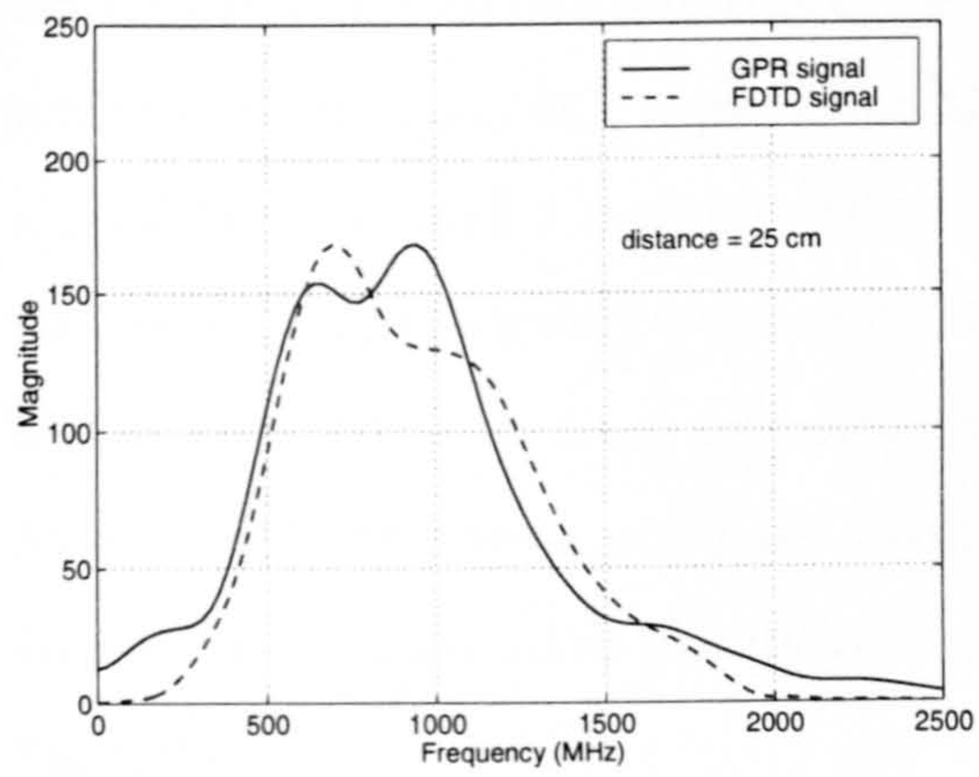

(e)

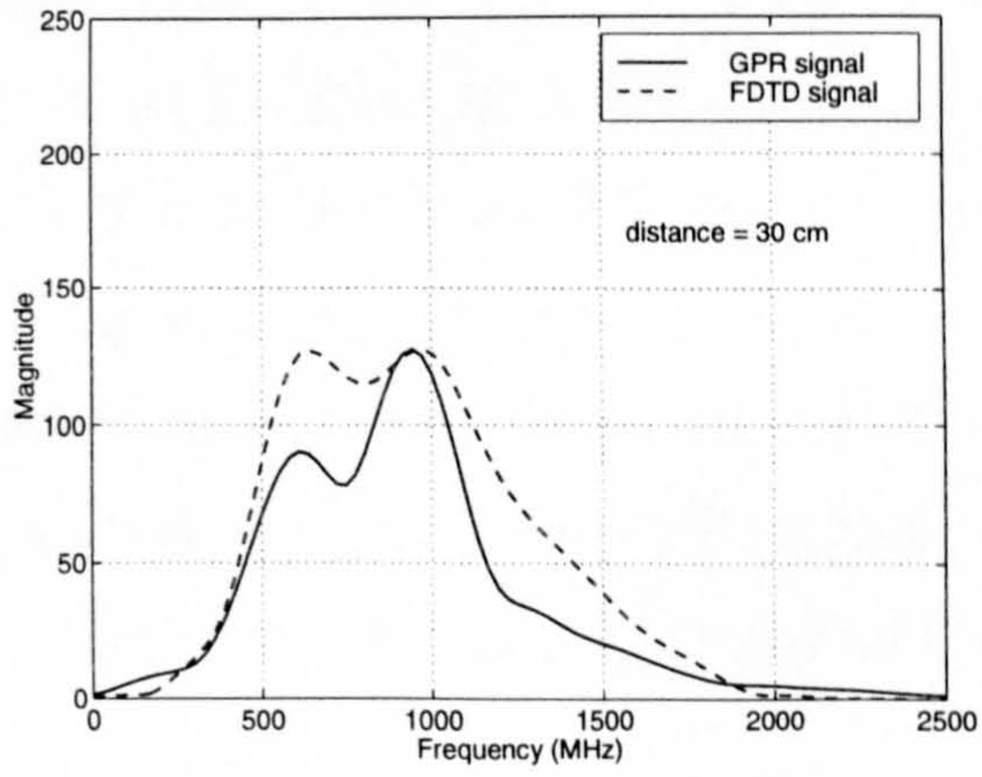

(f)

Figure 5.6: The same signals of Fig. 5.5 in the frequency domain.

Table 5.1: The minimum and maximum costs for the FDTD simulations presented in Fig. 5.5.

Separation distance	No. of cells	Memory needed	CPU time for 3071 time step
5 cm	6779520	540 MB	25680 sec
30 cm	10440000	806 MB	52610 sec

5.4 Results and Discussion

Several examples will be provided to evaluate the accuracy of the new models over the conventional one. Furthermore, the models will be tested using the RMBI to reconstruct the profile of multi-layered media. The data shown in this section and utilized in the processing are calibrated by removing the background from the original data. We refer to Equation (5.2.1) as the FR model in which only the First Reflection from the medium is considered. Equations (5.2.8) and (5.2.19) are respectively referred as the AM-MW (Metal-Water) model and the AM-MM (Metal-Metal) model in which the Antenna-Medium coupling is taken into account.

Example 5.1. The data in this example is generated by the FDTD simulation, which is carried out at 6 separations $d = 5, 10, 15, 20, 25, 30$ for a copper plate, a pool of water and a medium with ($\epsilon_r = 6$, $\sigma = 0.04$ S/m). The signals from the medium have already been shown in Fig. 5.5. The goal is to regenerate the signal due to the medium by using the FR model, AM-MW model and AM-MM model, and then compare them with the corresponding FDTD signal. In addition, the models are utilized to derive the reflection coefficient of the medium.

According to (5.2.19), it is possible to make 5 selections for d_b among the six separations for any fixed d_a. The selection, which yields the best correlation between the FDTD and the AM-MM model signals, is applied. The correlation

is defined by the Relative Mean Square Error (Relative MSE) as

$$\text{Relative MSE} = \frac{\sum_{n=1}^{N} \left| S^{MM}(\omega_n) - S^{FDTD}(\omega_n) \right|^2}{\sum_{n=1}^{N} \left| S^{FDTD}(\omega_n) \right|^2} \tag{5.4.1}$$

where $S^{FDTD}(\omega_n)$ is the frequency domain component of the FDTD signal with N samples and $S^{MM}(\omega_n)$ is the value calculated from the AM-MM model at angular frequency ω_n. Separation pairs (d_a, d_b) that resulted in good Relative MSE's were: (5 cm, 10 cm), (10 cm, 15 cm), (15 cm, 20 cm), (20 cm, 25 cm), (25 cm, 30 cm) and (30 cm, 25 cm).

Figures 5.7 and 5.8 show the resultant signals and reflection coefficients respectively. It is evident that the AM models provides a better approximation than the FR model. This fact is quantitatively illustrated in Fig. 5.9 where the Relative MSE between the FDTD signal and the model signals are shown. One can observe that the suitable separation for the simulated GPR antenna could be within [15 cm, 30 cm]. It is advantageous to use the shortest suitable separation in order to provide the highest signal to disturbance (noise) ratio, as Fig. 5.7 indicates that an increase of the separation reduces the received power. Besides, the power of the disturbances generated by the surrounding environment is an ascending function of the separation. In this example, the imperfect boundary condition in the FDTD method generates a little reflection that most influences the received signal at large separations. Of course, both models become less accurate when the separation is decreased. Consequently, there is an optimum separation, as Fig. 5.9 shows that $d = 15$ cm (it can hardly be seen) and $d = 20$ cm give the minimum error for the AM-MW model and AM-MM model respectively. Similar phenomenon could also happen for the FR model if the disturbances were more powerful. This hypothesis is verified in the next example where the experimental GPR data, bearing substantial disturbances, are involved.

Furthermore, it is observable from Fig. 5.9 that the AM-MM model presents smaller Relative MSE than AM-MW model for the separations of interest.

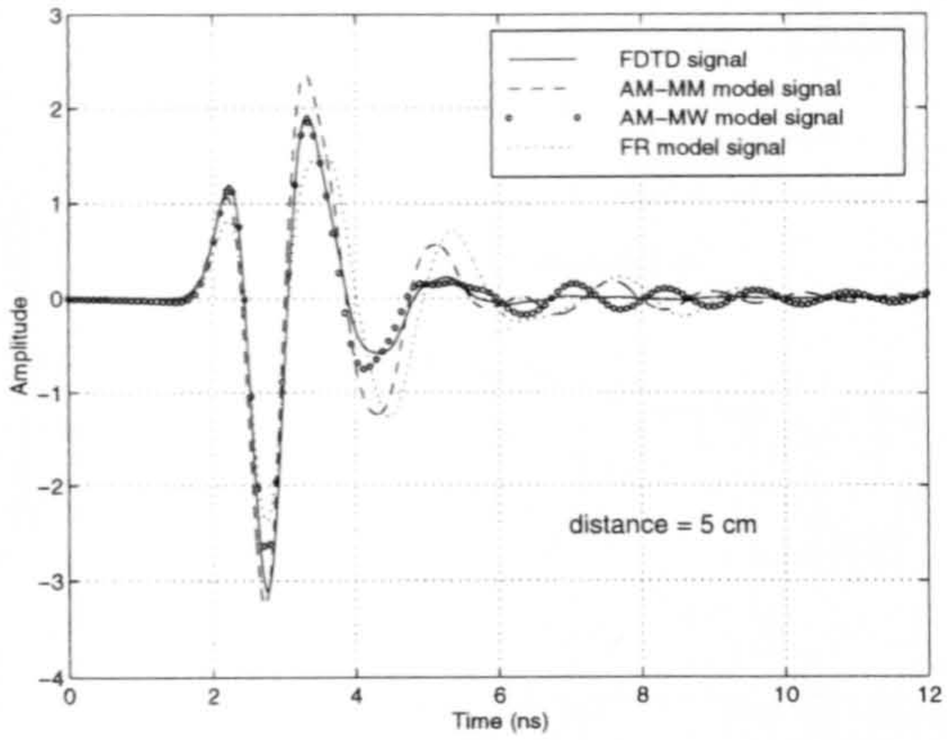

(a)

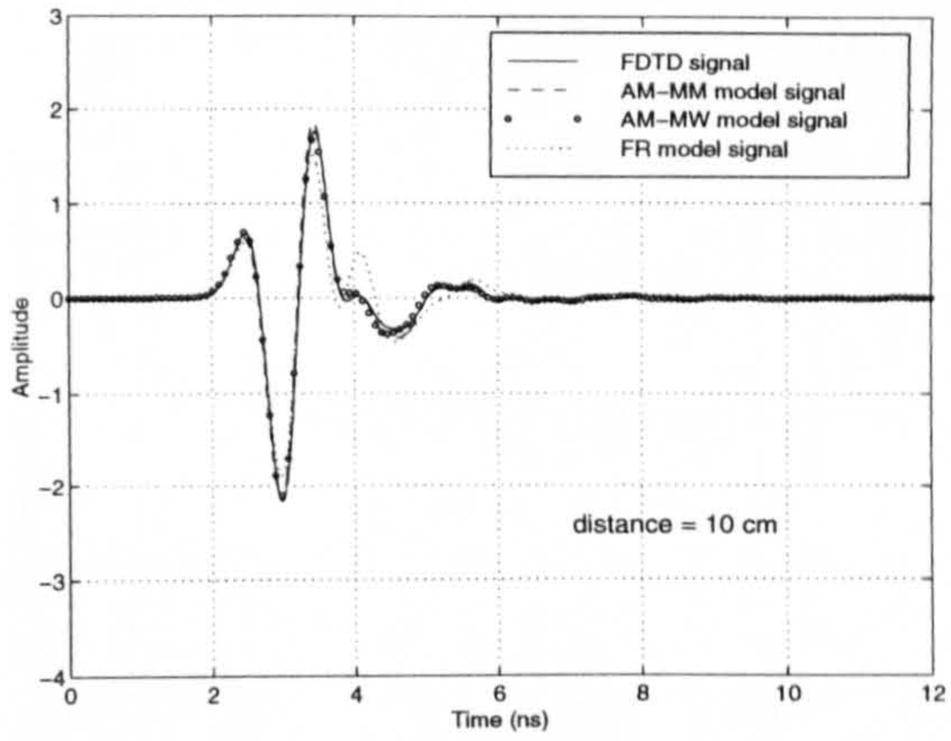

(b)

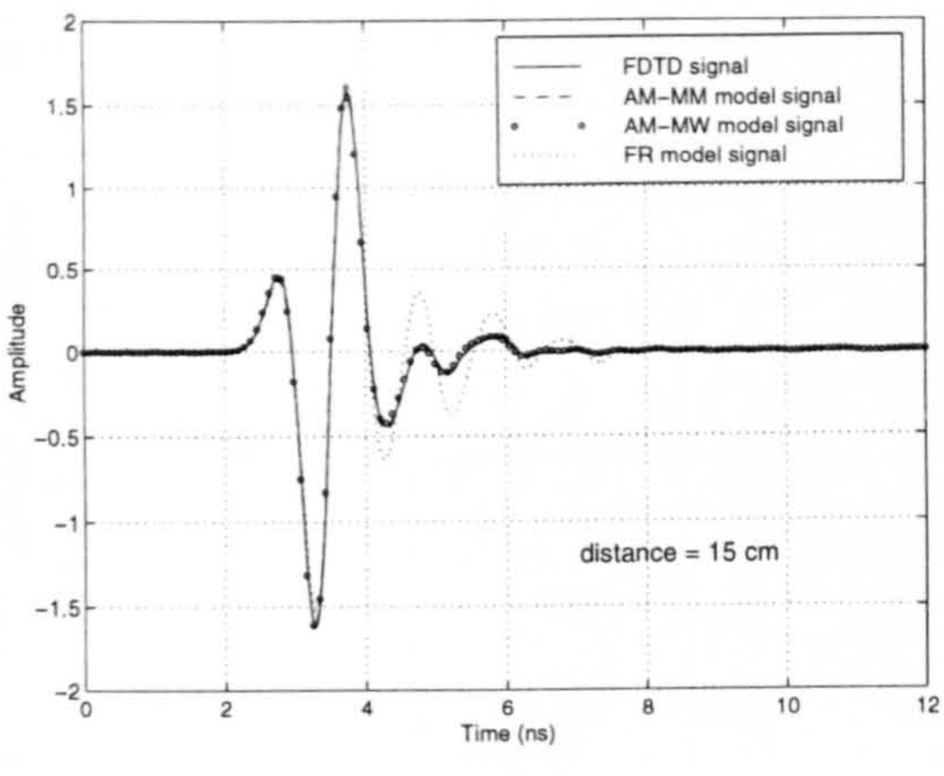

(c)

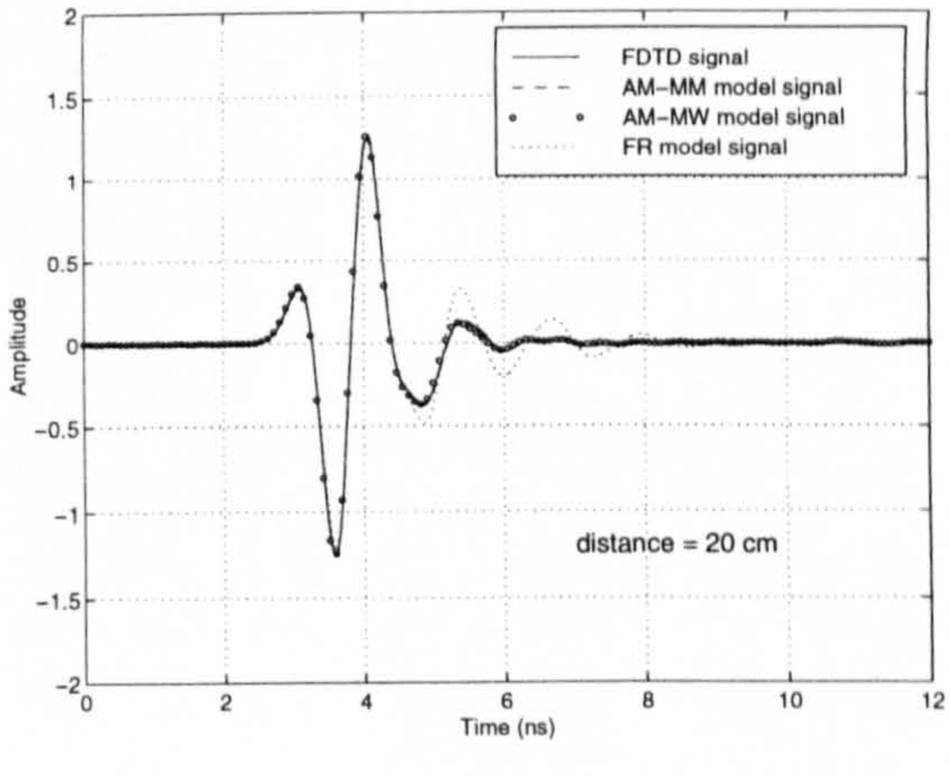

(d)

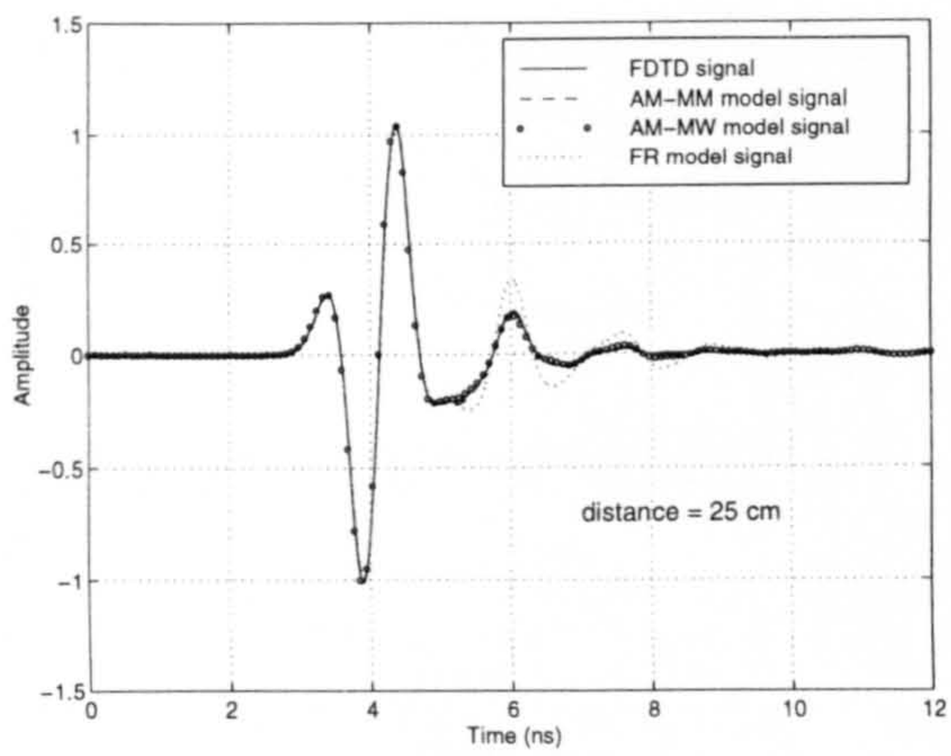

(e)

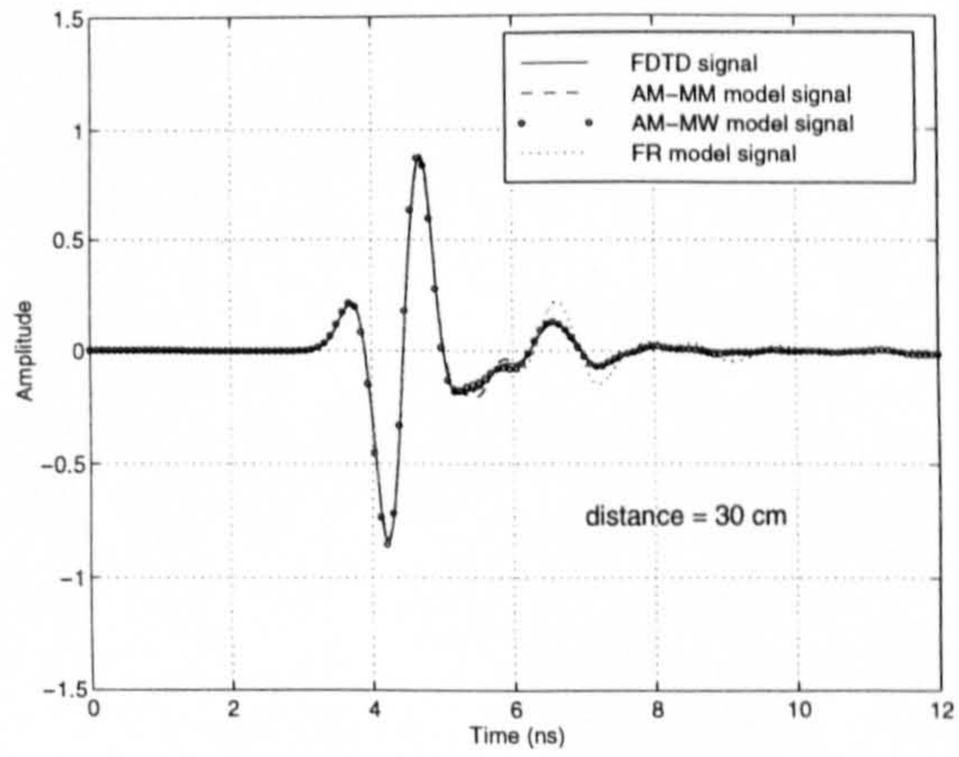

(f)

Figure 5.7: A comparison between the FDTD signals, AM-MM model signals, AM-MW model signals and FR model signals due to the presence of the medium with $\epsilon_r = 6$ and $\sigma = 0.04$ S/m.

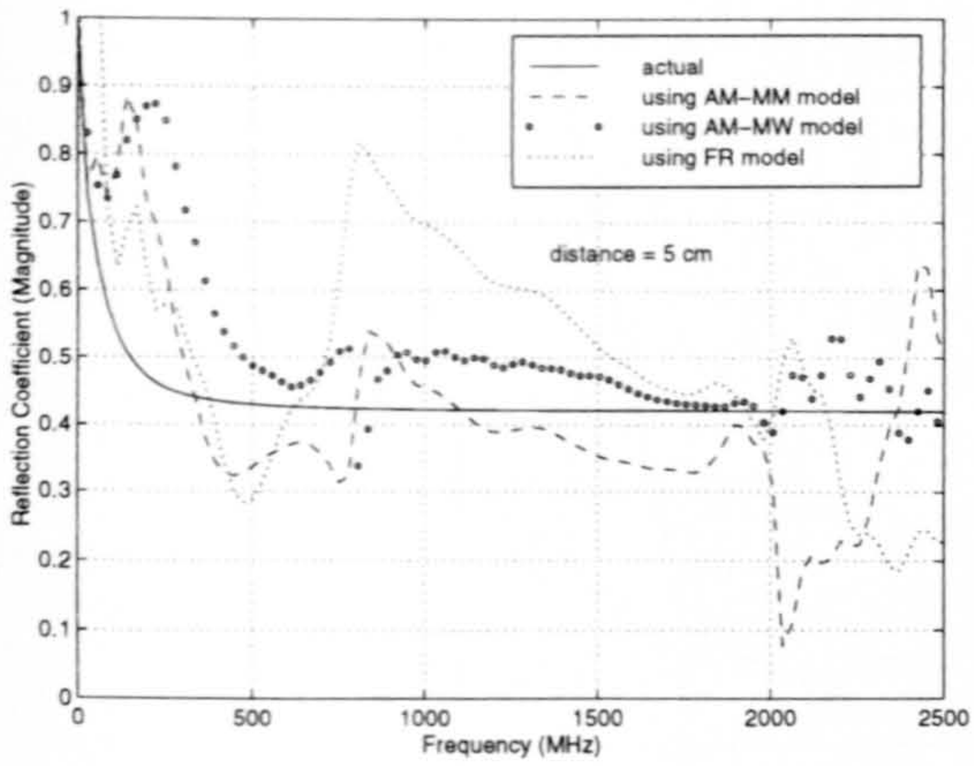

(a)

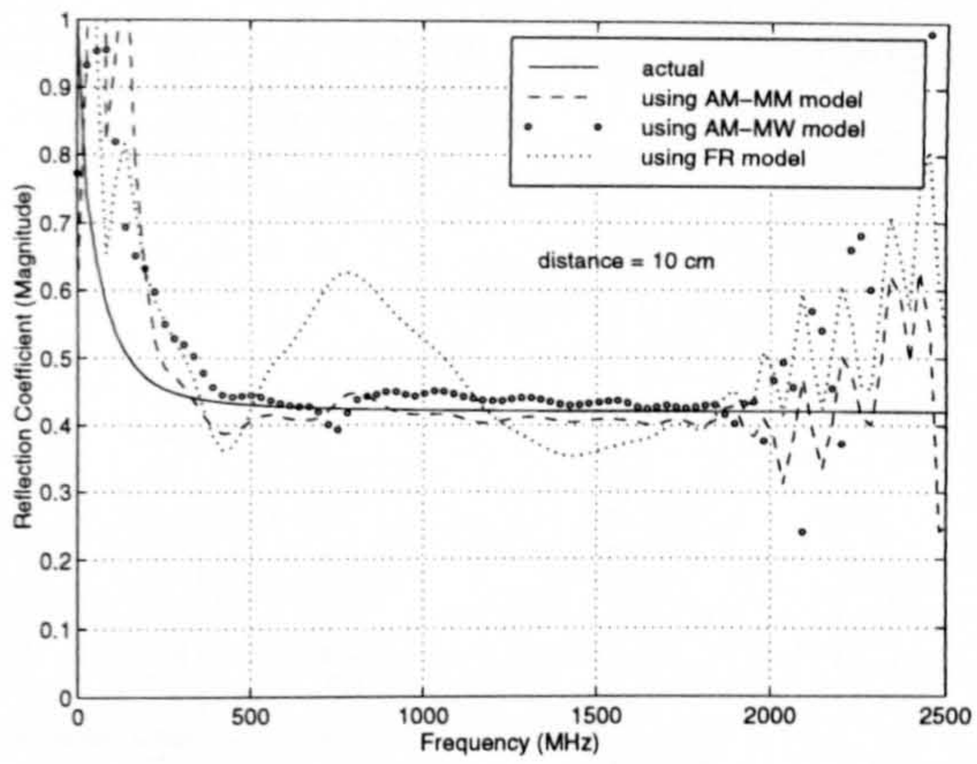

(b)

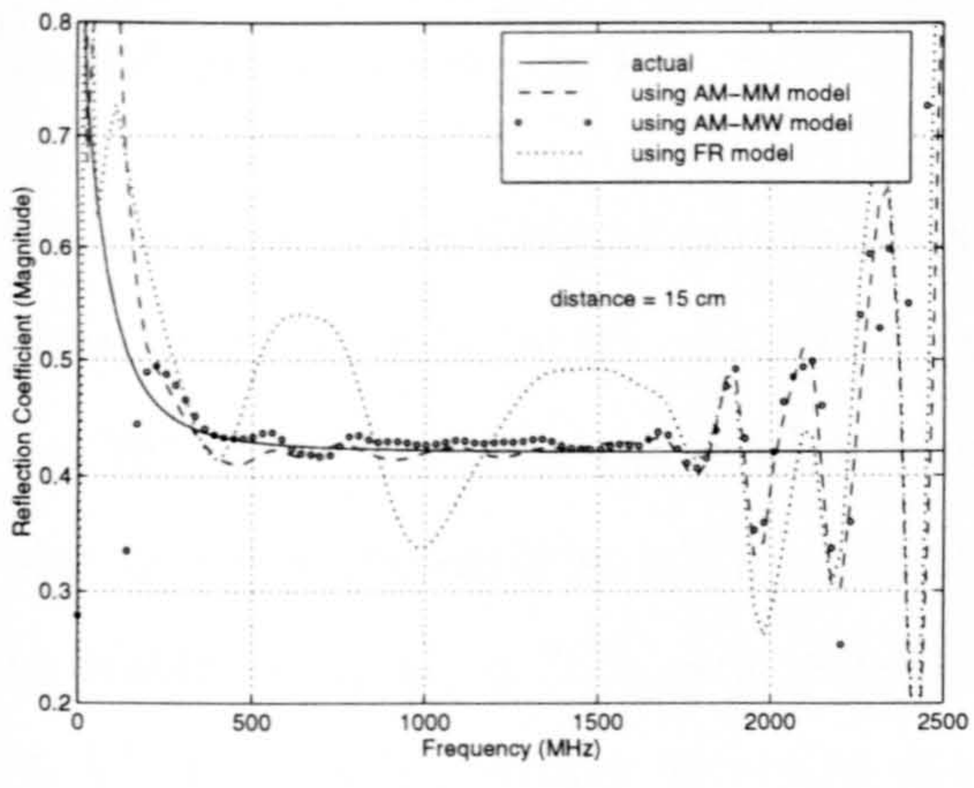

(c)

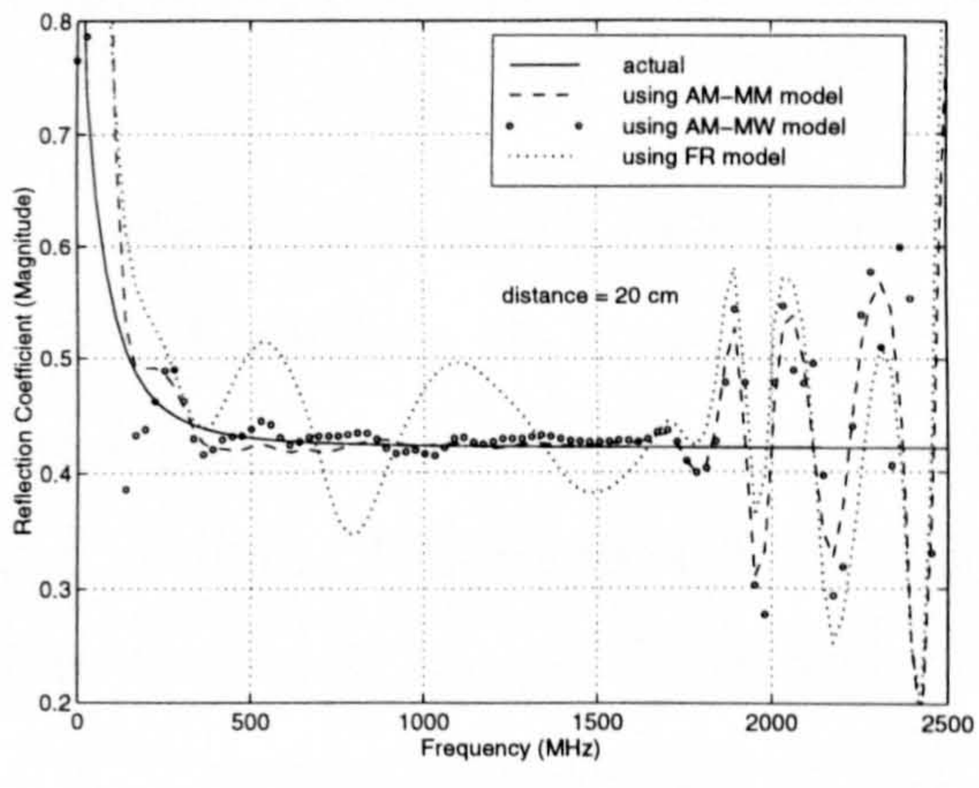

(d)

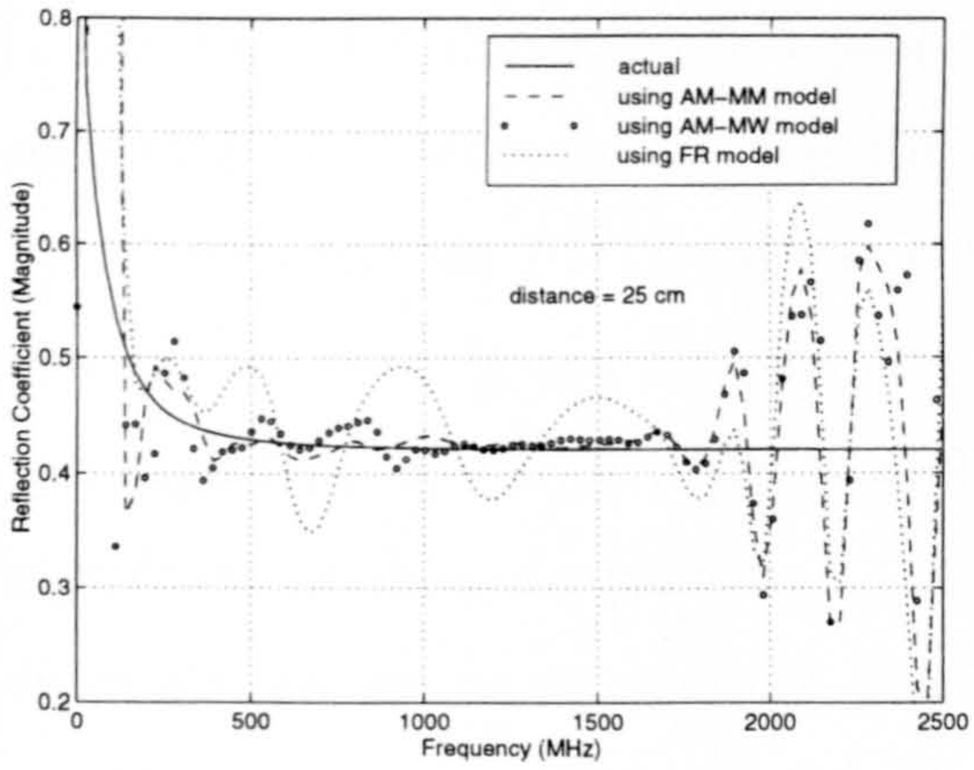

(e)

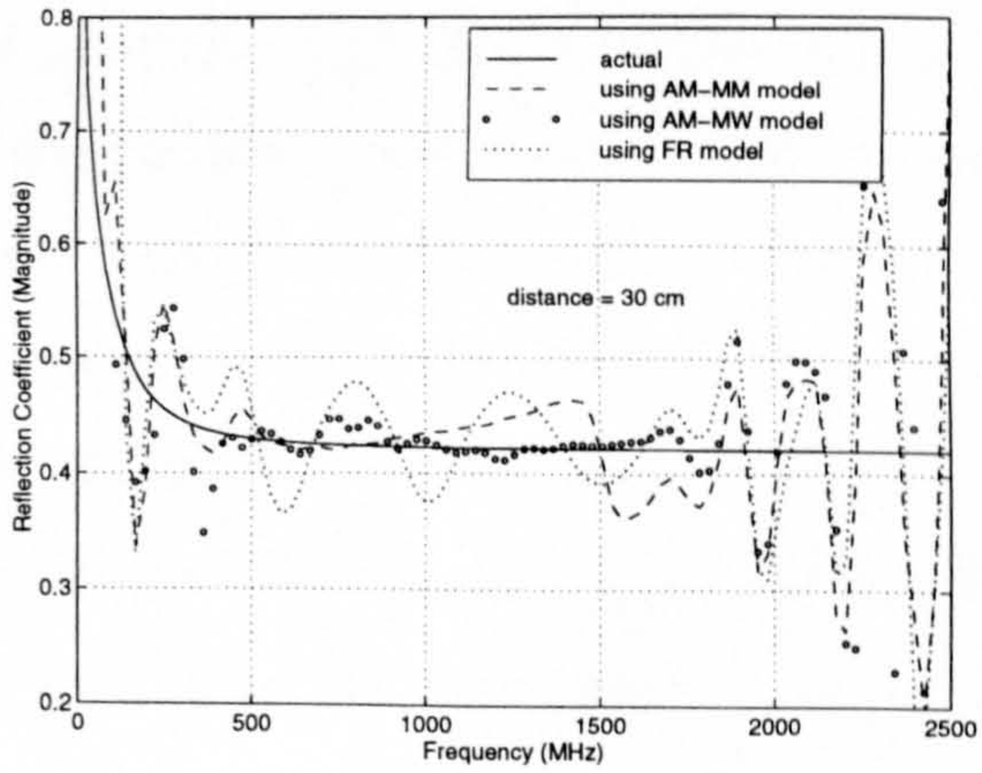

(f)

Figure 5.8: The reflection coefficients obtained from the FDTD signals appeared in Fig. 5.7 using different kinds of modelling.

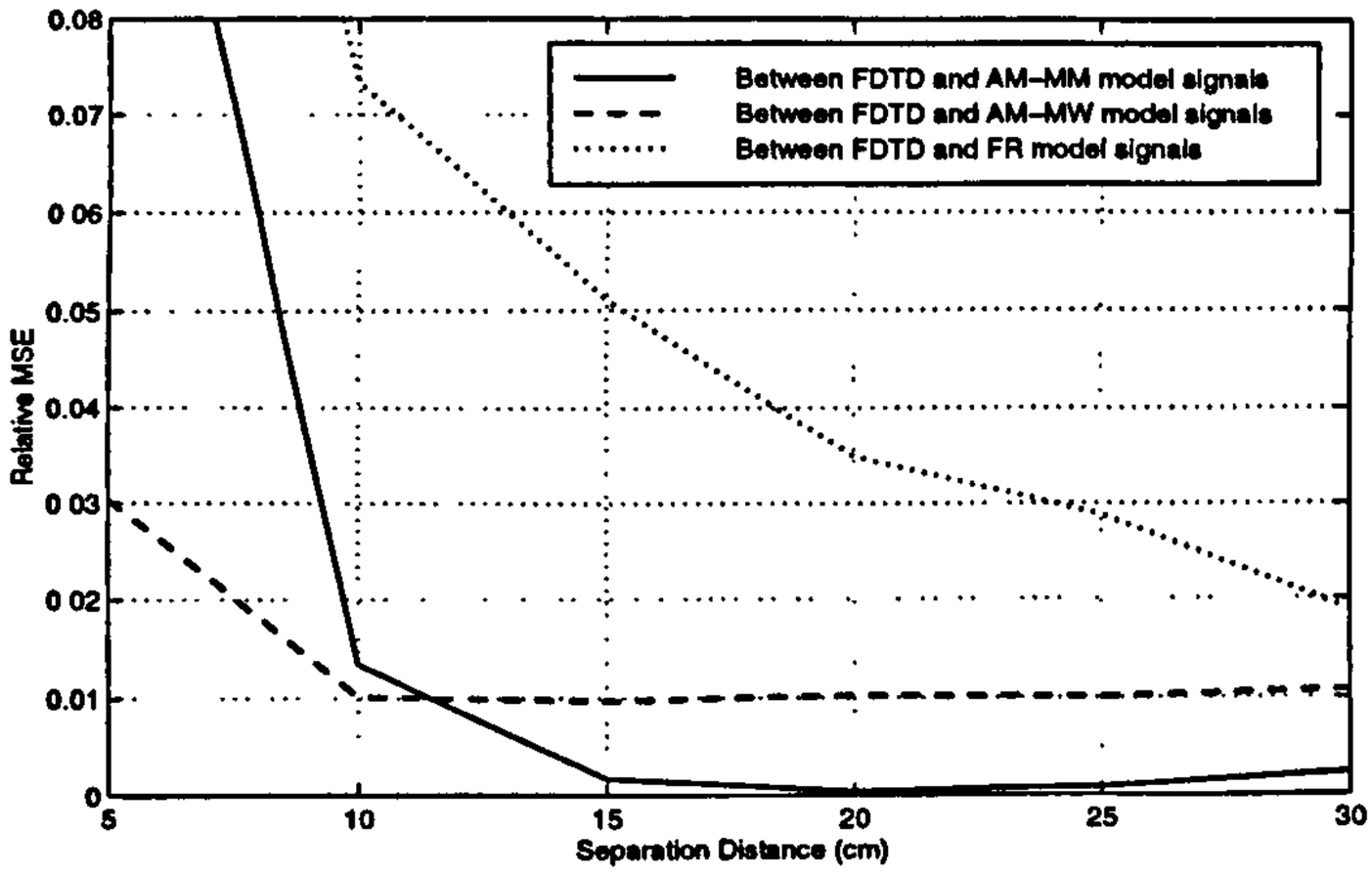

Figure 5.9: The relative mean square error between the FDTD and different model signals shown in Fig. 5.7.

This might be because of two reasons: Firstly the reflection coefficient of the simulated water ($\epsilon_r = 80, \sigma = 0.01$ S/m) is different from the constant $\Gamma^{Wat} = -0.797$ that is used in the model (Equation (5.2.8)). Secondly the FDTD cell size is not sufficiently small for the water medium. The wavelength at 1GHz in water is equal to 33.5 mm, which does not satisfy the condition: cell size $\leq \lambda/20$. This introduces errors in the FDTD simulation, especially at higher frequencies.

As Fig. 5.8 illustrates, all models produce large errors in the resulting reflection coefficients at low and high frequencies. This can be explained by Fig. 5.10 where the FDTD signals in the frequency domain are shown for the distance 20 cm. It can be seen that the power of the signals drops at low and high frequencies. The effect of disturbances and noise may therefore be significant at these frequencies. As mentioned in Section 5.2, the near-field effect also causes an error at low frequencies (large wavelengths).

The reflection coefficients can be used to calculate the permittivity and conductivity at individual frequencies. Since the medium consists of 1 layer, it is straightforward to analytically find the parameters from the real and imag-

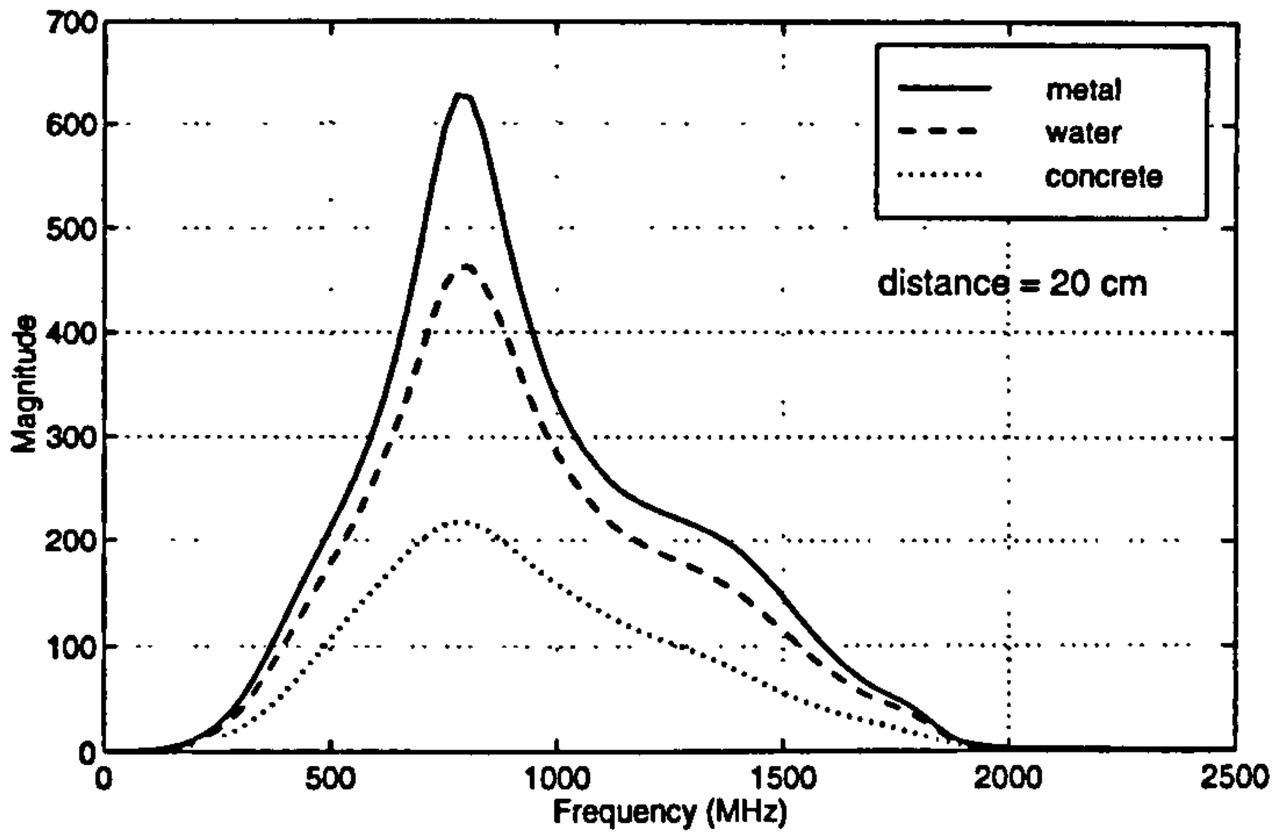

Figure 5.10: The frequency components of the FDTD signals for the separation distance = 20 cm.

inary parts of the reflection coefficients. Figure 5.11 shows the permittivity and conductivity of the medium, obtained in the frequency interval [400 MHz, 1500 MHz]. It is evident again that the AM models offer smaller errors.

The parameters of the medium can also be reconstructed numerically by minimizing the MSE function (the RMBI). Applying this method while using the frequency components of the FDTD signal at 8 frequencies equally spaced in the interval [600 MHz, 800 MHz], the resultant relative errors for the permittivity and conductivity are illustrated in Fig. 5.12. The relative error for a parameter p is defined by

$$e_r = \frac{|p_{derived} - p_{actual}|}{p_{actual}} \tag{5.4.2}$$

One may speculate that the FR model has given the minimum permittivity error at separation 30 cm. This can be explained by Fig. 5.11(b) where for example at separation 15 cm, the FR model provides zero error for the permittivity ($\epsilon_r = 6$) at three frequencies, which are roughly 425, 775 and 1210 MHz. In fact, if another frequency range were chosen instead of [600 MHz, 800 MHz], the relative permittivity error of the FR model at 30 cm would be higher than the present one. As a result, the models should be compared by a criteria in

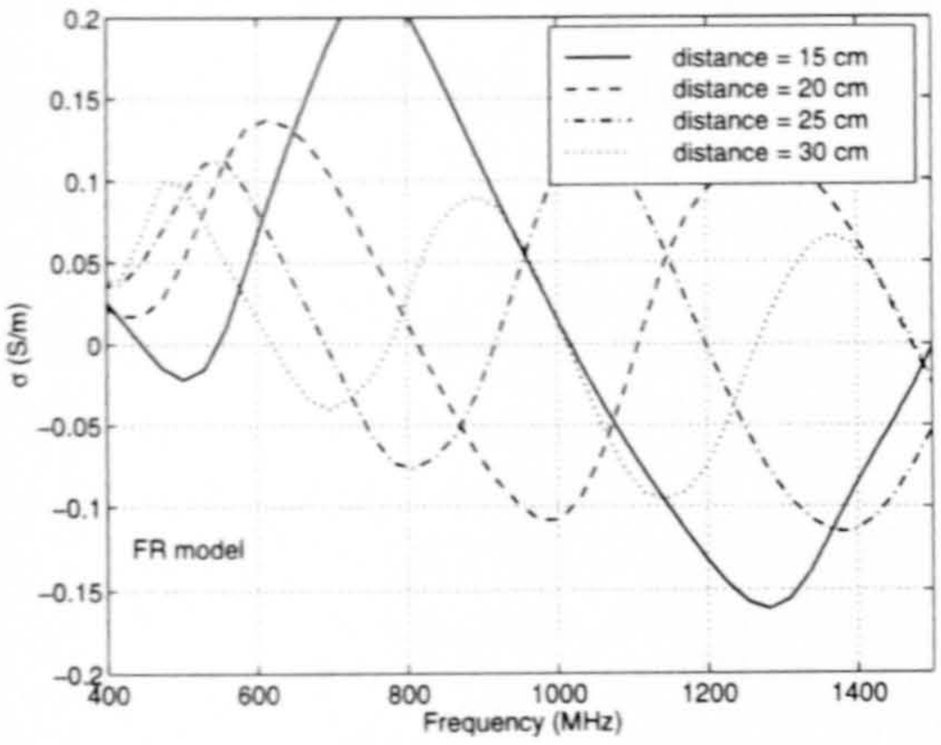

(a)

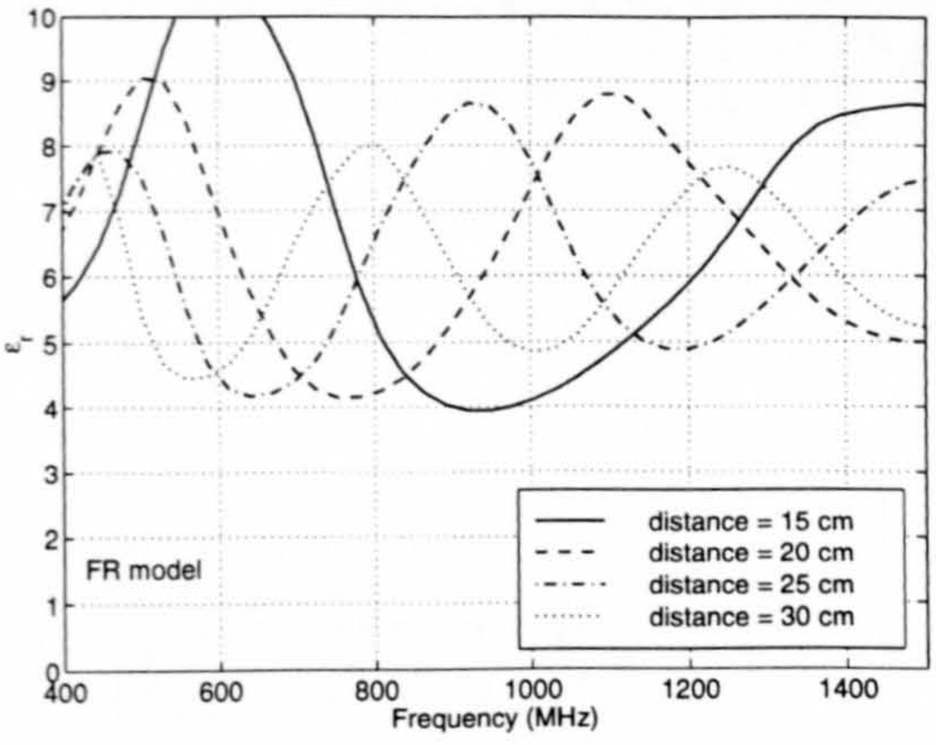

(b)

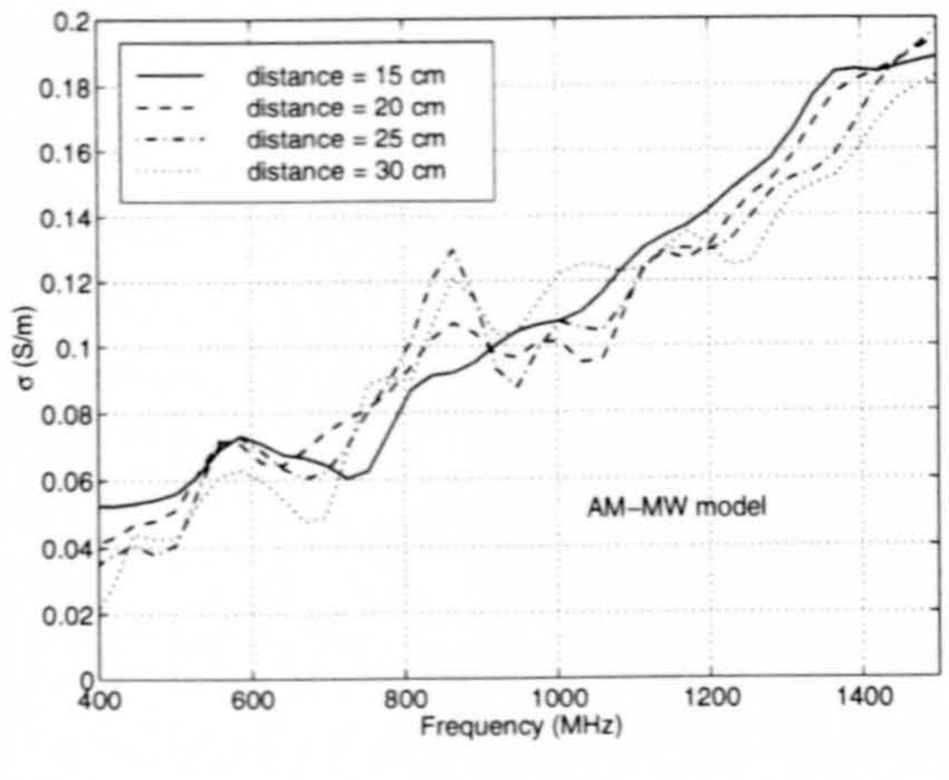

(c)

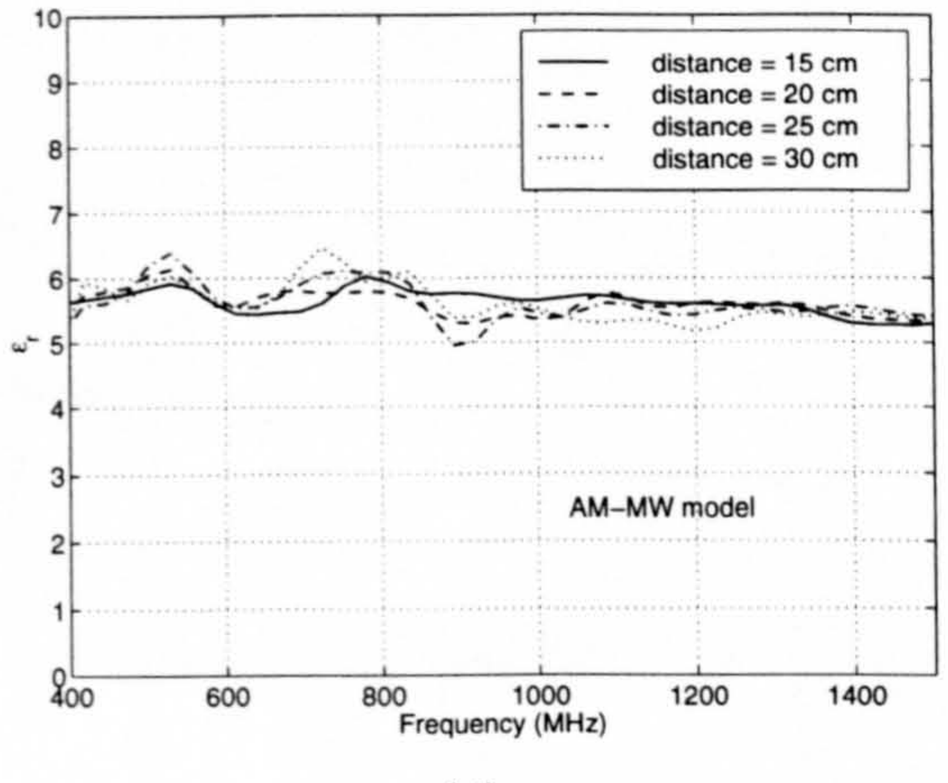

(d)

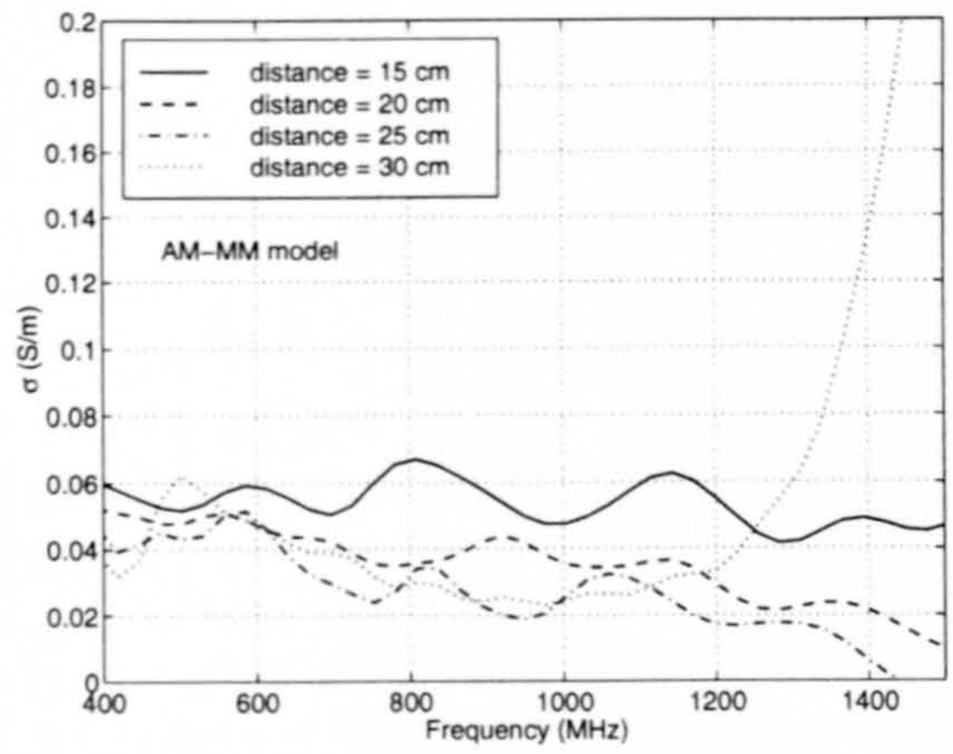

(e)

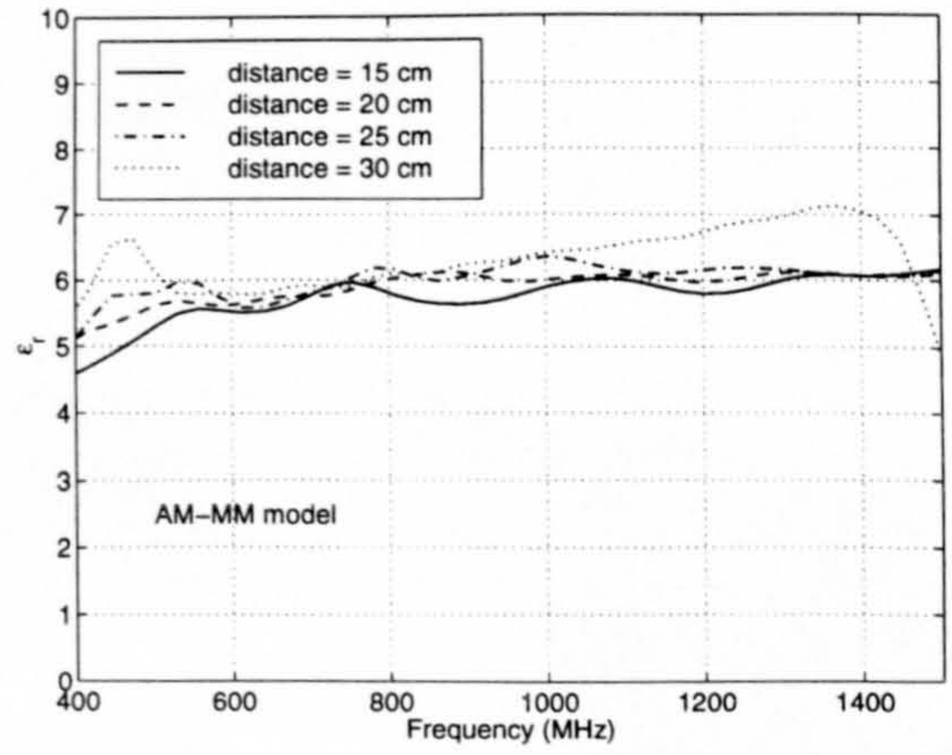

(f)

Figure 5.11: The permittivity and conductivity that are derived from the reflection coefficients shown in Fig. 5.8 at individual frequencies for a medium with $\epsilon_r = 6$ and $\sigma = 0.04$ S/m.

which the outputs of the models at all frequencies take part. Such a criteria can be Relative MSE, defined by Equation (5.4.1) and shown in Fig. 5.9 for this example.

Example 5.2. This example is the counterpart of the previous example but

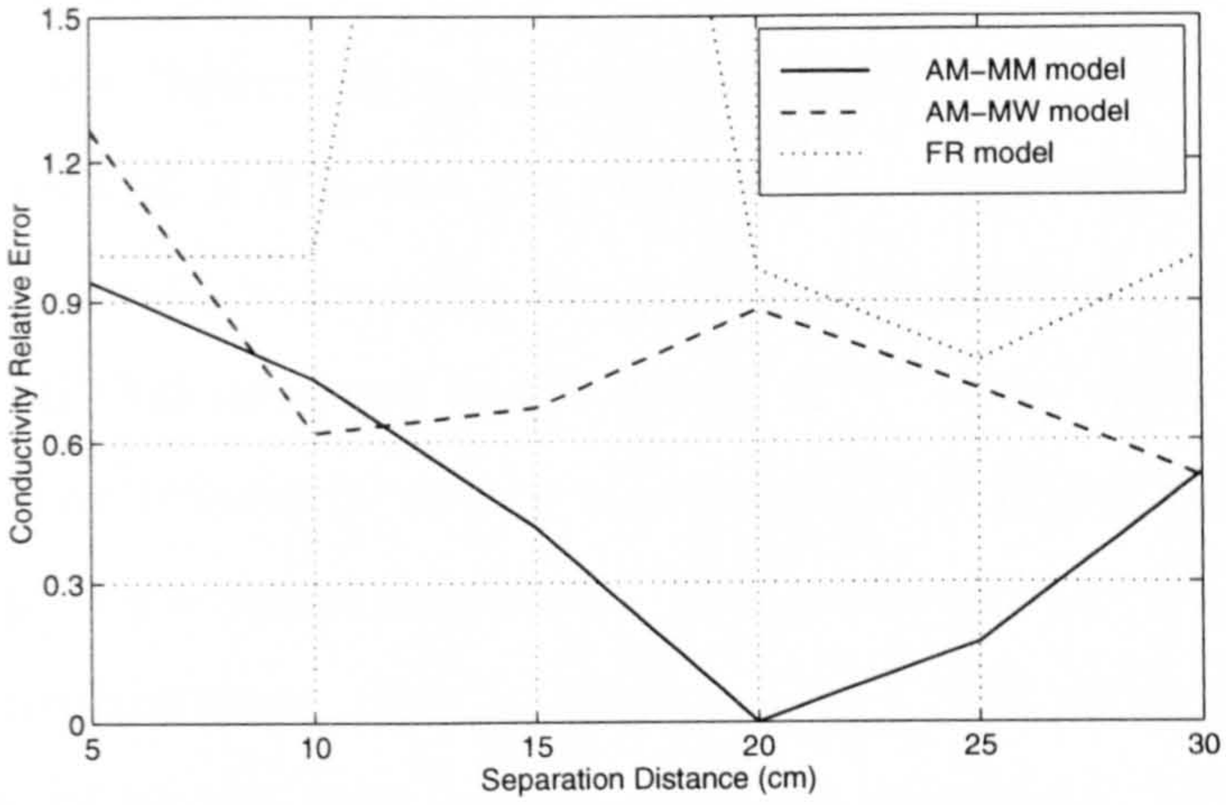

(a)

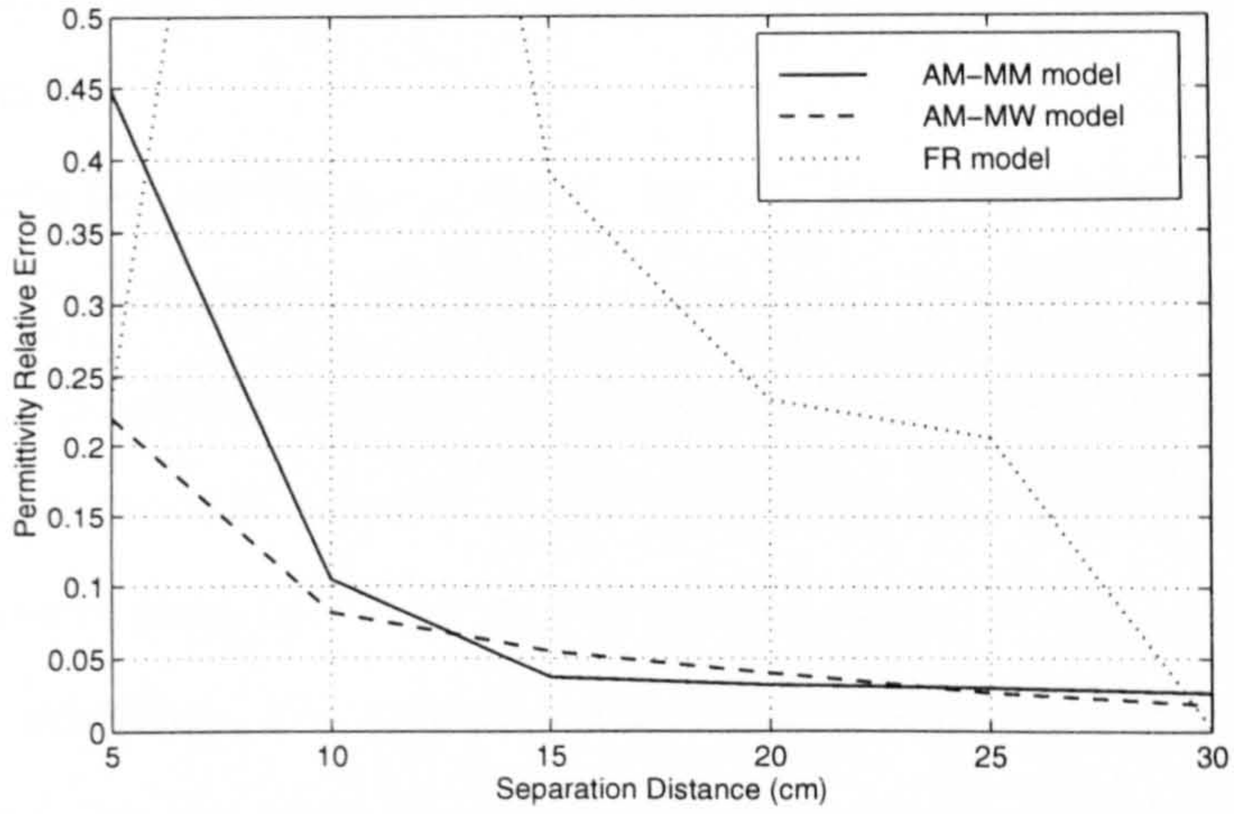

(b)

Figure 5.12: The relative errors of the medium parameters derived by the RMBI. The scattering data are the frequency components of the FDTD signals (shown in Fig. 5.7) at 8 frequencies over the range of [600 MHz, 800 MHz] with linear spacing

the data are experimental ones collected by the commercial GPR with 900 MHz antenna. The measurements were taken on the concrete block (Fig. 5.4(a)), a copper plate (100 cm × 90 cm) and a water container (100 cm × 75 cm × 25 cm). The separation pairs (d_a, d_b) that provided the best Relative MSE were: (5 cm, 10 cm), (10 cm, 15 cm), (15 cm, 20 cm), (20 cm, 15 cm), (25 cm, 20 cm) and (30 cm, 25 cm).

The results are illustrated in Fig. 5.13, 5.14 and 5.15. The first noteworthy thing is that the AM-MW model has presented a substantial error. As pointed out earlier, this could be because the reflection coefficient of the used water is different from that assumed in the model ($\Gamma^{Wat} = -0.797$). Nevertheless, we think the most influential source of error is the strong diffraction from the edge of the finite-size water container. This problem can be solved by using a large-aperture container. Due to some practical difficulties associated with the utilization of water, such as the accurate adjustment of the separation distance, the Metal-Water approach is to be given up and our attention is therefore paid to the Metal-Metal approach (although Metal-Water approach emerged at first).

As seen from the previous example, there is an optimum separation distance for each model, indicating by Fig. 5.15. The optimum separation for the FR model can however be seen readily in this example. When the distance is increased the models become more accurate. However, the power of the disturbances generated by the edge diffraction and unwanted reflections is also increased. In addition, the power received is reduced for larger distances. If the aperture of the concrete block and the copper plate were larger, it would be expected that the minimum points in Fig. 5.15 be shifted upwards.

Unlike Example 5.1, it can be observed from Fig. 5.14 that there is a considerable fluctuation in the reflection coefficients over the low-error frequency band [400 MHz, 1500 MHz] at separations 15, 20, 25 and 30 cm for the AM-MM model. This phenomenon also occurs due to the presence of strong diffractions,

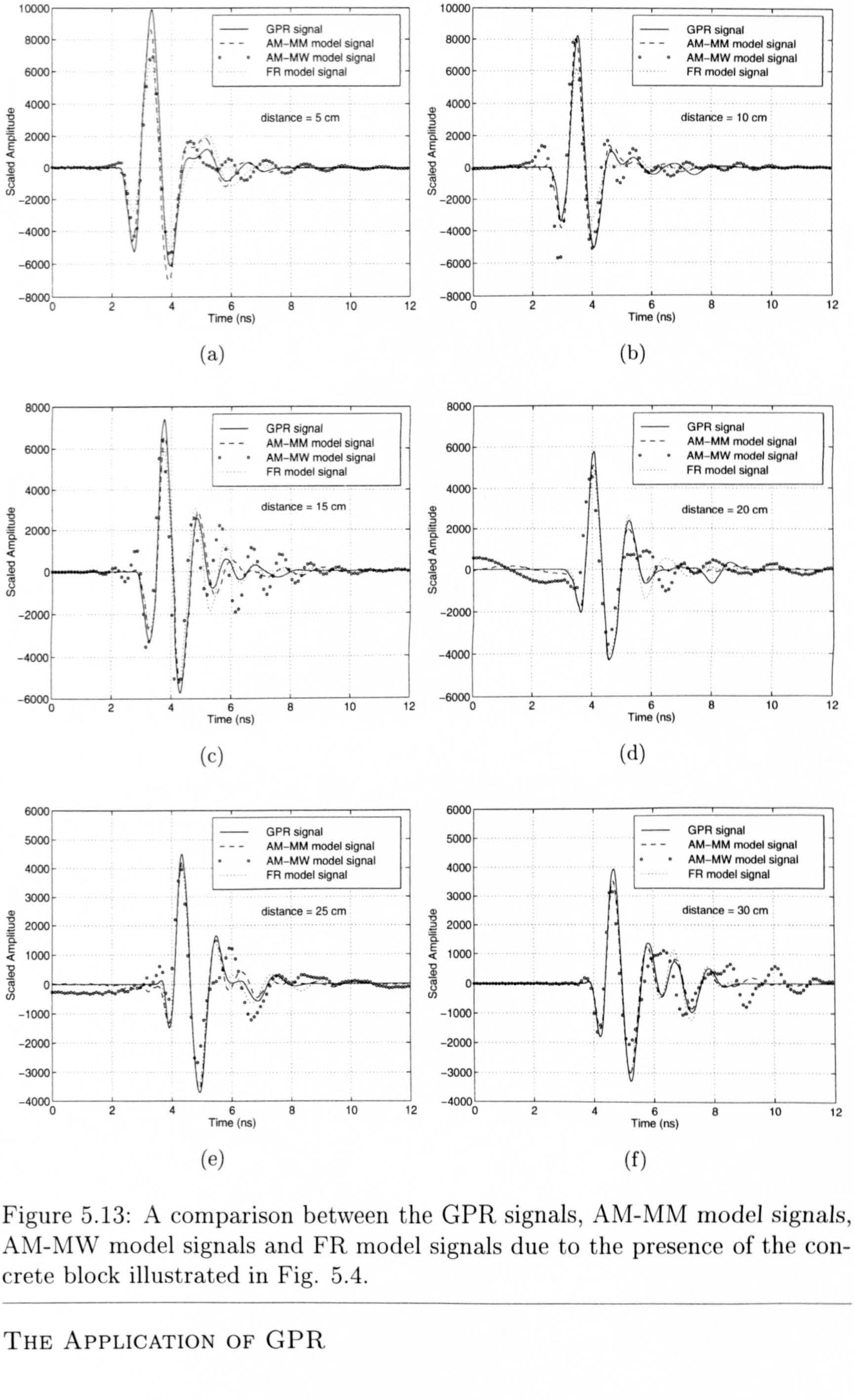

Figure 5.13: A comparison between the GPR signals, AM-MM model signals, AM-MW model signals and FR model signals due to the presence of the concrete block illustrated in Fig. 5.4.

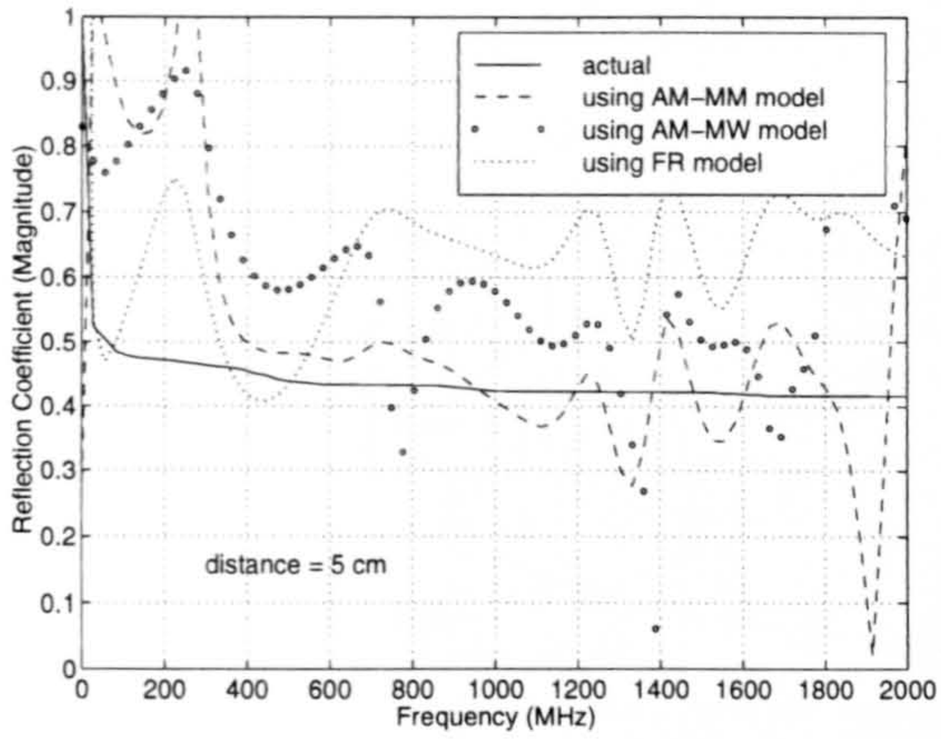

(a)

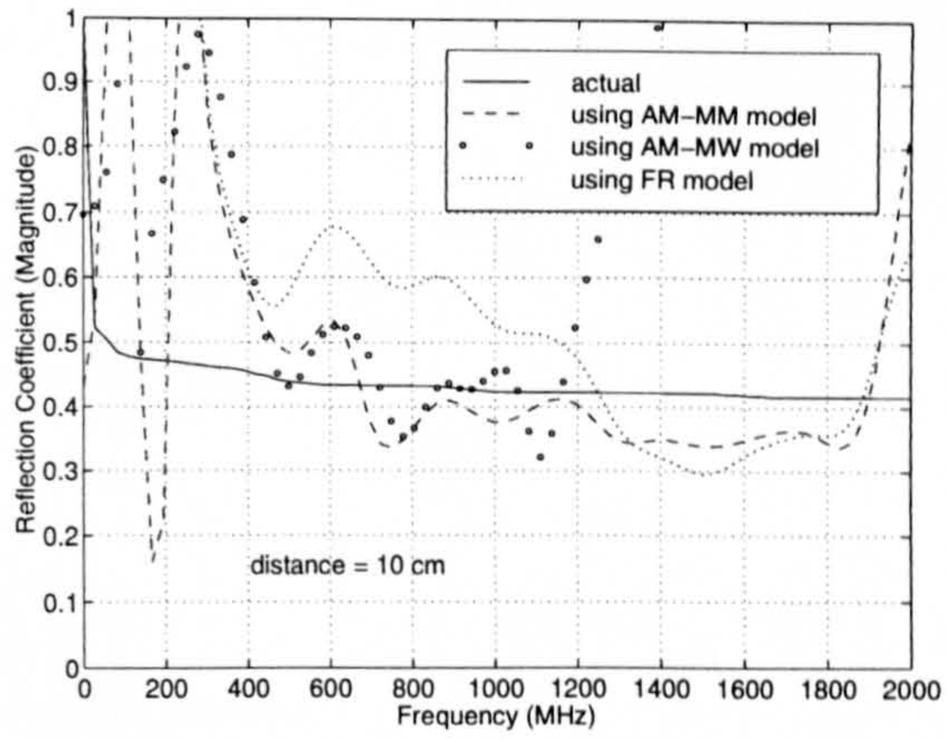

(b)

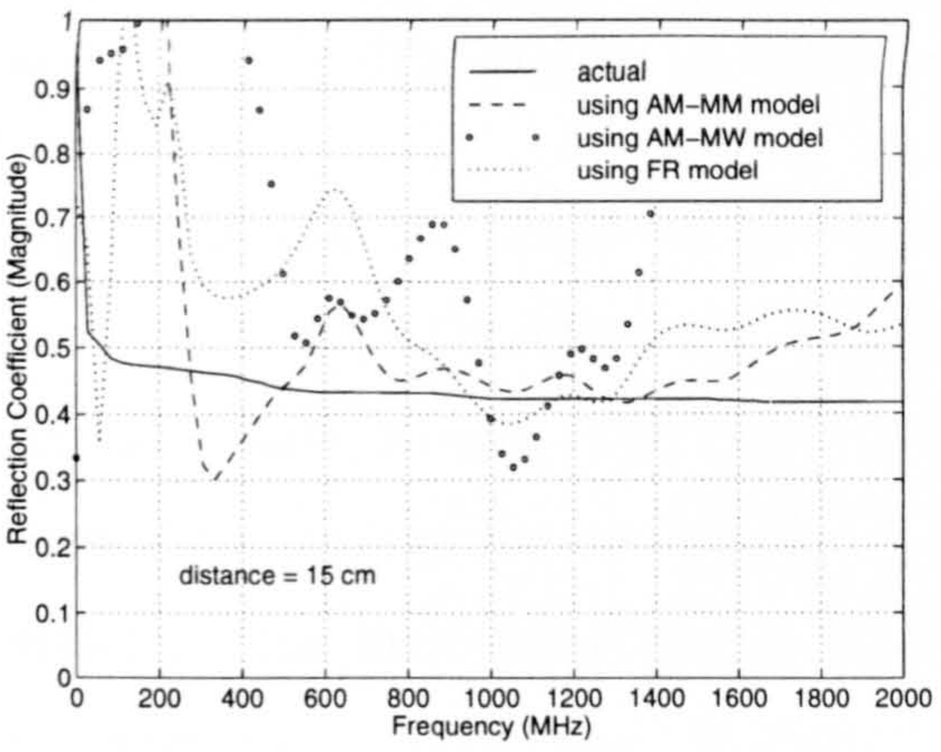

(c)

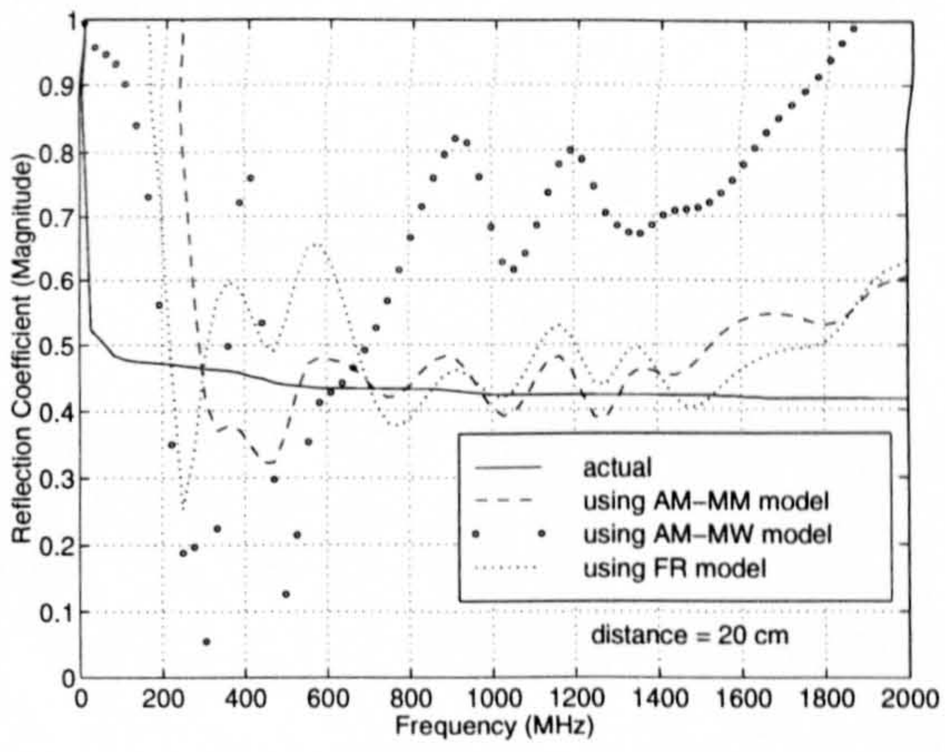

(d)

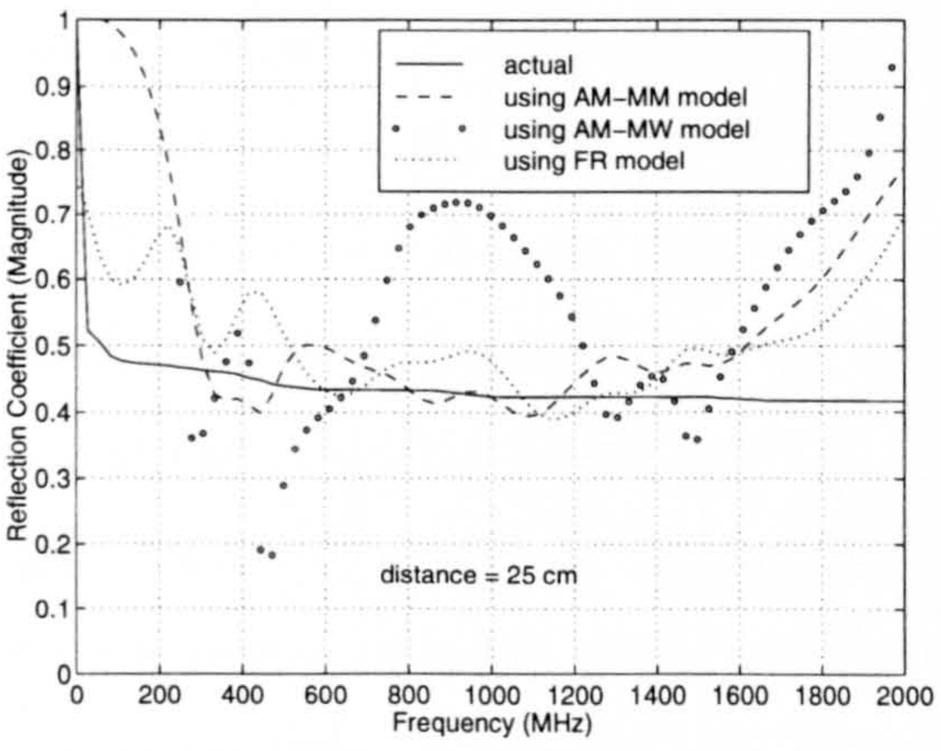

(e)

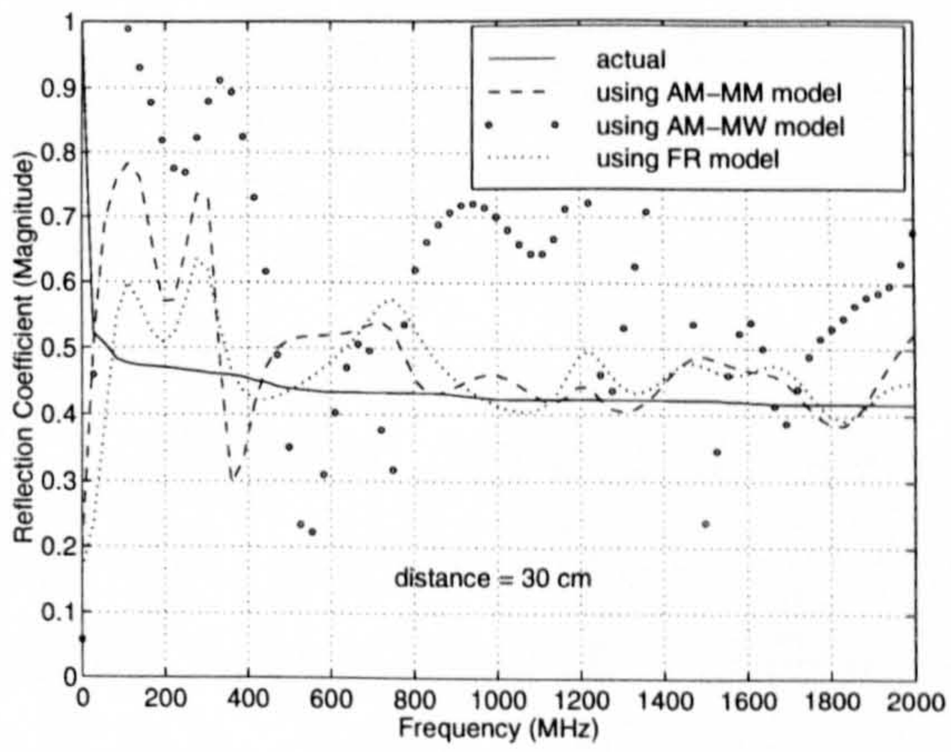

(f)

Figure 5.14: The reflection coefficients obtained from the GPR signals shown in Fig. 5.13 using AM-MM model, AM-MW model and FR model.

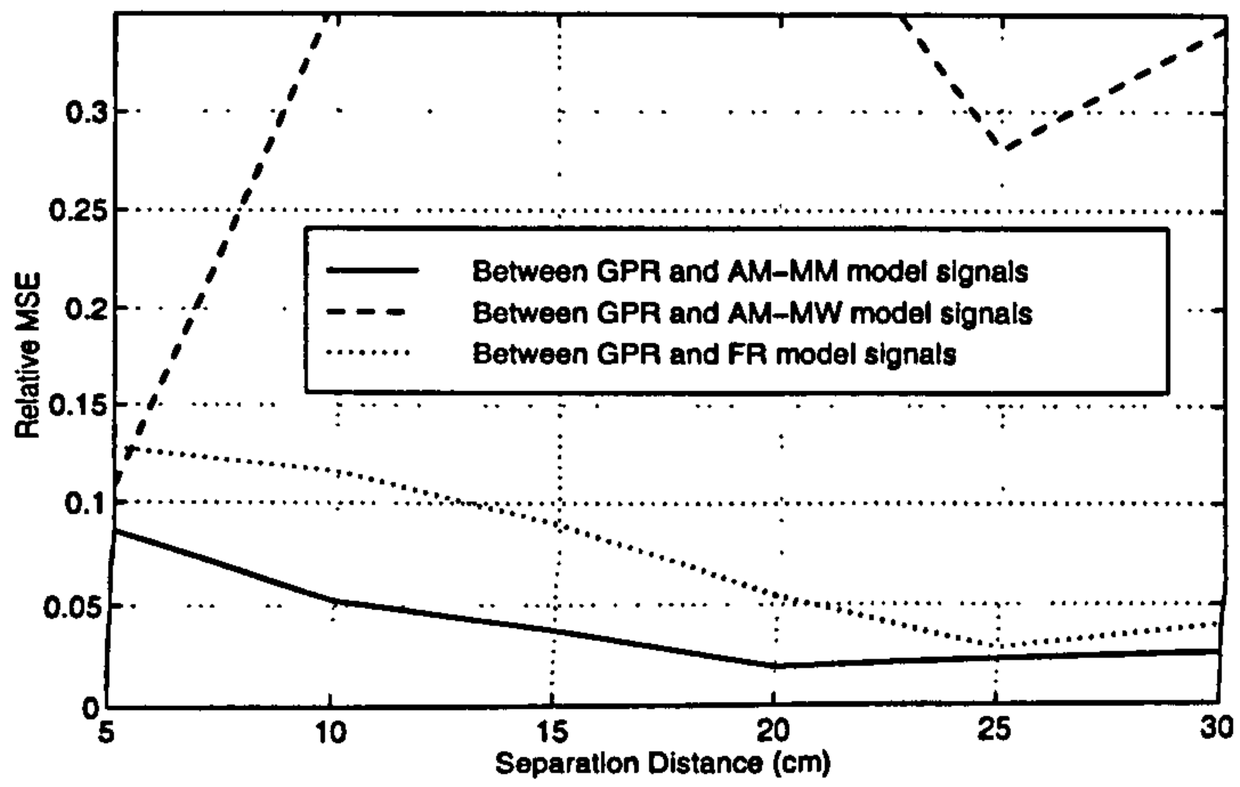

Figure 5.15: The relative mean square error between the GPR and different model signals. The signals are given in Fig. 5.13.

especially from the metal bar embedded in the concrete block. Attempts were made to remove the reflection arising from the metal bar by windowing the signals in time domain. However, the overlap between this reflection and those from the surface of the concrete block made it impossible to remove them completely. This fluctuation results in an oscillatory behaviour of the dielectric parameters derived at each frequency, similar to that already seen in Fig. 5.11 for the FR model (Example 5.1). Obviously, for precise measurements, the sample edges and other reflective objects ought to be covered by absorbing materials and a plain sample is utilized.

Figure 5.16 compares the permittivities and conductivities derived by the RMBI for three frequency ranges. One can see that at any separation, the use of the AM-MM model provides less variation in the parameters than the use of the FR model for different frequency bands. This desirable feature is an advantage of using the AM-MM model over the FR model. In addition, comparing Fig. 5.16 with Fig. 5.4(b) and 5.4(c), the best results are those obtained for the distance 20 cm when using the AM-MM model. It should be noted that the reflection from the metal bar dominates that from the other side

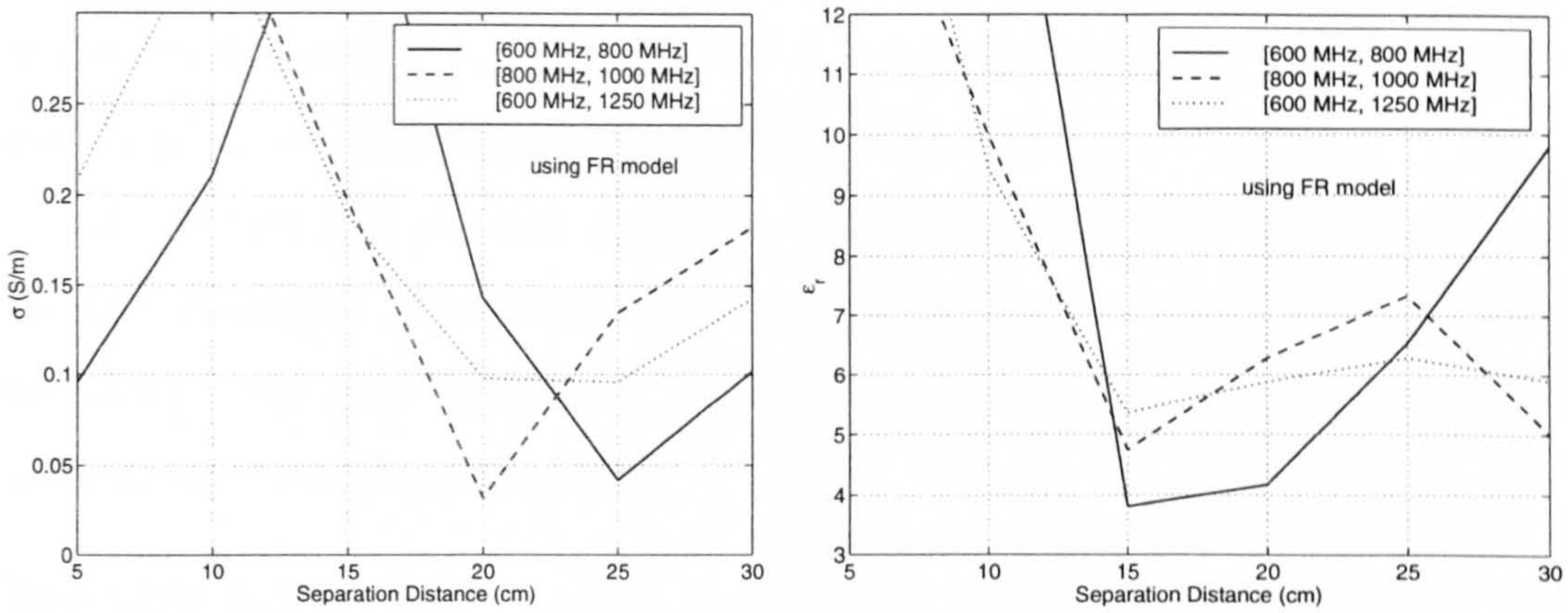

Figure 5.16: The resultant permittivity and conductivity of the concrete block obtained by the RMBI. The used data are the frequency components of the GPR signal.

of the concrete block. Thus, the reconstruction of the thickness of the block is subjected to a large error and is not considered in this example.

It is inevitable to have extraneous disturbances in GPR applications. This example has demonstrated that satisfactory results can be achieved by the application of the AM-MM model even if the GPR data contains considerable unwanted disturbances. It is possible to improve the results by using a larger copper plate which produces weaker edge diffractions.

Of the two AM models, only the Metal-Metal model is used in the subsequent examples. For convenience, this model is referred as the AM model hereafter. The data generated by the 3-dimensional FDTD simulations are used in the following examples.

Example 5.3. In this example, the medium is a one-layer slab with $\epsilon_r = 8$, $\sigma = 0.05$ S/m and h(thickness) $= 10$ cm, surrounded by free space. The same medium was used in several examples in Chapter 4 (e.g. Example 4.1).

Using the AM and FR models, the resultant reflection coefficients are shown in Fig. 5.17. The pairs (d_a, d_b) in the AM model are those given in Example 5.1. Figure 5.18 illustrates the Relative MSE obtained between the FDTD signals and the model signals. The superiority of the AM model to the FR model is evident here as well.

The RMBI is utilized to find the profile of both the slab and the bottom half-space medium (free space). The scattering data lies over the frequency band [500 MHz, 1000 MHz] (the same interval used in Chapter 4 for the reconstruction of this medium). The results are shown in Fig. 5.19.

Example 5.4. This example is concerned with the evaluation of the AM and FR models in retrieving the reflection coefficient and the parameters of the road pavement regarded in Example 4.10 Chapter 4. We consider a separation of 20 cm, which gives the minimum error for the AM model in all previous examples.

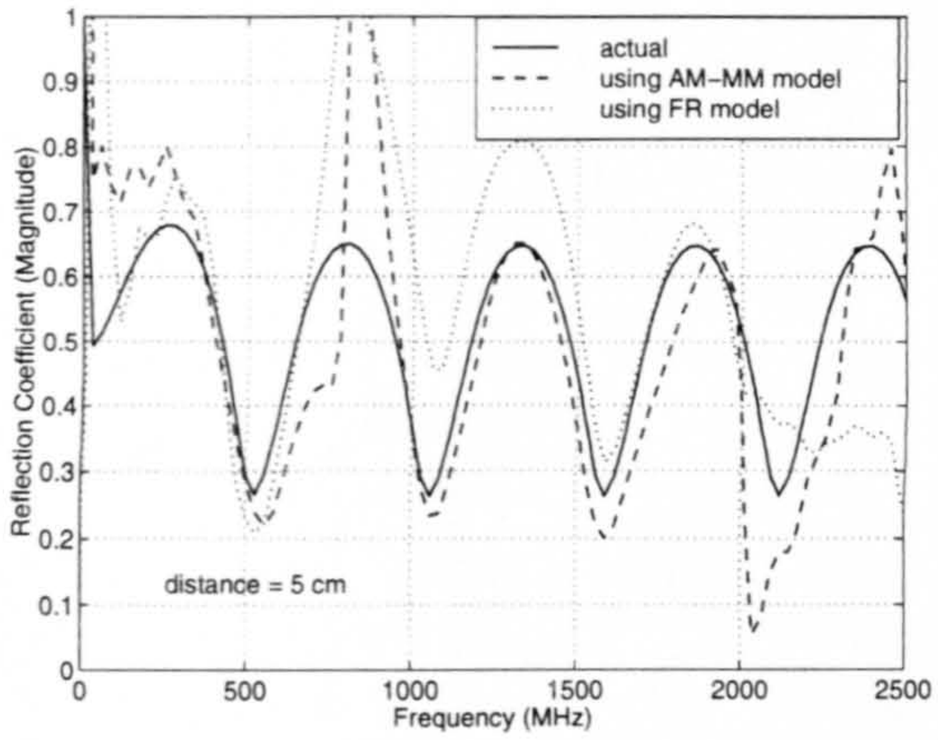

(a)

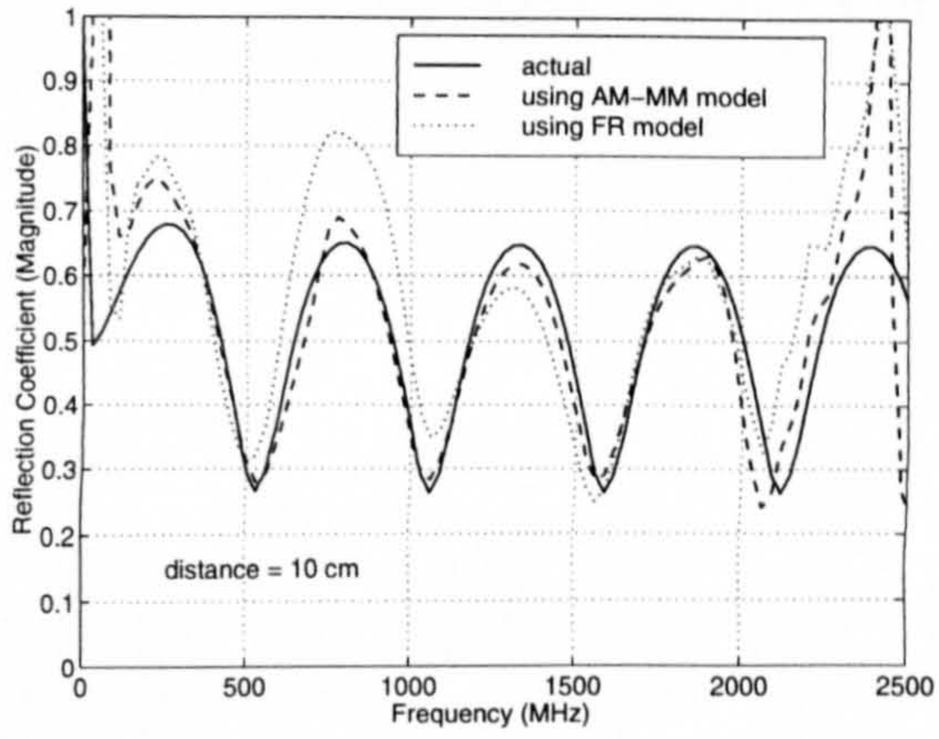

(b)

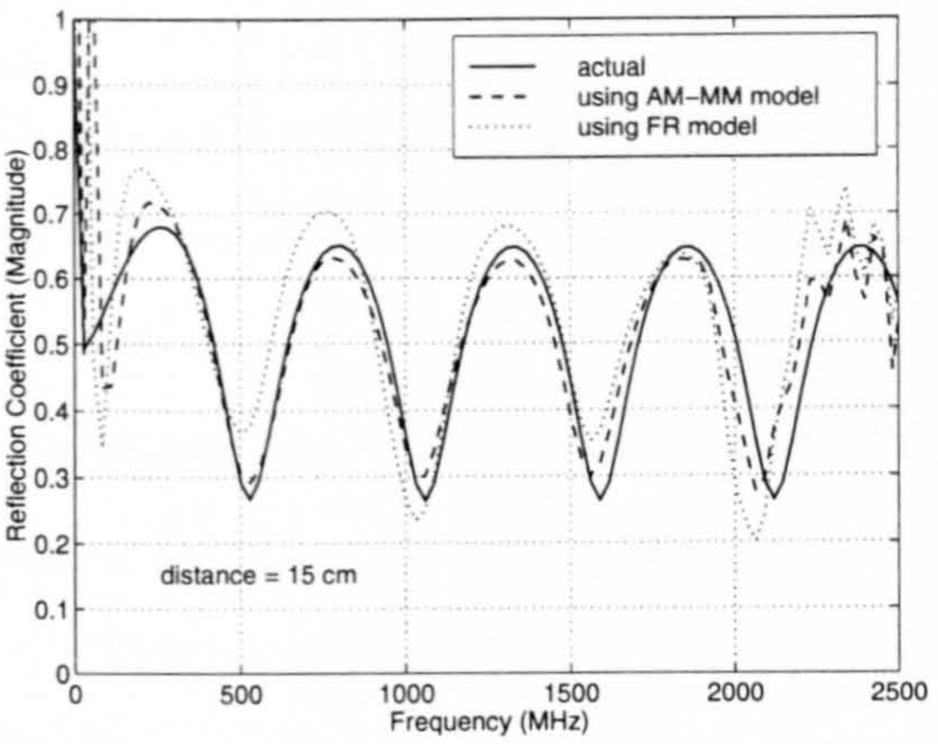

(c)

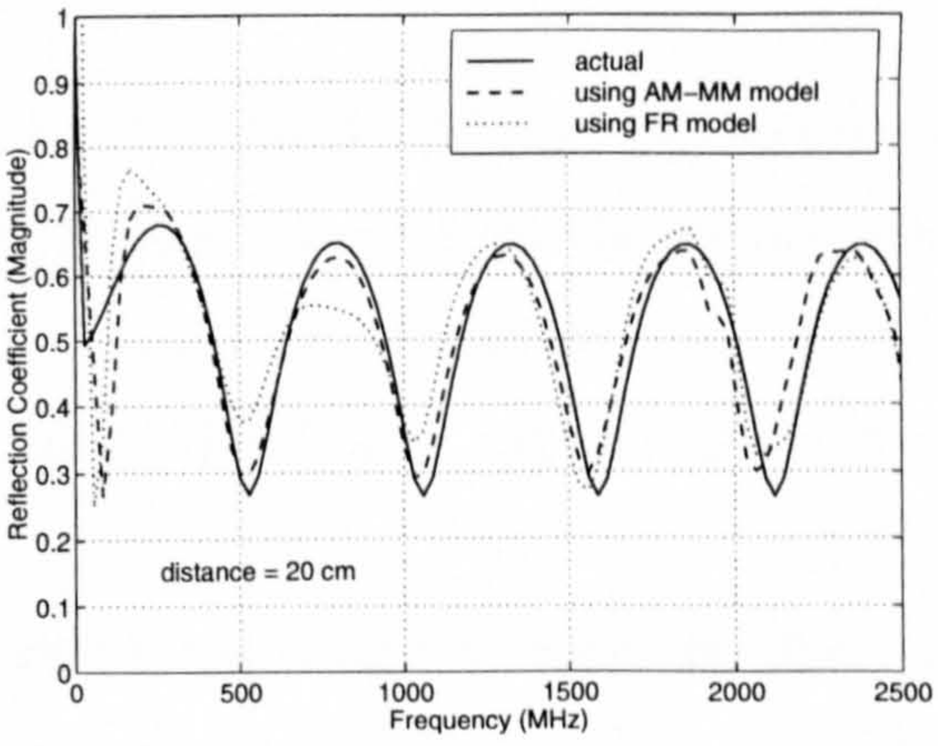

(d)

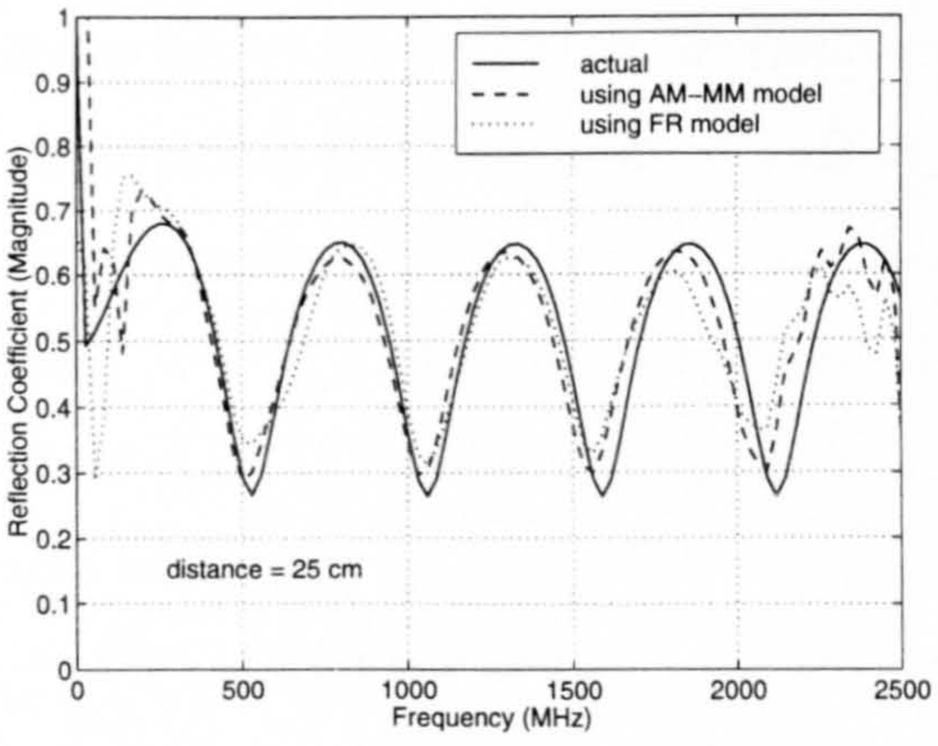

(e)

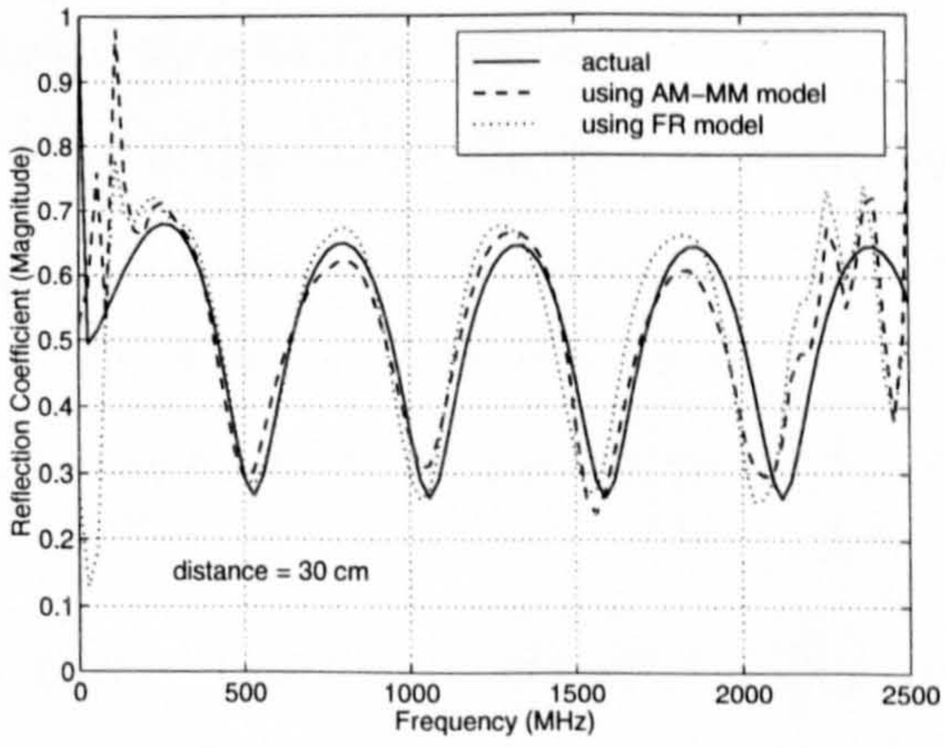

(f)

Figure 5.17: The reflection coefficients of a slab with $\epsilon_r = 8$, $\sigma = 0.05$ S/m and h(thickness) = 10 cm in free space.

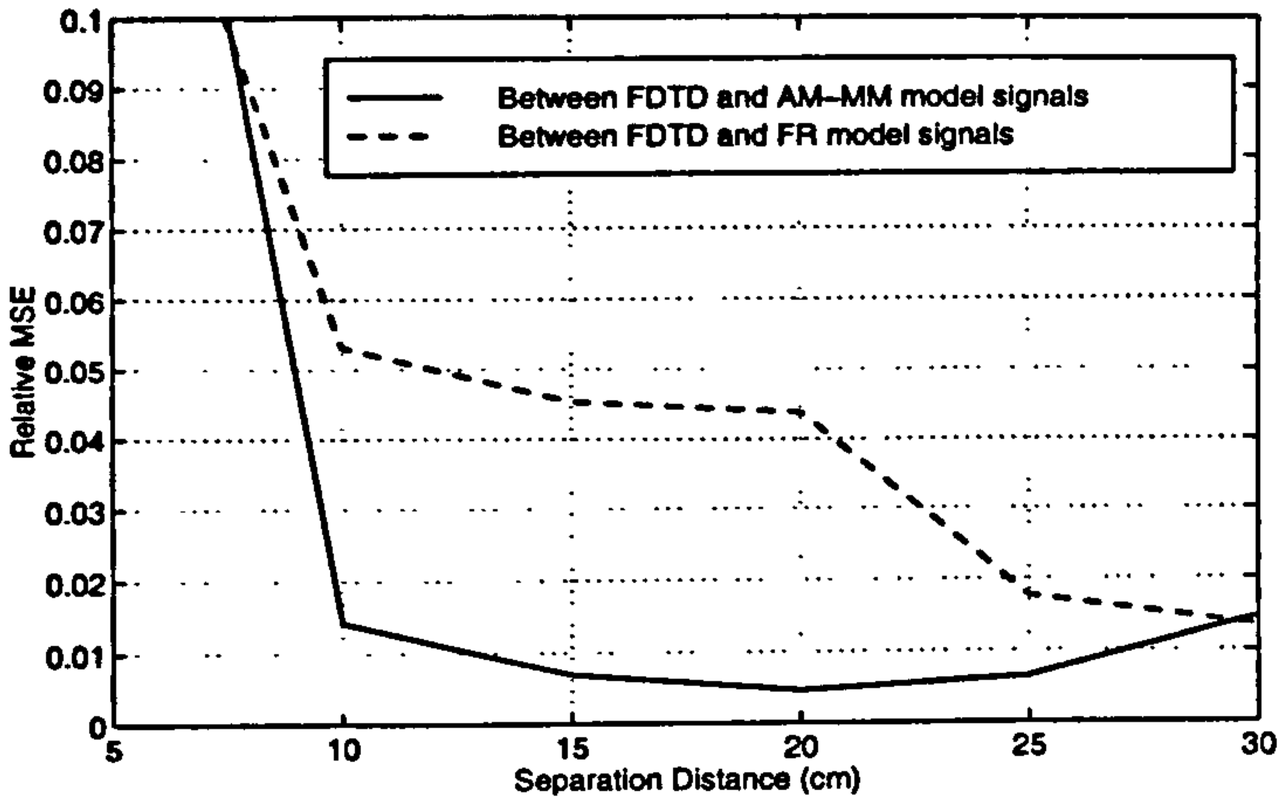

Figure 5.18: A illustration of the accuracy of the AM model over the FR model.

At first, the FDTD simulation is carried out for the 3-layer approximation of the pavement (Fig. 4.29). The FDTD signal along with the signals generated by the models are given in Fig. 5.20(a). Furthermore, Fig. 5.20(b) compares the actual reflection coefficient of the 3-layer approximation with those provided by the models.

The reconstructed profiles are illustrated and compared with the true one in Fig. 5.21. The frequency components of the FDTD signal in the range [650 MHz, 1150 MHz] are used as the scattering data. This range is the high frequency range employed for the reconstruction in Example 4.10.

Dividing the transition regions of the continuous profile into 5 steps, the corresponding results are shown in Fig. 5.22. Note that the transition regions were divided into 20 steps in Example 4.10. However, the cell size 2.625 mm in the FDTD simulation imposes a limitation on having finer discretisation in this example.

Figure 5.23 shows the resultant permittivity and conductivity profiles, using only the AM model, while the number of layers is set to 3 and 5. The scattering data lies in the interval [650 MHz, 1150 MHz]. The reconstructed conductivity bears a substantial error. As mentioned before, the conductivity

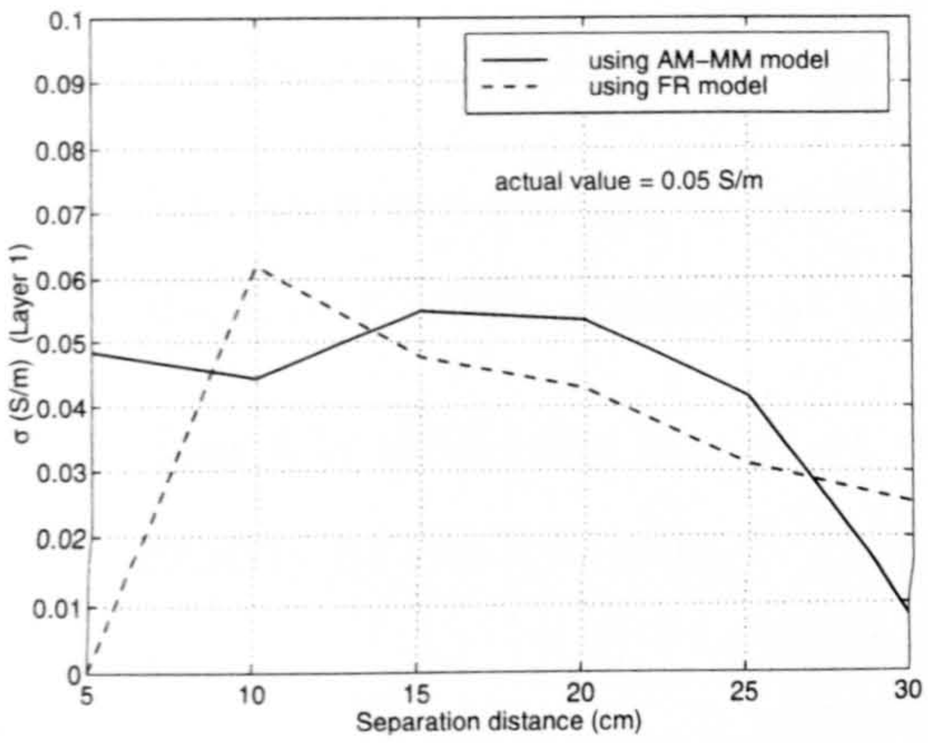

(a)

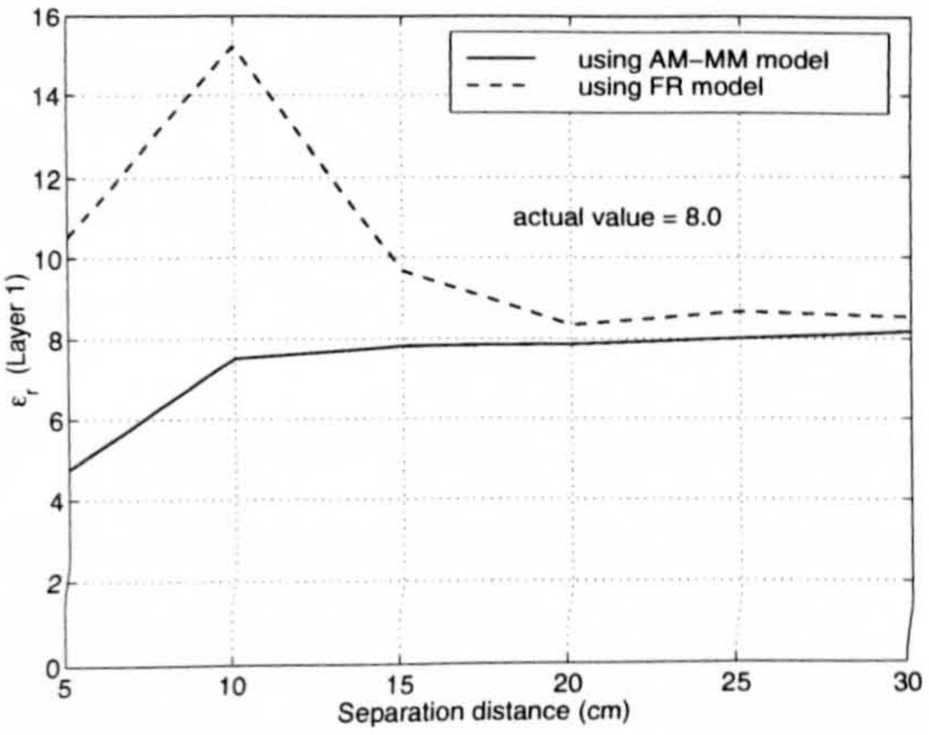

(b)

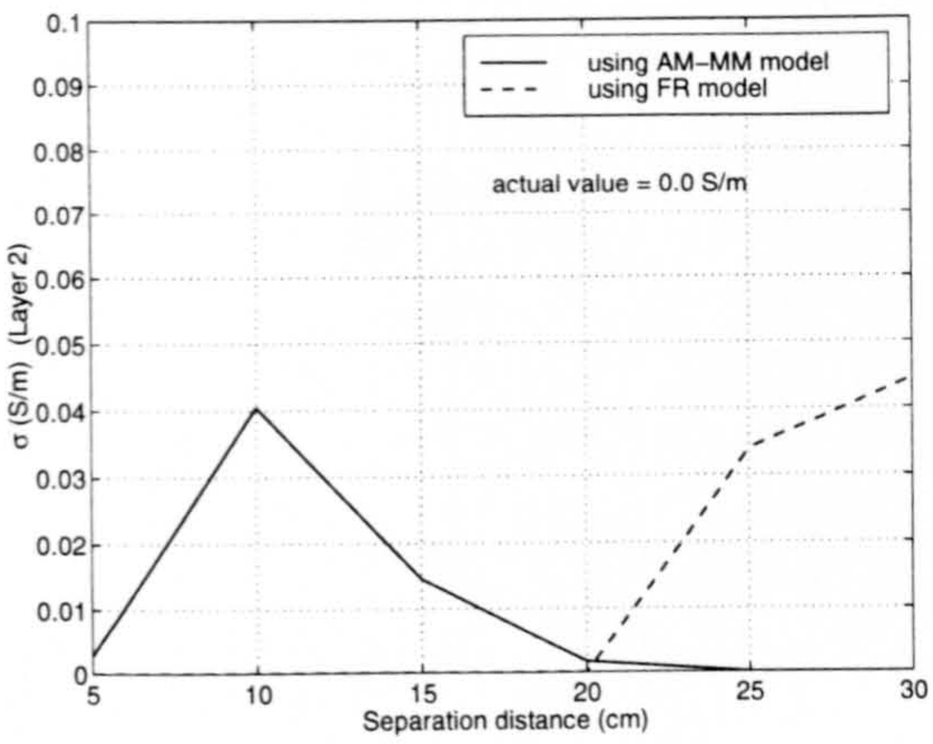

(c)

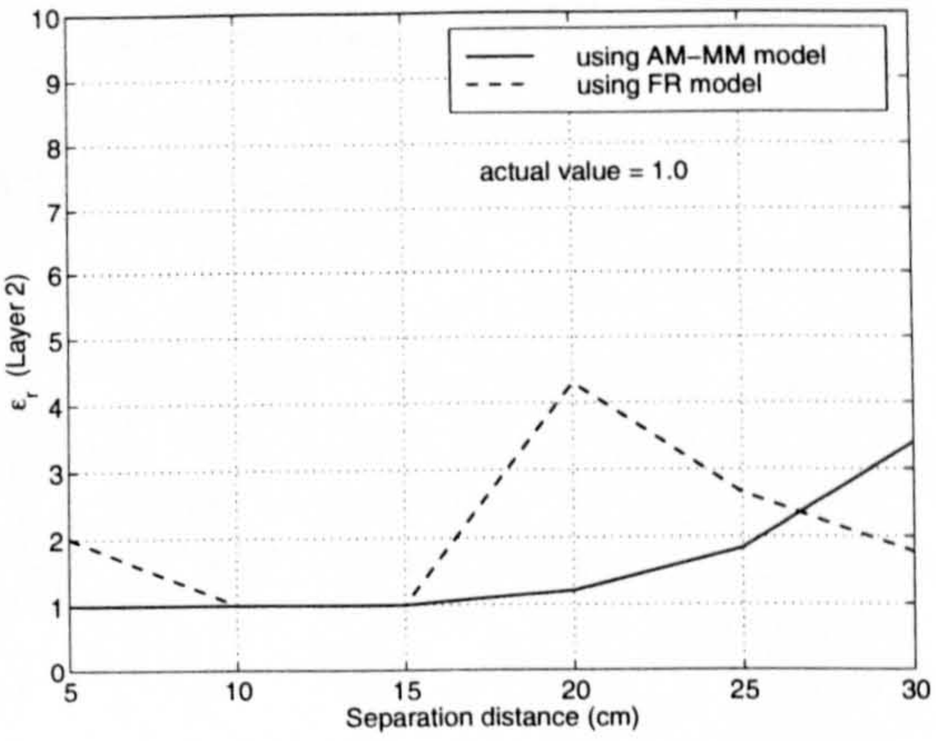

(d)

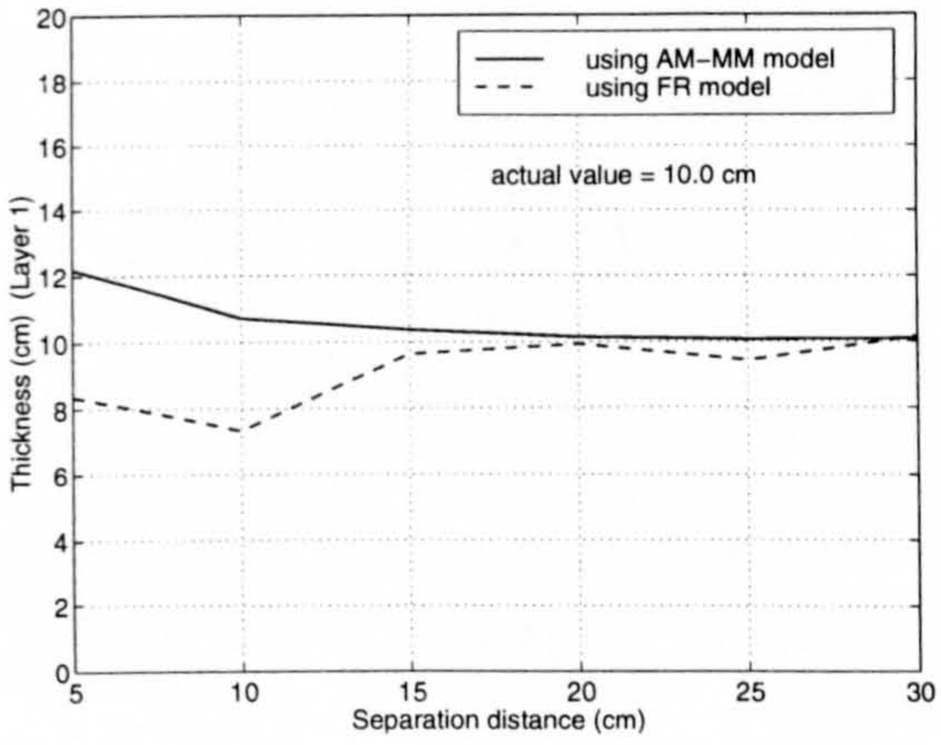

(e)

Figure 5.19: A comparison between the reconstructed parameters of a 2-layer medium using the AM and FR models.

is very sensitive to errors in the data, especially at high frequencies. There exist two sources of error in the inverse method:

1. The assumed number of layers is different from the actual one. In fact, the true medium consists of 11 layers (solid line in Fig. 5.23).

2. The AM modelling is inexact, i.e. the scattering data is not predicted exactly by the AM model. This can be observed from Fig. 5.22(a) where

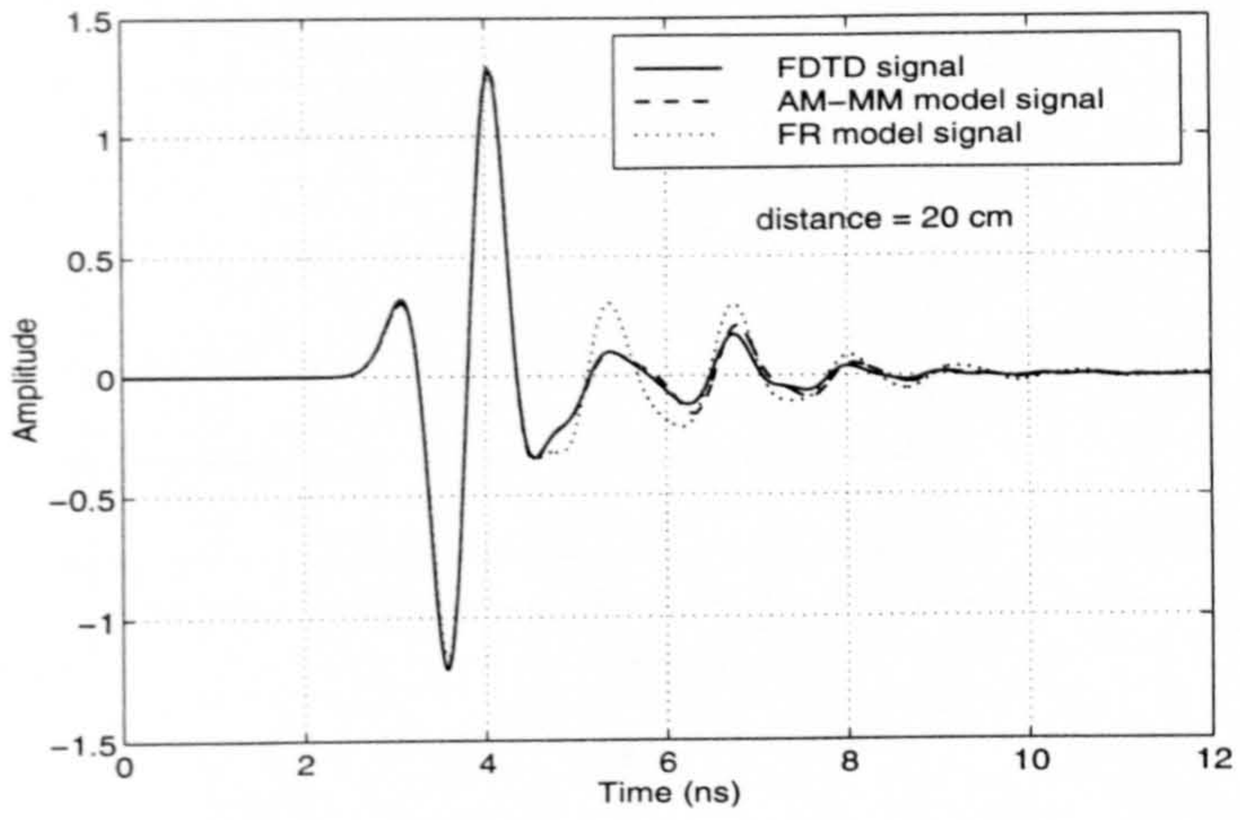

(a)

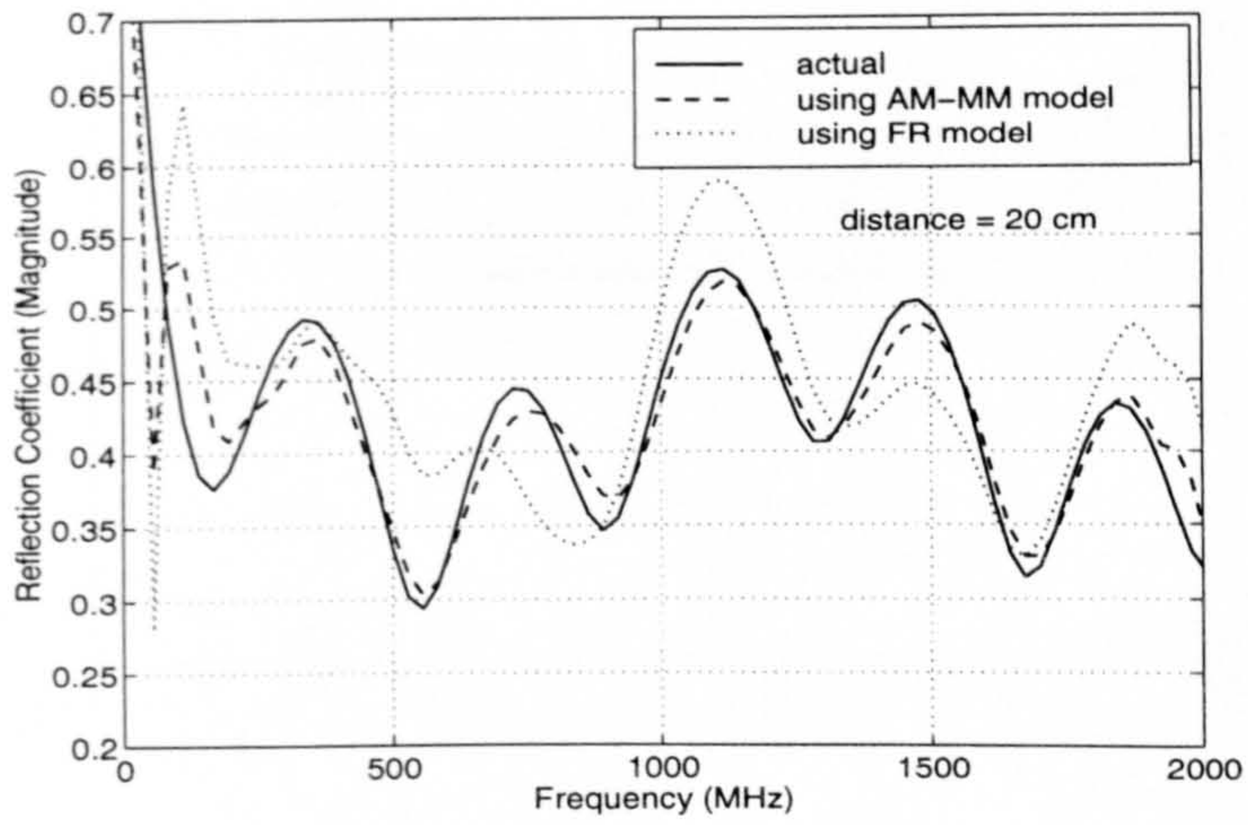

(b)

Figure 5.20: The evaluation of the AM and FR models in deriving (a) the received signal and (b) the reflection coefficient when the medium is 3-layer approximation of the road pavement considered in Example 4.10 Chapter 4

the FDTD signal differs from the one generated by the AM model.

One can also observe that the resultant 5-layer profile provides a larger error. This might be due to the second source of error, i.e. the inexact modelling makes the inverse problem ill-posed when the number of layers is 5 or more. Similar to Example 4.10, it is possible to use the scattering data at

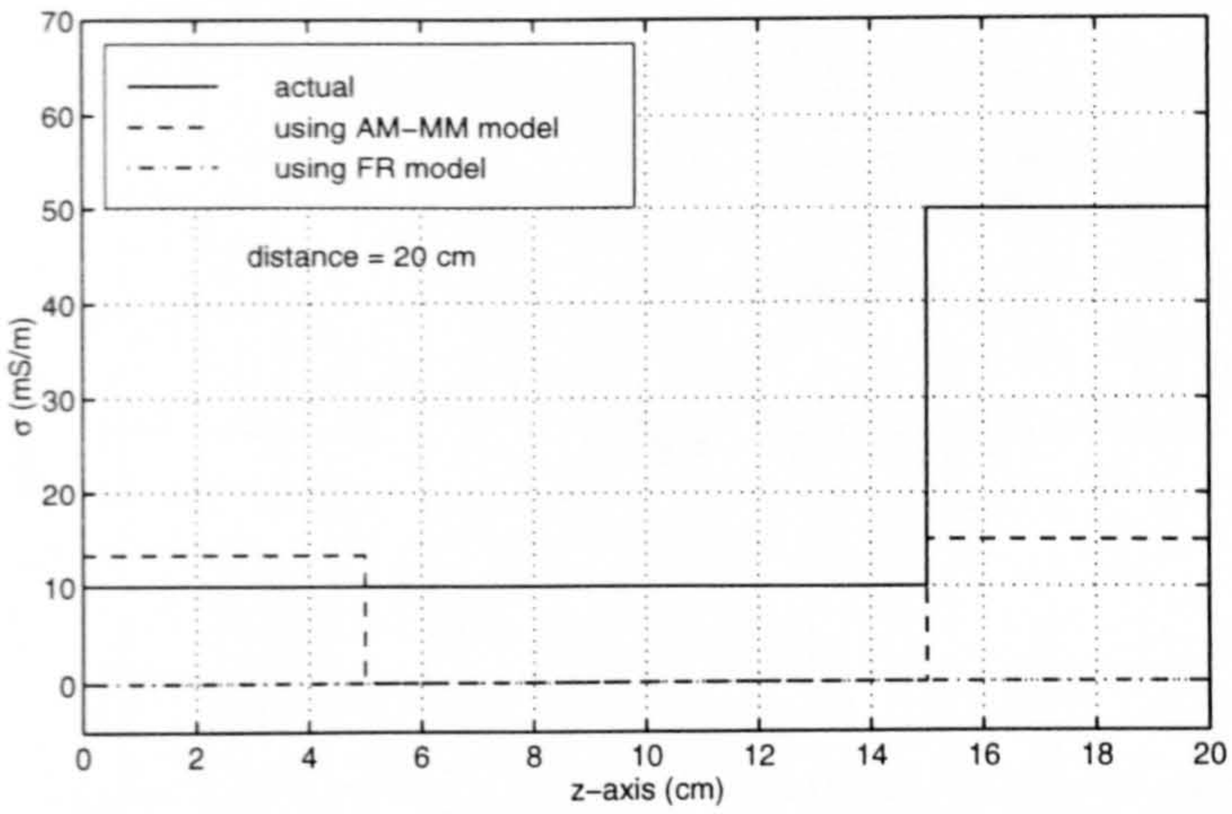

(a)

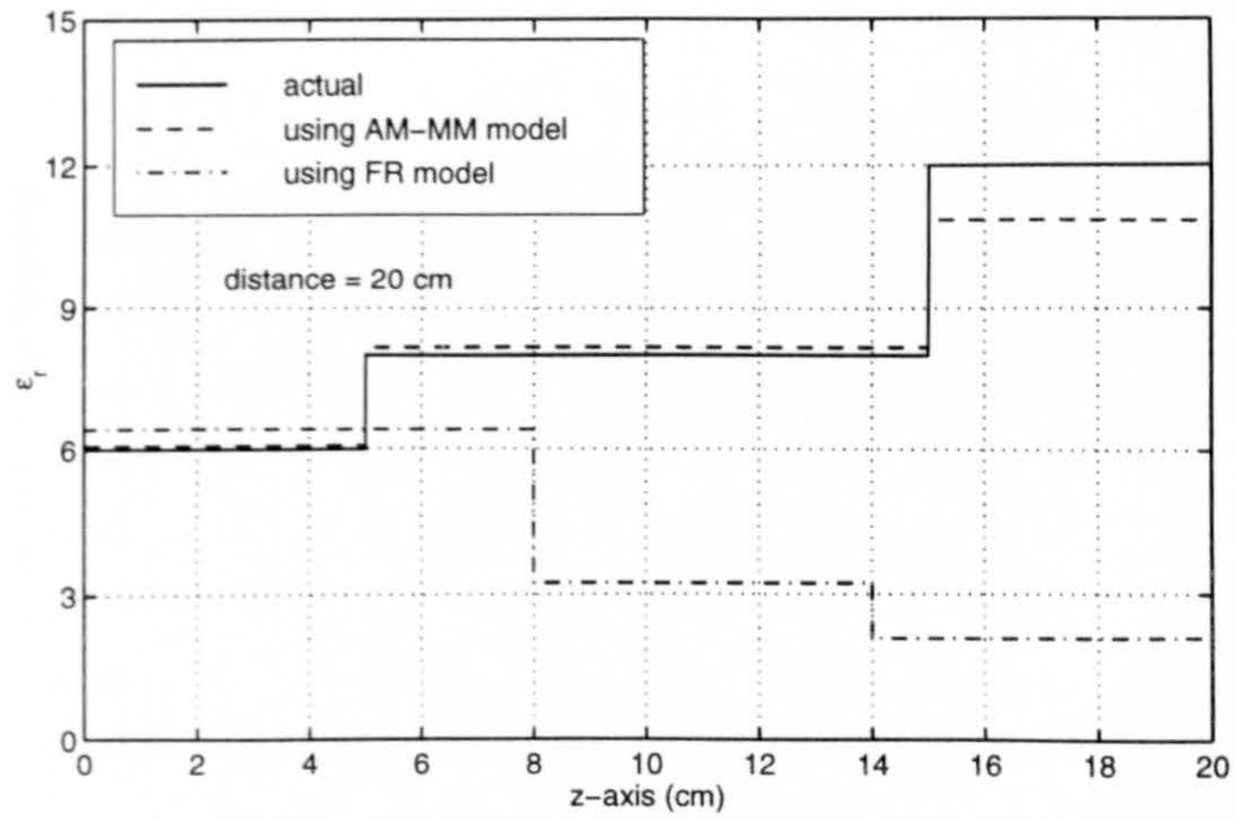

(b)

Figure 5.21: The resultant conductivity and permittivity of the 3-layer medium. The scattering data are the frequency components of the FDTD signal (shown in Fig. 5.20(a)) over the band (650 MHz, 1150 MHz).

---

lower frequencies ([250 MHz, 450 MHz]) to find a more accurate 3-layer profile (low resolution version). The low frequencies offer better accuracy because the conductivity is less sensitive to the error; In addition, the first source of noise introduces minor errors as it can be seen from Fig 4.30 (Chapter 4). The 5-layer profile can then be reconstructed from the high frequency data using narrowed bounds, obtained on the basis of the 3-layer profile. Such a scenario

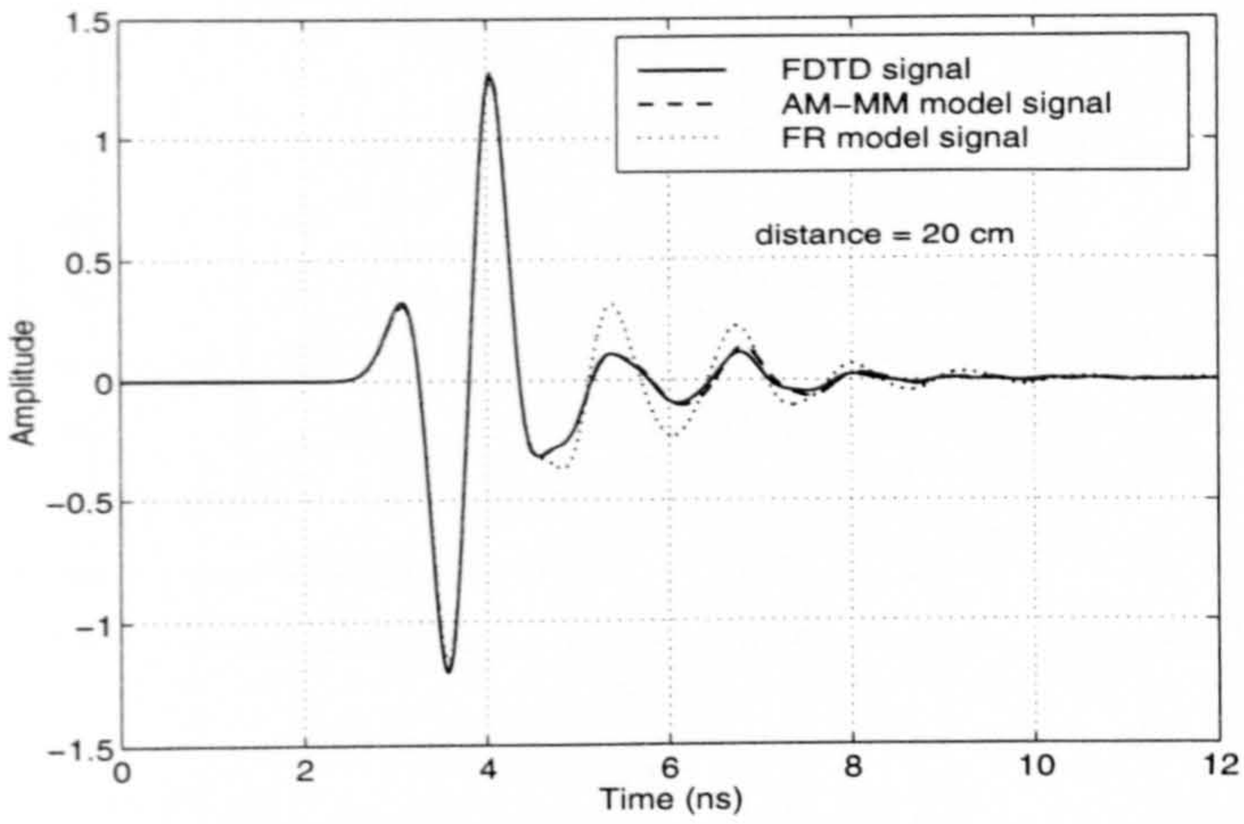

(a)

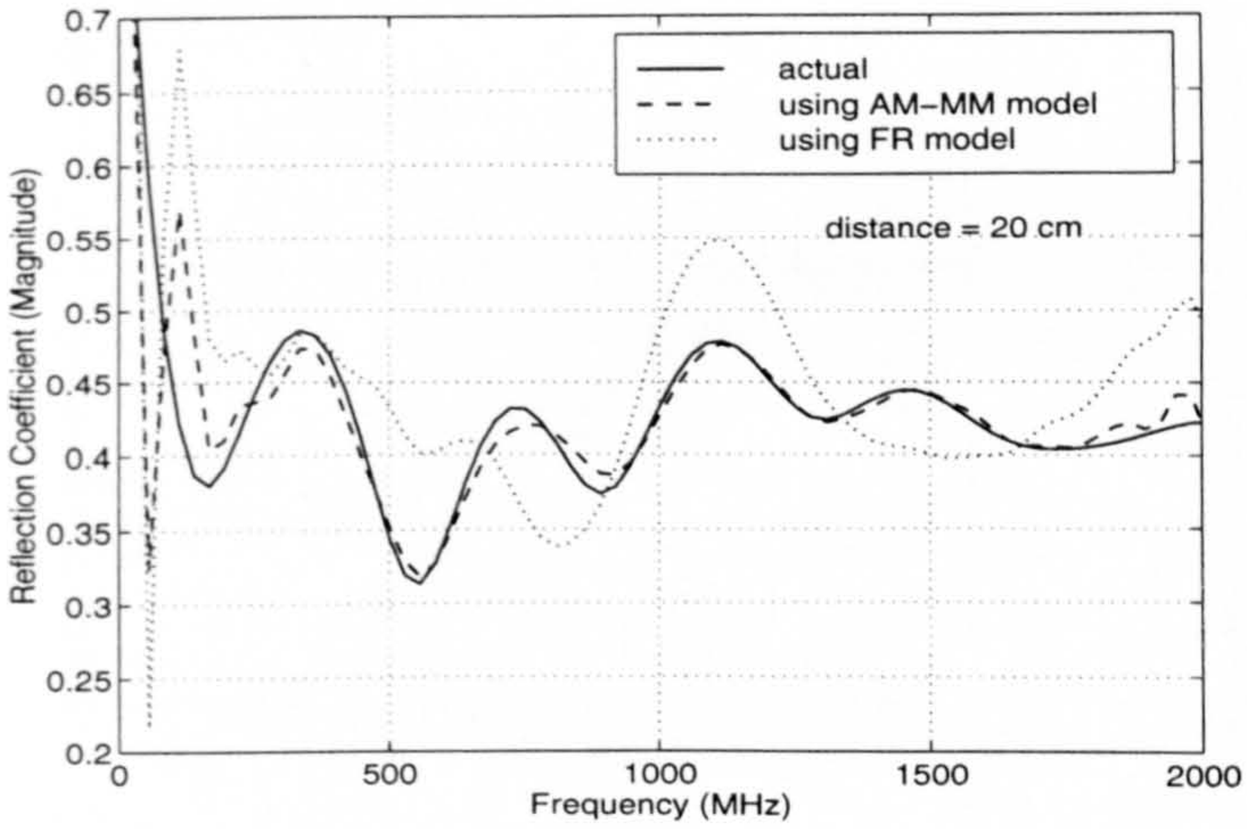

(b)

Figure 5.22: The evaluation of the AM and FR models in deriving (a) the received signal and (b) the reflection coefficient when the medium is that whose profile shown by the solid line in Fig. 5.23.

cannot be applied to this example owing to a considerable error in the data over the frequency band [250 MHz, 450 MHz]. Generally speaking, two surveys are required to be carried out by a GPR, one with low frequency (e.g. 300 MHz) and one with high frequency (e.g. 900 MHz) antennas so as to obtain accurate results.

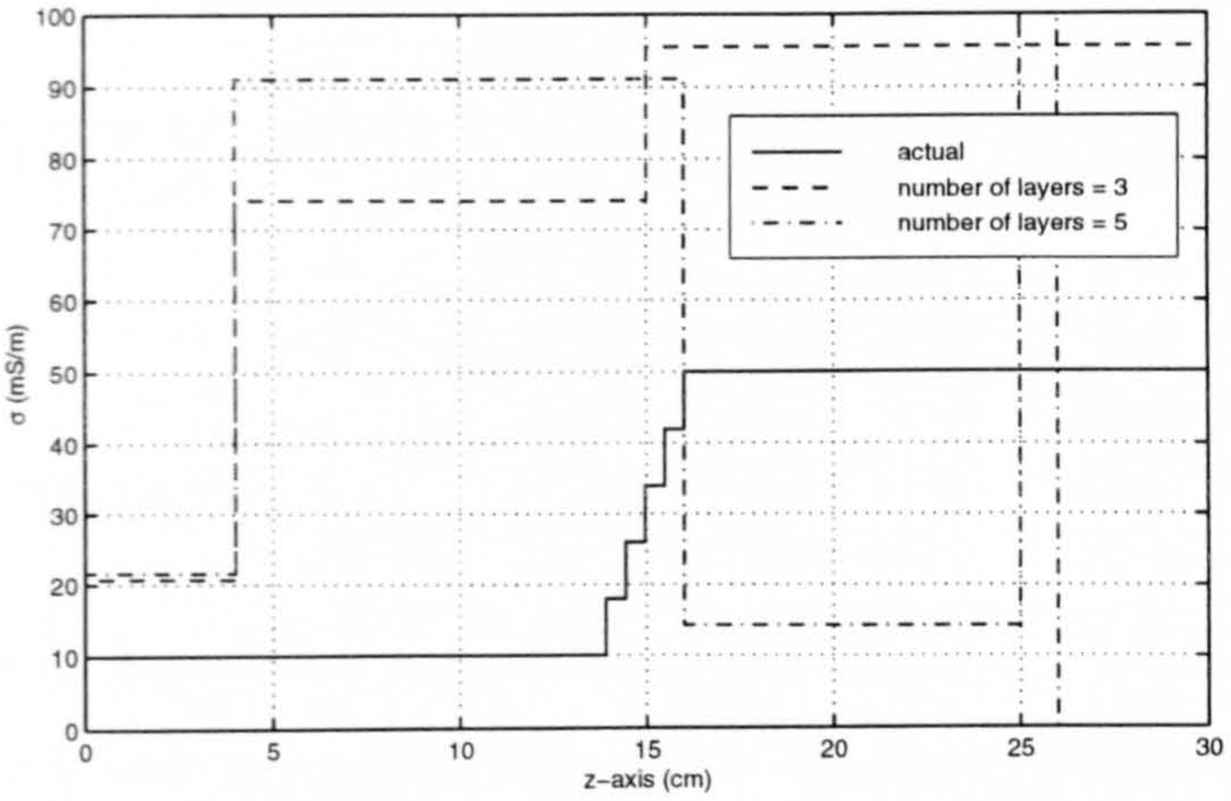

(a)

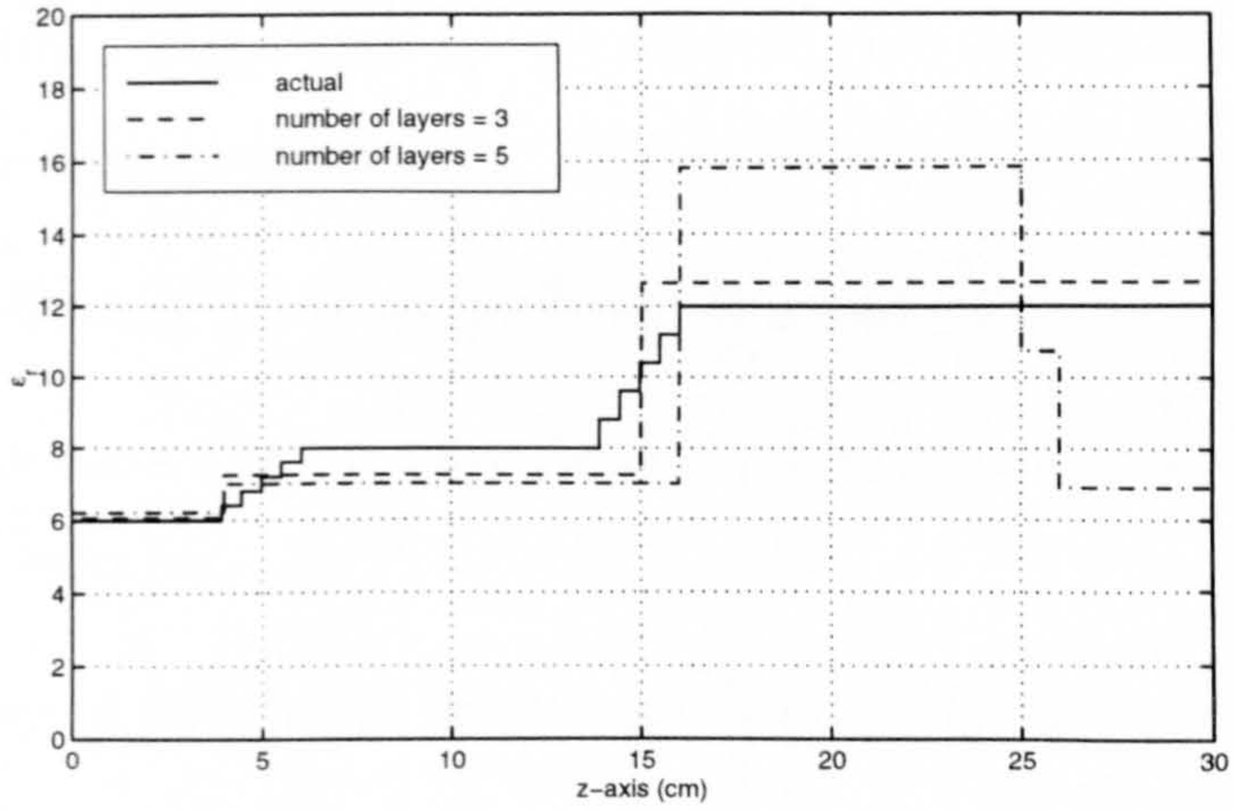

(b)

Figure 5.23: The derived conductivity and permittivity of a road pavement using the AM model. The scattering data are the frequency components of the FDTD signal (shown in Fig. 5.22(a)) over the frequency range (650 MHz, 1150 MHz).

Chapter 6

Summary and Future Work

6.1 Summary

The problems associated with the interpretation of GPR data have been investigated and new techniques have been developed and evaluated for the characterisation of multi-layered media. These methods are valuable for many GPR applications such as characterising the subsurface structure of the ground.

The model-based approach for the inversion was selected due to providing robustness and broad applicability. Three difficulties had to be tackled:

1. The inefficiency of the model-based approach.

2. The convergence of the optimisation procedure used in the inversion to the true solution.

3. Modelling of GPR when its antenna is illuminating a layered medium.

The inefficiency of the model-based approach has been remedied by employing the reflectivity formulation instead of the nonlinear integral equation and by deriving an analytical expression for the gradient of the objective function. In order to overcome the second difficulty, three well-known global optimisation techniques, genetic algorithm (GA), simulated annealing (SA) and multi-level

single-linkage (MLSL) method, have been investigated. The comparison between GA and the MLSL together with that between SA and the MLSL indicate that the MLSL method is the best candidate to be used in the inversion. In addition, the MLSL has been combined with a new optimisation technique, adaptive random search. Several reconstruction examples show that the resultant hybrid method provides better reliability and efficiency.

In order to apply the inverse method to GPR data, a model is required that relates the reflection coefficient of the layered medium under investigation to the signal received by GPR. Such a model has been proposed by taking account of the antenna-medium coupling into the formulation used in conventional free-space methods. Thus, the antenna-medium separation could be reduced significantly to increase signal to clutter ratio. Compared with the conventional free-space formulation, the proposed model provides more realistic modelling of the application of GPR.

In addition to the work performed to overcome the mentioned difficulties, the necessary condition for the unique solution to 1D EIS problem has been established. The detailed FDTD simulation of a commercial GPR has also been described. The comparison between the simulated and experimental results reveal that the FDTD method is a useful tool for the analysis and design of GPR antennas.

Numerous reconstructions of layered media based on experimental and simulated data have been carried out to test the methods developed in the thesis. The experimental data was obtained by using an HP-8753B network analyzer and a 900 MHz commercial GPR. The reflectivity formulation and the FDTD simulation were used to generate the simulated data.

6.2 Recommendation for Future Work

The framework of finding the profile of a multi-layered medium using GPR has been provided in this thesis. Accuracy of the reconstruction could be further improved by taking the following into account:

1. The wave spreading effect in the layered medium. This effect has not been taken into account although the wave spreading in the region between GPR and the upper surface has been considered. This is a source of systematic error, which can be avoided by considering the wave-spreading effect in the formulation of the reflection coefficient of the medium.

2. Compensation of path loss. As mentioned at the end of Chapter 4, the parameters of the deeper layers bear greater error. This is due to path loss making the reflections from the shallow layers are stronger than those from the deeper ones. Path loss can be compensated by applying a time-variable gain. In this way, the deeper reflections are weighed upwards so as to increase their power. Another method is to use time-frequency domain data [17] rather than merely frequency domain data. The time-frequency analysis (such as the wavelet transform) is more suited to separate the echoes contained in the GPR signal. These echoes can be weighed appropriately and employed as the observed scattering data for the inversion. The use of time-variable gain or the adoption of the time-frequency analysis requires the derivation of the expressions for the gradient of the MSE function.

The reconstruction of the profile of a continuous medium needs further refinement. Because a continuous medium may be regarded as comprising an infinite number of thin layers, the use of the data in a finite frequency range (i.e. incomplete data) makes the inverse problem ill-posed. This fact was shown in Example 4.10 where the reconstruction of the profile of a road pavement was

considered. One way to overcome this problem is to restrict the variation of the parameters in a small feasible region (Example 4.10). However, the general remedy is to impose the continuity of the profile by adding an appropriate regularisation factor to the MSE function [14, Chapter 4].

Bibliography

[1] E. Aarts and J. Korst, *Simulated annealing and boltzman machines*, Wiley, New York, 1989.

[2] M. N. AFSAR, J. R. Birch, and R. N. Clarke, *The measurement of the properties of materials*, Proceedings of the IEEE **74** (1986), no. 1, 183–199.

[3] W. Al-Nuaimy, Y. Huang, M. Nakhkash, and M.T.C. Fang, *Automatic detection of buried utilities and solid objects using neural networks and pattern recognition*, 7th International Conference on Ground Penetrating Radar (Kansas, USA), vol. 2, May 1998, pp. 425–429.

[4] R. Azencott (ed.), *Simulated annealing: parallelization techniques*, Wiley, New York, 1992.

[5] G. L. Bilbro and W. E. Snyder, *Optimization of functions with many minima*, IEEE Trans. on Systems, Man, and Cybernetics **21** (1991), no. 4, 840–849.

[6] J. CH. Bolomey, CH. Durix, and D. Lesselier, *Time domain integral equation approach for inhomogeneous and dispersive slab problems*, IEEE Trans. on Antennas and Propagation **AP-26** (1978), no. 5, 658–668.

[7] J. M. Bourgeois and G. S. Smith, *A fully three-dimensional simulation of a ground-penetrating radar: FDTD theory compared with experiment*, IEEE Trans. on Geoscience and Remote Sensing **34** (1996), no. 1, 36–44.

[8] J. M. Bourgeois and G. S. Smith, *A complete electromagnetic simulation of the separated-aperture sensor for detecting buried land mines*, IEEE Trans. on Antennas and Propagation **46** (1998), no. 10, 1419–1426.

[9] A. M. Bruckstein and T. Kailath, *Inverse scattering for discrete transmission-line models*, SIAM Review **29** (1987), no. 3, 359–389.

[10] J. H. Bungey, S. G. Millard, and M. R. SHAW, *Simulation tank to aid interpretation of radar results on concrete*, Magazine of Concrete Research **45** (1993), 187–195.

[11] R.H. Byrd, C.L. Dert, A.H.G. Rinnooy Kan, and R.B. Schnabel, *Concurrent stochastic methods for global optimization*, Mathematical Programming **46** (1990), 1–29.

[12] P. Chaturvedi and R. G. Plumb, *Electromagnetic imaging of underground targets using constrained optimization*, IEEE Trans. on Geoscience and Remote Sensing **33** (1995), no. 3, 551–561.

[13] H. C. Chen, *Theory of electromagnetic waves*, McGraw-Hill, New York, 1983.

[14] D. Colton and R. Kress, *Inverse acoustic and electromagnetic scattering theory*, Springer-Verlag, Berlin, 1992.

[15] D. J. Daniels, *Surface penetrating radar*, IEE, London, 1996.

[16] J. J. Daniels, R. Roberts, and M. Vendl, *Ground penetrating radar for the detection of liquid contaminants*, Journal of Applied Geophysics **33** (1995), 195–207.

[17] I. Daubechies, *Ten lectures on wavelets*, Society for Industrial and Applied Mathematics, Philadelphia, 1992.

---

[18] L.C.W. Dixon and G.P. Szego, *Towards global optimisation*, North-Holland Pub. Co., Amsterdam, 1975.

[19] R. Fletcher, *Practical methods of optimization*, Wiley, Chichester, 1987.

[20] M. Fritzsche, *Detection of buried landmines using ground penetrating radar*, SPIE Conf. on Detection Technologies for Mines and Minekind Targets (Orlando, FL., USA), vol. 2496, SPIE-INT, Apr. 17-21 1995, pp. 100–109.

[21] J. L. Frolik and A. E. Yagle, *Reconstruction of multilayered lossy dielectrics from plane wave impulse responses at two angles of incidence*, IEEE Trans. on Geoscience and Remote Sensing **33** (1995), no. 2, 268–279.

[22] J. L. Frolik and A. E. Yagle, *Forward and inverse scattering for discrete layered lossy and absorbing media*, IEEE Trans. on Circuits and Systems-II: Analog and Digital Signal Processing **44** (1997), no. 9, 710–722.

[23] L. Garnero, A. Franchois, J. P. Hugonin, C. Pichot, and N. Joachimowicz, *Microwave imaging-complex permitivity reconstruction by simulated annealing*, IEEE Trans. on Microwave theory and techniques **39** (1991), no. 11, 1801–1807.

[24] Geophysical Survey Systems, Inc. (GSSI), *Sir system-2 operation manual*, 1994.

[25] P. E. Gill, W. Murray, and M. H. Wright, *Practical optimization*, Academic Press, London, 1981.

[26] K. M. Golden, D. Borup, M. Cheney, E. Cherkaeva, M. S. Dawson, K. Ding, A. K. Fung, D. Isaacson, S. A. Johnson, A. K. Jordan, J. A.

Kong, R. Kwok, V. Nghiem, R. G. Onstott, J. Sylvester, D. P. Winebrenner, and I. H. H. Zabel, *Inverse electromagnetic scattering models for sea ice*, IEEE Trans. on Geoscience and Remote Sensing: Part II **36** (1998), no. 5, 1675–1704.

[27] D. L. Grumman and J. J. Daniels, *Experiments on the detection of organic contaminations in the vadose zone*, Journal of Environmental and Eng. Geophysics **0** (1995), no. 1, 31–38.

[28] S. Hamran, B. Erlingsson, Y. Gjessing, and P. Mo, *Estimate of the sub-glacier dielectric constant of an ice shelf using a ground-penetrating step-frequency radar*, IEEE Trans. on Geoscience and Remote Sensing **36** (1998), no. 2, 518–525.

[29] H. Harada, D.J.N. Wall, T. Takenaka, and M. Tanaka, *Conjugate gradient method applied to inverse scattering problem*, IEEE Trans. on Antennas and Propagation **43** (1995), no. 8, 784–792.

[30] S. He, P. Fuks, and G. W. Larson, *An optimization approach to time-domain electromagnetic inverse problem for a stratified dispersive and dissipative slab*, IEEE Trans. on Antennas and Propagation **44** (1996), no. 9, 1277–1282.

[31] Y. Huang and M. Nakhkash, *Characterisation of layered dielectric medium using reflection coefficient*, IEE Electronics Letters **34** (1998), no. 12, 1207–1208.

[32] L. Ingber, *Very fast simulated reannealing*, Mathl. Comput. Modeling **12** (1989), no. 8, 967–973.

[33] L. Ingber, *Adaptive simulated annealing: lessons learned*, Tech. report, Lester Ingber Research, McLean, VA 22101, USA, 1995.

[34] N. Joachimowicz, C. Pichot, and J. P. Hugonin, *Inverse scattering: an iterative numerical method for electromagnetic imaging*, IEEE Trans. on Antennas and Propagation **39** (1991), no. 12, 1742–1752.

[35] E. M. Johansson and J. E. Mast, *Three-dimensional ground penetrating radar imaging using synthetic aperture time-domain focusing*, SPIE Conf. on Advanced Microwave and Millimeter-Wave Detectors (San Diego, California, USA), vol. 2275, July 25-26 1994, pp. 205–214.

[36] R. T. Johnk and A. Ondrejka, *Electrical material properties from a free-space time-domain RF absorber reflectivity measurement system*, 1997 IEEE International Symposium on Electromagnetic Compatibility (Austin Convention Center, Austin, Texas, USA), August 18-22 1997, pp. 537–542.

[37] R. T. Johnk, A. Ondrejka, S. Tofani, and M. Kanda, *Time-domain measurements of the electromagnetic backscatter of pyramidal absorbers and metallic plates*, IEEE Trans. on electromagnetic compatibility **35** (1993), no. 4, 429–433.

[38] A.H.G. Rinnooy Kan and G.T. Timmer, *Stochastic global optimization methods. Part I: clustering methods*, Mathematical Programming **39** (1987), 27–56.

[39] A.H.G. Rinnooy Kan and G.T. Timmer, *Stochastic global optimization methods. Part II: multi level methods*, Mathematical Programming **39** (1987), 57–78.

[40] R.W.P. King, M. Owens, and T.T. Wu, *Lateral electromagnetic waves: theory and applications to communications, geophysical exploration and remote sensing*, Springer-Verlag, New York, 1992.

[41] L. Kleinmann, J. Laugks, and K. P. Nick, *Image processing and pattern recognition in ground penetrating radar data*, Int. Geoscience and Remote

Sensing Symposium (Tokyo, Japan), IEEE, August 18-21 1993, pp. 1903–1906.

[42] J. G. Maloney, G. S. Smith, and W. R. Scott, *Accurate computation of the radiation from simple antennas using the finite-difference time-domain method*, IEEE Trans. on Antennas and Propagation **38** (1990), no. 7, 1059–1068.

[43] J. E. Mast and E. M. Johansson, *Three-dimensional ground penetrating radar imaging using multi-frequency diffraction tomography*, SPIE Conf. on Advanced Microwave and Millimeter-Wave Detectors (San Diego, California, USA), vol. 2275, July 25-26 1994, pp. 196–204.

[44] Z. Michalewicz, *Genetic algorithms + data structures = evolution programs*, Springer-Verlag, New York, 1992.

[45] M. Nakhkash, Y. Huang, W. Al-Nuaimy, and M.T.C. Fang, *Inverse problem for a nonuniform LCRG transmission line using global optimisation techniques*, International Conference on Imaging Science, Systems and Technology (CISST 98) (Las Vegas, USA), CSREA Press, July 1998, pp. 47–51.

[46] M. Nakhkash, Y. Huang, and M.T.C. Fang, *A new free-space technique for measuring the complex permittivity and thickness of materials*, IEE Conference on Antennas and Propagation (CAP 99) (York, UK), IEE, 31 March-1 April 1999, pp. 23–26.

[47] M. Nakhkash, Y. Huang, and M.T.C. Fang, *Application of the multi-level singlelinkage method to one-dimensional electromagnetic inverse scattering problem*, to be appeared in October 1999 issue of IEEE Trans. on Antennas and Propagation.

[48] S. D. Nelson, *EM modeling for GPIR using 3D FDTD modeling codes*, SPIE **2275** (1994), 186–195.

[49] M. Norgren and S. He, *An optimization approach to the frequency-domain inverse problem for a nonuniform LCRG transmission line*, IEEE Trans. on Microwave Theory and Techniques **44** (1996), no. 8, 1503–1507.

[50] The Numerical Algorithm Group, Oxford, *N.A.G. fortran library manual, mark 16*, 1996.

[51] A. Papoulis, *Probability, random variables and stochastic processes*, McGraw-Hill, Maidenhead, 1984.

[52] M. Pastorino, *Short-range microwave inverse scattering techniques for image reconstruction and applications*, IEEE Trans. on Instrum. and Measurement **47** (1998), no. 6, 1419–1427.

[53] L. Peters, J. J. Daniels, and J. D. Young, *Ground penetrating radar as a subsurface environmental sensing tool*, Proceedings of the IEEE **82** (1994), no. 12, 1802–1821.

[54] M. H. Powers and G. R. Olhoeft, *GPRMODV2: One-dimensional full waveform forward modeling of dispersive ground penetrating radar data*, Tech. report, U.S. Geological Survey, Denver, CO 80225-0046, USA, 1995.

[55] S. Ramo, J. R. Whinnery, and T. V. Duzer, *Fields and waves in communication electronics*, Wiley, New York, 1994.

[56] J. M. Renders and S. P. Flasse, *Hybrid methods using genetic algorithms for global optimization*, IEEE Trans. on Systems, Man, and Cybernetics-Part B: Cybernetics **26** (1996), no. 2, 243–258.

[57] M. Sen and P. L. Stoffa, *Global optimization methods in geophysical inversion*, Elsevier, Amsterdam, 1995.

[58] Silicon Graphics, Inc., *LC: an electromagnetic analysis tool*, 1998.

[59] M. Slaney, A. C. Kak, and L. E. Larsen, *Limitations of imaging with first-order diffraction tomography*, IEEE Trans. on Microwave theory and techniques **MTT-32** (1984), no. 8, 860–874.

[60] G. S. Smith and W. R. Scott, *A scale model for studying ground penetrating radars*, IEEE Trans. on Geoscience and Remote Sensing **27** (1989), no. 4, 358–363.

[61] U. Spagnolini, *Permittivity measurements of multilayered media with monostatic pulse radar*, IEEE Trans. on Geoscience and Remote Sensing **35** (1997), no. 2, 454–463.

[62] M. R. Spiegel, *Mathematical handbook*, McGraw-Hill, New York, 1968.

[63] A. G. Tijhuis, *Iterative determination of permittivity and conductivity profiles of a dielectric slab in the time domain*, IEEE Trans. on Antennas and Propagation **AP-29** (1981), no. 2, 239–245.

[64] T. Uno and S. Adachi, *Inverse scattering method for one-dimensional inhomogeneous layered media*, IEEE Trans. on Antennas and Propagation **AP-35** (1987), no. 12, 1456–1466.

[65] J. R. Wait, *Wave propagation theory*, Pergamon Press, New York, 1981.

[66] W. H. Weedon, W. C. Chew, and C. A. Ruwe, *Step-frequency radar imaging for NDE and GPR applications*, SPIE Conf. on Advanced Microwave and Millimeter-Wave Detectors (San Diego, California, USA), vol. 2275, July 25-26 1994, pp. 156–167.

[67] A. E. Yagle and J. L. Frolik, *On the feasibility of impulse reflection response data for the two-dimensional inverse scattering problem*, IEEE Trans. on Antennas and Propagation 44 (1996), no. 12, 1551–1564.